Enhancing Performance of Next-Generation Vehicular and Spectrum Sharing Wireless Networks: Practical Algorithms and Fundamental Limits

Raghunandan M. Rao

Dissertation submitted to the Faculty of the
Virginia Polytechnic Institute and State University
in partial fulfillment of the requirements for the degree of

Doctor of Philosophy
in
Electrical Engineering

Jeffrey H. Reed, Chair
Vuk Marojevic, Co-Chair
Harpreet S. Dhillon
R. Michael Buehrer
Mazen H. Farhood

July 22, 2020
Blacksburg, Virginia

Keywords: Link Adaptation, Channel State Information Acquisition, Vehicular Communications, Radar-Cellular Coexistence, Spectrum Sharing, Stochastic Geometry

Enhancing Performance of Next-Generation Vehicular and Spectrum Sharing Wireless Networks: Practical Algorithms and Fundamental Limits

Raghunandan M. Rao

(ABSTRACT)

Over the last few decades, wireless networks have morphed from traditional cellular/wireless local area networks (WLAN), into a wide range of applications, such as the Internet-of-Things (IoT), vehicular-to-everything (V2X), and smart grid communication networks. This transition has been facilitated by research and development efforts in academia and industry, which has resulted in the standardization of fifth-generation (5G) wireless networks. To meet the performance requirements of these diverse use-cases, 5G networks demand higher performance in terms of data rate, latency, security, and reliability, etc. At the physical layer, these performance enhancements are achieved by (a) optimizing spectrum utilization shared amongst multiple technologies (termed as *spectrum sharing*), and (b) leveraging advanced spatial signal processing techniques using large antenna arrays (termed as *massive MIMO*). In this dissertation, we focus on enhancing the performance of next-generation vehicular communication and spectrum sharing systems.

In the first contribution, we present a novel pilot configuration design and adaptation mechanism for cellular vehicular-to-everything (C-V2X) networks. Drawing inspiration from 4G and 5G standards, the proposed approach is based on limited feedback of indices from a codebook comprised of quantized channel statistics information. We demonstrate significant rate improvements using our proposed approach in terrestrial and air-to-ground (A2G) vehicular channels.

In the second contribution, we demonstrate the occurrence of cellular link adaptation failure due to channel state information (CSI) contamination, because of coexisting pulsed radar signals that act as non-pilot interference. To mitigate this problem, we propose a low-complexity semi-blind SINR estimation scheme that is robust and accurate in a wide range of interference and noise conditions. We also propose a novel *dual CSI feedback* mechanism for cellular systems and demonstrate significant improvements in throughput, block error rate, and latency, when sharing spectrum with a pulsed radar.

In the third contribution, we develop fundamental insights on underlay radar-massive MIMO spectrum sharing, using mathematical tools from stochastic geometry. We consider a multi-antenna radar system, sharing spectrum with a network of massive MIMO base stations distributed as a homogeneous Poisson Point Process (PPP) outside a circular exclusion zone centered around the radar. We propose a tractable analytical framework, and characterize the impact of *worst-case downlink cellular interference* on radar performance, as a function of key system parameters. The analytical formulation enables network designers to systematically isolate and evaluate the impact of each parameter on the worst-case radar performance and complements industry-standard simulation methodologies by establishing a baseline performance for each set of system parameters, for current and future radar-cellular spectrum sharing deployments.

Finally, we highlight directions for future work to advance the research presented in this dissertation and discuss its broader impact across the wireless industry, and policy-making.

Enhancing Performance of Next-Generation Vehicular and Spectrum Sharing Wireless Networks: Practical Algorithms and Fundamental Limits

Raghunandan M. Rao

(GENERAL AUDIENCE ABSTRACT)

The impact of today's technologies has been magnified by wireless networks, due to the standardization and deployment of fifth-generation (5G) cellular networks. 5G promises faster data speeds, lower latency and higher user security, among other desirable features. This has made it capable of meeting the performance requirements of key infrastructure such as smart grid and mission-critical networks, and novel consumer applications such as smart home appliances, smart vehicles, and augmented/virtual reality. In part, these capabilities have been achieved by (a) better spectrum utilization among various wireless technologies (called spectrum sharing), and (b) serving multiple users on the same resource using large multi-antenna systems (called massive MIMO). In this dissertation, we make three contributions that enhance the performance of vehicular communications and spectrum sharing systems.

In the first contribution, we present a novel scheme wherein a vehicular communication link adapts to the channel conditions by controlling the resource overhead in real-time, to improve spectral utilization of data resources. The proposed scheme enhances those of current 4G and 5G networks, which are based on limited feedback of quantized channel statistics, fed back from the receiver to the transmitter.

In the second contribution, we show that conventional link adaptation methods fail when 4G/5G networks share spectrum with pulsed radars. To mitigate this problem, we develop a comprehensive signal processing framework, consisting of a hybrid SINR estimation method that is robust and accurate in a wide range of interference and noise conditions. Concurrently, we also propose a scheme to pass additional information that captures the channel conditions in the presence of *radar interference*, and analyze its performance in detail.

In the third contribution, we focus on characterizing the impact of 5G cellular interference on a radar system in shared spectrum, using mathematical tools from stochastic geometry. We model the *worst-case interference* scenario, and study the impact of the system parameters on the worst-case radar performance.

In summary, this dissertation advances the state-of-the-art in vehicular communications and spectrum sharing, through (a) novel contributions in protocol design and (b) development of mathematical tools for performance characterization.

To my Family

Acknowledgements

Writing this dissertation has come at the end of a long and fulfilling journey for me, one that I will cherish for the rest of my life. I am deeply indebted to my doctoral advisors Dr. Jeffrey Reed and Dr. Vuk Marojevic, for their consistent feedback that guided me through all aspects of academic research, ranging from problem formulation to publicizing the results. They always gave me the support and freedom to pursue research problems of my interest, and provided me with excellent professional development opportunities to further my career in wireless research.

I also owe my gratitude to Dr. Harpreet Dhillon for being an excellent mentor, and always taking an interest in my career. His precious guidance led me to develop crucial analytical and writing skills, and our collaboration spawned the third contribution of this dissertation. I also thank Dr. R. Michael Buehrer and Dr. Mazen Farhood for serving on my committee, and providing valuable feedback about my research contributions.

I would like to thank the U.S. National Science Foundation (Grants CNS-1564148 and CNS-1642873) and National Spectrum Consortium (Grant NSC-16-0403), for sponsoring my doctoral research. I also thank my mentors Ramesh C. Palat and Dilip Bethanabhotla at Blue Danube Systems, Anthony Fischetti at MACOM, and Boon L. Ng at Samsung Research America, for giving me terrific internship opportunities. My summers in Santa Clara, Lowell and Plano were some of the most productive periods during my time in Virginia Tech.

I would also like to thank Hilda, Nancy, Randall, and Makensi, for all the administrative and technical support they gave me during my stint in Wireless@VT.

I will deeply miss the companionship and support that I got from my fellow grad students in Wireless@VT. You guys are some of the brightest and fun people I've ever known. The strong friendships and collaborations that I developed here are probably the most important things that I'll carry forward. The same goes for my roommates, which I'm not even going to list here, I've had way too many!

I owe this success to my parents, grandparents, and dear sister Deepti. Their sacrifice, unconditional love, and support gave me the foundation and resources to undertake this journey. I would also like to thank Guru and Vasu Mama for giving tough love, being the devil's advocate, and strongly encouraging me to follow my dreams. I would also like to thank my lovely wife for her patience, and for being a cheerful companion.

Contents

List of Abbreviations

3GPP	Third generation partnership project
AAECC	Average area-equivalent circular cell
A2G	Air-to-ground
ACK	Acknowledgement
ARQ	Automatic repeat request
AMC	Adaptive modulation and coding
BEP	Bit error probability
BER	Bit error rate
BJ	Barrage jamming
BLER	Block error rate
BS	Base station
CA	Carrier aggregation
CBC	Circumcircle-based cell
CDF	Cumulative distribution function
CLT	Central limit theorem
CoMP	Cooperative Multipoint
CORNET	Cognitive radio network
CQI	Channel quality indicator
CRC	Cyclic redundancy check
CRS	Cell-specific reference signal
CSI	Channel state information
CSI-RS	Channel state information reference signal
C-V2X	Cellular V2X
DIUC	Dominant interfering user cluster
DoS	Denial of service
DMRS	Demodulation reference signal
eNB	Evolved node B
EPA	Extended Pedestrian A
FA	False alarm
FBMC	Filter-bank multicarrier
FCC	Federal communications commission

FDD	Frequency division duplex
FRESH	Frequency shift
FTN	Faster than Nyquist
HARQ	Hybrid automatic repeat request
ICC	Independence checking coding
ICI	Inter-carrier interference
I-CSI	Instantaneous CSI
IoT	Internet of things
ITU-T	International Telecommunication Union - Telecommunication standardization sector
JSDM	Joint spatial division and multiplexing
JSR	Jammer to signal ratio
LAA	License assisted access
LDPC	Low density parity check
LoS	Line of sight
LFM	Linear frequency modulation
LS	Least squares
LTE/LTE-A	Long-term evolution/LTE advanced
LTE-U	LTE-Unlicensed
MAC	Medium access control
MAP	Maximum a posteriori
MCS	Modulation and coding scheme
MI	Mutual information
MIMO	Multiple input multiple output
ML	Maximum likelihood
MMSE	Minimum mean squared error
MPC	Multipath component
MRT	Maximum ratio transmission
MSE	Mean square error
MU-MIMO	Multi-user MIMO
NACK	Negative ACK
NLoS	Non-line of sight
NOMA	Non-orthogonal multiple access
NPI	Non-pilot interference
NR	New Radio
NR-U	NR-Unlicensed
OFDM	Orthogonal frequency division multiplexing
OFDMA	Orthogonal frequency division multiple access
PCFICH	Physical control format indicator channel
PCI	Physical Cell Identity
PDSCH	Physical downlink shared channel
PHY	Physical layer

PI	Pilot interference
PMI	Precoding matrix indicator
PPP	Poisson point process
PRACH	Physical random access channel
PSS	Primary synchronization signal
PSUN	Precoded subcarrier nulling
PUCCH	Physical uplink control channel
QAM	Quadrature amplitude modulation
QPSK	Quadrature phase shift keying
RB	Resource Block
RE	Resource element
RF	Radio frequency
ROC	Receiver operating characteristic
RRM	Radio resource management
RTT	Round trip time
RZF	Regularized zero forcing
SAW	Stop-and-wait
S-CSI	Statistical CSI
SC-FDMA	Single carrier-frequency division multiple access
S(I)NR	Signal to (interference plus) noise ratio
SISO	Single input single output
SSS	Secondary synchronization signal
SU-MIMO	Single-user MIMO
TB	Transport block
TDD	Time division duplex
TM	Transmission mode
TTI	Transmission time interval
UAV	Unmanned aerial vehicle
UFMC	Universal filtered multicarrier
UMa	Urban macro
U-NII	Unlicensed national information infrastructure
URA	Uniform rectangular array
UE	User equipment
V2X	Vehicular-to-everything
Wi-Fi	Wireless fidelity
WLAN	Wireless local area network
ZF	Zero forcing

List of Figures

List of Tables

Chapter 1

Introduction

Wireless communication systems have become pervasive in the commercial and defense sectors over the last century. Over the last fifteen years in particular, cellular wireless networks have become the primary technology for broadband internet access, in addition to the voice and paging services that cellular was known for in the 20th century. Over the last decade, the demand for high speed and low latency wireless services have been increasing exponentially [3], and the trend is expected to continue over the next decade. In the quest for higher throughput and lower latency communications, the Third Generation Partnership Project (3GPP) has released the latest cellular standard: Release 15, which is also termed as 5G New Radio (5G NR). Compared to its predecessor, the Fourth Generation Long-Term Evolution (4G LTE) standard, 5G NR aims to enhance key performance metrics such as data rate, latency, security and scalability.

Among the various techniques that are part of the later releases of LTE (in particular Release 13, also termed as LTE-Advanced Pro) and NR, the role of two particular technologies play an important role in enhancing the spectral utilization: massive MIMO and spectrum sharing. In simple terms, massive MIMO refers to a class of advanced spatial signal processing techniques that leverage large antenna arrays at the base station to increase the dimension of spatial multiplexing by an order of magnitude compared to current LTE deployments, thereby promising an order of magnitude enhancement in spectral efficiency. Pioneering research by industry and academia on the fundamental aspects of massive MIMO [4, 5], real-world channel measurements [6, 7], prototyping and demonstration [8] and standardization [9, 10], have led to its commercial realization in LTE-A Pro and 5G NR.

On the other hand, spectrum sharing improves the spectral efficiency by sharing spectrum between multiple wireless technologies in the temporal and spatial dimensions. Spectrum sharing is especially effective if *licensed spectrum* is under-utilized, which is true for a lot of frequency bands in the sub-6 GHz spectrum. In the literature, spectrum sharing has been studied from a fundamental standpoint [11], as well as between different wireless technologies such as radar and wireless local area networks (WLAN) [12, 13], radar and cellular [14, 15, 16, 17], and cellular and WLAN [18, 19]. Through the support of various government agencies all over the world, spec-

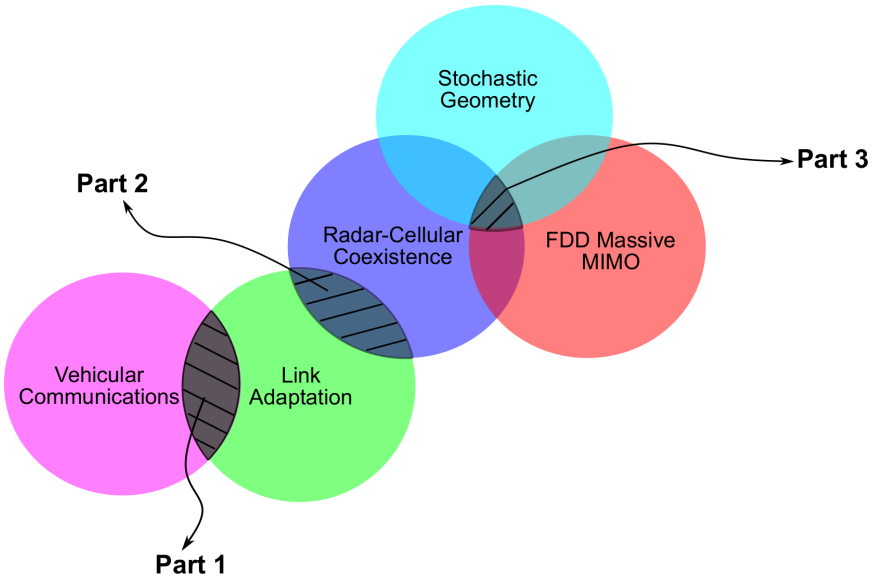

Figure 1.1: Research domains covered in this dissertation.

trum sharing in various frequency bands has been enabled by ratification of rules and policies governing spectrum usage by the parties involved. Particularly in the United States, spectrum policies have been designed for sharing in the 1.3 GHz [20], 3.5 GHz [21], 5 GHz [22], and the 28 GHz mmWave frequency bands [23]. Aided by these developments, standardization efforts for enabling harmonious coexistence of cellular technologies sharing spectrum with other wireless technologies in unlicensed or shared (such as the 3.5 GHz and 5 GHz) bands have resulted in standards such as License Assisted Access [24] and more recently, NR-Unlicensed [25].

In addition to enhancing the key performance metrics compared to its predecessors, 5G NR encompasses a wide variety of use cases and deployments ranging from the Internet of Things (IoT) to vehicular communications. To date, this makes it the most ambitious effort to incorporate a diverse set of use cases and technologies into a single wireless standard. Since low to medium mobility terrestrial cellular networking technologies have matured over the last two decades through extensive analysis and deployment, extremely mobile terrestrial and aerial communications at an unprecedented scale represents the next frontier in cellular communications. The standardization of 3GPP LTE Release 8 laid the foundation of high mobility cellular communications through its careful design of reference signals, in addition to other features [26]. However, the need for ultra-reliable low latency communications for vehicular safety applications led to modification of, among other things, the physical layer, resulting in the cellular-assisted vehicular-to-everything (CV2X) standard [27]. While CV2X has been standardized in 3GPP Release 14, the feasibility and protocol mechanisms for non-terrestrial channels, especially unmanned aerial vehicle (UAV)-to-ground (also known as A2G channels) and UAV-to-UAV communications, have been studied by 3GPP for standardization for Release 15 and beyond [28].

1.1 Research Contributions

This dissertation is composed of three contributions, with each part focusing on a different aspect of next-generation wireless networks. Specifically, it focuses on

1. Novel CSI estimation, feedback, and link adaptation schemes for next-generation vehicular communication systems,
2. Robust CSI estimation and feedback for current and future cellular systems in shared spectrum with pulsed radars, and
3. Mathematical modeling and fundamental characterization of the impact of massive MIMO cellular interference on radar systems in underlay spectrum sharing scenarios using stochastic geometry.

Fig. 1.1 shows the research domains covered in this dissertation. In the subsections below, we summarize the contribution of each part in more detail.

1.1.1 Novel CSI Estimation, Feedback, and Link Adaptation Scheme for Next-Generation Vehicular Communication Systems

Chapter 2 proposes a novel channel state information (CSI) estimation method and feedback mechanisms necessary to adapt the pilot/reference signal overhead in orthogonal frequency division multiplexing (OFDM)-based cellular systems. The key objective is to maximize the achievable rate, by trading off post-equalizer SINR enhancement and pilot overhead, in a *non-stationary vehicular channel*. In particular, the key contributions of this part are listed below.

1. Analysis of the channel estimation mean squared error, and derivation of closed-form expressions in doubly selective (temporal as well as spectral fading) wireless channels, for OFDM pilots arranged in a "diamond-pattern".
2. A novel CSI estimation and quantization scheme to adapt pilot patterns in *nonstationary channels* using feedback of indices from a 'channel statistics codebook', with low computational complexity and feedback overhead.
3. Design of limited CSI feedback mechanisms necessary to implement rate-maximizing pilot configuration design in nonstationary wireless channels. This is similar to codebook-based feedback schemes such as channel quality indicator/precoding matrix indicator (CQI/PMI), that are used in LTE and NR.
4. Extension of the CSI estimation and feedback schemes to carrier aggregation-OFDM (CA-OFDM) systems.

5. A comprehensive analysis of the performance of the proposed schemes using numerical simulations in vehicular and A2G channels, and its comparison with state-of-the-art schemes.

Peer-Reviewed Publications

The research presented in this part has been published in the following peer-reviewed publications:

(J1) **R. M. Rao**, V. Marojevic and J. H. Reed, "Adaptive Pilot Patterns for CA-OFDM Systems in Nonstationary Wireless Channels," *IEEE Transactions on Vehicular Technology*, vol. 67, no. 2, pp. 1231-1244, Feb. 2018.

(C1) **R. M. Rao**, V. Marojevic, and J. H. Reed, "Rate-Maximizing OFDM Pilot Patterns for UAV Communications in Nonstationary A2G Channels," *in Proceedings of the IEEE Vehicular Technology Conference (VTC-Fall2018)*, pp. 1–5, August, 2018.

1.1.2 Robust CSI Estimation and Feedback for 4G and 5G Cellular Systems in Shared Spectrum with Pulsed Radars

Modern cellular and WLAN standards use adaptive modulation, coding and MIMO transmission mode selection, commonly referred to as *link adaptation*, to maximize the throughput under a reliability constraint. Statistical-CSI (S-CSI) estimation and feedback plays a crucial role in optimizing link performance metrics such as throughput and block error rate (BLER). In order to facilitate a low-complexity and scalable implementation, LTE, NR and WiFi standards employ reference/pilot signals and limited feedback to implement accurate CSI acquisition. By design, these pilots are known to both the transmitter and receiver, and are sent concurrently with non-pilot signals (such as data and other control information). The underlying assumption is that statistics of the channel fading, interference and noise is the same on both pilot as well as non-pilot signals. However, this assumption is violated in non-pilot interference (NPI) scenarios, which selectively affects *non-pilot signals* and avoids the reference signal. This is opposed to selectively interfering with pilot symbols to cause the channel to look worse than it is. This part of the dissertation first shows that the link adaptation mechanisms fail in such interference scenarios, and focuses on optimizing cellular link-level performance in the presence of NPI.

1.1.3 Impact of NPI on S-CSI Acquisition and Link Adaptation

In Chapter 3, we demonstrate through hardware experiments and numerical link-level simulations that NPI degrades the throughput and BLER performance of the cellular downlink. Diagnostic evaluations reveal that this performance degradation is a result of *contaminated SINR estimates*,

which occur in the presence of NPI. We analyze the impact of NPI on the latency performance of the link, by deriving an approximate closed-form expression of the retransmission-induced latency as a function of the BLER.

1.1.4 Fundamental Insights on Demodulation and Limited CSI Feedback in Pulsed Radar-Cellular Spectrum Sharing Scenarios

In Chapter 4, we rigorously prove that *most pulsed radars are effectively non-pilot interferers* to cellular systems in underlay spectrum sharing scenarios. To prove this, we consider a cellular system with equispaced pilots, impaired by a periodic radar pulse train. By deriving the upper/lower bounds that one or more pilots are interfered by radar pulses in a finite estimation window, we show that pulsed radars are *a significant source* of non-pilot interference. Upon further analysis, exact analytical results reveal that most pulsed radars *are sources of non-pilot interference*, which impair pilot-aided S-CSI estimates of the *interference channel*.

1.1.5 Semi-Blind Post-Equalizer SINR Estimation and Dual CSI Feedback for Radar-Cellular Coexistence

For cellular systems sharing spectrum with radars, the presence of pulsed interference results in two states: *fading channel* and the *interference channel*. In Chapter 5, we present a novel semi-blind post-equalizer SINR estimation framework to reliably estimate the SINR for both channel states in the presence of pulsed radars. A key component of this framework is a *heuristic-based post-equalizer SINR estimation method*, whose performance is analytically characterized, and evaluated for different quadrature amplitude modulation (QAM) schemes. Our analysis of its accuracy and robustness performance reveals its usefulness as a low-complexity SINR estimator for pulsed radar-cellular spectrum sharing scenarios. Then, we propose a comprehensive framework to estimate the radar parameters and the post-equalizer SINR of the data block, and evaluate its performance under 3GPP-compliant system parameters and channel conditions. To facilitate efficient link adaptation, we propose a simple extension to cellular standards termed as *dual-CSI feedback*, which allows for accurate CSI feedback for *fading* as well as *interference channel* states. Using 3GPP-compliant link-level simulations for LTE-A, we demonstrate a significant improvement in key link performance metrics in radar-cellular coexistence scenarios using our proposed framework.

Peer-Reviewed Publications

The research presented in this part has been accepted or published in the following peer-reviewed publications:

(C2) **R. M. Rao**, V. Marojevic, and J. H. Reed, "Analysis of Non-Pilot Interference on Link Adaptation and Latency in Cellular Networks," *in Proceedings of the IEEE Vehicular Technology Conference (VTC-Spring2019)*, pp. 1–5, April 2019.

(J2) **R. M. Rao**, V. Marojevic, and J. H. Reed, "Probability of Pilot Interference in Pulsed Radar-Cellular Coexistence: Fundamental Insights on Demodulation and Limited CSI Feedback", *IEEE Communications Letters*, vol. 24, no. 8, pp. 1678-1682, Aug. 2020.

(J3) **R. M. Rao**, V. Marojevic, and J. H. Reed, "Semi-Blind Post-Equalizer SINR Estimation and Dual CSI Feedback for Radar-Cellular Coexistence", *IEEE Transactions on Vehicular Technology*, vol. 69, no. 9, pp. 1-1, Sep. 2020.

1.1.6 Fundamentals of Underlay Radar-Massive MIMO Spectrum Sharing Scenarios

In Chapter 6, we consider an underlay radar-cellular downlink spectrum sharing scenario, in which both the radar as well as the cellular base stations (BSs) are equipped with full-dimension massive MIMO (FD-MIMO) antenna arrays with 3D beamforming capabilities. We consider a single radar located at the origin, and model the locations of BSs using a homogeneous Poisson point process (PPP). A circular exclusion zone centered around the radar is established, such that only the BSs located outside the circle are allowed to operate. Assuming a line-of-sight (LoS), or near-LoS channel between the radar and each BS, we derive an analytical expression of a tight upper bound on the average interference power due to the massive MIMO downlink. This calculation is based on a novel construction, wherein each Poisson Voronoi (PV) cell is modeled by its circumcircle, to bound the effect of the random cell shapes on average interference.

However, this model is intractable for characterizing the interference distribution because of the correlation between the circumradii of adjacent PV cells. To circumvent this issue, we propose a tractable nominal interference model, where each PV cell is modeled as a circle with an area equal to the average area of the typical cell. We quantify the gap in the average interference power betweeen these two models, and show that the upper bound is tight for realistic deployment parameters. Under the nominal interference model, we derive the equal interference contour in closed-form, and characterize the interference distribution using the dominant interferer approximation.

Finally, we use tractable expressions for the interference distribution to characterize important radar performance metrics such as the *spatial probability of false alarm/detection* in a quasi-static target tracking scenario. We validate the accuracy of our analytical approximations using extensive numerical results, which (a) reveal useful trends in the average interference as a function of the deployment parameters (BS density, exclusion zone radius, antenna height, transmit power etc.), and (b) provide useful system design insights in the form of radar receiver operating characteristic (ROC) curves for the current and future radar-cellular spectrum sharing scenarios.

Peer-Reviewed Publications

The work presented in this chapter has been accepted, or is under review in the following peer-reviewed publications:

(J4) **R. M. Rao**, H. S. Dhillon, V. Marojevic and J. H. Reed, "Underlay Radar-Massive MIMO Spectrum Sharing: Modeling Fundamentals and Performance Analysis ," *Under Review, IEEE Transactions on Wireless Communications*, available *arXiv:2008.02100*, 2020.

(C3) **R. M. Rao**, H. S. Dhillon, V. Marojevic and J. H. Reed, "Analysis of Worst-Case Interference in Underlay Radar-Massive MIMO Spectrum Sharing Scenarios," *in Proceedings of the IEEE Global Communications Conference (GLOBECOM)*, pp. 1-6, Waikoloa, HI, USA, 2019.

1.2 Intellectual Property and Other Refereed Publications

The following peer-reviewed publications and patents are tangible outcomes of research projects undertaken as part of my graduate education and summer internships, but are not included in this dissertation.

Patents

(P1) **R. M. Rao**, D. Bethanabhotla, R. C. Palat, "Enhancing Throughput using Agile Beam Switching and User Scheduling in Cellular Systems," *US Patent App. No. 16/600428*, 2020.

Journal Papers and Magazine Articles

(J5) B. Shang, L. Liu, **R. M. Rao**, V. Marojevic, J. H. Reed, "3D Spectrum Sharing for Hybrid D2D and UAV Networks," *IEEE Transactions on Communications*, vol. 68, No. 9, pp. 1-1, 2020.

(M1) M. Lichtman, R. P. Jover, M. Labib, **R. M. Rao**, V. Marojevic and J. H. Reed, "LTE/LTE-A Jamming, Spoofing, and Sniffing: Threat Assessment and Mitigation," *IEEE Communications Magazine*, vol. 54, no. 4, pp. 54-61, April 2016.

Conference Papers

(C4) V. Marojevic, D. Chheda, **R. M. Rao**, R. Nealy, J. Park and J. H. Reed, "Software-Defined LTE Evolution Testbed Enabling Rapid Prototyping and Controlled Experimentation," *in Proceedings of the IEEE Wireless Communications and Networking Conference (WCNC)*, pp. 1-6, San Francisco, CA, 2017.

(C5) V. Marojevic, **R. M. Rao**, S. Ha and J. H. Reed, "Performance Analysis of a Mission-Critical Portable LTE System in Targeted RF Interference," *in Proceedings of the IEEE Vehicular Technology Conference (VTC-Fall2017)*, pp. 1-6, Toronto, ON, 2017.

(C6) **R. M. Rao**, S. Ha, V. Marojevic and J. H. Reed, "LTE PHY Layer Vulnerability Analysis and Testing Using Open-Source SDR Tools," *in Proceedings of the IEEE Military Communications Conference (MILCOM)*, pp. 744-749, Baltimore, MD, 2017.

(C7) M. Lichtman, **R. M. Rao**, V. Marojevic, J. Reed and R. P. Jover, "5G NR Jamming, Spoofing, and Sniffing: Threat Assessment and Mitigation," *in Proceedings of the IEEE International Conference on Communications Workshops (ICC Workshops)*, pp. 1-6, Kansas City, MO, 2018.

(C8) V. Marojevic, A. V. Padaki, **R. M. Rao**, J. H. Reed, "Measuring Hardware Impairments with Software-Defined Radios", *in Proceedings of the ASEE/IEEE Frontiers in Education (FIE)*, pp. 1-6, San Jose, CA, 2018.

(C9) **R. M. Rao**, D. Bethanabhotla and R. C. Palat, "Enhancing Throughput Using Agile Beam Switching and User Scheduling in Cellular Systems," *in Proceedings of the IEEE Vehicular Technology Conference (VTC-Fall2019)*, pp. 1-7, Honolulu, HI, USA, 2019.

Part I

Novel CSI Estimation, Feedback, and Link Adaptation Scheme for Next-Generation Vehicular Communication Systems

Chapter 2

Rate-Maximizing Pilot Configurations for Vehicular Communication Systems: Design, Feedback Mechanisms, and Performance

2.1 Introduction

The Third Generation Partnership Project (3GPP) froze the first set of technical specifications of Release 15, termed as 5G New Radio (NR) Non-Standalone in December 2017, and 5G NR Standalone and June 2018 [31]. Compared to the current 4G wireless networks, 5G NR brings enhancements in capacity, latency, coverage, spectrum utilization, and the ability to handle heterogeneous traffic [32]. In addition to mobile broadband access, 5G addresses a plethora of new use cases compared to its predecessor, such as Internet of Things (IoT), Cellular-assisted Vehicular-to-Everything (CV2X), and Ultra-Reliable Low Latency Communications (URLLC) etc.

In the quest for higher capacity, 5G introduces an Orthogonal Frequency Division Multiplexing (OFDM)-based physical layer (PHY) that is compatible with a diverse range of frequency bands (sub-6 GHz and millimeter-wave), and also introduces a high-order multi-user spatial multiplexing technology using massive antenna arrays, called 'Massive MIMO' [2]. To support the different wireless propagation environments encountered, the PHY has some flexibility by allowing multiple waveform configurations (subcarrier spacing, OFDM symbol duration, cyclic prefix duration etc.) [33].

As NR evolves, waveform flexibility will continue to be the key to enhance spectral efficiency while supporting users under different channel conditions such as terrestrial (frequency selective fading, low or high mobility), air to ground (frequency flat fading, low/high mobility) or

This chapter is based on the works published in [29], [30].

combinations of these two (which is encountered in applications such as IoT). The capabilities of spectrum aggregation (also known as carrier aggregation) which was introduced in 3GPP Long-Term Evolution-Advanced (LTE-A), has also been enhanced in NR to maximize utilization of fragmented and unfragmented spectrum in licensed and unlicensed bands.

Even though NR offers some flexibility in choosing the waveform configuration, (a) the number of candidates allowed is rather limited, and (b) the configuration, once chosen, is typically not changed for long durations of time (order of days). In other words, there are no provisions or mechanisms to support *real-time adaptation* of waveform configurations based on reliable channel state information (CSI). Open questions still remain in the area of waveform adaptation, especially those related to waveform parameter selection and feedback schemes, given a specific channel environment. In the evolution from 4G to 5G and beyond, there has considerable research regarding the adaptation of transmission parameters at the physical layer in order to enhance the spectral efficiency of the physical layer [34, 35, 36].

From a protocol standpoint in the PHY layer, one of the factors contributing to spectral (in)efficiency is control signal overhead. Although not all control channels can be eliminated to reduce system overhead, one class of control signals whose overhead *can be controlled* are 'pilots' or 'reference signals'. Pilot signals are known to both the transmitter and the receiver, which aid in (a) channel estimation, (b) equalization and demodulation, and (c) link adaptation [37]. Most standards define a fixed number of pilots to be deployed. However, the pilot density needs to be designed to trade off estimation performance versus resource overhead. Having a consistently high pilot density is a waste of resources when the channel remains flat in time or frequency, or both.

2.1.1 Motivation for Adaptive Pilot Configurations

Wireless channels exhibit different characteristics based on the terrain, propagation environment, obstructions, mobility of users etc. In sub-6 GHz frequency bands, (a) low mobility and strong line of sight (LoS) channels are is flat in time and frequency, while (b) high mobility with a strong multipath channel exhibit strong frequency selectivity and fast temporal fading. In addition, the propagation characteristics vary completely for millimeter-wave (mmmWave) frequency bands. Most wireless standards are designed to operate in the worst channel conditions. For example, the pilot spacing in LTE is designed to satisfactorily capture channel variations for root mean square delay spread $\tau_{rms} = 991$ ns and a user velocity of 500 km/h at a center frequency $f_c = 2$ GHz [37]. But the wireless channel statistics might be better for a significant number of users at a given point of time, which can be potentially leveraged to reduce resource overhead.

The key idea of pilot adaptation is shown in Fig. 2.1 where (a) pilot spacing along the time axis is a function of the *coherence time* of the channel; it is increased when the coherence time is high and decreased when it is low, and (b) pilot spacing along the frequency axis is a function of the *coherence bandwidth* of the channel; it is increased when the coherence bandwidth of the channel is high and decreased when it is low.

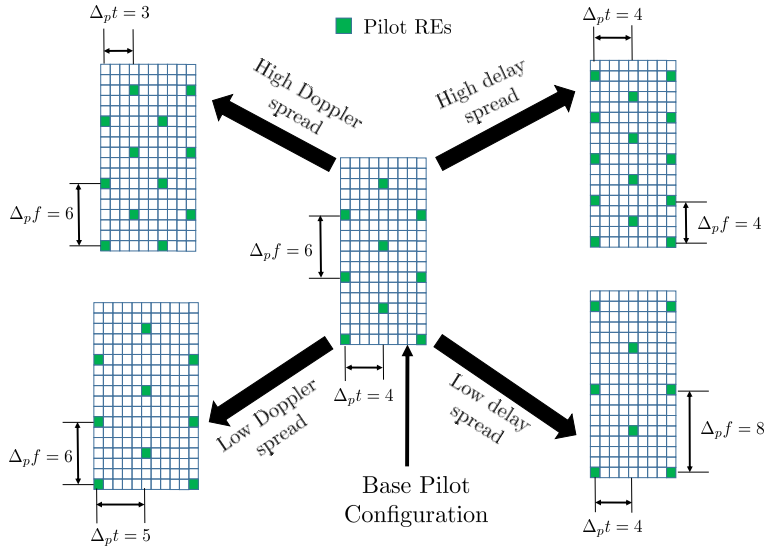

Figure 2.1: Illustration of pilot adaptation in the OFDM resource grid based on varying channel conditions. The sub-figures show a portion of the time-frequency resource grid. The pilot pattern can be adapted over time, adjusting to changing channel statistics *at a suitable time granularity.*

For high mobility 4G/5G channel environments such as vehicular-to-vehicular (V2V) and air-to-ground channels, the fading environment can change rapidly and significantly:

1. Channel temporal correlation varies due to changes in doppler frequency f_d (f_d scales linearly with vehicular velocity). This occurs when the vehicle accelerates, decelerates or changes its direction,

2. Channel spectral correlation varies due to changes in scattering environment as the vehicle moves from one multipath environment to another, and

3. Channel spatial correlation varies due to changes in angular spread as a vehicle moves from one scattering environment to another.

As the second-order channel fading statistics can vary in V2V and air-to-ground channels, they are *nonstationary* and are more likely to benefit from pilot spacing and power adaptation.

2.1.2 Related Work

2.1.2.1 Adaptive Pilot Configurations

One of the natural consequences of increasing pilot density in an OFDM waveform is an improvement in the channel estimation mean sqaured error (MSE) performance and the Bit Error Rate

(BER). The authors in [38] obtained pilot periods using mean square error (MSE) of channel estimates as the criterion, and showed that equal powered and equi-spaced pilot symbols lead to the least MSE. In [39], the pilot spacing was designed with Bit Error Rate (BER) as the cost function, and the authors proposed a new pilot-pattern which has the potential of reducing the noise power on the pilot sub-channel estimate by half. The authors in [40] demonstrated pilot configurations based on Kalman channel estimators, by limiting the effective Signal-to-Noise-Ratio (SNR) within a desired bound.

For 5G, since maximizing spectral efficiency is one of the key goals of 5G PHY layer technologies, the metrics fundamentally defined by these objectives such as *capacity, achievable rate, throughput* etc need to be considered as the cost function. Byun et al. [41] aim to minimize feedback delays and synchronization mismatch of pilot spacing information in an OFDM system. The authors prioritized maximization of bit error rate (BER) and channel estimation mean square error (MSE), sometimes at the cost of spectral efficiency. Ali et al. [42] adapt the pilot distribution in OFDM-based Wireless Local Area Networks (WLAN) according to the short-term channel gain variations to maximize the throughput. Sheng at al. [43] propose to maximize the sum rate using a power allocation scheme between pilot and data symbols for OFDM in a high-speed train (HST) environment. The authors use an information-theoretic approach to solve this problem, by first estimating the average channel complex gains and then using it in a HST basis expansion channel model to formulate a rate-maximization problem. Karami and Beaulieu [44] design a joint adaptive power loading and pilot spacing algorithm to maximize the average mutual information between the input and output of OFDM systems. Simko, Wang and Rupp [45] consider optimal power allocation between pilot and data symbols in an OFDM system, and apply it to the LTE downlink. The authors consider two channel estimation algorithms: Least Squares (LS) and Linear MMSE (LMMSE). This work was extended by the same authors in [46], which considers optimization of pilot spacing and power for SISO and MIMO-OFDM systems (without carrier aggregation). They propose mapping the pilot pattern to the channel quality indicator (CQI) of LTE.

The idea of pilot parameter adaptation has also been proposed for multi-user MIMO and 5G technologies such as massive MIMO. Kim et. al [47] proposed an uplink and downlink pilot power and rate adaptation approach to improve energy efficiency. When adapting pilot spacing, Ksairi et. al [48] proposed a scheduling algorithm to group users with similar channel statistics to improve spectral efficiency. Zhu et. al [35] designed a closed-loop compressive CSIT feedback and estimation framework in sparse multi-user (MU) massive MIMO channels to improve Channel State Information at the Transmitter (CSIT) estimation performance. They also designed a learning framework to use the minimum pilot and feedback resources needed under unknown and time-varying channel sparsity levels. Adapting pilot density has also been proposed to increase energy efficiency in future green networks, where the pilot density is increased in high traffic scenarios, and decreased in low traffic periods [49]. In cellular-assisted vehicular-to-everything (CV2X) technologies, standardized initially as a part of 3GPP Release 14, the pilot (Demodulation Reference Signal) density has been increased to support absolute vehicular speeds of 250 km/h and relative speeds of 500 km/h [50]. However, the standard does not support real-time adapta-

tion of pilot density based on time-varying small scale fading statistics of the wireless channel.

2.1.3 Main Contributions

The main contributions of this chapter are:

1. We derive closed-form expressions for the channel estimation mean squared error (MSE) in doubly selective (temporal as well as spectral fading) wireless channels, for OFDM pilots arranged in a "diamond-pattern." Compared to the state of the art [45], [46] our expressions (a) are analytical in order to individually isolate the effect of mobility (time fading) and multipath (frequency fading) on channel estimation MSE, and (b) can be used to quickly recompute the MSE for any general OFDM configuration if second order statistics of the fading channel are known.

2. We provide a novel scheme to adapt pilot patterns in *nonstationary channels* using feedback of indices from a 'channel statistics codebook', with low complexity and feedback overhead.

3. We propose two pilot configuration feedback mechanisms: implicit and explicit. This is similar to codebook-based feedback schemes such as channel quality indicator/precoding matrix indicator (CQI/PMI), which are standardized in LTE and NR.

4. We extend this framework to multi-band CA-OFDM systems with reduced feedback requirements, and analyze the computational complexity and feedback overhead of both schemes.

5. Using numerical simulations, we demonstrate rate gains using our pilot adaptation algorithm by comparing it with LTE and other fixed pilot patterns, in realistic vehicular-to-vehicular as well as air-to-ground channels. We consider two scenarios, (a) power control, where the transmitted power is adjusted to maintain a target SNR at the receiver, and (b) no power control, where the transmitted power is fixed irrespective of the SNR.

6. We quantify the value of pilot adaptation alone, and make the performance comparison agnostic to protocol-specific link adaptation mechanisms.

The rest of the chapter is organized as follows. Section 2.2 provides the details of the mathematical formulation of the cost function used to find the optimal pilot configuration. Section 2.3 outlines the derivation of closed form expressions for the channel estimation mean squared error (MSE). Section 2.4 presents the details of our framework based on design of a codebook of channel profiles, and introduces two practical CSI feedback schemes: explicit and implicit channel statistics feedback. Section 2.5 analyzes the feedback overhead and computational complexity incurred to implement explicit and implicit feedback-based pilot adaptation schemes. Section 2.6 shows the gains in achievable rate using adaptive pilot configurations compared to fixed pilot configurations for CA-OFDM in a variety of nonstationary wireless channel and power control scenarios.

Table 2.1: Important system parameters in Chapter 2

Parameter	**Description**
ρ	The data to pilot power ratio
σ_d^2	Average power of data symbols
σ_p^2	Average power of pilot symbols
$\Delta_p t$	Pilot spacing in time
$\Delta_p f$	Pilot spacing in frequency
$\bar{\gamma}$	Post-equalization SINR
σ_{ICI}^2	Inter-carrier interference power
σ_w^2	Noise power
δ_d	Channel estimation MSE of data resource elements
N_{tx}	Number of transmit antennas
N_{rx}	Number of receive antennas
N	Number of subcarriers per OFDM symbol
T_{ofdm}	Number of OFDM symbols used for channel statistics estimation
$\hat{\mathbf{H}}$	The $N \times T_{ofdm}$ channel matrix used to estimate the channel spectral and temporal correlation functions
T_s	OFDM symbol duration
f_d	Maximum Doppler frequency
τ_{rms}	Root mean square delay spread
$\hat{\mathbf{R}}_\mathbf{t}$	$(N_{\Delta t} \times 1)$ vector of estimated channel temporal correlation
$\hat{\mathbf{R}}_\mathbf{f}$	$(N_{\Delta f} \times 1)$ vector of estimated channel spectral correlation

We also provide a comprehensive comparison of our proposed scheme against state-of-the-art pilot adaptation schemes. Section 2.7 discusses extensions of our scheme to other multicarrier waveforms, and baseband equalization algorithms. We also highlight important practical considerations, that need to be accounted for when incorporating adaptive pilot configurations into NR. Finally, Section 2.8 concludes the chapter.

2.2 Problem Formulation

In this work, we are focusing on rate maximization, since improving spectral efficiency is one of the key goals in the PHY layer of NR and its successors. There is wide agreement that instantaneous achievable rate is the best indicator of the throughput of a wireless system [46, 51]. Since it is not possible to know the instantaneous rate beforehand, we maximize the upper bound of

the achievable rate based on estimation of necessary operating parameters [46].

It is to be noted that from a theoretical standpoint, second order statistics such as power spectrum and correlation do not exist for a nonstationary process. However, statistics such as *time-dependent* correlation functions and spectra can be defined for these processes, by means of the *Local Scattering Function* (see [52] for a more detailed discussion). Hence, nonstationary channels whose statistics vary in time and frequency can be modeled as locally stationary [53] using this formulation. However, the time scale over which we assume channel stationarity is crucial to accurately model nonstationary channels in a tractable manner. In this regard, the channel measurement results in [53] show that for nonstationary vehicular environments the time dependent doppler and rms delay spreads remain fairly constant for hundreds of milliseconds. Similar observations have also been reported for air-to-ground wireless channels over hilly [54], over-water [55], and Urban/Sub-urban settings [56]. Therefore, we assume the channel to be stationary for similar timescales in our work.

Pilot adaptation can be formulated as a maximization problem of the upper bound of the achievable rate [46, 51]

$$\begin{aligned} \underset{\rho,\Delta_p f,\Delta_p t}{\text{maximize}} \quad & S(\Delta_p f, \Delta_p t)\cdot \log_2(1+\overline{\gamma}) \\ \text{subject to} \quad & \overline{P}_t(\rho, \Delta_p f, \Delta_p t) \leq 1 \\ & 1 \leq \Delta_p t \leq T_{max} \\ & 2 \leq \Delta_p f \leq F_{max} \text{ and } \Delta_p f \pmod 2 = 0 \\ & \rho \leq \rho_{max}, \end{aligned} \tag{2.1}$$

where $\Delta_p t$ is the pilot spacing in time, $\Delta_p f$ the pilot spacing in frequency and $\rho = \sigma_d^2/\sigma_p^2$ the data-to-pilot-power-ratio (the reciprocal quantity is sometimes referred to as 'pilot boost'). σ_d^2 is the transmitted power for data symbols and σ_p^2 the transmitted power per pilot resource element (RE). $\overline{\gamma}$ is the post-equalization SINR under imperfect channel knowledge, $S(\Delta_p f, \Delta_p t)$ is the spectrum utilization function as a function of pilot spacing for OFDM, $\overline{P}_t$ is the average power per RE, and T_{max} is a function of the maximum tolerable latency by the receiver. Pilot spacing in the frequency domain is dictated by the sampling theorem. If τ_{max} is the maximum excess delay of the channel and T_{samp} the sampling interval, then by sampling theorem [57] we have

$$\frac{N}{\Delta_p f} > \frac{\tau_{max}}{T_{samp}}. \tag{2.2}$$

Therefore $\max(\Delta_p f) = F_{max} = \lceil \frac{NT_{samp}}{\tau_{max}} \rceil$ is the maximum allowable pilot spacing that is dictated by the maximum excess delay. If we space the channel taps in the Power Delay Profile (PDP) uniformly, then F_{max} depends on the maximum number of resolvable multipath components τ_{max}/T_{samp}. Pilots on alternate pilot bearing OFDM symbols are offset by an index of $\Delta_p f/2$ subcarriers, as shown in Fig. 2.1. It has been shown that channel estimation is optimal when the pilots spacing is equal and diamond-shaped [58]. To satisfy this pattern, $\Delta_p f/2$ must be a

positive integer. Therefore the additional constraint $\Delta_p f \pmod 2 = 0$ ensures that the $\Delta_p f$ is an even integer and hence, an optimal symmetric 'diamond-shaped' pilot pattern can be obtained. ρ_{max} is the maximum allowable data to pilot power ratio, which is dictated by peak to average power ratio (PAPR) considerations and high-power amplifier (HPA) characteristics. In this work, we consider the Zero Forcing (ZF) Receiver, whose post-equalization SINR $\overline{\gamma}$ is given as [46]

$$\overline{\gamma} = \frac{\sigma_d^2}{\sigma_w^2 + \sigma_{ICI}^2 + \sigma_d^2 \cdot \delta_d} \sigma_{ZF}, \tag{2.3}$$

where σ_w^2 is the average noise power and δ_d the MSE of the channel estimates for the data resource elements. σ_{ICI}^2 is the average intercarrier interference (ICI) power in received signal (after downconversion and demodulation). User mobility and carrier frequency offset (CFO) are the two major sources of ICI in a wireless system. We assume perfect synchronization and hence, the ICI due to CFO is zero, and user mobility is the only source of ICI in our work. The diversity order in a $N_{tx} \times N_{rx}$ MIMO system (when $N_{tx} \leq N_{rx}$) is given by $\sigma_{ZF} = (N_{rx} - N_{tx} + 1)$ in the absence of antenna correlation [59]. Hence for the SISO and $N_{tx} \times N_{tx}$ MIMO-OFDM scenarios (since $N_{tx} = N_{rx}$ in our case), $\sigma_{ZF} = 1$. The ICI power due to user mobility can be upper and lower bounded using [60]

$$\left[\frac{1}{3}(\pi f_d T_s)^2 - \frac{1}{90}(\pi f_d T_s)^4\right] \leq \frac{\sigma_{ICI}^2}{\sigma_d^2} \leq \left[\frac{1}{3}(\pi f_d T_s)^2\right]. \tag{2.4}$$

Note that the expression forming the lower bound in (2.4) will have to be used in equation (2.1) because we are optimizing the upper bound of the achievable rate.

In practical scenarios, the channel estimation MSE δ_d will not be known to the receiver beforehand, and hence it needs to be estimated. The spectral utilization function depends on the number of data resource elements N_d, which are limited only by the number of pilot REs N_p[1], which in turn depend on the pilot spacing $\Delta_p t$ and $\Delta_p f$. The instantaneous spectrum utilization function is given as

$$S(\Delta_p f, \Delta_p t) = \frac{N_d}{N_d + N_p}. \tag{2.5}$$

For N subcarriers per OFDM symbol with the diamond-shaped pilot arrangement, there will be N_{f1} and N_{f2} pilots in alternate pilot-bearing OFDM symbols. For ease of exposition, we define "resource block" to be a collection of contiguous resource elements such that the pilot density across all such blocks is uniform[2]. Hence, the resource block comprises of N subcarriers across $2\Delta_p t$ OFDM symbols, resulting in a total number of $2N\Delta_p t$ REs per RB. Among these, there are

[1]Modern wireless standards use control channels other than pilot signals, which also consume additional resources. We do not explicitly consider the presence of other control channels in this work. However, since other control channels typically have a fixed overhead, they can be considered in equation (2.5) by introducing a constant term in the denominator, related to overhead due to other control channels.

[2]This definition is different from that of LTE [37] and NR [2], where the number of OFDM symbols and subcarriers comprising the resource block of a particular configuration is standardized.

$N_p = N_{f1} + N_{f2}$ pilot REs, where $N_{f1} = \lceil N/\Delta_p f \rceil$ and

$$N_{f2} = \begin{cases} \lceil N/\Delta_p f \rceil & \text{if } N \pmod{\Delta_p f} > \Delta_p f/2 \\ \lfloor N/\Delta_p f \rfloor & \text{if } N \pmod{\Delta_p f} \leq \Delta_p f/2, \end{cases} \tag{2.6}$$

where N_d can be obtained by seeing that in a resource block of $N = (2N\Delta_p t)$ resource elements, N_p of them are occupied by pilots. If it is a MIMO system, then RE nulls would be necessary to transmit pilot signals from other antennas, as shown in Fig. 2.2. Therefore, for a $N_{tx} \times N_{rx}$ MIMO system, $N_d = (2N\Delta_p t - N_{tx}N_p)$ and

$$S(\Delta_p f, \Delta_p t) = \frac{2N\Delta_p t - N_{tx}N_p}{2N\Delta_p t}. \tag{2.7}$$

If $\bar{P}_t$ is the average power per RE, then $N_d\sigma_d^2 + N_p\sigma_p^2 = 2N\bar{P}_t\Delta_p t$. For a fixed ρ, the data and pilot powers can be obtained as

$$\sigma_d^2 = \frac{2N\bar{P}_t\Delta_p t}{N_p/\rho + N_d} \tag{2.8}$$

$$\sigma_p^2 = \frac{2N\bar{P}_t\Delta_p t}{N_p + \rho N_d}. \tag{2.9}$$

With this formulation, we still need to estimate some of the terms necessary to calculate the post-equalization SINR in equation (2.3). These quantities are

1. Channel estimation mean square error (MSE) δ_d.
2. f_d in order to estimate the lower bound of σ_{ICI}^2 and $R_t(\Delta t)$.
3. Channel correlation functions $R_f(\Delta f)$ and $R_t(\Delta t)$ in order to estimate the MSE δ_d.
4. Noise power σ_w^2.

The estimation of these parameters are outlined in the next two sections.

2.3 Channel Estimation Mean Squared Error (MSE)

In this section, we derive closed form expressions for the channel estimation MSE for 'diamond shaped' OFDM pilot configurations in doubly selective wireless channels. These expressions help in estimating the MSE due to imperfect channel estimation for a fixed pilot configuration, which is a factor that contributes significantly to the capacity of the MIMO-OFDM system.

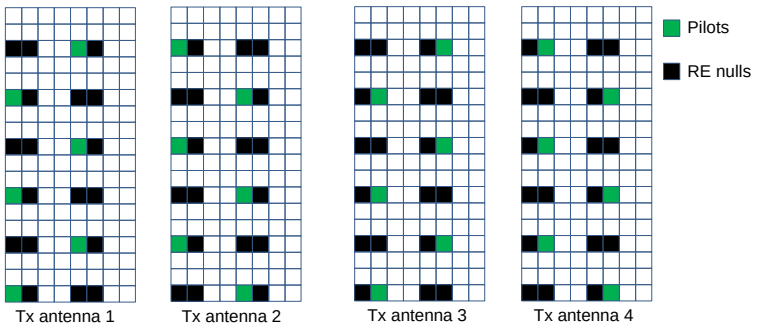

Figure 2.2: Illustration of the *diamond-shaped* OFDM pilot arrangement for $4 \times N_{rx}$ MIMO-OFDM.

2.3.1 Channel Model

We model the frequency selectivity of the wireless channel using a tapped-delay line model and temporal variations using the Jake's model [61]. We consider a wireless channel under the 'Wide Sense Stationary Uncorrelated Scattering' (WSSUS) approximation where the channel correlation $R_H(\Delta f, \Delta t)$ can be simplified as $R_H(\Delta t, \Delta f) = \sigma_H^2 R_t(\Delta t) R_f(\Delta f)$ [61]. $R_t(\Delta t)$ is the channel temporal correlation function and $R_f(\Delta f)$ the spectral correlation function. For simplicity, we assume a channel with unit channel gain, i.e. $\sigma_H^2 = 1$. The temporal correlation is given by Jake's model using $R_t(\Delta t) = J_0(2\pi f_d \Delta t)$ where $J_0(.)$ is the Bessel function of the first kind of zeroth order and the maximum doppler frequency $f_d = v f_c / c$ with v being the relative speed between the receiver and the transmitter, f_c the carrier frequency and c the speed of light.

2.3.2 Analysis Region

To simplify the performance analysis, we divide the OFDM block into four distinct types of resource elements:

1. Pilots: Their channel estimates are obtained using Least Squares (LS) channel estimation, as shown in equation (2.10).

2. Type A: Resource Elements that lie between 2 pilot subcarriers. Their channel estimates are obtained by linear interpolation of channel estimates in frequency, between these two pilot subcarriers, as shown in equation (2.11) with $t = 0$.

3. Type B and C: REs that lie after the last pilot subcarrier (Type B), or before the first pilot subcarrier (Type C). Their channel estimates are obtained by linear extrapolation of channel estimates in frequency, using the ultimate and penultimate pilots (Type B) and the first and second pilots (Type C). Since they are very few in number, they can been ignored in this analysis. The MSE analysis for these REs are similar to what is presented for Type-A subcarriers.

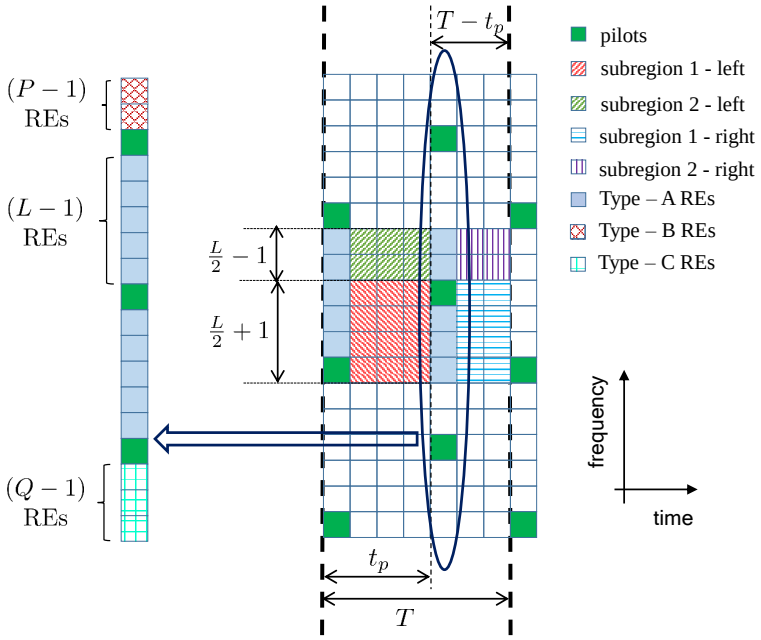

Figure 2.3: Diamond-shaped OFDM pilot arrangement for channel estimation MSE analysis.

4. Subregions 1 and 2 : Resource elements that lie between two pilot-bearing OFDM symbols. Their channel estimates are obtained by linear interpolation in *frequency as well as time*, as given by equations (2.11)-(2.12), for $t \neq 0$.

2.3.3 Channel Estimation

Fig. 2.3 shows the time-frequency resource grid, consisting of resource elements (REs), where the pilot symbols are located on the OFDM symbols at time $(n_1 t_p + n_2 T)$ seconds such that $n_2 \in \mathbb{Z}$ and $n_1 \in \{0, 1\}$. The pilot spacing is $\Delta_p f = L$ subcarriers on the frequency axis on the same OFDM symbol, with a relative cyclic frequency shift of $L/2$ between two consecutive pilot-bearing OFDM symbols.

Let $\mathcal{P}_{ref}$ be set of pilot locations in an OFDM symbol. Let its elements form an ordered pair given by $(l, n) \in \mathcal{P}_{ref}$, where l is the subcarrier index of the pilot with time index n. Let set $\mathcal{S}$ contain all possible time-frequency locations in the OFDM block, i.e. $(l, n) \in \mathcal{S}\ \forall\ 1 \leq l \leq N, 0 \leq n \leq (T-1)$. For the pilot at the location (l, n), the LS channel estimate $\hat{H}_l[n]$ will be

$$\hat{H}_l[n] = \frac{Y_l[n]}{P_l[n]} = H_l[n] + \frac{w_l[n]}{P_l[n]}, \tag{2.10}$$

where the overall noise $w_l[n]$ can be expressed as a sum of AWGN and ICI components $w_l[n] = w_l^{(AWGN)}[n] + w_l^{(ICI)}[n]$. We consider that $w_l^{(AWGN)}[n] \sim \mathcal{CN}(0, \sigma_w^2)$, $\mathbb{E}[w_l^{(ICI)}[n]] = 0$ and $\mathrm{Var}[w_l^{(ICI)}[n]] = \sigma_{ICI}^2$, where σ_w^2 is the average noise power and σ_{ICI}^2 the average ICI power. The

channel estimates of the data resource element at the location (k, n) in the left part of subregion 1 is given by linear interpolation along the time and frequency axes using

$$\hat{H}_k[n+t] = \eta\Big[\Big(\frac{1}{2}-\zeta\Big)\hat{H}_{\frac{-L}{2}}[n+t_p] + \Big(\frac{1}{2}+\zeta\Big)\hat{H}_{\frac{L}{2}}[n+t_p]\Big] + (1-\eta)\big[(1-\zeta)\hat{H}_0[n] + \zeta\hat{H}_L[n]\big], \tag{2.11}$$

where $\eta \triangleq t/t_p$ and $\zeta \triangleq k/L$, for $0 \leq t < t_p$ and $0 \leq k \leq L/2$. Similarly for $0 \leq t < t_p$ and $L/2 \leq k < L$ channel estimates are given by

$$\hat{H}_k[n+t] = \eta\Big[\Big(\frac{3}{2}-\zeta\Big)\hat{H}_{\frac{L}{2}}[n+t_p] + \Big(\zeta-\frac{1}{2}\Big)\hat{H}_{\frac{3L}{2}}[n+t_p]\Big] + (1-\eta)\big[(1-\zeta)\hat{H}_0[n] + \zeta\hat{H}_L[n]\big], \tag{2.12}$$

2.3.4 MSE Analysis

Fig. 2.3 shows the analysis region (marked by the colored regions) consisting of subregions 1 and 2, Type-A REs and pilots. Because of the periodic distribution of pilots, the performance in this region will *statistically be the same as that of the entire OFDM block*. Hence, we derive expressions for the average channel estimation MSE of all the REs in this analysis region.

The average MSE can computed as $\delta_{avg} = \frac{1}{L\cdot T}\sum\sum_{(k,n)\in\mathcal{A}} \mathbb{E}[|H_k[n] - \hat{H}_k[n]|^2]$, where $\mathcal{A}$ denotes the set containing locations of the REs in the analysis region. This can be expressed as a weighted mean of the MSE of the different RE types.

2.3.4.1 MSE of Pilots

For pilots, the channel estimates are given by (2.10). We consider the ICI term to be uncorrelated with the AWGN term and hence we have $\mathrm{Var}[w_l[n]/P_l[n]] = \frac{\sigma_w^2+\sigma_{ICI}^2}{\sigma_p^2}$ for $(l,n) \in \mathcal{P}_{ref}$, where σ_p^2 is the pilot signal power. Furthermore, we consider that the ICI term is uncorrelated with the channel coefficient $H_l[n]$, so that $\mathbb{E}[w_l[n]H_l^*[n]] = 0$ for $(l,n) \in \mathcal{S}$. The MSE of the pilot channel estimates can be given as

$$\delta_p = \frac{1}{|\mathcal{P}|}\sum_{(l,n)\in\mathcal{P}} \mathbb{E}[|H_l[n] - \hat{H}_l[n]|^2] = \frac{\sigma_w^2+\sigma_{ICI}^2}{\sigma_p^2}. \tag{2.13}$$

2.3.4.2 MSE of Type-A REs

The Mean Square Error of the channel estimates for Type A REs, denoted by $\delta_{f,A}$, is derived in [62]. Using our notation it can be represented as

$$\delta_{f,A} = \Big(\frac{5L-1}{3L}\Big)R_f(0) + \Big(\frac{2L-1}{3L}\Big)\Big(\frac{\sigma_w^2+\sigma_{ICI}^2}{\sigma_p^2}\Big) + \Big(\frac{L+1}{3L}\Big)\Re(R_f(L)) + \gamma, \tag{2.14}$$

where $\Re(x)$ is the real value of complex number x, and $\gamma = -\frac{2}{L-1}\sum_{i=1}^{L-1}\left[\left(\frac{L-i}{L}\right)\Re(R_f(i)) + \frac{i}{L}\Re(R_f(i-L))\right]$ represents the residual terms.

2.3.4.3 Left Part of Subregion 1 $(0 \leq k \leq L/2, 1 \leq t < t_p)$

For this subregion, the MSE expression for linear interpolation using Least Squares $\delta_{1,l}$, is

$$\delta_{1,l} = C_1 \sum_{k=0}^{L/2} \sum_{t=1}^{t_p-1} \mathbb{E}\{|\hat{H}_k[n+t] - H_k[n+t]|^2\}, \tag{2.15}$$

where $C_1 \triangleq \frac{1}{(L/2+1)(t_p-1)}$. After expanding the terms and simplifying, we get

$$\begin{aligned}\delta_{1,l} = (1+\lambda\omega)R_f(0)R_t(0) + \lambda(2-\omega)R_t(0)\Re(R_f(L)) + (1-2\lambda)R_t(t_p)\Re\Big[\omega' R_f\Big(\frac{L}{2}\Big) + \\ (1-\omega')R_f\Big(\frac{3L}{2}\Big)\Big] + \lambda\omega\Big(\frac{\sigma_w^2+\sigma_{ICI}^2}{\sigma_p^2}\Big) - \varepsilon_{1,l},\end{aligned} \tag{2.16}$$

where $\lambda \triangleq \frac{2t_p-1}{6t_p}; \omega \triangleq \frac{4L+1}{3L}; \omega' \triangleq \frac{23L+2}{24L}$ and the cross terms $\varepsilon_{1,l}$ is given by

$$\begin{aligned}\varepsilon_{1,l} =& 2C_1 \sum_{k=0}^{L/2} \sum_{t=1}^{t_p-1} \Big\{(1-\eta)R_t(t)\Re\Big[(1-\zeta)R_f(k) + \zeta R_f(L-k)\Big] + \eta R_t(t-t_p)\Re\Big[\Big(\frac{1}{2}-\zeta\Big)\cdot \\ & R_f\Big(\frac{L}{2}+k\Big) + \Big(\frac{1}{2}+\zeta\Big)R_f\Big(k-\frac{L}{2}\Big)\Big]\Big\}.\end{aligned} \tag{2.17}$$

2.3.4.4 Left Part of Subregion 2

The MSE for the left part of subregion 2, $\delta_{2,l}$, can be evaluated similarly as shown in equations (2.15)-(2.17).

2.3.4.5 Right Parts of Subregion 1 and 2

For the right part of subregions 1 and 2, the MSEs $\delta_{1,r}$ and $\delta_{2,r}$ can be obtained from equations (2.16)-(2.17) using the coordinate transformation $t \to -t$ and $t_p \to (T - t_p)$ appropriately. Noticing that $R_t(\Delta t) = R_t(-\Delta t)$ since $J_0(.)$ is an even function, the MSE expressions for $\delta_{1,r}$ and $\delta_{2,r}$ will take a similar form as (2.15)-(2.17).

2.3.4.6 Average MSE

The average MSE δ_{avg} will be the weighted mean of the MSEs of the different RE types in the analysis region. Therefore,

$$\delta_{avg} = \frac{1}{L \cdot T}\left[\frac{\delta_{1,l}}{C_1} + \frac{\delta_{2,l}}{C_2} + \frac{\delta_{1,r}}{C_3} + \frac{\delta_{2,r}}{C_4} + C_5\delta_{f,A} + 2\delta_p\right], \tag{2.18}$$

where $C_2 = \frac{1}{(L/2-1)(t_p-1)}, C_3 = \frac{1}{(L/2+1)(T-t_p-1)}, C_4 = \frac{1}{(L/2-1)(T-t_p-1)}$ and $C_5 = 2(L-1)$. For symmetric pilot spacing i.e. $L = \Delta_p f$ and $T = 2t_p = 2\Delta_p t$, we get $\delta_{1,l} = \delta_{1,r}, C_1 = C_3$ and $C_2 = C_4$ in (2.18). Therefore the MSE of the data REs δ_d will be given by

$$\delta_d = \frac{1}{(\Delta_p f \cdot \Delta_p t - 1)}\left[\frac{\delta_{1,l}}{C_1} + \frac{\delta_{2,l}}{C_2} + (\Delta_p f - 1)\delta_{f,A}\right]. \tag{2.19}$$

It is important to notice the following about the derived MSE expressions:

1. The channel estimation error is a function of the noise, ICI power, the channel statistics ($R_f(\cdot)$ and $R_t(\cdot)$), and the pilot spacing in time and frequency.
2. The expression is general, in that it is applicable for a valid set of OFDM waveform parameters (OFDM symbol duration, subcarrier spacing etc.).
3. The channel correlation functions can be parametrized using the root-mean square delay spread (for characterizing multipath), and the Doppler spread (for characterizing the mobility) [63]. Hence, channel correlations can be quickly recomputed for arbitrary values using closed-form expressions.

In light of the above features, and the fact that linear interpolation/extrapolation is used for channel estimation, predicting the MSE incurs low computational complexity at the receiver.

2.4 Optimal Pilot Spacing and Power

2.4.1 Estimation of Parameters

Noise power can be estimated using the methods proposed in [64, 65]. To estimate the channel statistics $\hat{R}_t(\Delta t)$ and $\hat{R}_f(\Delta f)$ in a nonstationary wireless channel, temporal averaging can be performed assuming local stationarity of the channel for the averaging duration [66]. For a $N \times T_{ofdm}$ channel matrix $\hat{\mathbf{H}}$ with N rows corresponding to frequency subcarriers, and T_{ofdm} columns

corresponding to OFDM symbol indices, second order statistics of the small-scale fading channel can be estimated using

$$\hat{R}_t(-i) = \frac{1}{T_{ofdm} - |i|} \sum_{t=1}^{T_{ofdm}-|i|} \left\{ \text{diag}_i \left[\hat{\mathbf{H}}^H \hat{\mathbf{H}} \right] \right\}_t$$
$$\hat{R}_f(-j) = \frac{1}{N - |j|} \sum_{f=1}^{N-|j|} \left\{ \text{diag}_j \left[\hat{\mathbf{H}} \hat{\mathbf{H}}^H \right] \right\}_f, \tag{2.20}$$

where $\text{diag}_i[\mathbf{X}]$ is the vectorized i^{th} diagonal of matrix $\mathbf{X}$ and $\left\{ \text{diag}_i[\mathbf{X}] \right\}_k$ its k^{th} element. Because $\hat{\mathbf{H}}^H \hat{\mathbf{H}}$ and $\hat{\mathbf{H}} \hat{\mathbf{H}}^H$ are Hermitian-symmetric matrices, the other elements can be found using $\hat{R}_t(-i) = \hat{R}_t^*(i)$ and $\hat{R}_f(-j) = \hat{R}_f^*(j)$. Using equation (2.20), we form the channel correlation vectors

$$\hat{\mathbf{R}}_\mathbf{f} = \left[\hat{R}_f(\tfrac{-N_{\Delta f}}{2}) \cdots \hat{R}_f(-1)\ \hat{R}_f(0)\ \hat{R}_f(1) \cdots \hat{R}_f(\tfrac{N_{\Delta f}-2}{2}) \right],$$
$$\hat{\mathbf{R}}_\mathbf{t} = \left[\hat{R}_t(\tfrac{-N_{\Delta t}}{2}) \cdots \hat{R}_t(-1)\ \hat{R}_t(0)\ \hat{R}_t(1) \cdots \hat{R}_t(\tfrac{N_{\Delta t}-2}{2}) \right]. \tag{2.21}$$

Without loss of generality, we assume that the vector lengths $N_{\Delta f}$ and $N_{\Delta t}$ are positive even integers. In practical scenarios where the channel statistics are estimated over a finite duration, the accuracy will be poor. This occurs due to (a) interpolation error, and (b) addition of noise. In the worst case, the estimated channel statistics can violate the properties of the autocorrelation function $|\hat{R}_t(\Delta t)| \leq \hat{R}_t(0)\ \forall\ \Delta t \neq 0$. This can happen especially in high noise, low mobility and/or flat fading scenarios. Therefore, using these estimated channel statistics directly can result in negative values for the MSE. Drawing inspiration from modern link adaptation techniques used in LTE and NR, we propose a codebook-based approach to increase the robustness of the feedback. The codebook contains the power delay profile (PDP) and maximum Doppler frequency values of typical channels that the radio expects to encounter. For typical cellular systems, the codebook can be standardized based on channel measurement data. A cognitive radio, on the other hand, can update the codebook over time as it learns more about its channel environment. The receiver calculates the channel statistics using equation (2.20) for a finite duration and finds the codebook profile that is closest to it in the minimum euclidean distance sense.

2.4.2 Channel Statistics Codebook

Let the codebook be denoted by set $\mathcal{R}_C$ with two set elements, i.e. $\mathcal{R}_C = \{\mathcal{R}_{C,t}, \mathcal{R}_{C,f}\}$. The sets are chosen such that $|\mathcal{R}_{C,f}| = M_f$ and $|\mathcal{R}_{C,t}| = M_t$. $\mathcal{R}_{C,f}$ is the set of channel frequency correlation profiles, with $N_{\Delta f} \times 1$ vector elements $\mathbf{R}_{\mathbf{fc,l}} \in \mathcal{R}_{C,f}$ for $1 \leq l \leq M_f$. Likewise, $\mathcal{R}_{C,t}$ is the set of channel temporal correlation profiles, with $N_{\Delta t} \times 1$ vector elements $\mathbf{R}_{\mathbf{tc,m}} \in \mathcal{R}_{C,t}$ for $1 \leq m \leq M_t$. Here, we model temporal fading using a classic Doppler spectrum where the Δt^{th} element is $[\mathbf{R}_{\mathbf{tc,m}}]_{\Delta t} = J_0(2\pi f_{d,m} \Delta t)$ [63]. Parameter $f_{d,m}$ is the maximum Doppler

Algorithm 1 Pilot Adaptation with Explicit Feedback: Receiver Processing

1: **Input:**
Codebook $\mathcal{R}_C$
Sets $\mathcal{D}_f, \mathcal{D}_t$ *and* $\mathcal{P}$*, that are known to the transmitter.*
2: Estimate $\hat{R}_t$ and $\hat{R}_f$ from equation (2.20) using $\hat{\mathbf{H}}$, computed using the most recent T_{ofdm} OFDM symbols.
3: Find the frequency and time domain channel profiles from the codebook, $\mathbf{R_{fc,l'}} \in \mathcal{R}_{C,f}$ and $\mathbf{R_{tc,m'}} \in \mathcal{R}_{C,t}$ by solving

$$l' = \underset{1 \leq l \leq M_f}{\arg\min} \quad \|\hat{\mathbf{R}}_\mathbf{f} - \mathbf{R_{fc,l}}\|$$
$$m' = \underset{1 \leq m \leq M_t}{\arg\min} \quad \|\hat{\mathbf{R}}_\mathbf{t} - \mathbf{R_{tc,m}}\|. \tag{2.22}$$

For a $N_{tx} \times N_{rx}$ MIMO-OFDM, there will be $N_{tx}N_{rx}$ channel matrices of dimension $N \times T_{ofdm}$ (one for each transmit-receive antenna pair). If $\mathbf{l'}$ and $\mathbf{m'}$ represent the $N_{tx}N_{rx} \times 1$ vectors of codebook indices found using equation (2.22) for each channel matrix, then $l' = \text{mode}(\mathbf{l'}), m' = \text{mode}(\mathbf{m'})$.
4: For $\rho \in \mathcal{P}, \Delta_p f \in \mathcal{D}_f, \Delta_p t \in \mathcal{D}_t$, compute channel estimation MSE δ_d assuming channel statistics $R_{fc,l'}$ and $R_{tc,m'}$ using equation (2.19).
5: Using the values of δ_d for each tuple $\nu = \{\rho, \Delta_p f, \Delta_p t\}$, solve equation (2.22) by calculating all the other necessary terms using equations (2.3)-(2.9). Let the resulting optimal tuple be $\nu_o = \{\rho_o, (\Delta_p f)_o, (\Delta_p t)_o\}$.
6: Feed back the optimal pilot configuration parameter $\nu_o = \{\rho_o, (\Delta_p f)_o, (\Delta_p t)_o\}$, and find the new pilot power and locations using ν_o.
7: For the next T_{ofdm} OFDM symbols received, estimate the channel matrix/matrices $\hat{\mathbf{H}}$.
8: Go back to step 1.

frequency for the m^{th} *temporal correlation profile*. This definition of the codebook channel profiles is motivated by the WSSUS approximation that we introduced in Section 2.3.1.

Initially, the profiles that comprise the codebook would correspond to the most common types of channels that the radio would be expected to encounter, based on reported field measurements. For example the channel profiles from the International Telecommunication Union (ITU-T) [67] or the 3GPP channel models [68] can be used as initial codebook entries. In the case of a cognitive radio, the codebook can be updated over time, when it learns more about its operating channel environment. The codebook can be designed to match the typical scenarios operation environment of the radios. For example vehicular to vehicular networks would have a large variation in Doppler spreads. On the other hand, UAV-to-UAV systems might have very low root mean square delay spread due to strong line of sight propagation [55, 69]. We will provide example codebooks when we present the numerical results in Section 2.6.

Algorithm 2 Pilot Adaptation with Implicit Feedback: Receiver Processing

1: **Input:**
Codebook $\mathcal{R}_C$
Sets $\mathcal{D}_f, \mathcal{D}_t$ *and* $\mathcal{P}$*, that are known to the transmitter.*
2: Estimate $\hat{R}_t$ and $\hat{R}_f$ from equation (2.20) using $\hat{\mathbf{H}}$, computed using the most recent T_{ofdm} OFDM symbols.
3: Find the frequency and time domain channel profiles from the codebook, $\mathbf{R_{fc,l'}} \in \mathcal{R}_{C,f}$ and $\mathbf{R_{tc,m'}} \in \mathcal{R}_{C,t}$ by solving

$$l' = \underset{1 \le l \le M_f}{\arg\min} \quad \|\hat{\mathbf{R}}_\mathbf{f} - \mathbf{R_{fc,l}}\|$$
$$m' = \underset{1 \le m \le M_t}{\arg\min} \quad \|\hat{\mathbf{R}}_\mathbf{t} - \mathbf{R_{tc,m}}\|. \tag{2.23}$$

For a $N_{tx} \times N_{rx}$ MIMO-OFDM, there will be $N_{tx}N_{rx}$ channel matrices of dimension $N \times T_{ofdm}$ (one for each transmit-receive antenna pair). If $\mathbf{l'}$ and $\mathbf{m'}$ represent the $N_{tx}N_{rx} \times 1$ vectors of codebook indices found using equation (2.23) for each channel matrix, then $l' = \text{mode}(\mathbf{l'}), m' = \text{mode}(\mathbf{m'})$.
4: Feed back the codebook indices l' and m' to the transmitter on the uplink.
5: For $\rho \in \mathcal{P}, \Delta_p f \in \mathcal{D}_f, \Delta_p t \in \mathcal{D}_t$, compute channel estimation MSE δ_d assuming channel statistics $R_{fc,l'}$ and $R_{tc,m'}$ using equation (2.19).
6: Using the values of δ_d for each tuple $\nu = \{\rho, \Delta_p f, \Delta_p t\}$, solve equation (2.23) by calculating all the other necessary terms using equations (2.3)-(2.9). Let the resulting optimal tuple be $\nu_o = \{\rho_o, (\Delta_p f)_o, (\Delta_p t)_o\}$.
7: Find the new pilot power and locations using ν_o.
8: For the next T_{ofdm} OFDM symbols received, estimate the channel matrix/matrices $\hat{\mathbf{H}}$.
9: Go back to step 1.

2.4.3 Explicit and Implicit Feedback of Optimal Pilot Spacing and Power

We assume that the transmitter and receiver both know and share a common $\mathcal{P}, \mathcal{D}_f$ and $\mathcal{D}_t$; the sets that contain allowable values for $\rho, \Delta_p f$ and $\Delta_p t$, respectively. With the range for each parameter predefined based on the constraints in (2.1), it is possible to estimate the maximum rate if second order statistics of the small-scale fading channel *are known, or can be reliably estimated.* Assuming that the pilot pattern of the downlink signal needs to be optimized to maximize the rate in a frequency division duplex (FDD) system, the optimal pilot configuration needs to be fed back from the receiver. This is because it's not possible for the transmitter to determine the optimal downlink pilot configuration using the uplink signal. Therefore especially for FDD systems, equation (2.1) has to be solved at the receiver[3]. For feeding back the optimal pilot configuration parameters, two mechansisms are possible:

1. Explicit Feedback: Here, the receiver feeds back the optimal pilot configuration parameters

[3]For time-division duplex (TDD) systems, feedback of the channel statistics might be necessary due to different characteristics of the RF chains of the transmitter and the receiver. If the system becomes interference-limited in the downlink, explicit feedback would be necessary [9].

Algorithm 3 Pilot Adaptation with Implicit Feedback: Transmitter Processing

1: **Input:**
Codebook $\mathcal{R}_C$
Sets $\mathcal{D}_f, \mathcal{D}_t$ *and* $\mathcal{P}$*, that are known to the receiver.*
2: Based on the received codebook indices l' and m', for $\rho \in \mathcal{P}, \Delta_p f \in \mathcal{D}_f, \Delta_p t \in \mathcal{D}_t$ compute channel estimation MSE δ_d assuming channel statistics $R_{fc,l'}$ and $R_{tc,m'}$ using equation (2.19).
3: Using the values of δ_d for each tuple $\nu = \{\rho, \Delta_p f, \Delta_p t\}$, solve equation (2.22) by calculating all the other necessary terms using equations (2.3)-(2.9). Let the resulting optimal tuple be $\nu_o = \{\rho_o, (\Delta_p f)_o, (\Delta_p t)_o\}$.
4: Find the new pilot power and locations using ν_o.
5: Transmit the next T_{ofdm} OFDM symbols using these new pilot locations and power, on the downlink.
6: Go back to step 1.

$\nu_o = \{\rho_o, (\Delta_p f)_o, (\Delta_p t)_o\}$ explicitly.

2. Implicit Feedback: Here, the receiver solves equation (2.1), and feeds back the codebook indices l' and m', of the channel statistics codebook $\mathcal{R}_C$. Using the codebook indices and accurate knowledge of the SNR at the receiver[4], the transmitter then solves equation (2.1) to find the optimal downlink pilot configuration.

The algorithms to find the optimal pilot spacing and power can be executed once every T_{ofdm} symbols as shown in Algorithm 1 (explicit feedback), and Algorithm 2 (implicit feedback) *at the receiver*. At the transmitter, no extra computation is necessary in the case of explicit feedback. However in the case of implicit feedback, the transmitter needs to solve equation (2.1) using knowledge of the channel statistics (l' and m') obtained from the codebook indices, which incurs additional computation. In cellular systems, since the base station has access to an extensive pool of computational infrastructure, implicit feedback for downlink pilot adaptation is feasible.

Figures 2.4 and 2.5 illustrates the explicit and implicit feedback mechanisms respectively, which are outlined in Algorithms 1 and 2-3 respectively.

2.5 Feedback Requirements and Computational Complexity

2.5.1 Single-Band SISO and MIMO-OFDM Systems

Based on the above feedback schemes for pilot adaptation, the receiver needs to (a) either feed back the codebook indices of the corresponding channel profile (implicit feedback), or (b) feed

[4]In wireless standards such as LTE and NR, a rough estimate of the SNR can be obtained by using the channel quality indicator (CQI) that is fed back by the receiver. The CQI can then be used to approximately estimate the SNR using tables such as the ones provided in [70].

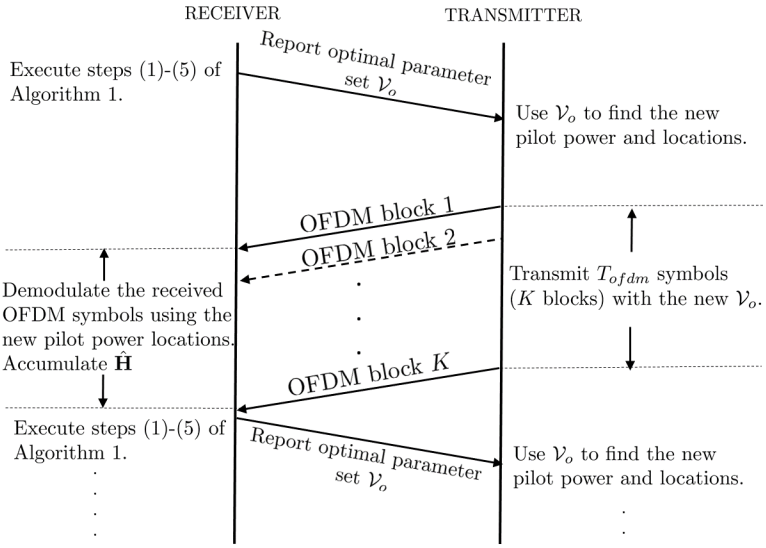

Figure 2.4: Illustration of the explicit feedback mechanism given in Algorithm 1, to enable pilot adaptation between the receiver and the transmitter. K OFDM blocks are equivalent to T_{ofdm} OFDM symbols.

back the optimal pilot configuration parameters ν_o (explicit feedback).

2.5.1.1 Implicit Feedback

When feeding back only the codebook indices, there are a total of $M_t M_f$ possible values that can be sent to the transmitter. Therefore, the receiver would need to feed back at least $b_{\texttt{exp}}^{(fb)} = \lceil \log_2(M_t M_f) \rceil$ raw bits. Therefore, $b_{\texttt{exp}}^{(fb)}$ bits are exchanged between the transmitter and receiver once in every $(T_{ofdm} \times T_s)$ seconds leading to a bit-rate of $R_{\texttt{imp}}^{(fb)} = \frac{b_{\texttt{imp}}^{(fb)}}{T_{ofdm} T_s}$ bits per second.

Estimation of channel statistics involve matrix multiplication, which can be accomplished with a complexity of $O(N^2 T_{ofdm})$ for each element of $\hat{\mathbf{R}}_{\mathbf{f}}$, and $O(T_{ofdm}^2 N)$ for $\hat{\mathbf{R}}_{\mathbf{t}}$. Values for T_{ofdm} and N have to be chosen to estimate the channel statistics accurately. Since these operations are similar to those used in an MMSE receiver which relies on accurate estimation of the channel statistics [71], its implementation does not consume additional computing resources in modern wireless receivers. The other steps involved in algorithm 2-3 are of low complexity and hence, do not put a burden on modern wireless radios.

For MIMO-OFDM, the computational complexity to estimate $\hat{\mathbf{R}}_{\mathbf{t}}$ and $\hat{\mathbf{R}}_{\mathbf{f}}$ are $O(N_{tx} N_{rx} T_{ofdm}^2 N)$ and $O(N_{tx} N_{rx} N^2 T_{ofdm})$, respectively. The feedback requirements will remain the same as in the case of SISO-OFDM[5].

[5]Typically, the spectral and temporal correlation are the same for the channel between each transmit-receive antenna pair, unless the antennas are distributed in different locations of the network.

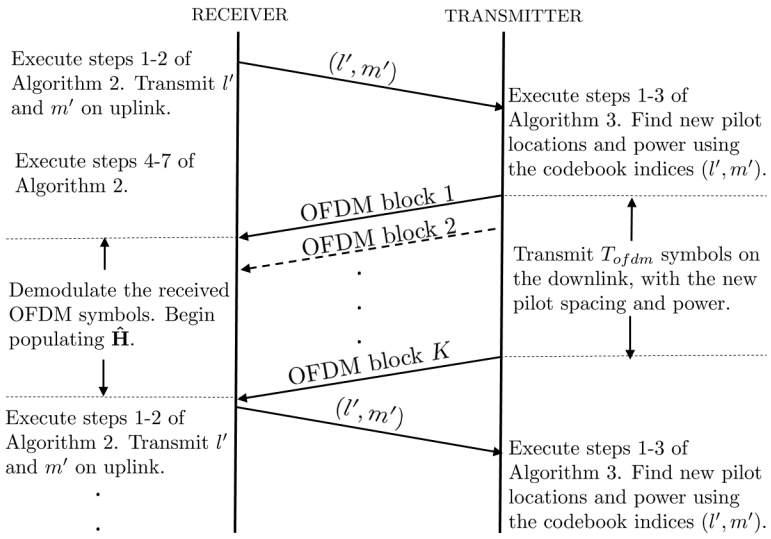

Figure 2.5: Illustration of the implicit feedback mechanism given in Algorithms 2-3, to enable pilot adaptation between the receiver and the transmitter. K OFDM blocks are equivalent to T_{ofdm} OFDM symbols.

At the transmitter, the computation pertaining to pilot adaptation is restricted to solving equation (2.1), which is of low complexity if the feasible set (number of candidate pilot configurations) is low enough (of the order of hundreds) such that a simple brute-force search can be implemented.

2.5.1.2 Explicit Feedback

In the feasible set of $\nu = \{\rho, \Delta_p f, \Delta_p t\}$, there are a total of $|\nu| = M_{\mathcal{P}} M_{\mathcal{D}_f} M_{\mathcal{D}_t}$ elements, where $M_{\mathcal{P}} = |\mathcal{P}|$, $M_{\mathcal{D}_f} = |\mathcal{D}_f|$ and $M_{\mathcal{D}_t} = |\mathcal{D}_t|$. Therefore, the feedback requirements for explicit feedback in single-band SISO and MIMO systems will be at least $b_{\mathtt{exp}}^{(fb)} = \lceil \log_2(M_{\mathcal{P}} M_{\mathcal{D}_f} M_{\mathcal{D}_t}) \rceil$ bits, resulting in a rate overhead of $R_{\mathtt{exp}}^{(fb)} = \frac{b_{\mathtt{exp}}^{(fb)}}{T_{ofdm} T_s}$ bits per second. The computational complexity to estimate the channel statistics at the receiver is the same as that at in the case of implicit feedback. However unlike the latter, no additional computation is necessary at the transmitter.

2.5.2 Multi-Band Carrier Aggregation

In multi-band carrier aggregation, resource blocks can be allocated to a user across two or more frequency bands. The bands pertaining to one comm. system are called *component carriers* [72]. In such a case, pilots will be sent on all N_b component carriers at $(f_1, f_2, \cdots f_{N_b})$, and the pilot spacing can be varied on each component carrier based on its channel statistics to maximize the rate on each component carrier.

2.5.2.1 Implicit Feedback

When implicit feedback is used, properties of Doppler spread can be exploited to reduce the computation and feedback requirements. We assume that the OFDM symbol duration, subcarrier spacing and all other parameters except for the pilot spacing and power, are the same across all component carriers. Since the Doppler frequency scales linearly with the center frequency f_c, only one codebook index specifying the temporal pilot spacing needs to be fed back for any one of the N_b bands. The temporal codebook index m' for the other $(N_b - 1)$ bands can be estimated at the transmitter by back calculations. Even in the case where each frequency band experiences a different root mean square delay spread, the total number of bits needed for feedback will be $b^{(fb)}_{\texttt{imp,CA}} = \lceil \log_2(M_t M_f + (N_b - 1) \times M_f) \rceil$ bits[6]. Hence with this method, at least $\left\lceil \log_2 \left(\frac{N_b M_t M_f}{M_t M_f + (N_b - 1) \times M_f} \right) \right\rceil$ bits of feedback can be saved. Similar to the case of single-band OFDM systems, the bit rate overhead incurred by implementing adaptive pilot spacing and power is $\frac{b^{(fb)}_{\texttt{imp,CA}}}{T_{ofdm} T_s}$ bits per second.

2.5.2.2 Explicit Feedback

In general, it is not possible to leverage the properties of the doppler spread if accurate downlink SNR information is not present at the transmitter. Assuming the same codebook is used for all the component carriers in the CA-OFDM system, the feedback requirements for enabling pilot adaptation will be $b^{(fb)}_{\texttt{exp,CA}} = \lceil \log_2(N_b M_{\mathcal{P}} M_{\mathcal{D}_f} M_{\mathcal{D}_t}) \rceil$ bits, and the resulting rate overhead will be $R^{(fb)}_{\texttt{exp,CA}} = \frac{b^{(fb)}_{\texttt{exp,CA}}}{T_{ofdm} T_s}$ bits per second.

2.6 Numerical Results

We present the numerical results in this section. We simulated an OFDM system in a doubly selective fading channel. Jakes Doppler spectrum models the mobility effects in the channel, with Rayleigh fading due to multipath modeled using a tapped delay-line model. The root-mean square delay spread (τ_{rms}) controls the frequency selectivity of the channel, and doppler spread (f_d) controls the temporal fading of the channel. Table 2.2 summarizes the parameters of the OFDM waveform as illustrated in Fig. 2.1 for SISO-OFDM and Fig. 2.2 for MIMO-OFDM. We also simulated CA-OFDM systems with two component subcarriers at $f_1 = 700$ MHz and $f_2 = 2$ GHz.

[6] If all the component carriers are very close in frequency, the multipath characteristics will be the same as well. In this case, the feedback requirements using implicit feedback will be the same as that for $N_b = 1$.

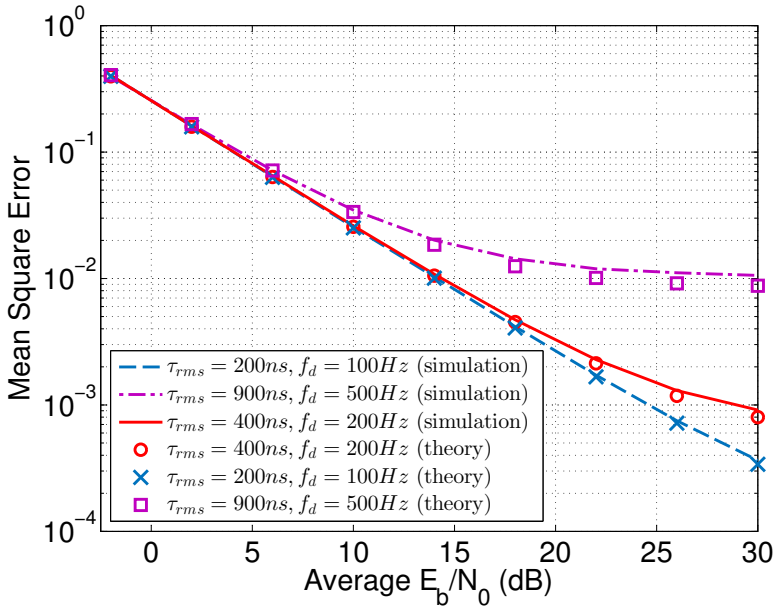

Figure 2.6: Comparison of theoretical and simulated channel estimation MSE values for different channel conditions for SISO-OFDM.

2.6.1 Channel Estimation MSE Performance

Fig. 2.6 shows the comparison between the theoretical and simulated channel estimation performance for doubly selective channels of different characteristics. We have computed the ICI power using the lower bound in equation (2.4). We see that the curves match well, validating the derived MSE expressions in equations (2.10)-(2.18) in section 2.3. We see that there is a slight mismatch at higher values of E_b/N_0 as f_d increases, because the ICI power that we have considered in our theoretical expression is approximate. The contribution of ICI becomes prominent at higher E_b/N_0 and f_d. The deviation is negligible in relatively low frequency selective and mobility conditions. Even in high mobility conditions ($f_d = 500$ Hz), the theoretical expressions form a tight lower bound to the channel estimation MSE. Hence our derived MSE expressions can be used to maximize the upper bound of the achievable rate in Algorithms 1-3.

2.6.2 Pilot Adaptation in Doubly Selective Nonstationary Wireless Channels with Power Control

We simulate a doubly selective nonstationary wireless channel with slowly varying second order statistics, as illustrated in Fig. 2.7. We consider the following channel scenarios: (a) UAV to ground wireless channel and (b) terrestrial wireless channel. UAV-to-UAV or UAV-to-ground wireless channels are typically characterized by a low τ_{rms} when compared to terrestrial channels [55, 69].

We model τ_{rms} to be the same for both frequency bands at any given time. On the other hand, the

Table 2.2: Simulation parameters

Parameter	**Value**
Antenna Configuration	SISO and 4×4 MIMO
FFT-length	128
Number of OFDM subcarriers	72
Number of Guard Subcarriers	28 on each band edge
Center Frequency f_c	700 MHz and 2.0 GHz
Subcarrier Spacing f_{sub}	15 kHz
OFDM symbol duration T_s	71.875 μs
Cyclic Prefix Duration	5.21 μs
Base pilot spacing in time t_p	4 OFDM symbols (0.2875 ms)
Base pilot spacing in frequency L	6 subcarriers (90 kHz)
Channel parameters	Doubly selective: Jakes Doppler spectrum with multipath fading.
Vehicular speed	0-500 km/h
rms delay spread	0-300 ns (air-to-ground) 0-1000 ns (V2V)
Channel Estimation	Least Squares (pilots) 2D-Linear Interpolation (data REs)
Equalization	Zero Forcing (ZF)

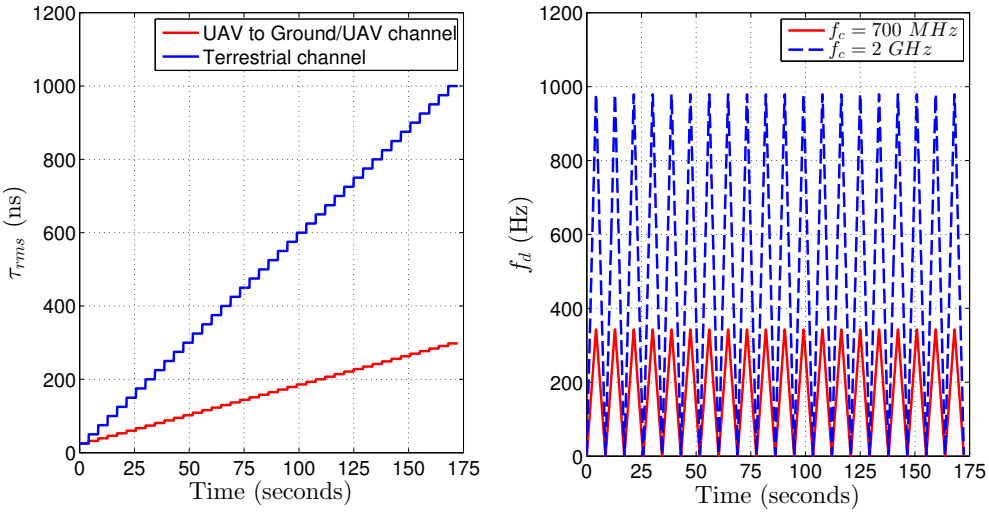

(a) (b)

Figure 2.7: Variation of the (a) root mean square delay spread and (b) maximum Doppler frequency, of the simulated doubly selective nonstationary wireless channel scenarios.

maximum Doppler frequency f_d is directly proportional to f_c, as shown in Fig. 2.7. We assume *perfect power control*, where the transmitted power is controlled in such a manner that the large-scale path loss is compensated to maintain the long-term SNR of the received signal. In addition, we assume the absence of co-channel interference in this study.

Typically, the feasible sets should be chosen such that (a) ρ satisfies the PAPR requirements, (b) $\Delta_p t$ is able to capture the channel variations accurately enough for a large range of vehicular velocities, and (c) $\Delta_p f$ gives reasonably accurate channel estimates for a wide range of multipath environments. In our work, the parameter ranges considered are $\rho \in \mathcal{P} = \{-9 \text{ dB}, -8 \text{ dB}, \cdots, 0 \text{ dB}\}$, $\Delta_p t \in \mathcal{D}_t = \{2, 3, \cdots, 10\}$ and $\Delta_p f \in \mathcal{D}_f = \{2, 4, \cdots, 12\}$. The channel statistics are estimated once every $T_{ofdm} = 1500$ OFDM symbols over $N = 72$ subcarriers.

Channel estimation needs to be performed before any data symbol can be decoded by the receiver. Since we are using linear interpolation between two pilot-carrying OFDM symbols, this operation needs to be performed once every $\Delta_p t \times T_s$ seconds in our work, where $\Delta_p t$ is the pilot spacing in time, and T_s the OFDM symbol duration. Since $2 \leq \Delta_p t \leq 10$ and $T_s = 71.875 \mu s$, we perform channel estimation once every 144 to $719 \mu s$, depending on the value of $\Delta_p t$. Popular wireless standards such as LTE, WiFi and NR perform channel estimation on a similar timescale.

For the channel scenarios shown in Fig. 2.7 we compare the throughput performance of adaptive pilot configuration against the following fixed pilot configurations: (a) $\Delta_p t = \Delta_p f = 6, \rho = -3$ dB, (b) $\Delta_p t = \Delta_p f = 8, \rho = -3$ dB and (c) pilot configuration of Normal-Cyclic Prefix (CP) LTE [37] with $\rho = -3$ dB. We consider both SISO-OFDM and 4×4 MIMO-OFDM with full spatial multiplexing.

The designed codebook to implement adaptive pilot configurations using Algorithms 1-3 is shown in Table 2.3. The codebook vectors lengths in $\mathcal{R}_{C,f}$ and $\mathcal{R}_{C,t}$ are chosen to be $N_{\Delta f} = 62$ and $N_{\Delta t} = 40$ respectively. The channel profiles correspond to standard 3GPP and ITU-T channel models [67, 68], and additional codebook entries ensure that the entire range of τ_{rms} and f_d is efficiently handled by the adaptive OFDM waveform.

Fig. 2.8 shows the achievable rate (throughput) of adaptive pilot configurations for SISO and MIMO with fixed pilot configurations, for UAV to ground/UAV channels at $f_c = 2$ GHz. We observe that it outperforms fixed pilot schemes for all SNR values for both SISO and MIMO scenarios. The performance gap increases with SNR, thus showing that the pilot pattern adaptation performs better in low noise (low σ_n^2) conditions. Fig. 2.9 shows that using our algorithm, adaptive pilot patterns can achieve up to 35% more throughput w.r.t. LTE pilot spacing in SISO and 4×4 MIMO-OFDM modes. Compared to other fixed pilot configurations, this gain can be as high as 45%.

2.6.3 Comparison with other Pilot Adaptation Schemes

In this subsection we compare the performance of our pilot adaptation scheme (without carrier aggregation) with other schemes in the literature. To ensure that there is a uniform metric for comparison, we have considered only those works for which the results of data rate improvement with pilot adaptation are available.

Byun and Natarajan [41] aim to minimize feedback delays and synchronization mismatch of pilot spacing information in an OFDM system. Since they prioritize channel estimation MSE and BER

Table 2.3: Codebook of channel profiles, $\mathcal{R}_C$

A: Channel profiles for Doppler frequency $(\mathcal{R}_{C,t})$

Codebook Index (m)	Mobility Type/Velocity†	f_d (Hz)
1	Pedestrian (3km/hr)	5.6
2	Urban Vehicular (32km/hr)	60
3	Highway Vehicular (120km/hr)	222.22
4	High Speed Train/UAV low (300km/hr)	555.56
5	High Speed Train/UAV medium (400km/hr)	750
6	High Speed Train/UAV high (500km/hr)	925

B: Channel profiles for frequency selectivity $(\mathcal{R}_{C,f})$

Codebook Index (l)	Normalized PDP	Delay taps*	τ_{rms} (ns)
1	[0.9310, 0.3425, 0.126]	[0,1,2]	221.5
2	[0.8882, 0.3152, 0.2809, 0.158, 0.0888]	[0,1,2,3,5]	476.4
3	[0.778, 0.4426, 0.3097, 0.3169, 0.0497]	[0,1,2,4,7]	791.2
4	[0.5795, 0.4745, 0.3885, 0.318, 0.2604, 0.213, 0.1745, 0.143, 0.117, 0.096]	[0,1,2,3,4, 5,6,7,8,9]	1440

*Normalized tap coefficients for a sampling duration of $T_s = 520.833$ ns.
† Velocity values shown for a center frequency of $f_c = 2$ GHz. For the 700 MHz band, velocity scales by a factor of $\frac{20}{7}$.

performance over spectral efficiency, they lose spectral efficiency in some scenarios. In the best case, their approach yields a 5.9% gain in average spectral efficiency (please refer Fig. 8 of [41]).

Ali et al. [42] adapt the pilot distribution in OFDM-based WLAN according to the variations in the short-term channel gain to maximize the throughput. They adapt pilot spacing in time by using six threshold levels for Doppler spread. Their approach performs best in slow-varying channels.

Sheng at al. [43] propose to maximize the sum rate using a power allocation scheme between pilot and data symbols for OFDM in a high-speed train (HST) environment. The authors use an information-theoretic approach to solve this problem, by first estimating the average channel complex gains and then using it in a HST basis expansion channel model to formulate a rate-maximization problem.

Karami and Beaulieu [44] design a joint adaptive power loading and pilot spacing algorithm to maximize the average mutual information between the input and output of OFDM systems. They derive expressions for the optimal power distribution across all OFDM subcarriers as well. They obtain the best rate improvements in low mobility and low SNR conditions. For high mobility, the throughput improvement reduces significantly. For SNR $>$ 5dB, there is no noticeable im-

Table 2.4: Comparison of our proposed scheme with state-of-the-art single-band pilot adaptation schemes in the literature.

Reference	**Optimization Metric**	**Adaptation Parameters**	**Channel Environment**	**Throughput Gain**	**Additional Details**
Byun et al. [41]	MSE/BER	$\Delta_p t$	Indoor, Pedestrian and Vehicular (max. $f_d = 83$ Hz)	max. 5.88%	Used a look up table based approach.
Ali et al. [42]	Throughput	$\Delta_p t$	Indoor with max. $\tau_{rms} = 550$ ns, max. $f_d T_s = 1.2 \times 10^{-2}$	max. 4.58%	Used six threshold levels of Doppler spread.
Sheng et al. [43]	Sum rate	ρ	High-speed train max. $\tau_{rms} = 5\mu s$, max. $f_d = 740$Hz	9-21%	Information-theoretic approach.
Karami et al. [44]	Mutual information	$(\Delta_p t, \Delta_p f, \rho)$	max. $\tau_{rms} = 16T_s$, max. $f_d = 224$ Hz	14.29 - 42.86% *	Derives optimal power allocation across all OFDM subcarriers.
Simko et al. [45]	Throughput	ρ	ITU Vehicular A	max. 10%	Results presented for LTE with pilot power adaptation.
Simko et al. [46]	Throughput	$(\Delta_p t, \Delta_p f, \rho)$	max. $\tau_{rms} = 800$ns, max. $f_d = 1200$Hz	3 - 80% † (SISO) max. 8.5×† (4×4-MIMO)	Gains partially due to LTE PHY features‡
Our work	Throughput	$(\Delta_p t, \Delta_p f, \rho)$	max. $\tau_{rms} = 1\mu s$, max. $f_d \approx 950$Hz doubly selective and nonstationary	4.33 - 32.24% (SISO) 4.81 - 40.26% (4×4-MIMO)	Agnostic to LTE PHY features. Gains averaged over SNR from -3 to 33dB in nonstationary channels.

* Results for SNR $= -5$ dB. Rate improvement is negligible for SNR > 5 dB.

† Because a pilot pattern is associated with a modulation and coding scheme, the throughput gains at high vehicular speeds is much higher. This value is for $f_d = 1200$Hz, SNR $= 14$ dB and $\tau_{rms} = 400$ns [46].

‡ Features such as link adaptation, where the modulation order and coding rate is changed based on the channel quality.

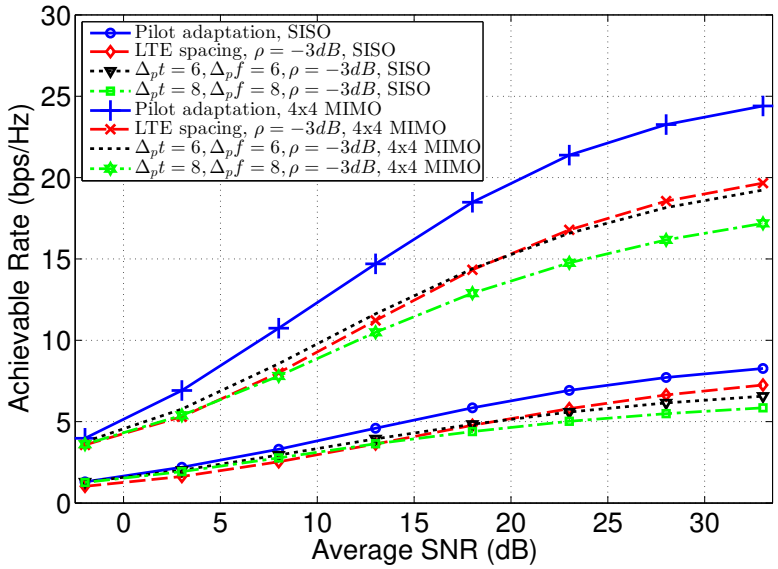

Figure 2.8: Performance of adaptive and pilot schemes for SISO and 4×4 MIMO-OFDM at $f_c = 2$ GHz in nonstationary UAV to ground/UAV wireless channels.

provement in the rate.

Simko, Wang and Rupp [45] consider optimal power allocation between pilot and data symbols in an OFDM system, and apply it to a LTE system. The authors consider two channel estimation algorithms: Least Squares (LS) and Linear MMSE (LMMSE). The best case throughput improvement is reported to be 10%.

Simko et al. [46] consider joint optimization of pilot spacing and power for SISO and MIMO-OFDM systems (without carrier aggregation). Similar to their earlier work in [45], they compare the throughput of their adaptation and power allocation algorithm with that of a standard LTE system. They propose mapping the pilot pattern to the modulation and coding scheme (MCS) of LTE. The combination of (a) change in modulation order and code rate and (b) change in pilot power and spacing, can result in very high gains (upto $8.5\times$) at very high vehicular speeds with 4×4-MIMO.

In contrast to the above, our results are agnostic to the LTE standard, and hence applies to any general OFDM-based system. However, we do compare the throughput performance of our scheme with Normal Cyclic Prefix (CP) LTE [37] for vehicular and air-to-ground wireless channels. For both channels, the performance gains w.r.t. LTE range from 16.7-27.5% (refer Table 2.5). Unlike the other works mentioned above, our results are averaged for a nonstationary channel scenario of a slow fading line-of-sight channel that evolves to a fast fading multipath channel. Our results demonstrate that even when channel statistics gradually changes in a timescale of a few hundred milliseconds (in our case, $\sim$ 108ms), our proposed scheme gives a significant throughput improvement which has not been reported before, to the best of our knowledge. The summary of the key results from the above works is provided in Table 2.4.

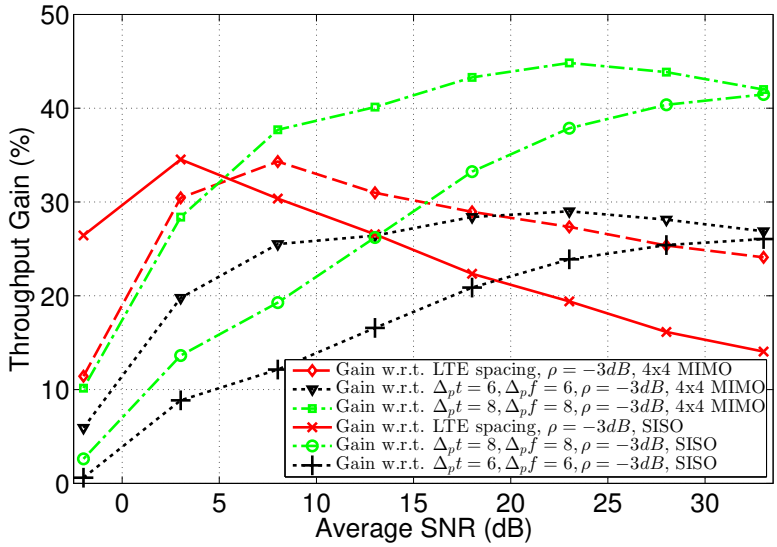

Figure 2.9: Throughput improvement of adaptive pilot configuration over fixed pilot schemes for SISO and 4×4 MIMO-OFDM at $f_c = 2$ GHz in nonstationary UAV to ground/UAV wireless channels.

2.6.4 Pilot Adaptation in Multi-band CA-OFDM Systems

We simulated adaptive pilot configurations for multi-band carrier aggregation OFDM (CA-OFDM) systems, for the nonstationary channel scenarios shown in Fig. 2.7 for $N_b = 2, f_1 = 700$ MHz and $f_2 = 2$ GHz. We use the channel profile codebook $\mathcal{R}_C$ shown in Table 2.3 for both frequency bands. We compare the throughput results for CA SISO and MIMO-OFDM systems in (a) UAV to ground/UAV channels and (b) terrestrial channels, when there is *perfect power control*.

Figures 2.10 and 2.11 show the throughput gains achieved by adaptive pilot configurations w.r.t. the fixed pilot configurations considered for UAV to ground/UAV and terrestrial wireless channels respectively. The gain is generally higher for UAV wireless channels as compared to terrestrial systems. This is so because $\Delta_p f$ can be increased to significantly improve the spectral efficiency of the typically frequency-flat air-to-ground/air-to-air wireless channels.

Similarly, the channel in the 700 MHz band will tend to be more benign in terms of temporal fading, due to the relatively low Doppler spread when compared to that at $f_2 = 2$ GHz. Hence, in this case $\Delta_p t$ of the component carrier in the 700 MHz band can be increased w.r.t. that in the 2 GHz band. Fig. 2.12 shows the relative performance enhancement in the 700 MHz band, validating the above. Hence, adapting the pilot density in two or more different operating frequency bands presents a means to increase the channel capacity, and offers an additional degree of freedom for cross-layer optimization and load-balancing algorithms in CA-OFDM systems.

Table 2.5 summarizes the average throughput gain achieved by pilot adaptation (averaged over SNR) w.r.t. the fixed pilot schemes considered in this section. It shows that adaptive pilot con-

Table 2.5: Average throughput gain of adaptive pilot configuration compared to fixed pilot configurations

A: Terrestrial channels

Pilot Spacing $\rho = -3$ dB	$f_c = 700$ MHz		$f_c = 2$ GHz		CA	
	SISO	MIMO	SISO	MIMO	SISO	MIMO
$\Delta_p f = \Delta_p t = 6$	4.33%	10.96%	20.44%	26.30%	11.35%	17.31%
$\Delta_p f = \Delta_p t = 8$	4.81%	9.82%	32.24%	40.26%	16.17%	21.59%
LTE normal CP	19.36%	27.49%	20.58%	27.13%	19.93%	27.33%

B: UAV to Ground/UAV channels

Pilot Spacing $\rho = -3$ dB	$f_c = 700$ MHz		$f_c = 2$ GHz		CA	
	SISO	MIMO	SISO	MIMO	SISO	MIMO
$\Delta_p f = \Delta_p t = 6$	4.32%	9.46%	16.53%	20.18%	9.69%	13.97%
$\Delta_p f = \Delta_p t = 8$	8.99%	14.94%	31.98%	39.62%	18.64%	24.72%
LTE normal CP	18.83%	24.84%	16.68%	20.60%	17.82%	22.92%

figurations provide an average throughput (achievable rate) gain of $\sim 20\%$ when compared to current LTE systems, with peak capacity improvements of 35%.

This enhancement comes without noticeably increasing the computational complexity, or the communication overhead between the transmitter and the receiver. Typical MMSE receivers rely on estimated second order channel statistics to enhance performance [71], and turbo decoders rely on estimated noise power to compute the log-likelihood ratios (LLRs). The signaling involved for implicit feedback using the codebooks of Table 2.3 is negligible: up to $\lceil \log_2(M_t M_f) \rceil = \lceil \log_2(6 \times 4) \rceil = 5$ bits are required once in every $T_{ofdm} = 1500$ OFDM symbols (107.8 ms for the typical 15 kHz subcarrier spacing). For CA-OFDM with $N_b = 2$ for our example, $\lceil \log_2[M_t M_f + (N_b - 1)M_f] \rceil = \lceil \log_2(6 \times 4 + 4) \rceil = 5$ bits are necessary with our reduced feedback scheme, as compared to $\lceil \log_2(N_b M_t M_f) \rceil = \lceil \log_2(2 \times 6 \times 4) \rceil = 6$ bits that would have been necessary otherwise. In both cases (with and without CA), the feedback of codebook indices translates to a data rate overhead of 46.38 bps. In the case of explicit feedback, we have $|\mathcal{P}| = 10$, $|\mathcal{D}_t| = 9$ and $|\mathcal{D}_f| = 6$, resulting in $b^{(fb)}_{\texttt{exp}} = \lceil \log_2(10 \times 9 \times 6) \rceil = 10$ bits of feedback overhead. In the case of dual-band carrier aggregation, the feedback overhead becomes $b^{(fb)}_{\texttt{exp,CA}} = \lceil \log_2(10 \times 9 \times 6 \times 2) \rceil = 11$ bits. The rates corresponding to these cases are $R^{(fb)}_{\texttt{exp}} = \frac{10}{1500 \times 71.875 \mu s} = 92.75$ bps and $R^{(fb)}_{\texttt{exp,CA}} = \frac{11}{1500 \times 71.875 \mu s} = 102.03$ bps respectively, which is twice the overhead of the implicit feedback scheme.

2.6.5 Pilot Adaptation Without Power Control

To demonstrate the performance of our proposed scheme in the case of *no power control*, we consider an A2G wireless channel in the 5 GHz band. The wireless channel can be parametrized

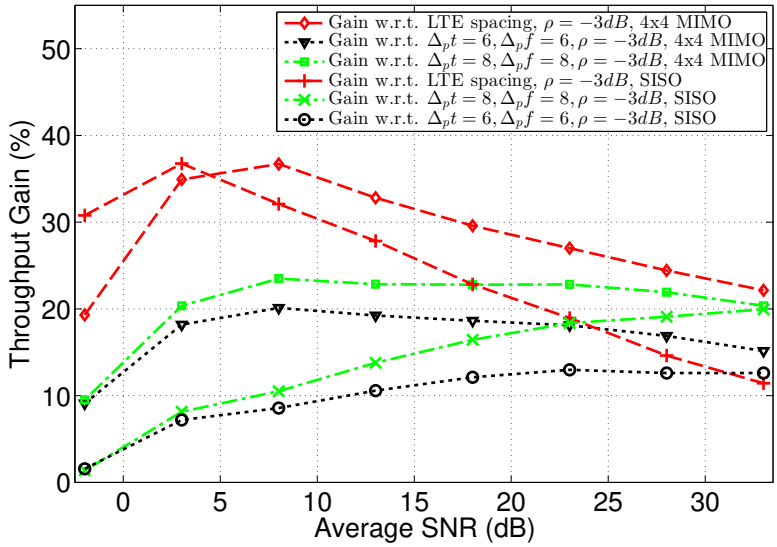

Figure 2.10: Throughput improvement of adaptive pilot configuration over fixed pilot schemes for a multi-band CA-OFDM system with component carriers at $f_1 = 700$ MHz and $f_2 = 2$ GHz, in nonstationary UAV to ground/UAV wireless channels.

by the signal-to-noise ratio (SNR), Doppler spread (f_d) and the root-mean squared (r.m.s.) delay spread (τ_{rms}).

For A2G scenarios, the nonstationary channel can be approximated to be stationary within a distance called the stationarity distance (SD). For A2G channels, extensive channel measurements reported in [54], [56] have shown that the SD ranges between 10 and 35 m. For a UAV traveling at an average speed of 75 m/s this corresponds to a stationarity time of up to 450 ms.

2.6.6 Scenario

We consider a scenario where a UAV is communicating with a ground station (GS) using an OFDM (LTE or NR-like) PHY layer (Table 2.6). The scenario consists of three stages, each lasting for about 2 minutes:

- Stage 1: The UAV flies in a hilly section towards a city. Due to reflections from hills, there is a presence of strong multipath components ($\tau_{rms} \sim 1\mu s$ [54]), and the UAV decelerates from 300 km/h to 200 km/h.
- Stage 2: The UAV then enters the suburban section, where τ_{rms} fluctuates between 50 ns and 500 ns [56]. The UAV uniformly decelerates from 200 km/h to 100 km/h.
- Stage 3: The UAV enters the urban section, where the contributions of multipath become prominent due to the presence of tall buildings [56]. The UAV velocity decelerates further to 50 km/h.

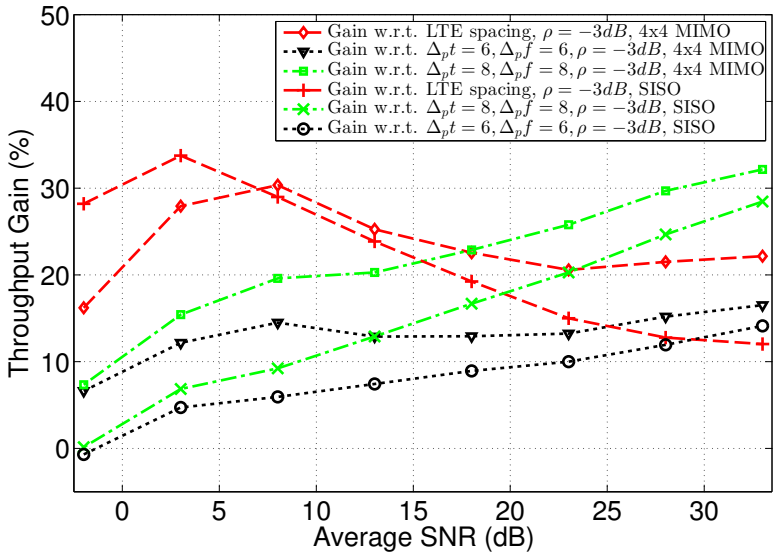

Figure 2.11: Throughput improvement of adaptive pilot configuration over fixed pilot schemes for a multi-band CA-OFDM system with component carriers at $f_1 = 700$ MHz and $f_2 = 2$ GHz, in nonstationary terrestrial wireless channels.

Regulations or UAV mission may be the cause for the varying UAV speeds, for e.g. a package delivery mission. The maximum doppler frequency $f_{d,m}$ is related to the velocity v by $f_{d,m} = vf_c/c$, where c is the velocity of light and f_c the carrier frequency. The SNR varies with distance based on the pathloss model parameters shown in Table 2.6, using the distance-based path loss with log-normal shadow fading [56]

$$PL(d) = A + 10n\log(d/R_{min}) + X - F \ \ [\text{dB}], \tag{2.24}$$

where $R_{min} \leq d \leq R_{max}$ and $X[\text{dB}] \sim \mathcal{N}(0, \sigma_X^2)$.

2.6.7 Performance Comparison with Fixed Pilot Configurations

We compare our rate-maximizing pilot scheme to the fixed pilot configurations $\mathcal{V}_{2,2}, \mathcal{V}_{4,2}, \mathcal{V}_{6,4}$ (similar to LTE), $\mathcal{V}_{6,6}$ and $\mathcal{V}_{8,8}$, where we denote $\mathcal{V}_{a,b} = \{\rho, \Delta_p f, \Delta_p t\} = \{-3 \text{ dB}, a, b\}$. Table 2.7 shows the channel statistics codebook $\mathcal{R}_C$ with $N_{\Delta f} = 62$ and $N_{\Delta t} = 40$, which is designed to cover most of the PDP and Doppler profiles. The pilot configuration $\mathcal{V}$ takes values from the following: $\mathcal{P}(\text{dB}) = \{-10, -9, -7, -5, -3, 0\}$, $\mathcal{D}_f = \{2, 4, \cdots, 10, 12\}$ and $\mathcal{D}_t = \{1, 2, \cdots, 9, 10\}$.

In order to estimate the optimal pilot configuration, we use $T_{ofdm} = 1500$ OFDM symbols across $N_{sub} = 72$ subcarriers to implement Algorithm 1. For this case the maximum time duration between the estimation and the use of $\mathcal{V}_o$ is 200 ms, which is less than the stationarity interval of 450 ms.

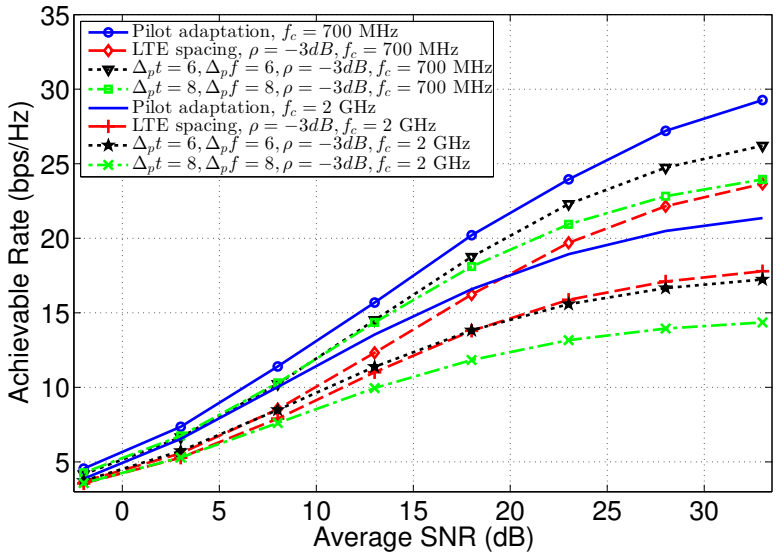

Figure 2.12: Enhancement of the achievable rate at $f_1 = 700$ MHz compared to $f_2 = 2$ GHz, for a 4×4 MIMO-OFDM system in nonstationary terrestrial wireless channels.

Fig. 2.14 shows the cumulative distribution function (CDF) of the achievable rates for all considered pilot configurations. We observe that our proposed adaptive pilot configuration outperforms all the other fixed pilot schemes considered, with the average throughput gain ranging from 9% to 80%. Fig. 2.15 shows the CDF of the ratio of the instantaneous rates ($\eta_{\texttt{inst}}$) obtained by the adaptive pilot configuration w.r.t. each considered fixed configuration. Table 2.8 compares the different percentile values of instantaneous rate gain, with $\Delta\eta_{\texttt{inst}}^{(x\%)}$ representing the x-percentile rate gain. We observe that due to the high Doppler frequencies, the throughput performance deteriorates with higher values of $\Delta_p t$. Even compared to a high pilot density configuration such as $\mathcal{V}_{2,2}$ and $\mathcal{V}_{4,2}$ the proposed pilot adaptation procedure has rate gains ranging from 3.6% to 34.6%, demonstrating its efficacy. The feedback overhead for explicit and implicit feedback mechanisms is is $\lceil \log_2(6 \times 6 \times 10) \rceil / (1500 \times 71.875\ \mu s) = 83.5$ bps and $\lceil \log_2(6 \times 4) \rceil / (1500 \times 71.875\ \mu s) = 46.4$ bps respectively. Both of these values are negligible compared to the data rates supported by current wireless networks.

2.7 Discussion

2.7.1 Extension to Other Types of Receivers

In this work, we have focused on least squares with linear interpolation channel estimation, and ZF equalization. There are more robust channel estimation and equalization methods such as Minimum mean square error (MMSE) and Linear MMSE (LMMSE). The derivation of the mean square error for these estimators is beyond the scope of this dissertation. We direct interested

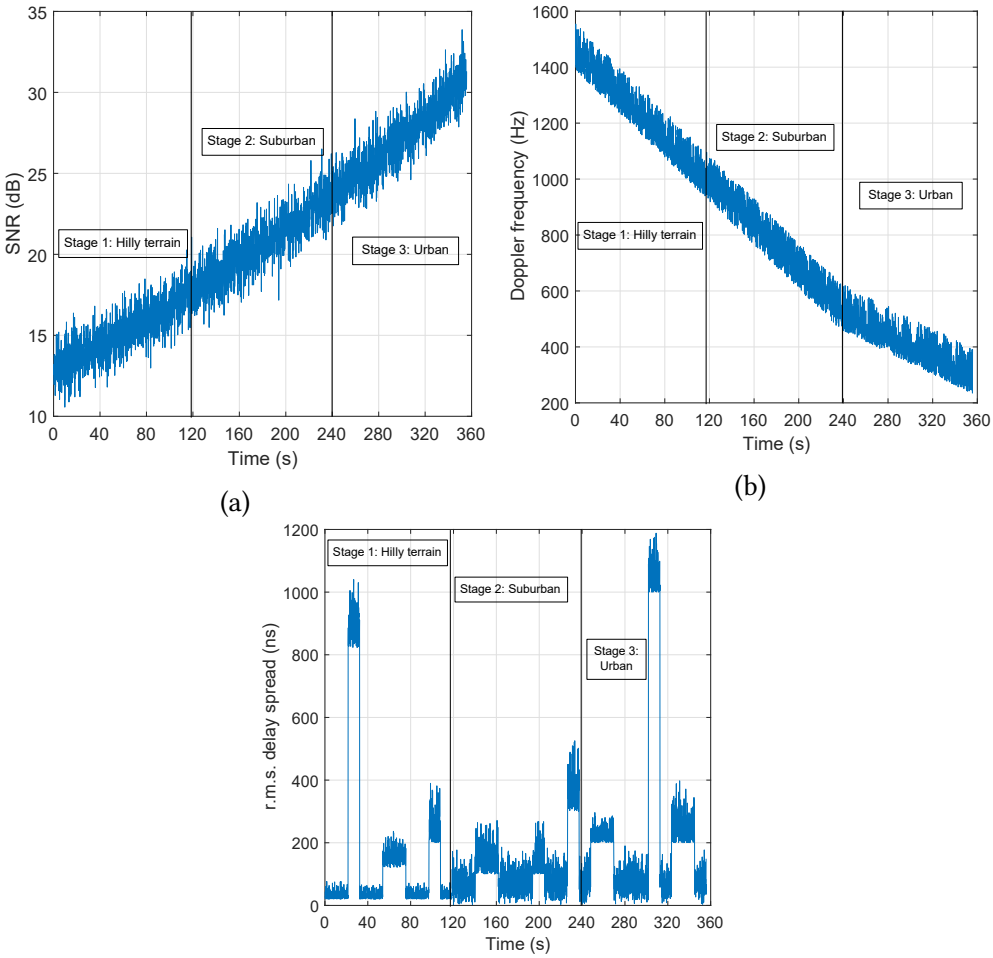

Figure 2.13: Variation of (a) SNR, (b) f_d and (c) τ_{rms} over time in the simulation scenario.

readers to [45] (equations (32)-(36)) for the MSE expression for LMMSE. However, using our framework, some simplifications are possible to ease the burden on numerical computation by using the WSSUS approximation for the channel correlation matrices:

1. The elements of matrices $\mathbf{R}_{\mathbf{h_p},\mathbf{h_p}}$, $\mathbf{R}_{\mathbf{h_d},\mathbf{h_p}}$ and $\mathbf{R}_{\mathbf{h_d},\mathbf{h_d}}$ (in equation (36) of [45]) take the form $R_t(\Delta t) \cdot R_f(\Delta f)$ when simplified using the WSSUS model.

2. We can use the codebook to populate the correlation matrices, since channel statistics vary fairly slowly. After finding l' and m' in equation (2.22), we can use the codebook entries to rapidly compute the channel autocorrelation and crosscorrelation matrices and hence, the MSE for each pilot configuration.

3. σ^2_{ICI} can be directly obtained using our codebook $\mathcal{R}_{C,t}$ and (2.4).

Table 2.6: Simulation Parameters

Parameter	**Value**
Antenna Configuration	SISO
FFT-length	128
No. of subcarriers (N_{sub})	72
Center Frequency (f_c)	5 GHz
Subcarrier Spacing (Δf)	15 kHz
OFDM symbol duration (T_s)	71.875 μs
Cyclic Prefix Duration	5.21 μs
Base pilot spacing	$\Delta_p t = 0.2875$ ms, $\Delta_p f = 90$ kHz
Channel parameters	Doubly selective: Jakes Doppler spectrum with multipath fading.
Transmit power	37.5 dBm
Noise Power Spectral Density	-174 dBm/Hz
Pathloss parameters [56]	$A = 116$ dB, $n = 1.8$, $\sigma_X = 3.1$ dB $F = 2.3$ dB, $R_{max} = 19$ km $R_{min} = 1.7$ km
Channel Estimation	Least Squares (pilots) 2D-Linear Interpolation (data REs)
Equalization	Zero Forcing (ZF)

Table 2.7: Codebook of channel profiles, $\mathcal{R}_C$

$\mathcal{R}_{C,t}$: Channel profiles for Doppler frequency

Index (m)	Mobility Type	Velocity	$f_d^{\dagger}$ (Hz)
1	Almost stationary	1 km/h	4.6
2	Low speed (taxiing)	15 km/h	70
3	High speed (taxiing)	55 km/h	250
4	Takeoff/Landing	120 km/h	550
5	Medium speed (airborne)	160 km/h	750
6	High Speed (airborne)	250 km/h	1150

†Doppler frequency for a center frequency of $f_c = 5$ GHz.

$\mathcal{R}_{C,f}$: Channel profiles for Power Delay Profiles (PDP)

Index (l)	Type of Scattering	τ_{rms}
1	Low (near-LoS)	221.5
2	Medium (Suburban air-to-ground)	476.4
3	High (Near-Urban air-to-ground)	791.2
4	Very High (Urban/Hilly air-to-ground)	1440

It is important to note that our scheme is general and can be used with any OFDM channel estimator and equalizer when the channel estimation MSE, ICI power and the diversity order per stream σ (σ_{ZF} in this chapter) can be estimated with a reasonable accuracy at the receiver.

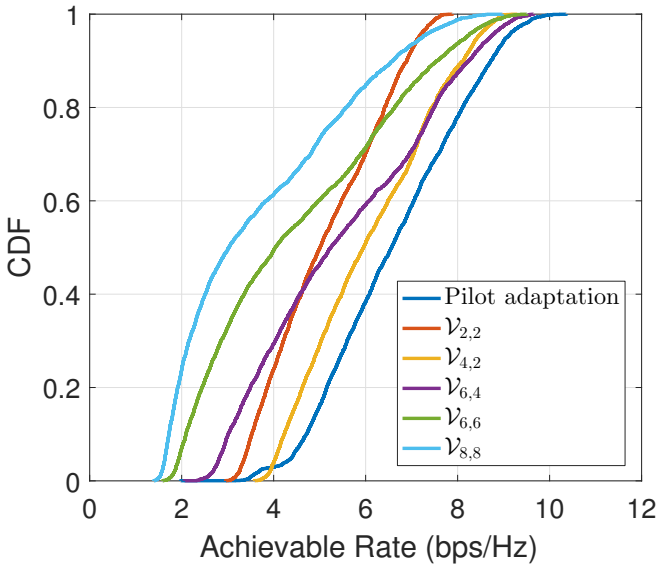

Figure 2.14: CDF comparison of the average achievable rate of pilot adaptation scheme versus fixed pilot configuration schemes.

Table 2.8: Instantaneous rate gains of adaptive pilot over fixed pilot configurations

Scheme	$\Delta\eta_{\mathtt{inst}}^{(10\%)}$	$\Delta\eta_{\mathtt{inst}}^{(50\%)}$	$\Delta\eta_{\mathtt{inst}}^{(90\%)}$
$\mathcal{V}_{2,2}$	21.8%	32%	34.6%
$\mathcal{V}_{4,2}$	3.8%	11.1%	12%
$\mathcal{V}_{6,4}$	3.6%	23.9%	54.9%
$\mathcal{V}_{6,6}$	14%	62.8%	122.4%
$\mathcal{V}_{8,8}$	31.5%	113.6%	179.7%

2.7.2 Practical Considerations

For pilot adaptation in the downlink frame, the proposed scheme relies on channel statistics estimated by the user, which are fed back to the base station. Hence, the pilot patterns can potentially vary among users in a cell because different users generally experience different channel statistics. This implies that implementing pilot adaptation is not straightforward for pilots that are broadcasted in a cell, such as the Cell-Specific Reference Signal (CRS) in LTE [37].

Moreover, there are possibilities of pilot corruption due to pilot contamination between two cells if all types of pilots are adapted. Hence, we provide a few guidelines for pilot pattern adaptation:

1. It is well suited for user-specific pilots, for example UE specific Reference Signals of LTE [37].

2. It is also applicable for peer-to-peer links such as wireless backhaul, vehicular-to-vehicular, UAV-to-ground/UAV-to-UAV systems. In such systems, the issue of interference with other

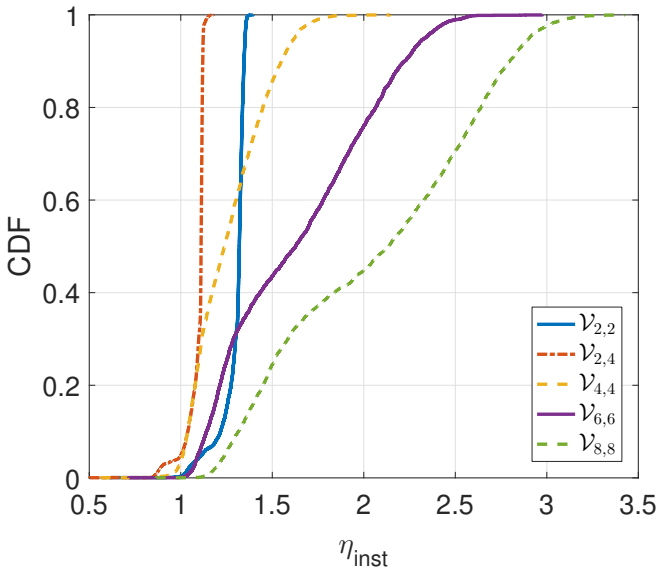

Figure 2.15: CDF comparison of the instantaneous rate gain ($\eta_{\texttt{inst}}$) of pilot adaptation versus fixed pilot configurations.

pilots typically does not arise.

3. It can be extended to grouping of users having similar channel conditions during resource allocation [48]. Active user-aware dynamic pilot distribution as well as joint pilot and user scheduling can help better utilize maximize system spectral efficiency.

4. Leveraging CA-OFDM, users can be grouped and scheduled to different component carriers according to their channel statistics.

5. In multiuser-MIMO (MU-MIMO), the scheduling of users with (a) similar second order channel statistics and (b) orthogonal precoding vectors is necessary to perform pilot pattern adaptation.

2.8 Conclusion

Flexibility is a key trait of future wireless standards, where the communications protocols can be customized on a per-user or network basis to optimize performance. In this chapter, we provided an efficient heuristic scheme to design rate maximizing pilot configurations in SISO and MIMO-OFDM systems based on the second order statistics of doubly selective nonstationary wireless channels. We also extended this concept to CA-OFDM systems. We derived closed form expressions for channel estimation MSE for pilots arranged in a diamond-pattern. Using the derived MSE expressions and the lower bound on ICI, we devised a codebook-based approach to adapt the pilot spacing and power based on estimated channel statistics. Our scheme adds negligible

computational complexity since (a) modern wireless receivers implementing the MMSE receiver already implement such channel statistics estimators, and (b) finding the closest codebook profile and the optimal pilot configuration are also low-complexity operations. Also, the feedback overhead is shown to be negligible in current, high-capacity wireless standards.

Our numerical results for two communications environments have shown that the average throughput gain of our scheme w.r.t. LTE pilot spacing is 16 to 20% for SISO and 20 to 28% for 4×4 MIMO in the case of perfect power control. In the case of no power control, the average rate gains ranged from 9% to 80%. Our algorithm is agnostic to standard-specific mechanisms such as adaptive modulation and coding. Therefore, the presented results are fundamental and represent throughput gains achieved by using adaptive pilot configurations in OFDM-based wireless standards.

Adaptive waveforms is the theme of physical layer design of future 5G wireless communication systems in order to maximize the spectral efficiency. This work can be extended to other multicarrier waveforms such as Filter-bank Multicarrier (FBMC) and Non-orthogonal multiple access (NOMA) schemes, enhancing the spectral efficiency of other candidate physical layers for 5G.

Pertaining to cross-layer optimization using adaptive pilot configurations, open research areas include joint pilot design and user scheduling in carrier-aggregation and MU-MIMO wireless systems. Protocol designs built around this framework which drive the selection of other radio resource management (RRM) parameters, and characterization of their performance, would be crucial to evaluating the enhancement in overall network throughput of such systems.

Part II

Robust CSI Estimation and Feedback for Current and Future Cellular Systems in Shared Spectrum with Pulsed Radars

Chapter 3

Impact of Non-Pilot Interference (NPI) on Channel State Information (CSI) Acquisition and Link Adaptation

3.1 Introduction

LTE has succeeded in meeting its goals and objectives as a global cellular standard since its first release (Release 8). Through its evolution to 5G New Radio (5G NR), it has acquired enhancements across all layers, with new capabilities such as support for vehicular communications [27], device to device (D2D) and the Internet of Things (Narrowband-IoT) [74]. Because of its success in the commercial and civilian sectors, LTE is being targeted to be used in public safety [75], military networks, and control of the smart grid [76]. To meet the demand in capacity in the face of spectrum shortage, NR leverages multiple technologies ranging from spectrum sharing with LTE, WiFi and other wireless technologies and services, to Massive MIMO.

However, LTE is not without its shortcomings. It has been shown to be vulnerable to protocol-aware attacks across all layers [77], especially the physical layer [78], [79]. In part, this is a result of the vulnerability of its PHY layer waveform, Orthogonal Frequency Division Multiplexing (OFDM) [80] and its variants such as Single Carrier Frequency Division Multiple Access (SC-FDMA). In addition to the waveform itself, several control channels of 4G LTE have been shown to be vulnerable to intentional (jamming) as well as unintentional interference. In light of its branching into mission-critical communications, enhancing the resilience of cellular standards to RF interference is of paramount importance at the lower (Physical and Medium Access Control) layers.

This chapter is based on the work published in [73].

3.1.1 Related Work

RF Interference in OFDM systems have been studied from a theoretical perspective for critical PHY functions such as synchronization and channel estimation. Keyi et al. [81] proposed a synchronization algorithm based on adaptive filtering to mitigate partial band jamming. Clancy [82] has demonstrated the effectiveness of pilot-tone (also known as 'reference signal') jamming as an effective strategy to cause denial of service in wireless networks. The authors in [83] quantify the bit error probability (BEP) in the case of imperfect channel estimation. The authors in [84] mitigate the degradation due to pilot jamming using pilot tone randomization at the cost of reduced channel performance due to unequally spaced pilot resource elements (REs). Karlsson et al. [85] theoretically analyzed the vulnerability of TDD-massive MIMO to pilot interference. Xu et al. [86] develop a novel coding scheme to authenticate the channel training phase using an independence checking coding (ICC)-based protocol.

LTE has been known to be vulnerable to protocol-aware jamming, also known as smart jamming. Kakar et al. [87] investigate the performance of the Physical Control Format Indicator Channel (PCFICH) in harsh interference conditions and propose mitigation strategies. Lichtman et al. [88] consider the problem of targeted interference on the Physical Uplink Control Channel (PUCCH) and propose detection and mitigation strategies to counter protocol-aware jammers. Labib et al. [89] introduce and demonstrate *LTE control channel spoofing*, which refers to deceiving a user terminal by a fake eNodeB (eNB) that transmits a partial LTE downlink frame at a higher power than the legitimate control channel. The authors demonstrated that this attack resulted in Denial of service (DoS), and proposed mitigation strategies that require a simple modification to the cell selection process of LTE [90].

A comprehensive threat assessment of LTE/LTE-A is provided in [77], highlighting the vulnerabilities of various LTE physical channels and signals, and surveying the mitigation techniques proposed in the open literature. Jover et al. [91] focus on the analysis of LTE network jamming, and propose a series of security research directions to force a jammer to resort to wideband jamming methods. In our prior works [78], [79], we have have empirically demonstrated the vulnerability of various LTE control channels to protocol-aware interference, and identified the most vulnerable control channels using effective jammer-to-signal-ratio (JSR) as a metric. Since 5G NR reuses some of the philosophies of 4G networks in the aspects of control channel signaling, and its reliance on accurate channel state information (CSI), some of the PHY layer vulnerabilites of LTE apply to 5G NR as well [92]. Recently, Jover et al. [93] highlighted the potential security vulnerabilities of 5G NR at higher layers.

3.1.2 Main Contributions

The main contributions of this chapter are:

1. We present link-level simulation and hardware experimental results to demonstrate the

degradation of cellular link adaptation performance in the presence of 'non-pilot interference' (NPI).

2. We also show that this performance degradation is a result of contaminated *channel state information (CSI)*, which occurs in the presence of NPI.
3. We analyze the impact of NPI on the latency performance of the link, by deriving an approximate closed-form expression of the retransmission-induced latency as a function of the block error rate (BLER).

The rest of the chapter is organized as follows: Section 3.2 provides a brief overview of (a) link adaptation and CSI feedback in cellular systems, (b) the quantities that represent CSI in LTE and NR, and (c) the system model of the cellular downlink impaired by interference. Section 3.3 introduces the notion of NPI, and considers a case study of the LTE downlink impaired by NPI. It presents experimental and link-level simulation results quantifying the detrimental impact of NPI on cellular link adaptation performance. In Section 3.4, we use a tractable retransmission model to derive the relationship between BLER and *average retransmission-induced latency*, and demonstrate the accuracy of the derived expression using link-level simulations. Finally, Section 3.5 summarizes the key takeaways from the chapter, and its implications on low-latency communications.

3.2 Background on Link Adaptation and CSI Feedback in Cellular Systems

3.2.1 Link Adaptation and CSI Feedback

Link adaptation is the process of adapting the transmission parameters and hence, the data rate, as a function of the SINR at the receiver. In modern cellular standards such as 4G LTE and 5G NR, the transmission parameters include the transmission mode (TM) and modulation and coding scheme (MCS). Example of TMs include single-input-single-output (SISO), multiple-input-multiple-output (MIMO), diversity and beamforming. Examples of MCS include a combination of digital modulation schemes such as BPSK/QPSK/QAM, and different forward error correction (FEC) coding schemes and rates [37]. In 3GPP terminology, all the MIMO transmission modes are classified under a common term called as 'precoding'.

From a theoretical standpoint, channel state information (CSI) refers to knowledge pertaining to the channel conditions between (a) transmitter and the receiver (downlink CSI), or (b) receiver and the transmitter (uplink CSI). CSI is classified into two main categories:

1. Instantaneous CSI: It refers to knowledge of the instantaneous properties of the channel under consideration. For e.g. the instantaneous MIMO channel matrix between the eNB and the UE.

2. Statistical CSI: It refers to knowledge of the statistical properties of the channel under consideration, such as the mean, covariance, joint probability density function etc.

For TDD systems in the absence of interference, it is possible to leverage instantaneous CSI due to the uplink-downlink channel reciprocity (assuming the channel estimates are perfect). However, in FDD systems, it is impractical to obtain instantaneous CSI due to the high feedback overhead. On the other hand, obtaining statistical CSI is possible in practical scenarios. Fundamental research on novel beamforming and CSI feedback schemes for FDD Massive MIMO such as Joint Spatial Division Multiplexing (JSDM) [5],[94], has inspired practical CSI feedback mechanisms for FDD Massive MIMO systems in 5G NR [10].

3.2.2 CSI Feedback in LTE and NR

For FDD-based LTE and NR systems, the channel state information at the receiver (CSIR) is periodically fed back to the transmitter to successfully implement link adaptation schemes. Specifically, the transmitter sends pilot/reference signals to the receiver to aid in CSIR estimation. This is possible since the reference signals are known to both the transmitter and reciever. The receiver quantizes the pilot-aided CSIR estimate to limit feedback overhead, and this quantization function depends on the cellular standard and the transmission mode (TM) used. Up to Third Generation Partnership Project (3GPP) Release 14, CSI consists of the following parameters:

1. Channel Quality Indicator (CQI): A 4-bit value that is mapped to a 5-bit MCS value.
2. Precoding Matrix Indicator (PMI): An index from a fixed library of precoding matrix elements.
3. Rank Indicator (RI): Index of transmission rank that the user can support.

The 3GPP standard specifies that for the downlink, up to two LTE codewords can be transmitted for each user, where the MCS value for each codeword must be chosen to keep the BLER below 10% [37]. In practical deployments, a lookup table-based approach is used for each TM to map the SINR to a CQI value [70]. For MIMO transmission modes, LTE and NR standards support *codebook-based precoding*, where the precoding matrices used are always chosen from a standardized library of matrices, called in the 3GPP standards as a codebook[1].

In LTE and NR, the typical sequence of CSI estimation is:

1. The optimal rank and the corresponding precoding matrix are estimated to obtain the RI and PMI components of CSI.

[1]LTE and NR also support non-codebook based precoding operations in several transmission modes [37]. Typically, it makes sense to use this mode in TDD systems, or channels where the uplink and downlink channels have similar spatial correlation [95].

2. *Conditioned on the RI and PMI*, the *post-equalizer SINR* is estimated for each LTE codeword, and the resultant SINR is quantized to derive the 4-bit channel quality indicator (CQI).

5G NR also used the above parameters for assessing the CSI of the link. However at mmWave bands, estimation of phase noise also becomes important for assessing the baseband post-equalization SINR. Phase tracking reference signals (PTRS) are used for the purpose of estimating phase noise in mmWave 5G NR systems.

3.2.3 LTE and NR System Model

Consider the LTE/NR downlink with a single eNB and a single UE, where the eNB has N and the UE K antenna ports. The received symbol vector on the k^{th} subcarrier can be modeled as

$$\mathbf{y}_k = \mathbf{H}_k \mathbf{W}_k \mathbf{d}_k + \mathbf{h}_{r,k} i_k + \mathbf{n}_k, \tag{3.1}$$

where $\mathbf{y}_k \in \mathbb{C}^{K\times 1}$ is the received data symbol vector, $\mathbf{H}_k \in \mathbb{C}^{K\times N}$ the channel matrix, $\mathbf{W}_k \in \mathbb{C}^{N\times K}$ the precoding matrix, $\mathbf{d}_k \in \mathbb{C}^{K\times 1}$ the transmitted data symbols and $\mathbf{n}_k \sim \mathcal{CN}(0, \sigma_n^2 \mathbf{I})$ the K-dimensional i.i.d. complex Gaussian noise vector. The interferer-to-UE channel vector on the k^{th} subcarrier is given by $\mathbf{h}_{r,k} \in \mathbb{C}^{K\times 1}$, and the corresponding interference symbol is i_k. Without loss of generality, we assume that the interferer has a single transmit antenna. For ease of notation, we suppress the subcarrier index henceforth. Choosing the transmission mode parameters involves choosing the precoding matrix (selects the rank indirectly) and the MCS for the data symbols [37].

It is important that link adaptation be based on the *post-equalization SINR*, i.e. the SINR after the received OFDM grid across multiple antenna ports and spatial layers are combined into demodulated symbols that are later decoded to retrieve the LTE codeword. After receiving the signal in (5.3), if $\hat{\mathbf{H}}$ is the estimated channel matrix and $\hat{\sigma}_n^2$ the estimated noise variance, then the decoded data symbols using a MMSE equalizer are given by

$$\hat{\mathbf{d}} = (\mathbf{W}^H \hat{\mathbf{H}}^H \hat{\mathbf{H}} \mathbf{W} + \hat{\sigma}_n^2 \mathbf{I}_K)^{-1} \mathbf{W}^H \hat{\mathbf{H}}^H \mathbf{y}, \tag{3.2}$$

where $\mathbf{I}_K$ is the K-dimensional identity matrix. Defining $\hat{\mathbf{G}}_{\mathbf{w}} = (\mathbf{W}^H \hat{\mathbf{H}}^H \hat{\mathbf{H}} \mathbf{W} + \hat{\sigma}_n^2 \mathbf{I})^{-1} \mathbf{W}^H \hat{\mathbf{H}}^H$, the post-equalization SINR γ_i for the i^{th} spatial layer is

$$\gamma_i = \frac{|d_i|^2}{|\left[(\hat{\mathbf{G}}_{\mathbf{w}} \mathbf{H} \mathbf{W} - \mathbf{I})\mathbf{d} + \hat{\mathbf{G}}_{\mathbf{w}} \mathbf{h}_r i + \hat{\mathbf{G}}_{\mathbf{w}} \mathbf{n}\right]_i|^2}. \tag{3.3}$$

For SISO and low-ranked MIMO modes, there is very little distinction between an LTE codeword and a spatial layer as far as link adaptation is concerned. However for transmission rank of 3 or greater, the symbols of an LTE codeword can be transmitted on different spatial layers. In these cases, care must be taken to choose the MCS that is *appropriate for all the spatial layers* from which an LTE codeword is transmitted. For ease of exposition of the key ideas, we focus the demonstration and discussion to SISO-OFDM systems in this chapter, although similar effects can be observed in MIMO-OFDM systems as well.

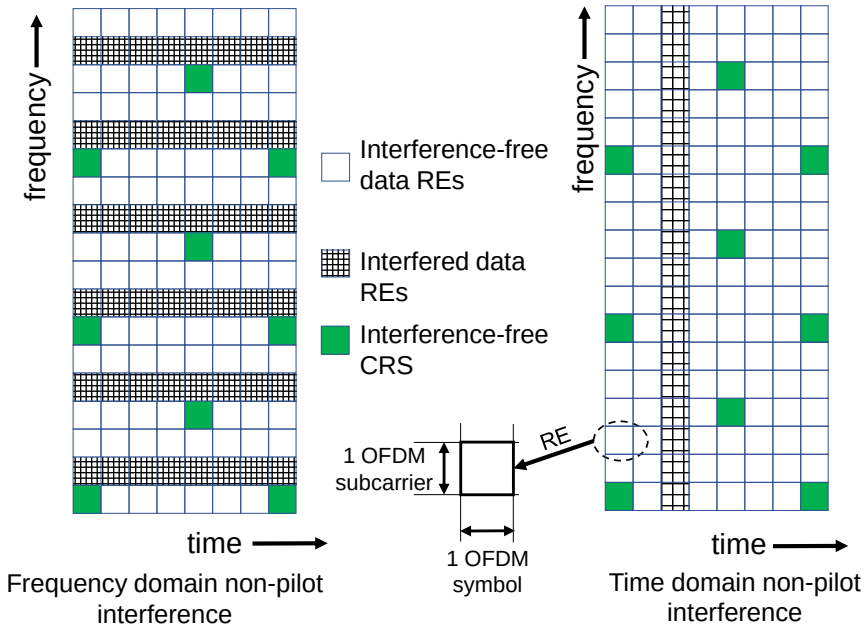

Figure 3.1: Illustration of non-pilot interference (NPI) on the LTE resource grid, and its different types: Frequency-domain NPI and Time-domain NPI.

3.3 Impact of Non-Pilot Interference on the LTE Downlink

3.3.1 Non-Pilot Interference

For *pilot-aided CSI estimates*, the CSIR is accurate as long as the noise and interference statistics on the pilot and the non-pilot resources are the same. While this is true in typical multi-cellular co-channel interference, it will not be the case in the presence on interference that *only affects non-pilot resources*.

In typical cellular signals, pilots are sparsely allocated resources in time, frequency and spatial layers. Fig. 3.1 shows the example of cell-specific reference signals (CRS), which are pilot resource elements in LTE [37]. In later releases of LTE and 5G NR, there are additional pilots such as demodulation reference signals (DMRS) and CSI-Reference Signals (CSI-RS), which are used for coherent demodulation and CSI estimation for more advanced multi-antenna techniques [37]. Similar to CRS, these reference signals are also sparsely located in the OFDM resource grid.

In prior works [77], [78], [79], [96], it has been demonstrated that control channels with sparse resource allocation in the OFDM grid are more vulnerable to hostile interference, especially from a signal-to-interference-ratio (ISR) perspective. To an extent, this is true for non-pilot interference as well: they can leverage the sparsity of pilot resources to localize interference on non-pilot resources, as shown in Fig. 3.1, to *contaminate the CSI estimated by the receiver*. In contrast to

Table 3.1: Important system parameters in Chapter 3

Parameter	**Description**
γ	Signal-to-interference-plus-noise ratio (SINR)
$\gamma_{\texttt{act}}$	Actual SINR
$\texttt{CQI}$	Channel quality indicator
$\gamma_{\texttt{CQI}}^{(\texttt{med})}$	SINR inferred from the median CQI
$\bar{\tau}_{\texttt{retx}}$	Average retransmission-induced latency
$\bar{\tau}_{\texttt{wait}}$	Average wait-time between consecutive retransmissions
$\bar{N}_{\texttt{harq}}$	Average Hybrid ARQ retransmissions
$\texttt{BLER}$	Block error rate

pilot interference (PI) which contaminates the channel estimates at the receiver [77], non-pilot interference (NPI) contaminates the CSIR (CQI/PMI/RI estimates). Hence, the CSI reports (CQI, PMI and PI) fed back to the transmitter will be inaccurate in the case of NPI.

Based on the localization of power in time and frequency, non-pilot interference can be broadly classified into:

1. Time-domain non-pilot interference (TD-NPI): The interference can take a pulsed form targeting OFDM symbols between two pilots, as shown in Fig. 3.1. Example: On-off jammers, and pulsed-radar signals.

2. Frequency-domain non-pilot interference (FD-NPI): Interference can be localized in between pilot subcarriers, as shown in Fig. 3.1. Example: Multi-tone NPI.

Unintentional interference such as a pulsed radar signal may not exclusively affect non-pilot resources *all the time*. However, for large pilot spacing (in time) or large radar pulse repetition intervals, the probability of radar affecting non-pilot resources is high. This will be formalized in Chapter 4.

3.3.2 Case Study: Interference Experiments with the LTE Downlink

We consider the LTE downlink with an eNodeB serving a single user equipment (UE) in the presence of multi-tone interference. We consider three scenarios:

1. Pilot interference (PI): The interference is localized on pilot subcarriers, and non-pilot subcarriers are unaffected. Such interference has been studied in [77], [78], [79], [80], [82], [84], [83], [85], [86].

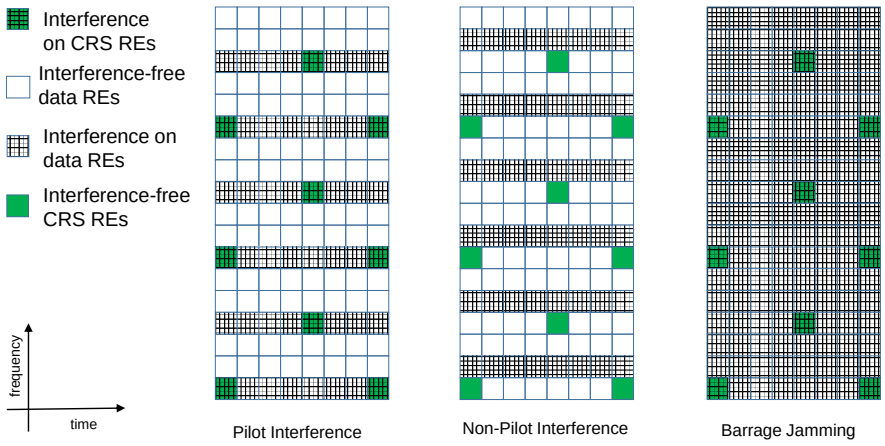

Figure 3.2: Schematic of the multi-tone interference strategies considered: PI, NPI and barrage jamming. For the same power per subcarrier, barrage jamming needs three times the power than PI and NPI.

2. Non-Pilot Interference (NPI): In contrast to pilot interference, the interference is localized exclusively on non-pilot subcarriers.

3. Barrage Jamming: This is a common technique of wideband interference, where all subcarriers are affected.

These interference strategies are shown in Fig. 3.2. Prior work on OFDM pilot jamming has shown that the reduction in performance can be mitigated by pseudo-randomly changing the pilot locations to evade the jammer [82, 84]. It is interesting to note that the resulting scenario will be equivalent to NPI. As our results will show, evading pilot interference will not provide performance improvements predicted by the theoretical analysis in [82], [84].

We consider a multi-tone non-pilot interferer with equal spacing between adjacent frequency tones and equal power allocation across all the targeted OFDM subcarriers. Below, we describe the experimental and simulation methodology to evaluate the impact of these interference strategies.

3.3.3 Experimental Setup

The experimental setup to evaluate LTE's performance in multi-tone interference is shown in Fig. 3.3. We used Amarisoft™, a proprietary SDR-based LTE eNodeB, and LTE test UEs of Virginia Tech's LTE-CORNET Testbed [1]. We used a cabled setup enclosed in a shielded box to isolate the experiment to/from external RF signals. The Amarisoft eNB was interfaced with a Universal Software Radio peripheral (USRP) to generate the LTE downlink signal. Commercial LTE UE dongles

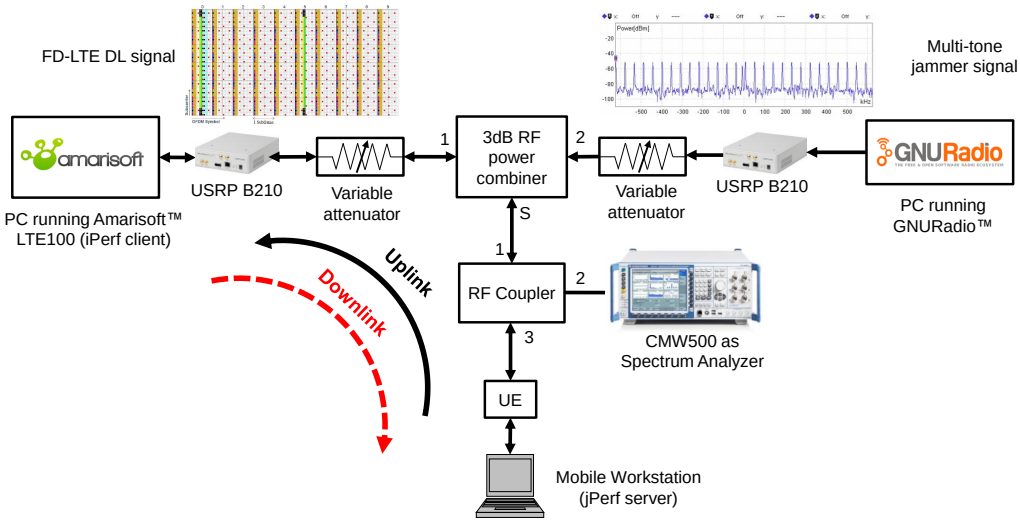

Figure 3.3: Schematic of the LTE downlink multi-tone interference experiments using the Virginia Tech LTE-CORNET Testbed [1].

were connected to a laptop through a USB interface, to emulate a practical scenario. We monitored the LTE downlink and the jammer spectrum using the CMW 500 Rohde and Schwarz™ LTE test equipment, and control the LTE and multi-tone interference power using variable attenuators as shown in Fig. 3.3. For each SINR value, full buffer traffic was generated using an iPerf client at the PC running Amarisoft, and a jPerf server running on the laptop connected to the LTE UE. We generated custom multi-tone interference waveforms using GNURadio™. The experimental parameters are shown in Table 3.2. For each SINR value and interference scenario (PI/NPI/barrage), the average throughput and the BLER is measured for 10^5 frames of LTE downlink traffic to the UE.

3.3.4 Link-level Simulation Study

We simulated the LTE downlink using a link-level simulator using the MATLAB™ LTE Toolbox, consisting of an eNB serving a single UE in the presence of multi-tone interference in a doubly selective (time and frequency) fading channel.

We used the extended pedestrian-A (EPA) channel model to simulate the multipath fading characteristics with a Doppler frequency of 20 Hz and SNR $\geq$ 25 dB. The rest of the parameters are the same as shown in Table 3.2.

For the case of SISO-systems, the CSI feedback is equivalent to the 4-bit CQI value in LTE, which takes a value from 0 to 15. In most practical implementations, the SINR-to-CQI conversion is based on a lookup table approach with an SINR granularity of approximately 2 dB [97]. For SISO transmissions from LTE Port 0, the SINR-to-CQI mapping we have used (which is the same as

Table 3.2: Experimental parameters

Parameter	**Description**
LTE Release	3GPP Release 10
Frequency band	Band 7
Bandwidth	10 MHz
Reference signal received power (RSRP)	-72 dBm
Transmission Mode	TM 0 (SISO) from Port 0 [37]
Channel	Cabled setup with SNR $>$ 30 dB.
CSI feedback mode	Periodic and Wideband
CSI periodicity	10 ms
HARQ mode	Asynchronous and Non-Adaptive with upto 4 retransmissions

that in the MATLAB LTE Toolbox®) is given by

$$\texttt{CQI} = \begin{cases} 0 & \text{if } \gamma \leq -9.24 \text{ dB} \\ \left\lfloor \frac{\gamma + 9.24}{2.11} \right\rfloor & \text{if } -9.24 \text{ dB} < \gamma \leq 24.3 \text{ dB} \\ 15 & \text{if } \gamma > 24.3 \text{ dB}, \end{cases} \tag{3.4}$$

where γ is the SINR value in dB. This relation is valid only for the TM 0 transmission mode [37]. Other transmission modes use a different SINR-to-CQI table, which are typically obtained using comprehensive link-level simulations in practice [98].

3.3.5 Experimental and Link-Level Simulation Results

In the absence of multi-tone interference, we measured an average throughput of 36.5 Mbps, which is very close to the theoretical maximum throughput of 37.5 Mbps achievable with a 10 MHz LTE system. In addition, the measured BLER was consistently under 10% in the absence of any interference, indicating successful link adaptation. Fig. 3.4a shows the measured BLER performance for different multi-tone interference scenarios, in our hardware experiment from Fig. 3.3. We observe that the BLER in non-pilot interference is above 50% which *indicates link adaptation failure*, since successful link adaptation has a BLER $\leq 10\%$. On the other hand, the BLER in pilot and barrage interference fluctuates around 10% up to an SINR of 0 dB, and then gradually begins to deteriorate. We observe a similar trend in Fig. 3.4b, which shows the BLER performance in our link-level simulations.

During our hardware experiments described in Section 3.3.3, the actual SINR ($\gamma_{\texttt{act}}$) was measured

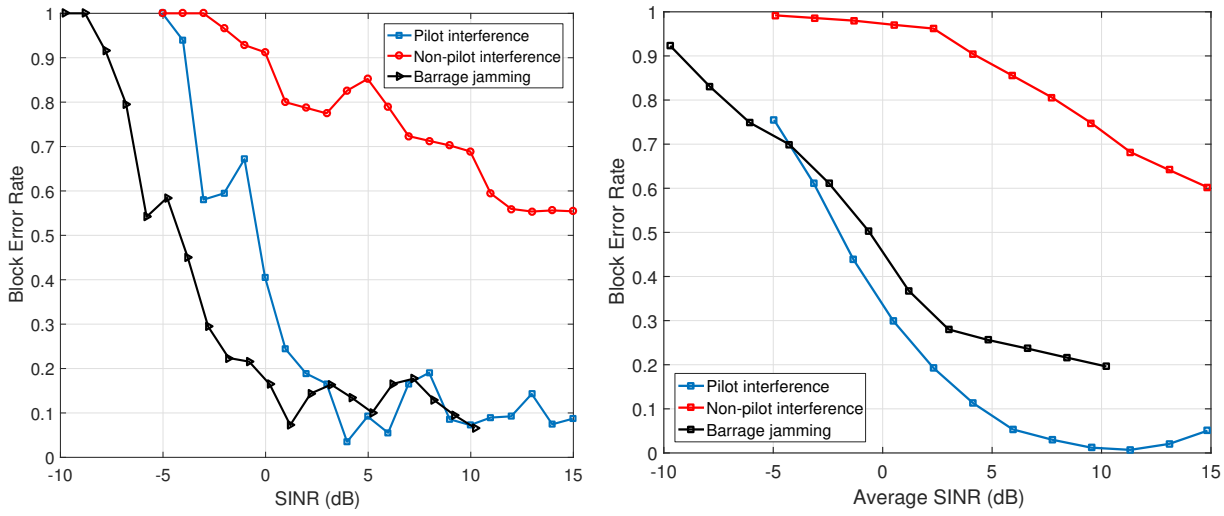

(a) (b)

Figure 3.4: BLER as a function of SINR for PI, NPI and barrage interference, measured during (a) hardware experiments, and (b) link-level simulations.

for each interference scenario using a spectrum analyzer before each downlink transmission. The *SINR estimated by the UEs* was inferred by monitoring the CQI reports sent by the UE to the eNB for all interference scenarios. Most UE manufacturers use a lookup table (LUT)-based approach to calculate CQI from the pilot-aided SINR estimate. Assuming a SINR-to-CQI mapping given by[2] $\gamma_{\texttt{CQI}}\,(\text{dB}) = 2.11 \cdot \texttt{CQI} - 9$, the SINR inferred from the median user-reported CQI ($\gamma_{\texttt{CQI}}^{(\texttt{med})}$) was calculated. Fig. 3.5 shows the actual SINR versus the quantized SINR reported by the UE to the eNB in its periodic CQI reports. Defining $\Delta\gamma \triangleq \gamma_{\texttt{act}} - \gamma_{\texttt{CQI}}^{(\texttt{med})}$, we observe that while $|\Delta\gamma| \approx 3$ dB for PI and barrage jamming, for NPI the value of $|\Delta\gamma|$ ranges from $7 - 10$ dB. The steep decline in $\gamma_{\texttt{CQI}}^{(\texttt{med})}$ at $\gamma_{\texttt{act}} = -3$ dB for NPI is an artifact of the SINR-to-CQI mapping. When the UE experiences outage after detaching from the eNB, the CQI is taken to be 0 by default, for which the corresponding $\gamma_{\texttt{CQI}}^{(\texttt{med})} = -9$ dB.

Such overly optimistic SINR estimates with NPI leads to the use of a higher MCS which is not supported by the downlink data channel. Wrongly decoded blocks are retransmitted and when the BLER is high, retransmissions are more frequent. This means that the link adaptation procedure optimized for 3GPP small scale channel fading models fail when the channel is impaired by non-pilot multitone interference.

Fig. 3.6a shows the measured throughput of the LTE downlink for different interference scenarios. We observe that the throughput performance is close for PI and NPI. However, we observe that outage occurs in NPI at a higher SINR when compared to PI. This behavior can also be ob-

[2]We obtained this mapping from MATLAB's LTE Toolbox. The SINR-to-CQI mapping is not unique, but varies from one transmission mode to another, and from one vendor to another. Similar SINR-to-CQI mappings have been reported in the literature, for e.g. in [70].

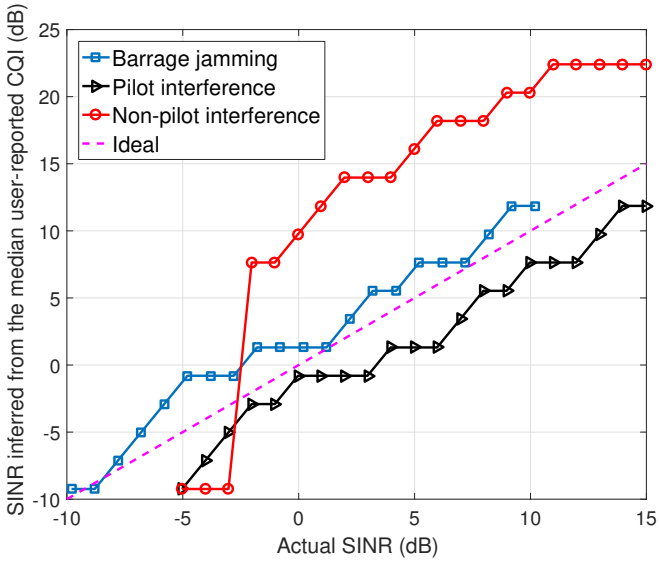

Figure 3.5: Comparison of the actual SINR ($\gamma_{\mathtt{act}}$) versus the SINR inferred from the median user-reported CQI ($\gamma_{\mathtt{CQI}}^{(\mathtt{med})}$), during our hardware experiments for PI, NPI and barrage interference with the testbed described in Fig. 3.3.

served in our link-level simulation throughput results in Fig. 3.6b. We also observe that barrage jamming requires about 5 dB more power than PI/NPI to cause the same reduction in throughput. This apparent *"jammer power gain"* with respect to the pilot interferer is intuitive, since the barrage jammer targets all OFDM subcarriers. Because corrupted channel estimates cause significant degradation in SINR [82], [84], pilot jamming can cause the same amount of throughput degradation with $10\log_{10} 3 \approx 4.77$ dB (one out of three OFDM subcarriers contains a pilot symbol in LTE) less power than the barrage jammer.

3.4 Impact of Non-Pilot Interference on Low-latency Communications

The end-to-end latency in a wireless link encompasses contributions from various sources such as propagation, queuing, scheduling and signal processing. Here, we are particularly interested in the *retransmission-induced latency* $\tau_{\mathtt{retx}}$, which we define as the latency to a user *only due to retransmissions*. The initial transmission is excluded from this latency metric, so that $\tau_{\mathtt{retx}} = 0$ if the initial transmission succeeds.

To develop useful insights on the impact of NPI on latency, we make the following assumptions to derive a closed-form expression between the BLER and average $\tau_{\mathtt{retx}}$ ($\bar{\tau}_{\mathtt{retx}}$).

Assumption 3.1. *Each user is allocated resources in entities of blocks, in which the bits are inter-*

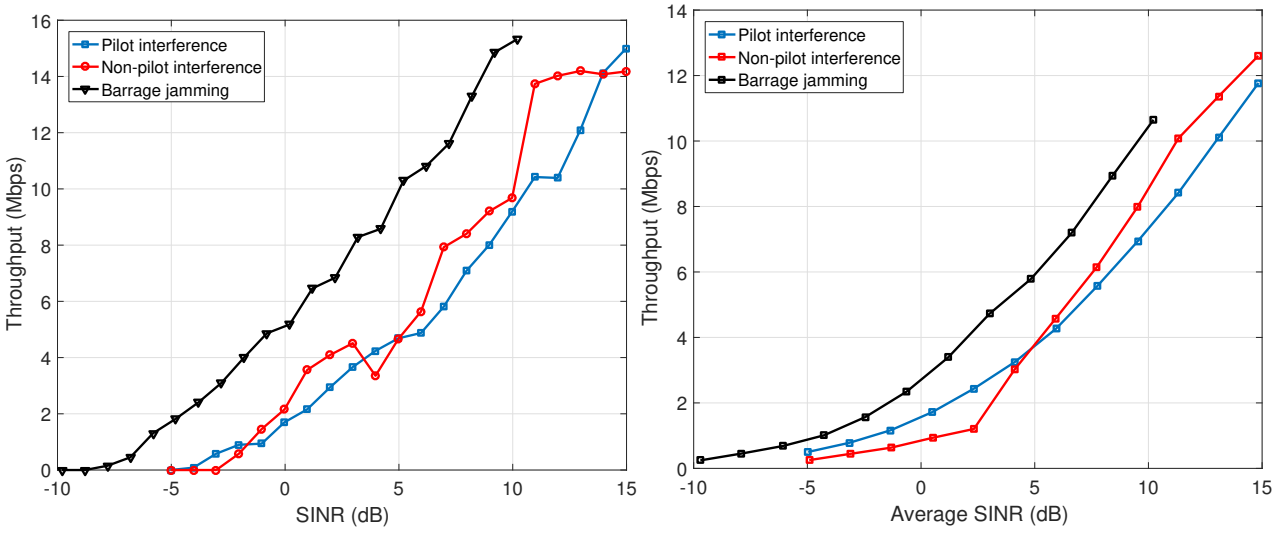

(a) (b)

Figure 3.6: Throughput as a function of SINR for PI, NPI and barrage interference, measured during (a) hardware experiments, and (b) link-level simulations.

leaved and encoded[3].

Assumption 3.2. *For each user, the channel and interference is assumed to be quasi-static. The outcome of each scheduling interval forms an i.i.d. sequence* $\mathcal{B}_N = \{X_1, X_2, \cdots, X_N\}$ *of Bernoulli trials* X_i $(i = 1, 2, \cdots, N)$*, with each trial having a probability of success* p*.*

Assumption 3.3. *'Success' is defined as the successful decoding of the data block.*

Assumption 3.4. *Random process* $\mathcal{B}_N$ *is assumed to be ergodic. Hence* $p = (1 - \texttt{BLER})$ *for* $N \to \infty$*, since* $(1 - \texttt{BLER})$ *represents the fraction of blocks successfully decoded.*

Assumption 3.5. *The number of HARQ retransmissions* $(N_{\texttt{harq}})$ *to a user, and the wait time* $(\tau_{\texttt{wait}})$ *between each consecutive retransmission to the same user, are statistically independent*

In reality the channel is non-stationary and non-ergodic due to time-varying SINR. In addition, LTE allows a maximum of 4 HARQ retransmissions. Accounting for these factors is beyond the scope of the current work, and we refer interested readers to [99] for more details. In the following theorem, we derive the relationship between BLER and $\bar{\tau}_{\texttt{retx}}$.

Theorem 3.1. *The average retransmission-induced latency is given as*

$$\bar{\tau}_{\texttt{retx}} = \frac{\texttt{BLER} \times \bar{\tau}_{\texttt{wait}}}{1 - \texttt{BLER}}, \tag{3.5}$$

where $\bar{\tau}_{\texttt{wait}}$ *is the average waiting time between consecutive retransmissions to the same user.*

[3] In LTE, this is called a transport block which is sent over a transmission time interval (TTI) of 1 ms [37].

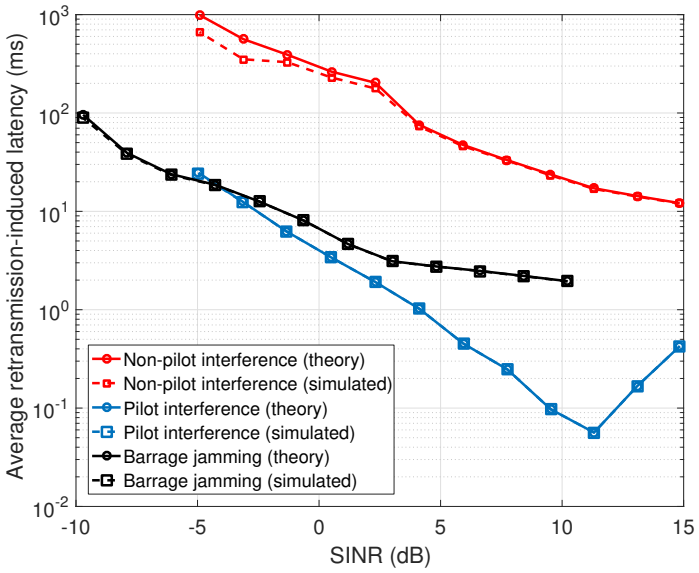

Figure 3.7: Comparison of theoretical (solid lines) versus numerical (dashed lines) values of $\bar{\tau}_{\texttt{retx}}$ as a function of SINR for PI, NPI and barrage interference. The numerical values are obtained from our link-level simulations.

Proof. By assumption 3.2, the number of retransmissions $N_{\texttt{retx}} \in \{0\} \cup \mathbb{N}$ required to successfully decode the transport block is a *geometric random variable*. Therefore, its mean $\bar{N}_{\texttt{harq}} = \mathbb{E}[N_{\texttt{harq}}]$ is given by $\bar{N}_{\texttt{harq}} = \frac{1-p}{p} = \frac{\texttt{BLER}}{1-\texttt{BLER}}$. If $\bar{\tau}_{\texttt{wait}}$ is the average waiting time between consecutive retransmissions to the same user, then by assumption 3.5 we have $\bar{\tau}_{\texttt{retx}} = \mathbb{E}[N_{\texttt{harq}} \tau_{\texttt{wait}}] = \bar{N}_{\texttt{harq}} \bar{\tau}_{\texttt{wait}}$. By substituting the value of $\bar{N}_{\texttt{harq}}$, we obtain the desired result. ■

We notice that if $\texttt{BLER} \to 1$, then $\bar{\tau}_{\texttt{retx}} \to \infty$ irrespective of $\bar{\tau}_{\texttt{wait}}$. In contrast, for perfect link adaptation with $\texttt{BLER} = 0$, we have $\bar{\tau}_{\texttt{retx}} = 0$. 4G LTE and 5G NR specify that the TM and MCS should be chosen such that $\texttt{BLER} \leq 10\%$. Substituting this target BLER in (3.5), we get the acceptable average retransmission-induced latency to be $\bar{\tau}_{\texttt{retx}} \leq 0.89$ ms.

3.4.1 Numerical Results

Fig. 3.7 shows the variation of theoretical and simulated values of $\bar{\tau}_{\texttt{retx}}$ with SINR, for different interference scenarios. We considered $\bar{\tau}_{\texttt{wait}} = 8$ ms in our link-level simulations, which is the typical round-trip time in LTE [37]. We observe that there is a good agreement between the theoretical and simulated values of $\bar{\tau}_{\texttt{retx}}$. In the case of PI, the non-monotonic behavior of $\bar{\tau}_{\texttt{retx}}$ is a direct consequence of the non-monotonic behavior of BLER in Fig. 3.4(b). Our model overestimates $\bar{\tau}_{\texttt{retx}}$ for high values of BLER, which is due to the assumption of ergodicity. The intuition behind this trend is the following. Since the instantaneous BLER can vary due to time fading in the channel, a high BLER in the denominator of (3.5) makes $\bar{\tau}_{\texttt{retx}}$ very sensitive to perturbations

in the SINR. However for low to moderate values of BLER, our results suggest that ergodicity is a reasonable approximation, since small perturbations in BLER will not cause large deviations in $\bar{\tau}_{\texttt{retx}}$.

We observe that NPI has an order of magnitude higher $\bar{\tau}_{\texttt{retx}}$ when compared to the other interference scenarios. It results in additional latencies of 10-1000 ms for the considered SINRs, whereas a balanced 4G LTE system with $\texttt{BLER} \leq 0.1$ would have $\bar{\tau}_{\texttt{retx}} < 1$ ms, irrespective of the SNR. Even for high SINR in NPI the $\bar{\tau}_{\texttt{retx}} \geq 10$ ms, which is unacceptable for low-latency applications. Hence, CV2X systems are particularly vulnerable to delay outage in the presence of NPI, especially since a maximum of two retransmissions are allowed [100].

3.5 Conclusion

In this chapter, we highlighted and analyzed the problem of link adaptation failure in cellular systems caused by NPI. Using LTE as an example, we demonstrated through experiments and link-level simulations that pilot-aided SINR estimates in NPI are inaccurate and severely degrade link adaptation performance, especially the BLER and throughput. We also derived approximate expressions that relate BLER and *retransmission-induced latency*. Our results indicate that the links affected by NPI becomes unreliable for vehicular communications and low-latency applications of 4G LTE and 5G NR. Further research into robust SINR estimation and link adaptation is necessary to mitigate this problem in current and future cellular networks, and applications such as virtual/augmented reality and connected and autonomous vehicles.

While we demonstrated the issue of inaccurate pilot-aided SINR estimates in the presence of frequency-domain NPI waveforms, we rigorously prove in the next chapter that a pulsed radar signal is also a source of NPI with high probability.

Chapter 4

Probability of Pilot Interference (PI) in Pulsed Radar-Cellular Coexistence: Fundamental Insights on Demodulation and Limited CSI Feedback

4.1 Introduction

Over the last decade, radar-cellular spectrum sharing has been actively pursued by academia and industry, due to its high potential to maximize spectral utilization of heavily congested sub-6 GHz frequency bands. Due to the support for underlay spectrum sharing in radar-incumbent 3.5 GHz [21], 5 GHz [22] and 1.3 GHz [20] bands, cellular technologies have progressed from licensed bands to unlicensed and shared bands through standards such as License Assisted Access (LAA) and 5G New Radio-Unlicensed (NR-U) [102]. Therefore, in the case where both systems are allowed to coexist in the same time-frequency resource grid, evaluating the impact of radar co-channel and adjacent channel interference on cellular signals is important for network providers. In particular, pulsed radar systems occupying these bands [103] can intermittently interfere with control channels of the cellular signal, thus disrupting critical functionalities of the cellular network.

4.1.1 Background and Prior Work

Pilot/Reference signals are used in modern cellular systems to estimate the instantaneous channel state information (I-CSI), and statistical CSI (S-CSI) of the wireless channel. Due to practical

This chapter is based on the work published in [101].

considerations, I-CSI is used at the receiver for channel equalization and coherent demodulation, whereas S-CSI is leveraged at the transmitter to choose the optimal transmission mode for data blocks in subsequent time slots [104], [105]. Frequency division duplex (FDD) systems quantize *pilot-aided S-CSI estimates* at the receiver and feed the information back to the transmitter using 'limited feedback' schemes [106]. This methodology is used in the Long-Term Evolution-Advanced (LTE-A) and NR standards, where I-CSI is estimated using demodulation reference signals (DMRS), and S-CSI estimates are based on CSI-reference signals (CSI-RS) [107].

Pilot interference due to pulsed radar signals impact the accuracy of CSI estimates. It has been demonstrated that pilot-aided I-CSI estimates are corrupted when pilot signals are interfered [82], [78], [85]. As we demonstrated in Chapter 3, pilot interference is desirable in an interference channel, since pilot-aided S-CSI estimates are accurate only when fading and interference statistics are the same on pilot and non-pilot resources. Similar results have been shown in Safavi-Naeini et al. [108], where the authors reported degraded turbo decoder performance in the case of pulsed radar-LTE spectrum sharing scenarios due to inaccurate interference estimates, resulting in block decoding failures.

Unlike conventional multi-cellular scenarios where the interference statistics is homogeneous on all resources, for the radar-cellular coexistence scenarios considered in this chapter, the radar is *co-channel, pulsed, and periodic* in nature. Hence, the cellular channel is bimodal with two states: (a) *'interference channel'*, on data blocks impaired by pulsed radar interference as well as fading, and (b) *'fading channel'*, on data blocks that are impaired only by fading. While it is desirable to acquire I-CSI using pilots in the *fading channel* state, it is necessary to acquire S-CSI for *both channel states* to maximize cellular performance using link adaptation and scheduling.

For robust link adaptation, estimating the S-CSI of the *interference channel* is fundamentally important to maximize performance of the cellular link, as well as to minimize interference to the radar using multi-antenna techniques [105]. However, since pulsed radar interference is time-selective, the absence of pilot interference can result in inaccurate pilot-aided S-CSI estimates of the interference channel.

Therefore, before we investigate the effectiveness of pilot-aided S-CSI and I-CSI estimation methods in radar-cellular coexistence scenarios, we need to characterize the *probability of pilot interference*. While an exact analysis can be done by considering a finite radar pulse width [109], the resulting expression involving recurrence relations does not facilitate intuitive interpretation. To remedy this, we use a realistic *infinitesimal wideband radar pulse* model that allows us to derive the bounds as a rational function of the waveform parameters, and then prove the achievability of the lower bound. This helps us develop important insights regarding the efficacy of pilot-aided I-CSI estimation, S-CSI acquisition and limited feedback schemes.

4.1.2 Contributions

In this chapter, we consider an underlay pulsed radar-cellular spectrum sharing scenario, where the radar waveform and cellular pilots are modeled as independent pulse trains with a random initial offset, having different pulse widths and repetition rates. The cellular system employs two different pilot signals, one for S-CSI acquisition and the other for I-CSI estimation. The cellular receiver performs S-CSI estimation using multiple equispaced pilots in a finite *estimation window* and uses *limited S-CSI feedback* to aid in scheduling and link adaptation at the transmitter. Also, the receiver estimates the I-CSI using a different equispaced pilot sequence, for coherent data demodulation [107]. Using this system model, we make the following contributions:

1. We derive upper and lower bounds on the probability that a pulsed radar with an infinitesimal pulse width and uniformly distributed time of arrival [109] interferes with (a) at least one pilot-bearing OFDM symbol (henceforth referred to as a pilot signal/pilot), and (b) more than m pilot symbols, in an *arbitrary estimation window*.
2. We relax the infinitesimal radar pulse assumption, and extend the derivation of these bounds to multipath scenarios due to (a) localized scattering near the receiver, and (b) far-away specular reflections.
3. Under the infinitesimal radar pulse model, we derive exact expressions for important special cases where the lower bound is achieved.
4. Using the results on lower bound achievability, (a) we design pilot interference-minimizing radar schemes for accurate I-CSI estimation, and (b) deduce that blind S-CSI estimation methods need to augment pilot-aided methods for a wide range of radar repetition intervals in pulsed radar-cellular coexistence scenarios.
5. We present numerical results to validate the derived expressions under each contribution, using commonly used radar, LTE and NR system parameters.

The rest of this chapter is organized as follows. Section 4.2 presents the system model. Section 4.3 derives (a) the bounds on probability of single and multiple pilot interference in a finite CSI estimation window, under the infinitesimal radar pulse and multipath fading scenarios, and (b) the exact conditions in which the lower bound is achieved. Using the lower bound achievability results, Section 4.4 provides insights on minimizing I-CSI contamination using pilot adaptation, and the necessity of blind S-CSI estimation methods in spectrum sharing with radar systems. Finally, Section 4.5 concludes the chapter, and discusses extensions for future research.

4.2 System Model

We consider an underlay radar-cellular spectrum sharing scenario, where the orthogonal frequency division multiplexing (OFDM)-based cellular signal has a symbol duration of $T_{\texttt{ofdm}}$. The

Table 4.1: Important system parameters in Chapter 4

Parameter	Description
$T_{\texttt{ofdm}}$	OFDM symbol duration
$T_{\texttt{rep}}$	Pulsed radar repetition interval
$T_{\texttt{pulse}}$	Radar pulse width
$T_{\texttt{pil}}$	Temporal spacing of cellular pilot signals
T_{CSI}	CSI estimation window length
N_p	Number of pilot signal in the CSI estimation window
$N_{\texttt{ofdm}}$	Maximum number of radar pulses in the CSI estimation window
t_f	Time-of-arrival of the first radar pulse in the CSI estimation window
M	Number of pilot signals interfered by radar pulses in the CSI estimation window
$T_{\texttt{coh}}$	Coherence time of fading channel

pulsed radar system has a repetition interval of $T_{\texttt{rep}}$, where $T_{\texttt{rep}} > T_{\texttt{ofdm}}$. Therefore, an OFDM symbol is interfered by at most one radar pulse[1]. Typical high bandwidth radar pulse widths ($T_{\texttt{pulse}}$) satisfy $T_{\texttt{pulse}} \ll T_{\texttt{ofdm}}$[2]. Hence, we assume that $T_{\texttt{pulse}} \to 0$ and that the radar can be represented by a periodic impulse train, as shown in Fig. 4.1.

The cellular system employs pilot-aided CSI estimation techniques, where $T_{\texttt{pil}}$ denotes the temporal spacing between pilots. For example, $T_{\texttt{DMRS}}$ denotes the DMRS spacing and $T_{\texttt{CSIRS}}$ denotes the CSI-RS spacing. In the rest of the chapter, we consider pilot signals used for *statistical CSI (S-CSI) estimation*, unless otherwise specified. However, this analysis is general and is also applicable to pilot design for minimizing I-CSI (I-CSI) acquisition, as discussed in section 4.4.

In an estimation window of interest denoted by $[0.T_{CSI}]$, the S-CSI is estimated for each pilot-bearing OFDM symbol, where $T_{CSI} = N_p T_{\texttt{pil}} = N_{\texttt{ofdm}} T_{\texttt{ofdm}}$ for $N_p, N_{\texttt{ofdm}} \in \mathbb{N}$ and $1 \leq N_p < N_{\texttt{ofdm}}$. Here, N_p is the number of pilots, and $N_{\texttt{ofdm}}$ the total number of OFDM symbols in the estimation window[3]. The estimated S-CSI using the l^{th} pilot ($\texttt{CSI}_l$) is mapped to the achievable rate[4] $R_l = r(\texttt{CSI}_l)$ using a non-zero real-valued function $r(\cdot)$. Defining $\mathbf{R} \triangleq [R_1, R_2, \cdots, R_{N_p}]^T$ as the vector of achievable rates estimated by the receiver, we consider two S-CSI feedback schemes $Q(\mathbf{R})$, given by:

1. Minimum S-CSI, calculated using $Q_{\texttt{min}}(\mathbf{R}) = \min(\mathbf{R})$,

[1] If $T_{\texttt{rep}} \leq T_{\texttt{ofdm}}$, then each OFDM symbol will be interfered by the radar, and the probability of pilot interference will be 1.

[2] In sub-6 GHz systems, typical radar systems have $T_{\texttt{pulse}} \sim 1$ μs [103], while typical values of $T_{\texttt{ofdm}} \sim 70$ μs [107].

[3] Based on the reference signal under consideration, typical values of $N_p \sim 1 - 100$ in LTE and NR.

[4] LTE and NR define the quantized S-CSI values, how they are fed back, and the S-CSI-to-throughput mapping function $r(\cdot)$ [107]. An example was presented in our prior work [110].

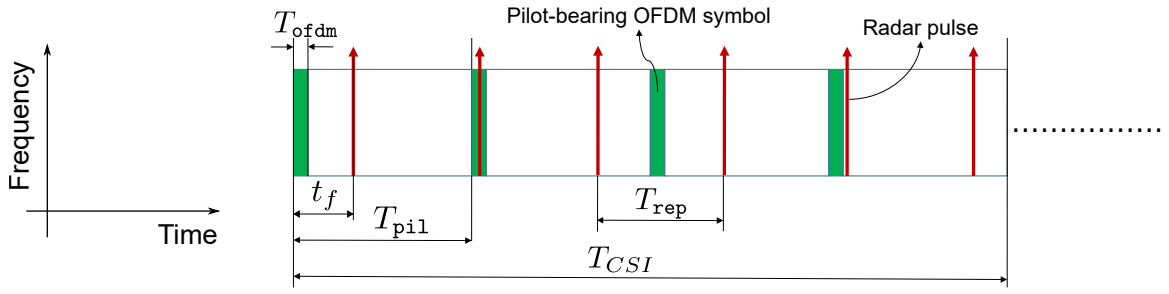

Figure 4.1: Illustration of the radar-cellular coexistence scenario. A pulsed radar with repetition interval $T_{\texttt{rep}}$ interferes with an OFDM signal with pilots spaced $T_{\texttt{pil}}$ seconds apart. Here, the CSI estimation interval (T_{CSI}) is comprised of $N_p = 4$ pilot-bearing OFDM symbols.

2. Window-averaged S-CSI, calculated using $Q_{\texttt{avg}}(\mathbf{R}) = A(\mathbf{R})$, where $A(\cdot)$ is a window-averaging function [104].

As a first-order approximation, a pilot-aided S-CSI estimate of the *interference channel* is considered to be accurate if the pilot is affected by interference. The maximum number of radar pulses that occur in the estimation window is $N_r = \lceil T_{CSI}/T_{\texttt{rep}} \rceil$, where $\lceil \cdot \rceil$ denotes the ceiling function. Since typical cellular systems continuously transmit pilot signals for CSI acquisition, and pilot interference is the event of interest, we consider the pilot start and end times to be deterministic. In the estimation window $[0, T_{CSI}]$, the pilot signals occupy the time intervals $[kT_{\texttt{pil}}, kT_{\texttt{pil}} + T_{\texttt{ofdm}}]$ for $k = 0, 1, \cdots, (N_p - 1)$. Due to deterministic pilot intervals, the time of arrival (ToA) of the first radar pulse t_f is assumed to be uniformly distributed, i.e. $t_f \sim \texttt{U}([0, T_{\texttt{rep}}])$ [109].

4.3 Probability of Pilot Interference in a Finite CSI Estimation Window

Let the random variable $M \in \{1, 2, \cdots, N_p\}$ denote the number of pilots affected by the pulsed radar signal in the estimation window. In the following analysis, we are interested in the probability that (a) $\{M \geq 1\}$, and (b) $\{M \geq m\}$, for $m = 2, 3, \cdots, N_p$.

4.3.1 Bounds on Probability of Pilot Interference when $T_{\texttt{pulse}} \to 0$

Since $t_f \sim \texttt{U}[0, T_{\texttt{rep}}]$, we have $\mathbb{P}[M \geq 1]$ when $N_r \geq 1$, as shown in the following key result.

Lemma 4.1. *If* $T_{\texttt{rep}} \leq T_{CSI}$, *for* $m = 2, 3, \cdots, N_p$, *we have*

$$\frac{T_{\texttt{ofdm}}}{T_{\texttt{pil}}} \leq \mathbb{P}[M \geq 1] \leq \min\left(1, \frac{N_p T_{\texttt{ofdm}}}{T_{\texttt{rep}}}\right) \tag{4.1}$$

$$0 \leq \mathbb{P}[M \geq m] \leq \min\left(1, \frac{N_p T_{\texttt{ofdm}}}{m T_{\texttt{rep}}}\right). \tag{4.2}$$

Proof. Since $T_{\texttt{rep}} \leq T_{CSI}$, $\mathbb{P}[M \geq 1]$ cannot be smaller than the fraction of time allocated to pilots in the CSI estimation window. Hence, $\mathbb{P}[M \geq 1] \geq \frac{N_p T_{\texttt{ofdm}}}{T_{CSI}}$. Substituting $T_{CSI} = N_p T_{\texttt{pil}}$ and simplifying, we obtain the lower bound in equation (4.1). Similarly, $\mathbb{P}[M \geq 1]$ cannot be greater than the ratio between the total time allocated to the N_p pilots per estimation window and the radar pulse repetition interval. Therefore, $\mathbb{P}[M \geq 1] \leq \min\left(1, \frac{N_p T_{\texttt{ofdm}}}{T_{\texttt{rep}}}\right)$.

For m pilot signals to be interfered by radar in an estimation window T_{CSI}, at least one pilot signal must be affected every $\frac{T_{CSI}}{m}$ seconds, since both pilots and radar pulses are equispaced in our model. Hence, using the upper bound in equation 4.1, and noting that there are an average of $\frac{N_p}{m}$ pilot signals every $\frac{T_{CSI}}{m}$ seconds, we obtain the upper bound in (4.2). ■

When the multipath in the radar-to-cellular user channel is strong, the assumption that $T_{\texttt{pulse}} \ll T_{\texttt{ofdm}}$ may not always be accurate. In the following subsection, we analyze the probability bounds in the case of significant scattering in the spectrum sharing environment.

4.3.2 Bounds on Probability of Pilot Interference in Multipath Channels

The multipath characteristics of the radar-to-cellular user channel (assuming that the pulsed radar is coexisting with the cellular downlink) is a function of the (a) scattering geometry, (b) reflection/absorption properties of the scatterers, and (c) transmission/receive beamforming techniques at the radar/cellular user respectively.

The typical scalar-valued radar-to-cellular user multipath channel can be written as [111]

$$h(\tau) = \sum_{c=0}^{N_c-1} \sum_{m=0}^{N_m-1} \gamma_{m,c} \delta(\tau - \tau_{m,c} - \tau_c), \tag{4.3}$$

where $\delta(\cdot)$ is the Dirac-delta function, N_c is the number of discrete multipath clusters, N_m is the number of multipath components (MPC) per cluster, $\gamma_{m,c}$ is the scalar channel coefficient of the m^{th} MPC of the c^{th} cluster, τ_c is the mean delay corresponding to the c^{th} cluster center, and $\tau_{m,c}$ the relative delay of the m^{th} MPC in the c^{th} cluster. Based on the radar and cellular system deployment, different multipath scenarios are possible, some of which are outlined below:

1. LoS channel: A strong line-of-sight component between the cellular user and the radar can result in no significant multipath, such as in the case of a coastal cellular user coexisting with a naval radar [112], i.e. $N_m = N_c = 1$ and $\tau_{0,0} = 0$ s.

2. NLoS channel with local scattering near user: in the case of a radar mounted at a higher elevation and tracking an aerial target, such as in the case of a weather or military surveillance radar [105], the scattering geometry near the user will dominate the characteristics of the multipath channel. In this case, the typical delay spread of the multipath channel, i.e. $(\tau_c + \tau_{m,c})$ typically does not exceed a few microseconds [113]. Since the typical OFDM symbol duration ($T_{\texttt{ofdm}}$) in sub-6 GHz cellular systems is ~ 70 μs [37], [2], the approximation that the radar pulse width $T_{\texttt{pulse}} \ll T_{\texttt{ofdm}}$ ($T_{\texttt{pulse}} \to 0$) is highly accurate.

3. NLoS channel due to strong reflectors: In the case of a far-away radar, multipath due strong reflections in the environment (such as the radar target, water, metallic reflectors etc.) result in echoes that appear as discrete pulses at the cellular user. A typical characteristic of this environment is

   - the mean delay between two clusters is much greater than the relative delay of each MPC in each cluster, i.e. $|\tau_{m_1} - \tau_{m_2}| >> |\tau_{m,c}|$ for $m, m_1, m_2 = 0, 2, \cdots, (N_c - 1), m_1 \neq m_2$ and $c = 0, 1, \cdots, (N_c - 1)$, and
   - the number of resolvable MPCs in each cluster is small, i.e. $N_m = 1$ or 2 with $\tau_{m,c} \sim 100$ ns for $m = 0, \cdots, (N_m - 1)$ and $c = 0, \cdots, (N_c - 1)$.

We consider the second and third special cases in the following, which represent two edge-cases of multipath fading. It is worthwhile to note that it is possible for multipath scenarios to have both far-away reflections as well as localized scattering. Naive upper and lower bounds can be derived for such hybrid scenarios using the approach presented below. However, deriving tighter bounds for the general case requires a more comprehensive mathematical framework and hence, is beyond the scope of this work.

Below, we derive bounds on the probability of partial pilot interference in the case of (a) diffused multipath due to local scattering near the cellular receiver, and (b) specular far-away reflections.

4.3.2.1 Multipath due to Diffused Local Scattering Near Cellular Receiver

Due to local scattering near the cellular user, the received radar pulse broadens. Let the received radar pulse width be $T_{\texttt{pulse}}$ as shown in Fig. 4.2. In the case when $T_{\texttt{pulse}}$ is comparable to $T_{\texttt{ofdm}}$ and $T_{\texttt{pulse}} < T_{\texttt{rep}}$, there is a possibility of partial radar interference on pilots. Intuitively, we anticipate this probability to increase compared to the case when $T_{\texttt{pulse}} \to 0$ since there is a larger chance of overlap between the pilots and radar pulses [109]. Similar to the case of the infinitesimally small radar pulse width, if we assume that $t_f \sim \texttt{U}[0, T_{\texttt{rep}}]$, bounds on the probability of partial pilot interference are derived in the following theorem.

Lemma 4.2. *In the case of a static diffused multipath environment which results in a received radar pulse width $T_{\texttt{pulse}}$, bounds on probability of partial pilot interference in the case of $T_{\texttt{rep}} \leq T_{CSI}$ are*

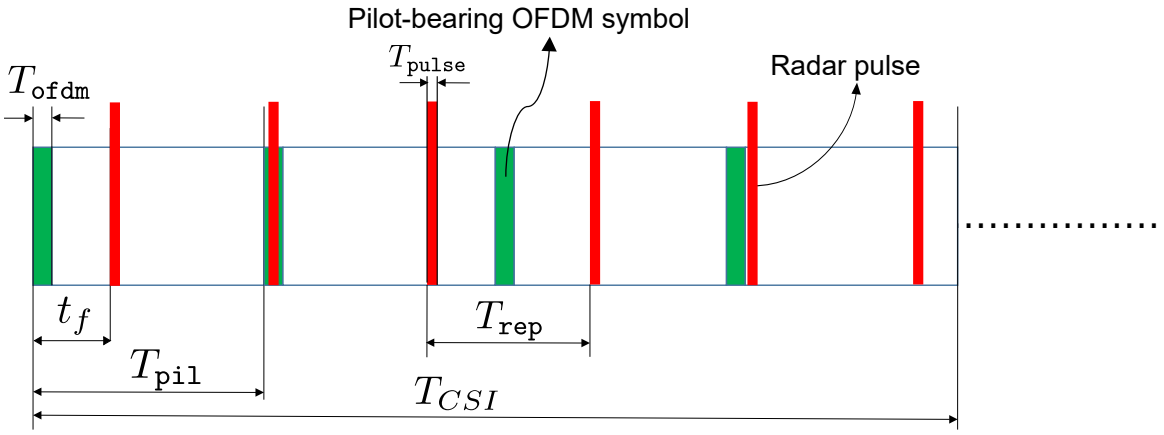

Figure 4.2: Illustration of multipath due to local scattering near the cellular user. The resultant effect is the broadening of the radar pulse, resulting in a finite pulse width $T_{\texttt{pulse}}$.

given by

$$\frac{T_{\texttt{ofdm}}+T_{\texttt{pulse}}}{T_{\texttt{pil}}} \leq \mathbb{P}[M \geq 1] \leq \min\left(1, \frac{N_p(T_{\texttt{ofdm}}+T_{\texttt{pulse}})}{T_{\texttt{rep}}}\right) \tag{4.4}$$

$$0 \leq \mathbb{P}[M \geq m] \leq \min\left(1, \frac{N_p(T_{\texttt{ofdm}}+T_{\texttt{pulse}})}{mT_{\texttt{rep}}}\right). \tag{4.5}$$

Proof. When the received radar pulse width is $T_{\texttt{pulse}}$, the lower bound is obtained by noticing that $\mathbb{P}[M \geq 1]$ cannot be smaller than the probability of partial pilot interference due to the first radar pulse, which is equal to $\frac{T_{\texttt{ofdm}}+T_{\texttt{pulse}}}{T_{\texttt{pil}}}$. The upper bound is obtained using the union bound, by noticing that $\mathbb{P}[M \geq 1]$ cannot be greater than the sum of the probabilities of partial radar pulse overlap on each pilot signal.

The upper bound of $\mathbb{P}[M \geq m]$ is obtained using the same approach presented in Lemma 4.1. ■

4.3.2.2 Multipath due to $(p-1)$ Resolvable Distant Specular Reflections

Fig. 4.3 shows an example of the scenario of a cellular user coexisting with a pulsed radar in a multipath environment, with one LoS path and $(p-1)$ specular reflections. Assuming that the multipath scattering geometry is time-invariant in this case, the resultant radar interference can be modeled as p dependent pulse trains, where

1. The pulse train corresponding to each MPC is composed of pulses with infinitesimally zero width (i.e. $T_{\texttt{pulse}} \to 0$ for each discrete MPC), and
2. The time offset between the i^{th} and the $(i+1)^{th}$ pulse is denoted by τ_i, where the 0^{th} pulse denotes the LoS component in Fig. 4.3.

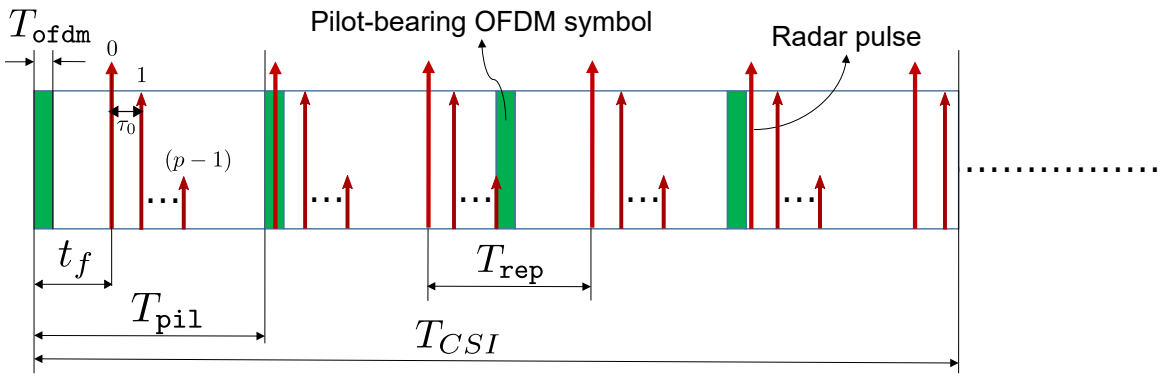

Figure 4.3: Illustration of multipath due to $p > 1$ far-away specular reflections of the radar pulse interfering with the cellular user. For each transmitted radar pulse, τ_i denotes the time elapsed between the i^{th} pulse reflection and the $(i+1)^{th}$ pulse reflection arriving at the cellular user, where the 0^{th} pulse corresponds to the LoS component.

Below we derive bounds on the probability of pilot interference in such multipath scenarios.

Lemma 4.3. *In the case of a static multipath environment with p echoes due to $(p-1)$ specular reflectors in the environment, the probabilities of pilot interference in the case of $T_{\texttt{rep}} \leq T_{CSI}$ can be bounded by*

$$\frac{T_{\texttt{ofdm}}}{T_{\texttt{pil}}} \leq \mathbb{P}[M \geq 1] \leq \min\left(1, \frac{pN_pT_{\texttt{ofdm}}}{T_{\texttt{rep}}}\right) \tag{4.6}$$

$$0 \leq \mathbb{P}[M \geq m] \leq \min\left(1, \frac{pN_pT_{\texttt{ofdm}}}{mT_{\texttt{rep}}}\right). \tag{4.7}$$

Proof. The lower bound remains the same when compared to the infinitesimal single pulse scenario. The upper bounds are obtained by treating pilot interference due to each pulse train as disjoint events. Using the union bound, the upper bound of $\mathbb{P}[M \geq m]$ for $m = 1, 2, \cdots, N_p$ scales by a factor of p when compared to Lemma 4.1. ■

As we will later demonstrate in Section 4.3.4, the presence of multipath does not change the trends and system design insights inferred from our analysis. Therefore, for ease of analysis, we assume that $T_{\texttt{pulse}} \to 0$ in the rest of the chapter, unless otherwise specified. In the following subsection, we provide exact results for important special cases.

4.3.3 Exact Analysis for Important Special Cases

Let the indicator function $\mathbb{1}(l, t_f)$ denote the event that the l^{th} pilot ($l = 1, 2, \cdots, N_p$) is interfered by a radar pulse in the estimation window $[0, T_{CSI}]$, when the ToA of the first radar pulse is t_f.

It can be written as

$$\mathbb{1}(l,t_f)=\begin{cases}1 & \text{if } \exists j=1,2,\cdots,N_r \text{ such that } (t_f+jT_{\texttt{rep}}-lT_{\texttt{pil}})\in[0,T_{\texttt{ofdm}}]\\ 0 & \text{otherwise.}\end{cases} \tag{4.8}$$

We can write the conditional probability of the event $\{M\geq m|t_f\}$ $(m=1,2,\cdots,N_p)$ as

$$\mathbb{P}[M\geq m|t_f]=\begin{cases}1 & \text{if } \sum_{l=1}^{N_p}\mathbb{1}(l,t_f)\geq m,\\ 0 & \text{otherwise.}\end{cases} \tag{4.9}$$

Using (4.9), $\mathbb{P}[M\geq 1]$ is obtained by marginalizing t_f using $f_{T_f}(t_f)=\frac{1}{T_{\texttt{rep}}}, 0\leq t_f\leq T_{\texttt{rep}}$ to get

$$\mathbb{P}[M\geq 1]=\int_0^{\min(T_{CSI},T_{\texttt{rep}})}\frac{1}{T_{\texttt{rep}}}\mathbb{P}[M\geq 1|t_f]\mathrm{d}t_f. \tag{4.10}$$

Since the observation window of interest is limited to $[0,T_{CSI}]$, the upper limit of the integral is $\min(T_{\texttt{rep}},T_{CSI})$ and accounts for cases where $T_{\texttt{rep}}\geq T_{CSI}$.

Theorem 4.1. *The lower bound* $\mathbb{P}[M\geq 1]=\frac{T_{\texttt{ofdm}}}{T_{\texttt{pil}}}$ *is obtained for* $T_{\texttt{rep}}\leq T_{CSI}$ *if* $T_{\texttt{rep}}=kT_{\texttt{pil}}$, *where* $k\in\{1,2,\cdots,N_p\}$.

Proof. If $T_{\texttt{rep}}=kT_{\texttt{pil}}$ and $k\in\mathbb{N}$, we have the following *mutually exclusive events*:

1. $\mathcal{E}_0$: If no pilot in $[0,T_{\texttt{rep}}]$ is interfered by the radar, then no pilot will ever be interfered. In other words, $\mathbb{P}[M\geq 1|\mathcal{E}_0]=0$.
2. $\mathcal{E}_1$: If the l^{th} pilot is affected by radar, then the $(l+mk)^{th}$ pilot will be interfered $\forall\, m\in\mathbb{Z}$. Therefore, $\mathbb{P}[M\geq 1|t_f]=1$ for $t_f\in[lT_{\texttt{pil}},lT_{\texttt{pil}}+T_{\texttt{ofdm}}]$ where $l=0,1,\cdots,(k-1)$.

Applying the total probability theorem in (4.10), we get

$$\mathbb{P}[M\geq 1]=\frac{1}{T_{\texttt{rep}}}\sum_{l=0}^{k-1}\int_{lT_{\texttt{pil}}}^{lT_{\texttt{pil}}+T_{\texttt{ofdm}}}1\,\mathrm{d}t_f. \tag{4.11}$$

Using $T_{\texttt{rep}}=kT_{\texttt{pil}}$ in the above and simplifying, we obtain the desired result. ■

The exact value of $\mathbb{P}[M\geq 1]$ for $T_{\texttt{rep}}\geq T_{CSI}$ is provided in the following corollary.

Corollary 4.1. $\mathbb{P}[M\geq 1]=\frac{N_pT_{\texttt{ofdm}}}{T_{\texttt{rep}}}$ *for* $T_{\texttt{rep}}\geq T_{CSI}$.

Proof. The proof is similar to Theorem 4.1, obtained by direct substitution of (4.9) in (4.10). ■

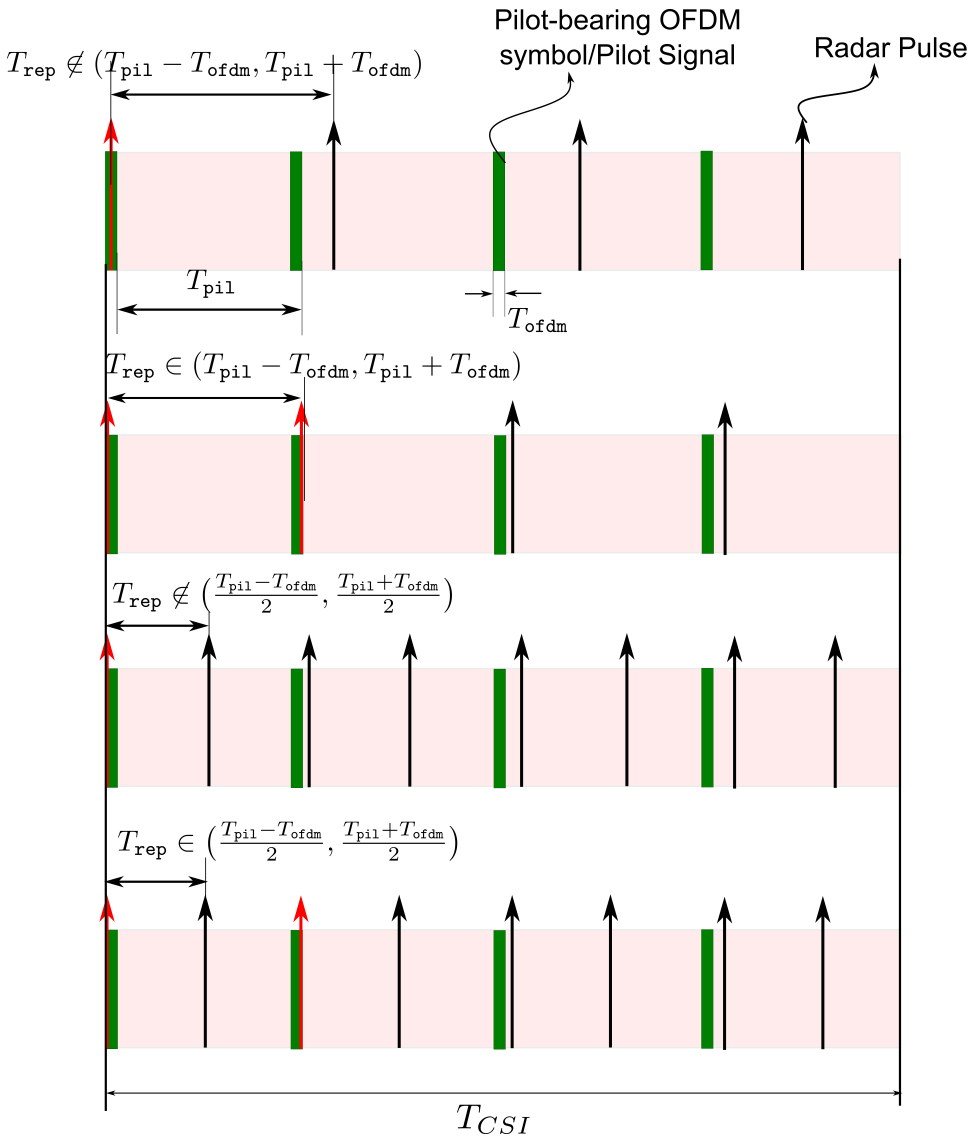

Figure 4.4: Illustration of Theorem 4.2, for $N_p = 4, k = 1$ when $m = 2$ pilots are interfered by radar pulses (indicated in red). For the top 2 plots, $q = 1$ and for the bottom 2 plots, $q = 2$.

Finally, we derive the set of values of $T_{\texttt{rep}}$ for which $\mathbb{P}[M \geq m]$ is non-zero.

Theorem 4.2. *For $N_p > 1$ and $m = 2, \cdots, N_p$,*

$$\mathbb{P}[M \geq m] = \begin{cases} \textit{non-zero} & \textit{if } T_{\texttt{rep}} \in \mathcal{T}_{m,N_p} \\ 0 & \textit{if } T_{\texttt{rep}} \notin \mathcal{T}_{m,N_p} \cap (T_{\texttt{ofdm}}, \infty), \end{cases} \tag{4.12}$$

$$\textit{where } \mathcal{T}_{m,N_p} = \bigcup_{k \in \mathcal{K}, q \in \mathbb{N}} \left(\frac{(m-1)kT_{\texttt{pil}} - T_{\texttt{ofdm}}}{(m-1)q}, \frac{(m-1)kT_{\texttt{pil}} + T_{\texttt{ofdm}}}{(m-1)q} \right), \mathcal{K} = \left\{1, 2, \cdots, \left\lceil \tfrac{N_p - 1}{m-1} \right\rceil \right\}.$$

Proof. Due to equispaced pilots, it can be deduced using Theorem 4.1 (specifically, event $\mathcal{E}_1$) that multiple pilots are interfered when $T_{\texttt{rep}}$ is *in some neighborhood* of $kT_{\texttt{pil}}$, where $k \in \mathbb{N}$. To interfere with *at least* m pilots in the CSI estimation window, one such neighborhood can be shown to be $\left(\frac{-T_{\texttt{ofdm}}}{m-1}, \frac{T_{\texttt{ofdm}}}{m-1}\right)$ using the following construction. Conditioned on the event that the first pilot is interfered, there exists some $t_f \in [0, T_{\texttt{ofdm}}]$ for which the subsequent $(m-1)$ radar pulses interfere with a pilot if $T_{\texttt{rep}} \in \left(kT_{\texttt{pil}} - \frac{T_{\texttt{ofdm}}}{m-1}, kT_{\texttt{pil}} + \frac{T_{\texttt{ofdm}}}{m-1}\right)$. The lower and upper limits of this interval correspond to $t_f = T_{\texttt{ofdm}}$ and $t_f = 0$ respectively. In addition, k must satisfy $k \leq \left\lceil \frac{N_p-1}{m-1} \right\rceil$ to ensure that at least m radar pulses are present in $[0, (N_p-1)T_{\texttt{pil}} + T_{\texttt{ofdm}}]$ for $\{\mathbb{P}[M \geq m] > 0\}$ to be true. Since $\left(kT_{\texttt{pil}} - \frac{T_{\texttt{ofdm}}}{m}, kT_{\texttt{pil}} + \frac{T_{\texttt{ofdm}}}{m}\right) \subset \left(kT_{\texttt{pil}} - \frac{T_{\texttt{ofdm}}}{m-1}, kT_{\texttt{pil}} + \frac{T_{\texttt{ofdm}}}{m-1}\right)$ for all $m > 1$, *at least* m pilots are interfered by the radar in the estimation window if $T_{\texttt{rep}} \in \mathcal{T}^{(1)}_{m,N_p} = \bigcup_{k\in\mathcal{K}} \left(kT_{\texttt{pil}} - \frac{T_{\texttt{ofdm}}}{m-1}, kT_{\texttt{pil}} + \frac{T_{\texttt{ofdm}}}{m-1}\right)$. In addition, $T_{\texttt{rep}} \in \mathcal{T}^{(q)}_{m,N_p} = \{\frac{T}{q} | T \in \mathcal{T}^{(1)}_m, q \in \mathbb{N}\}$ can also result in non-zero $\mathbb{P}[M \geq m]$, since $T_{\texttt{rep}} \in \mathcal{T}^{(1)}_{m,N_p}$ scaled down by an integer factor preserves the time offset relationship between the radar pulse train and the pilots, as shown in Fig. 4.4. Therefore, $\mathbb{P}[M \geq m]$ *is non-zero* if $T_{\texttt{rep}} \in \bigcup_{q\in\mathbb{N}} \mathcal{T}^{(q)}_{m,N_p} = \mathcal{T}_{m,N_p}$.

Furthermore, if $\mathbb{1}(1, t_f) = \cdots = \mathbb{1}(j, t_f) = 0$ and $\mathbb{1}(j+1, t_f) = 1$ for $j = 1, \cdots, (N_p-1)$, it can be shown that $\mathbb{P}[M \geq m] > 0$ if $T_{\texttt{rep}} \in \mathcal{T}_{m,N_p-j} \subset \mathcal{T}_{m,N_p}$, using a similar construction.

Finally, we notice that $\mathbb{P}[M \geq m] = 1 \; \forall \; m = 1, 2, \cdots, N_p$ if $T_{\texttt{rep}} \in [0, T_{\texttt{ofdm}}]$, since every OFDM symbol will be interfered in this case. Since *all the feasible* $T_{\texttt{rep}}$ values which ensure that $P[M \geq m]$ is non-zero are contained in $\mathcal{T}_{m,N_p}$, we have $\mathbb{P}[M \geq m] = 0$ if $T_{\texttt{rep}} \notin \mathcal{T}_{m,N_p} \cap (T_{\texttt{ofdm}}, \infty)$. ■

Before we discuss the implications of these results on I-CSI estimation and S-CSI feedback, we validate their accuracy using numerical results in the following subsection.

4.3.4 Numerical Results

Case 1: $T_{\texttt{pulse}} \to 0$

We consider a cellular system with a typical OFDM symbol duration of $T_{\texttt{ofdm}} = 71.43\ \mu s$, and $N_p \in \mathbb{N}$ periodically spaced pilot-bearing OFDM symbols per estimation window of length $T_{CSI} = 5$ ms. Fig. 4.5a shows the values of $\mathbb{P}[M \geq 1]$, along with the corresponding upper and lower bounds for different values of $T_{\texttt{rep}}$ and N_p. We observe that the upper and lower bounds derived in Lemma 4.1 are in agreement with the numerical results. Furthermore, we also observe that the lower bound is achieved for $T_{\texttt{rep}} = kT_{\texttt{pil}}, k \in \mathbb{N}$, as proven in Theorem 4.1.

Fig. 4.5b shows the variation of $\mathbb{P}[M \geq m]$, for $m = 1, 2, \cdots, 5$ in an estimation window of length $T_{CSI} = 5$ ms. We observe that the upper bound in (4.2) is in agreement with the numerical results. More importantly, the numerical results confirm that $\mathbb{P}[M \geq m]$ is non-zero iff $T_{\texttt{rep}} \in \mathcal{T}_{m,5}$, as shown in Theorem 4.2.

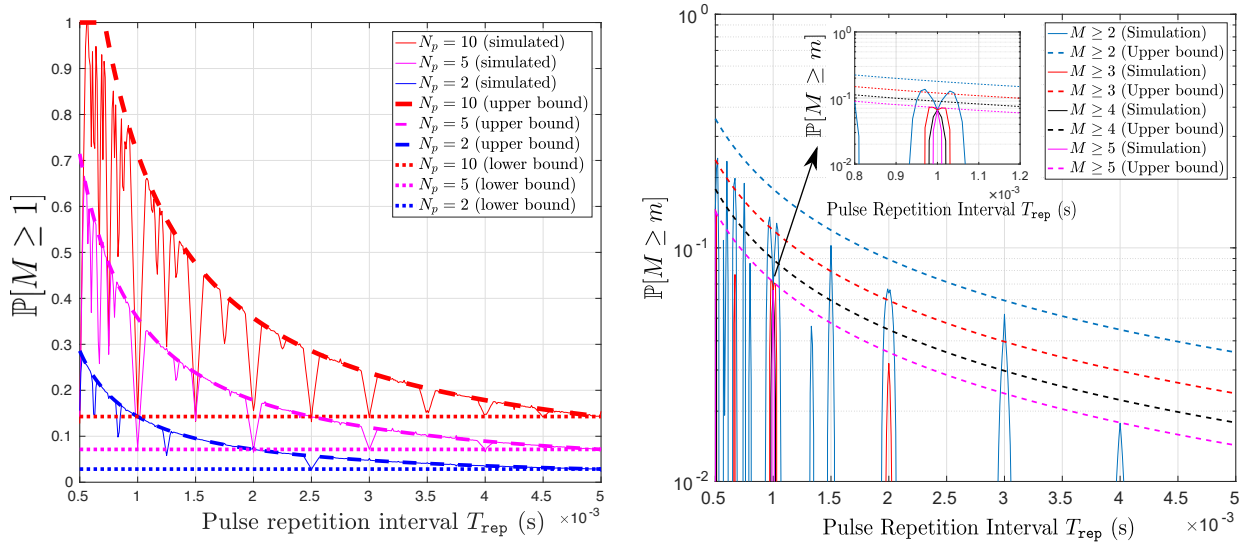

(a) (b)

Figure 4.5: (a) $\mathbb{P}[M \geq 1]$, and its upper and lower bounds as a function of $T_{\mathtt{rep}}$ and N_p for $T_{\mathtt{ofdm}} = 71.43\ \mu$s and $T_{\mathtt{CSI}} = 5$ ms. (b) $\mathbb{P}[M \geq m]$ for $m > 1$, and its upper bound as a function of m, for $N_p = 5$. As shown in Theorem 4.2, $\mathbb{P}[M \geq m]$ is non-zero only when $T_{\mathtt{rep}}$ lies in a small neighborhood of a rational fraction of $T_{\mathtt{pil}}$.

Case 2: Multipath due to Diffused Local Scattering Near Cellular Receiver

Fig. 4.6 shows the impact of diffused scatterers in the environment on the probability of pilot interference, in an extreme local scattering scenario that results in a broadened radar pulse with $T_{\mathtt{pulse}} = 10\ \mu s$. We observe that the bounds increase by a factor of $\frac{T_{\mathtt{pulse}}}{T_{\mathtt{rep}}}$. Since the observed trends remain the same, we can leverage the exact results in Theorems 4.1 and 4.2 to develop useful system design insights. Furthermore, in typical multipath scenarios where local scatterers dominate the interference power, $T_{\mathtt{pulse}} \sim 1\mu s$ [113], which results in a negligible increase of 1.4% when compared to the infinitesimal radar pulse width scenario.

Case 3: Multipath due to $(p-1)$ Resolvable Far-away Specular Reflections

Fig. 4.7 shows the results of the impact of one specular reflection in the environment on the probability of pilot interference when $T_{\mathtt{pulse}} \to 0$. The time offset between the LoS path and the first specular reflection is assumed to be $\tau_0 = 50\ \mu$s. We observe that the bounds increase by a factor of the total number of pulses $p = 2$. However, we observe that the trends in the lower bound remain the same when compared to Case 1 (infinitesimal radar pulse model).

Since modeling multipath fading does not impact the observed trends in achievability of the lower bound, we develop useful system design insights in the next section using the exact results

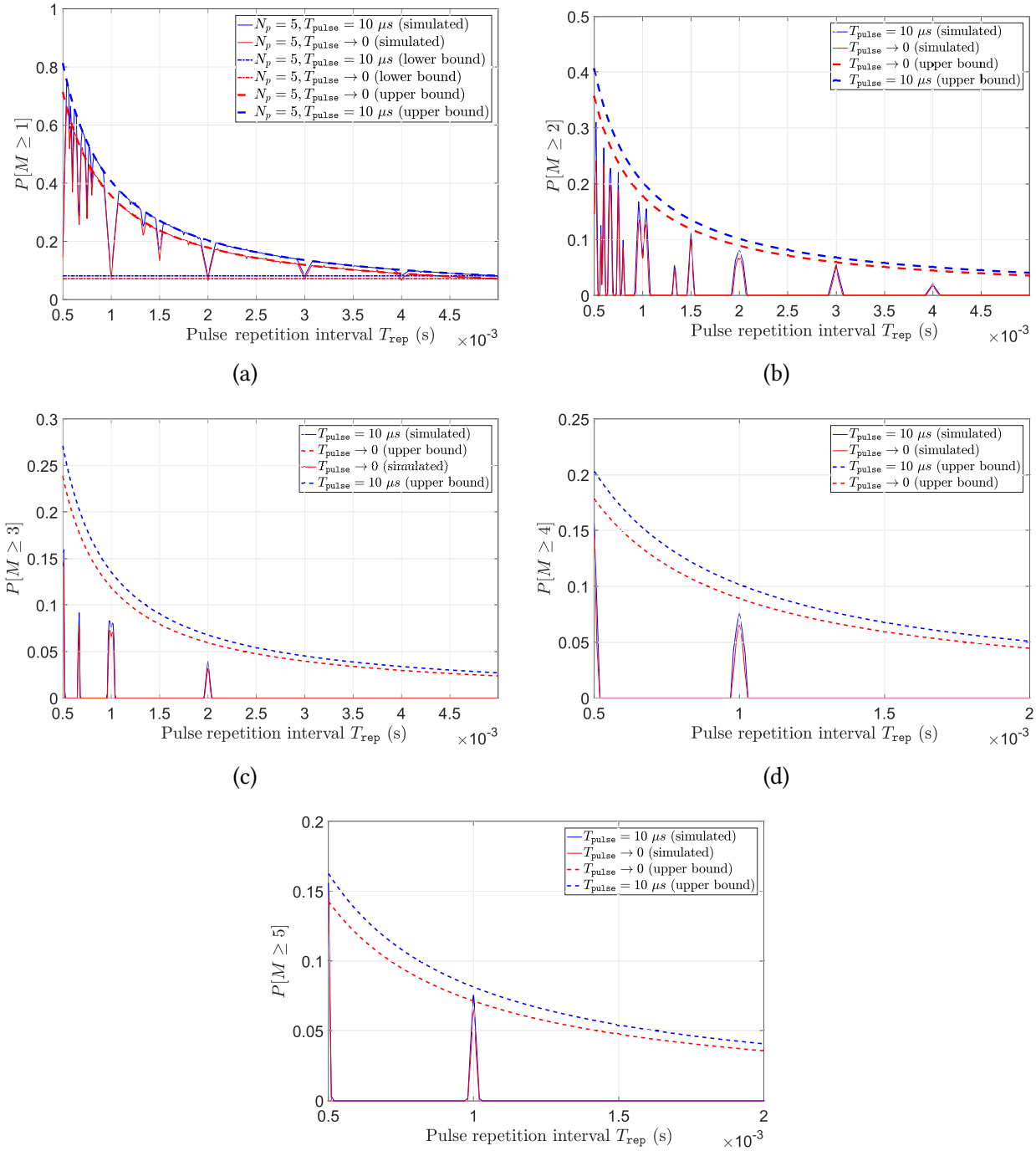

Figure 4.6: Comparison of the analytical results of $P[M \geq m]$ $(m = 1, 2, \cdots, 5)$ for Case 1: $T_{\texttt{pulse}} \to 0$ and Case 2: $T_{\texttt{pulse}} = 10\ \mu s$, for $T_{CSI} = 5$ ms, $T_{\texttt{ofdm}} = 71.43\ \mu s$, $T_{\texttt{pil}} = 1$ ms, and $T_{\texttt{rep}} = 0.5 - 5$ ms.

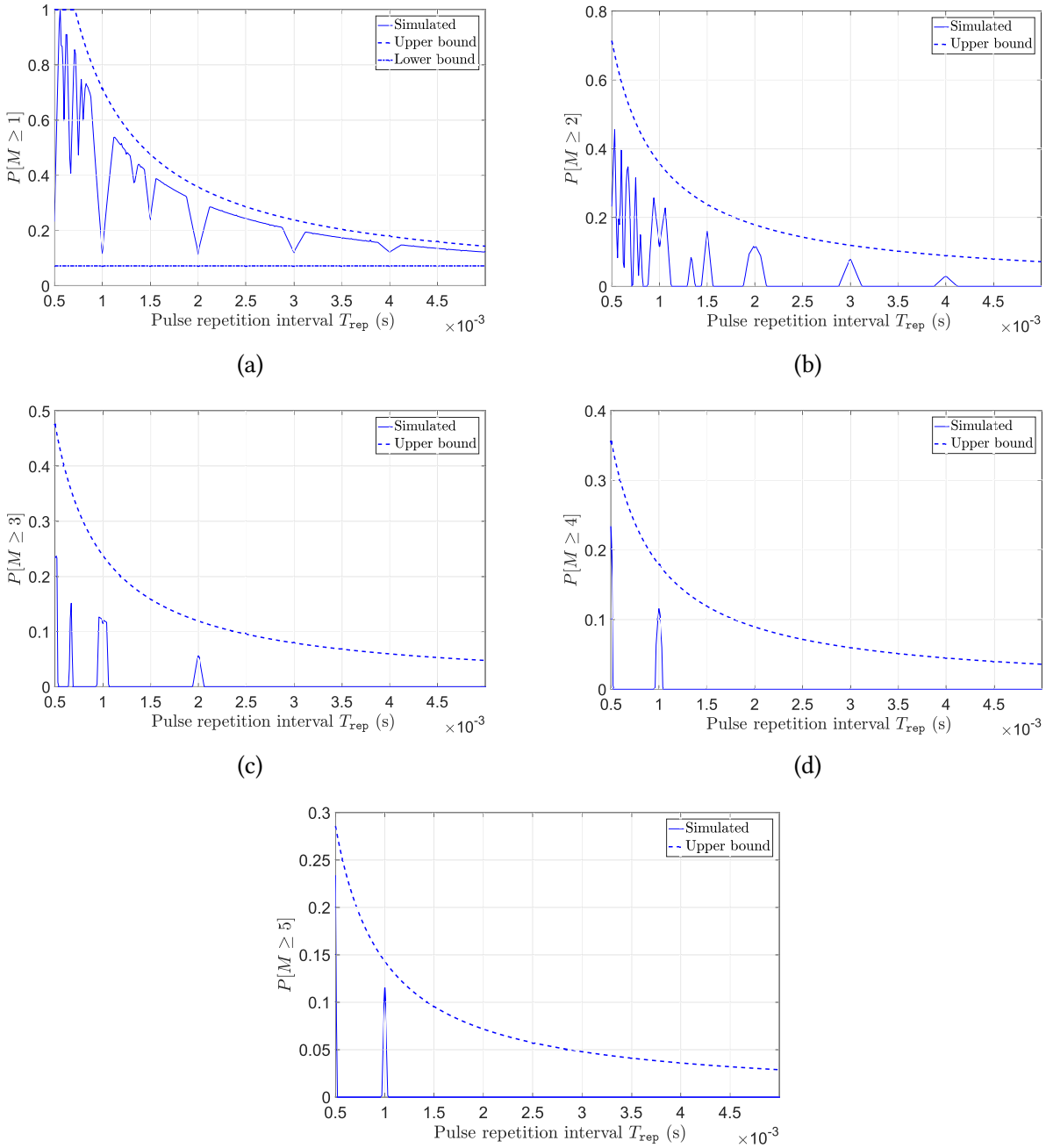

Figure 4.7: $\mathbb{P}[M \geq m]$ for $m = 1, 2, \cdots, 5$ in the case of $p = 2$ sub-pulses (due 1 specular reflection and 1 LoS component) per radar pulse, for $T_{\mathtt{pulse}} \to 0$ and $\tau_0 = 50$ μs for $T_{CSI} = 5$ ms, $T_{\mathtt{ofdm}} = 71.43$ μs, $T_{\mathtt{pil}} = 1$ ms, and $T_{\mathtt{rep}} = 0.5 - 5$ ms.

developed in Theorem 4.1 and 4.2.

4.4 Fundamental Insights on Coherent Demodulation and Limited S-CSI Feedback

As we discussed in Section 4.1.1, pilot interference is detrimental for I-CSI estimation, but is desirable for S-CSI estimation. Therefore, a low probability of pilot interference is detrimental for I-CSI estimation, but beneficial for S-CSI estimation. Below, we develop important system design insights, based on the lower bound achievability results in Theorem 4.1 and 4.2.

4.4.1 Minimizing Impact on Coherent Demodulation

It is well known that corrupted I-CSI is detrimental to coherent demodulation [85], [82], [78]. Therefore, minimizing $\mathbb{P}[M \geq 1]$ for DMRS over an infinite observation interval ($T_{CSI} \to \infty$) *on average* minimizes the occurrence of pulsed radar-induced I-CSI contamination. Using Theorem 4.1, we observe that the lower bound of $\mathbb{P}[M \geq 1]$ is achieved if $T_{\mathtt{rep}} = kT_{\mathtt{DMRS}}$ for finite $k \in \mathbb{N}$. Therefore, DMRS interference can be minimized in the following scenarios.

4.4.1.1 Partial Radar-Cellular Cooperation

If partial radar-cellular cooperation is feasible, the radar can choose $T_{\mathtt{rep}} = kT_{\mathtt{DMRS}}, k \in \mathbb{N}$ to minimize pilot interference. However in order to do so, the radar needs to have prior knowledge of $T_{\mathtt{DMRS}}$, or the cellular system has to explicitly feed back the value of $T_{\mathtt{DMRS}}$ to the radar.

4.4.1.2 Absence of Radar-Cellular Cooperation

If the radar operation does not allow real-time adaptation of its repetition interval, the cellular system needs to adapt its pilot spacing. As we described in Chapter 2, the pilot spacing can be adapted in time and frequency in real-time, as a function of the channel conditions, if the cellular receiver is (a) capable of estimating the channel parameters, and (b) feed the channel parameters back to the cellular transmitter.

Adding more pilot signals improves the channel estimation performance, but incurs resource overhead as they do not carry data. However, to ensure accurate downlink channel estimation performance in the case of a mobile user, the pilot temporal spacing ($T_{\mathtt{pil}}$) should be shorter than the coherence time $T_{\mathtt{coh}}$ of the channel [114]. In addition to this, the pilot spacing should simultaneously minimize the probability of pilot interference, which is also a function of $T_{\mathtt{rep}}$. Therefore, we propose adapting the DMRS spacing $T_{\mathtt{pil}} = T_{\mathtt{DMRS}}$ as a function of the radar parameters, as well as the coherence time of the fading channel. Minimizing $\mathbb{P}[M \geq 1]$ for DMRS over an infinite observation interval ($T_{CSI} \to \infty$) *on average* is a simple method to mitigate I-CSI contamination.

The equivalent minimization problem can be written as

$$\begin{aligned} T_{\texttt{DMRS,opt}} =& \arg\min_{T_{\texttt{DMRS}} \in \mathbb{R}^+} \mathbb{P}[M \geq 1 | T_{\texttt{rep}}]. \\ & \text{s.t. } T_{\texttt{DMRS}} \leq T_{\texttt{coh}} \end{aligned} \tag{4.13}$$

The constraint is introduced to ensure accurate channel estimation, whereby the DMRS spacing should be smaller than the coherence time ($T_{\texttt{coh}}$) of the fading channel [114]. In general, an exact solution cannot be obtained due to the aforementioned constraint.

Nevertheless, a heuristic solution can be obtained using Theorem 4.1 by observing that local minima occur at $T_{\texttt{DMRS}} = T_{\texttt{rep}}/k, k \in \mathbb{N}$, where $\mathbb{P}[M \geq 1 | T_{\texttt{rep}}] = \frac{kT_{\texttt{ofdm}}}{T_{\texttt{rep}}}$. The best case scenario occurs when $k = 1$, and $T_{\texttt{DMRS,opt}} = T_{\texttt{rep}}$. In order to satisfy the constraint, the pilot spacing can be chosen as $T_{\texttt{DMRS}} = \frac{T_{\texttt{rep}}}{k_{\texttt{opt}}}$, where $k_{\texttt{opt}} = \left\lceil \frac{T_{\texttt{rep}}}{T_{\texttt{coh}}} \right\rceil$. To perform this adaptation in real-time, $\hat{T}_{\texttt{rep}}$ should be estimated, especially in the case of military radar systems where $T_{\texttt{rep}}$ is often unknown. In practice, $\hat{T}_{\texttt{rep}}$ can be estimated by using Fourier transform methods as described in Section 5.4.1, or by monitoring the times-of-arrival of radar pulses [115].

4.4.2 Impact on Limited S-CSI Feedback of the Interference Channel

Pilot-aided S-CSI estimates of the *interference channel* are inaccurate if pilots are impaired with low probability, or not impacted at all [108]. Under our system model, (a) $\mathbb{P}[M \geq 1]$ is equivalent to the probability that S-CSI of the *interference channel* is accurately acquired using $Q_{\texttt{min}}(\mathbf{R})$, and (b) $\mathbb{P}[M \geq m]$ ($m > 1$) denotes the probability that S-CSI of the *interference channel* is accurately acquired using $Q_{\texttt{avg}}(\mathbf{R})$.

In contrast to I-CSI, limited feedback of $Q_{\texttt{min}}(\mathbf{R})$ is inaccurate for the interference channel when $T_{\texttt{rep}} = kT_{\texttt{CSIRS}}, k \in \mathbb{N}$. Furthermore, (a) the upper bound of the probability of obtaining m accurate S-CSI estimates of the *interference channel state* decreases with increasing m (Lemma 4.1), and (b) this probability *is non-zero* only when $T_{\texttt{rep}} \in \mathcal{T}_{m,N_p}$ (Theorem 4.2). Both of these results imply that window-averaged S-CSI ($Q_{\texttt{avg}}(\mathbf{R})$) is not reliable for S-CSI acquisition of the interference channel state, since $\mathbb{P}[M \geq N_p/2] = 0$ for a large range of $T_{\texttt{rep}}$ values. As a result, link adaptation and scheduling schemes in LTE and NR will be inefficient, especially in the presence of high-power radar pulses with low $T_{\texttt{rep}}$, since pilot-aided schemes fail to capture S-CSI of the *interference channel*. Therefore, *blind S-CSI estimation methods* need to be used to augment pilot-aided estimates, when sharing spectrum with pulsed radars.

4.4.3 Numerical Results

Fig. 4.8 shows the impact of the estimation window length on limited S-CSI feedback schemes based on the *mean/median S-CSI* in 5G NR, for $T_{\texttt{ofdm}} = 71.43$ μs, $T_{CSI} = 4, 8, \cdots, 64$ ms [107], and 2 ms $\leq T_{\texttt{rep}} \leq$ 3 ms. We observe that for a fixed pilot spacing of $T_{\texttt{CSIRS}} = 2$ ms,

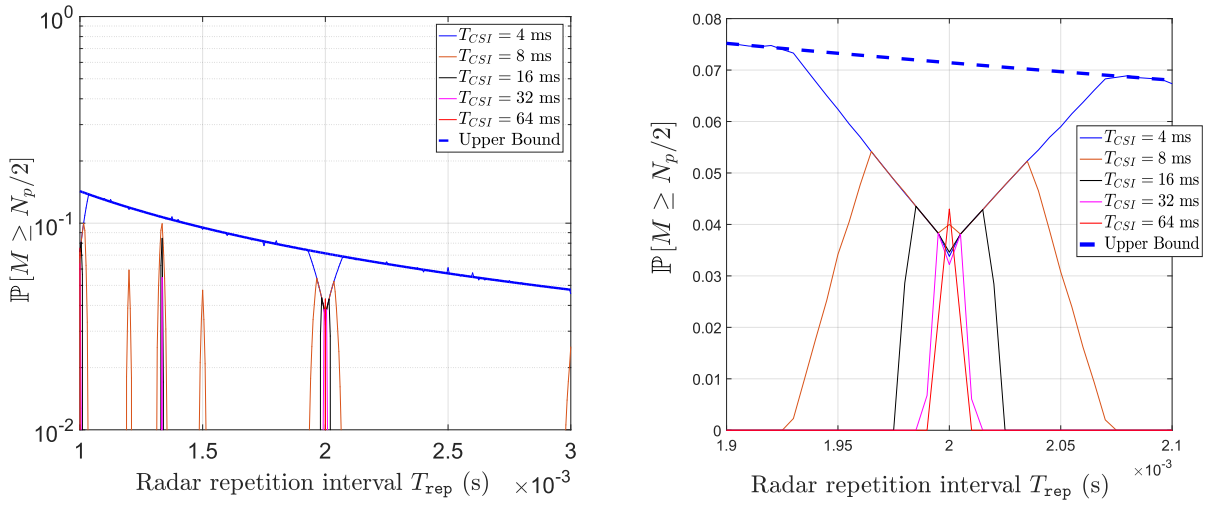

(a) (b)

Figure 4.8: Plot of $\mathbb{P}\left[M \geq \frac{N_p}{2}\right]$ and its upper bound as a function of $T_{\texttt{rep}}$, for fixed pilot spacing $T_{\texttt{CSIRS}} = 2$ ms and estimation window lengths $T_{CSI} = 4, 8, 16, \cdots, 64$ ms.

the upper bound of $\mathbb{P}[M \geq \frac{N_p}{2}]$ is the same for all cases. However, we also observe that increasing T_{CSI} shrinks the set of $T_{\texttt{rep}}$ values for which mean/median S-CSI will be accurate for the *interference channel*. This behavior can be explained using Theorem 4.2: Since $\mathcal{T}_{N_p/2,N_p} = \bigcup_{k\in\{1,2\},q\in\mathbb{N}} \left(kT_{\texttt{CSIRS}} - \frac{T_{\texttt{ofdm}}}{(N_p/2-1)q}, kT_{\texttt{CSIRS}} + \frac{T_{\texttt{ofdm}}}{(N_p/2-1)q}\right)$, increasing T_{CSI} while keeping $T_{\texttt{CSRIS}}$ constant increases N_p, thus contracting the size of $\mathcal{T}_{N_p/2,N_p}$. Therefore, increasing the estimation window length while keeping the pilot spacing fixed degrades the availability of accurate S-CSI estimates for the *interference channel state*, when mean or median S-CSI feedback is used. In particular, the CSI-RS patterns in NR have high temporal pilot spacing, to enable S-CSI estimation and feedback for massive MIMO transmission modes with reasonable overhead in pilot resources. Thus, sparsity of CSI-RS in the time domain [107] induces vulnerabilities in pilot-aided S-CSI estimation and limited feedback schemes in pulsed radar-NR spectrum sharing scenarios.

4.5 Conclusion

Considering an underlay pulsed radar-cellular spectrum sharing scenario, we derived bounds on the probability that single and multiple pilot-bearing OFDM symbols are interfered by radar pulses in a finite estimation window, under an infinitesimal radar pulse width model. We extended these analyses to multipath scenarios due to (a) localized scattering and (b) far-away specular reflectors.

We proved achievability of the lower bound, and provided insights on designing *pilot interference-minimizing schemes* as a function of the pilot spacing, radar pulse repetition interval, and coher-

ence time of the cellular fading channel. We also proved that the probability of multiple cellular pilots being interfered by radar pulses in the estimation window is zero for a large set of radar repetition intervals. This is detrimental for pilot-aided statistical CSI estimation in the *interference channel state* which highlights the need for blind methods in NR and beyond-5G systems sharing spectrum with radars. We demonstrated the accuracy of the derived expressions using numerical results, and usefulness of the design principles using examples from 5G NR.

As cellular networks evolve beyond 5G, these results and insights will be crucial for demodulation reference signal design and robust S-CSI acquisition and feedback schemes. This work can be extended to analyze these probabilities in the case of a pulse radar with an arbitrary staggering sequence, and extended to coexistence scenarios between MIMO radars that can transmit independent pulse streams from multiple antenna, and MIMO communication systems.

In the next chapter, we extend this work to study the impact of interference power on S-CSI estimation on degradation of link-level metrics such as throughput, block error rate and latency in pulsed radar-cellular coexistence scenarios.

Chapter 5

Semi-Blind Post-Equalizer SINR Estimation and Dual CSI Feedback for Radar-Cellular Coexistence

5.1 Introduction

In order to address the problem of severe spectrum shortage in sub-6 GHz bands and meet the exponentially increasing demand for user data, spectrum sharing has been investigated, standardized and implemented in the last few years. In sub 6-GHz frequency bands, radar systems are the major primary consumers of spectrum, where most commercial cellular and wireless local area network (WLAN) systems currently operate. Spectrum sharing with radars is efficient because of its waveform characteristics, and sparse deployment. In particular, spectrum sharing with *pulsed radar systems* is more desirable because of the interference-free time duration that can be leveraged for secondary user operations.

In the United States, the Federal Communications Commission (FCC) has ratified the rules for radar-communications coexistence in the 3550-3650 MHz [21] and 5 GHz [22] bands. More recently, the radar-incumbent 1.3 GHz [20] and 3450-3550 MHz [117] bands have also been identified for spectrum sharing. Due to these ongoing developments, cellular standardization has evolved into support for operation in unlicensed frequency bands, such as License Assisted Access (LAA) [24] and the Third Generation Partnership Project (3GPP) 5G New Radio-Unlicensed (5G NR-U) standards.

In addition, current vehicular communication systems are supported by cellular radio access technologies (RAT). More recently, 3GPP Release 14 introduced the cellular vehicle-to-everything (C-

This chapter is based on the work published in [116].

V2X) protocol [118], which can operate either in the 5.9 GHz band, or the cellular operator's licensed band [119]. Therefore, C-V2X systems would also have to share spectrum with other wireless systems such as Wi-Fi and radar. In particular, high-powered radars operating in the 5 GHz Unlicensed National Information Infrastructure B (U-NII B) bands [22] can cause adjacent channel interference to C-V2X systems.

Often, cooperation between radar and cellular systems is (a) impractical in the case of outdated civilian radar systems, and (b) impossible with military radars due to security concerns. In addition, due to the rapid progress of cellular technology compared to that of radar systems, the burden of harmonious coexistence is usually placed on cellular systems, which is the premise for this chapter.

5.1.1 Related Work

Prior works have proposed harmonious radar-cellular coexistence mechanisms in different operational regimes using multi-antenana techniques, waveform optimization, and opportunistic spectrum access. Multi-antenna techniques exploit the spatial degrees of freedom to minimize mutual interference, and methods such as subspace projection [15], [120], robust beamforming [121], and MIMO matrix completion [122] have been investigated in the past. These works assume the availability of accurate channel state information (CSI) at the radar and/or the cellular system, which is often infeasible, especially in the case of spectrum sharing with military radars.

Radar waveform optimization approaches using mutual information (MI)-based metrics have been investigated in [123], [124] to mitigate interference to secondary users. In addition, new multicarrier waveforms such as Precoded SUbcarrier Nulled-Orthogonal Frequency Division Multiplexing (PSUN-OFDM) [125], and FREquency SHift (FRESH)-filtered OFDM [126] have been proposed to improve their resilience to pulsed interference. Unfortunately, these waveforms require significant changes to existing radar systems and cellular standards, which makes their implementation infeasible in the near future.

Opportunistic spectrum sharing approaches have also been studied in the context of spectrum sharing with a *rotating radar* [14], [17], that leverages partial or complete information about the radar behavior to maximize spectral utilization in time/frequency/spatial dimensions. However these techniques are not applicable to spectrum sharing with *search-and-track radar systems*, where a radar that is continuously tracking a target results in uninterrupted interference to a cellular network in the spatial region of the tracking beam.

Numerical and experimental studies of underlay radar-LTE spectrum sharing scenarios [127], [16] have demonstrated that practical LTE deployments can operate with negligible degradation with an exclusion zone radius of tens of kilometers, which is significantly smaller than what is used in current deployments. However in these regimes, the pulsed radar intermittently impairs the cellular signal, disrupting data resources and critical control mechanisms of the cellular system.

Table 5.1: Simulation parameters: underlay spectrum sharing between an LFM pulsed radar and LTE-A Pro downlink

Parameter	**Description**
3GPP Releases	8 to 14 (LTE to LTE-A Pro)
Center Frequency	2 GHz
System Bandwidth	10 MHz
Transmission Mode	TM 0 (SISO) from Port 0 [37]
Small-scale Fading	Extended Pedestrian A (EPA) Doppler frequency $f_d = 10$ Hz
CSI feedback mode	Periodic and Wideband
CSI estimation interval [37]	10 ms
CSI delay	8 ms
HARQ mode	Asynchronous and Non-Adaptive with up to 4 retransmissions
Radar Pulse repetition Interval	3.125 ms
Radar pulse width $(T_{\texttt{pul}})$	5 μs
Radar relative carrier frequency offset (Δf_r)	0 Hz
Radar sweep frequency (f_s)	5 MHz

5.1.2 Motivation

Statistical-CSI (S-CSI) such as channel spatial covariance and *post-equalizer SINR* [128] are important quantities, forming the basis of link adaptation and user scheduling schemes in modern wireless communication systems. LTE and NR systems use *pilot-aided* S-CSI estimation schemes, and limited feedback mechanisms to balance link-level performance with feedback overhead [37], [2]. Since pilots occupy a tiny fraction (at most 5% [78], [96]) of time-frequency resources in cellular signals, pilot-aided S-CSI is accurate if interference and fading statistics are the same on pilot and non-pilot resources, as shown in Chapter 3.

While this is generally true in conventional cellular deployments, it does not hold in the presence of periodic pulsed interference. In Chapter 4, we rigorously proved that accurate S-CSI acquisition is hindered due to (a) low probability of pilot interference in a finite estimation window, and (b) zero probability of multiple pilot interference for a large set of radar repetition intervals. Below, we demonstrate link-level degradation in practical systems as a result of these phenomena. Consider a linear frequency modulated (LFM) pulsed radar coexisting with the LTE-A Pro downlink between a single evolved NodeB (eNB) and a single user equipment (UE). The system parameters shown in Table 5.1. The baseband transmitted waveform of a single LFM radar pulse

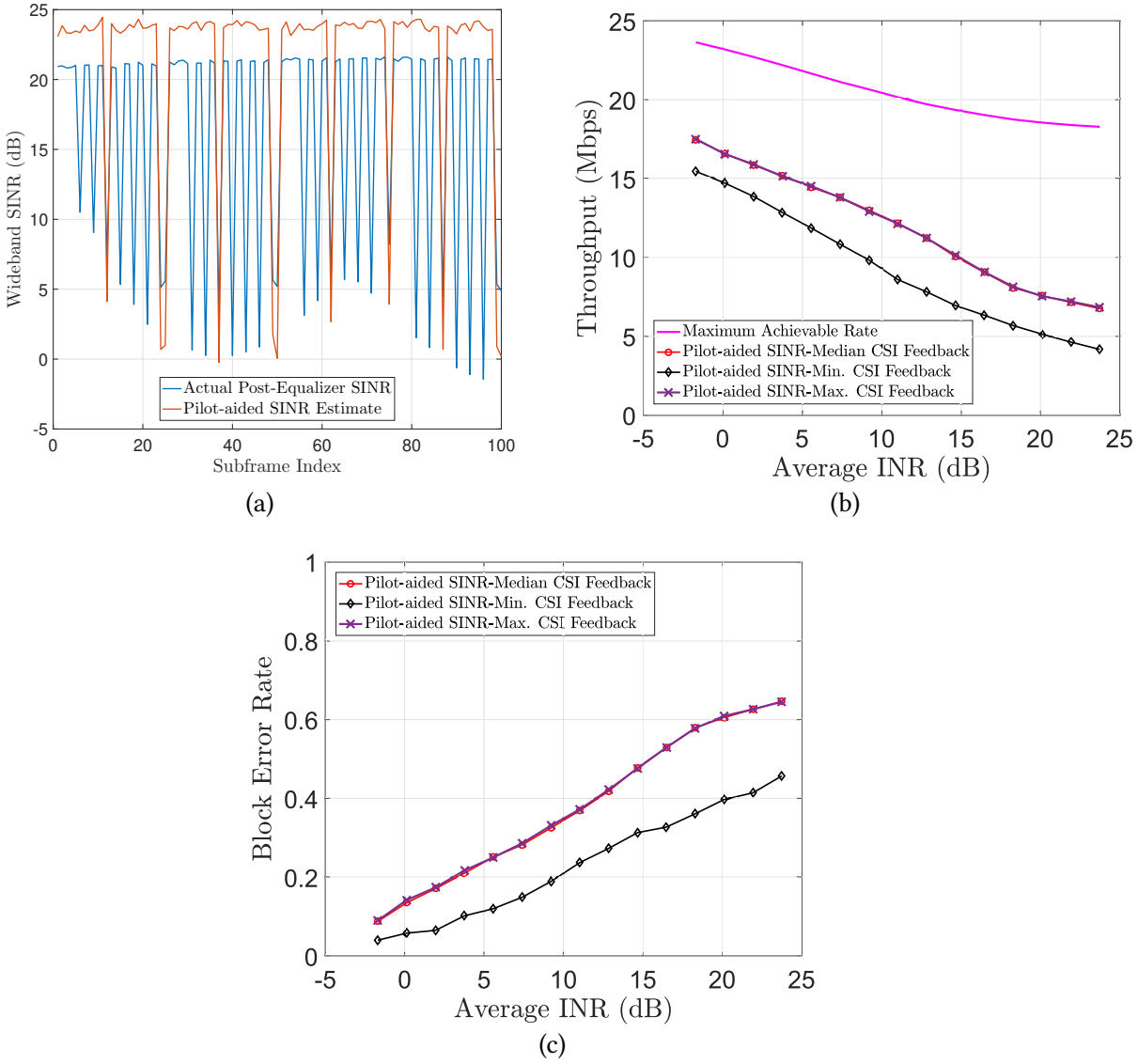

Figure 5.1: Illustration of (a) inaccurate pilot-aided SINR estimates due to pulsed radar interference, and degradation of (b) throughput, and (c) block error rate (BLER) performance. The average SNR of the eNB-to-UE fading channel is 19.5 dB.

is given by [129]

$$i_{\texttt{LFM}}(t) = \sqrt{P_{\texttt{rad}}} e^{j\left(\frac{\pi f_s t}{T_{\texttt{pul}}} + 2\pi \Delta f_r\right) t} \text{ for } -\frac{T_{\texttt{pul}}}{2} \leq t \leq \frac{T_{\texttt{pul}}}{2}, \tag{5.1}$$

where $P_{\texttt{rad}}$ is the radar transmitted power, $T_{\texttt{pul}}$ is the radar pulse width, f_s the sweep frequency, and Δf_r the offset w.r.t. the center frequency of the cellular signal. Hence, the *radar pulse train*

can be written as

$$i_{\texttt{LFM,train}}(t) = \sqrt{P_{\texttt{rad}}} \sum_{k=-\infty}^{+\infty} \Big\{ e^{j\left(\frac{\pi f_s (t - kT_{\texttt{rep}})}{T_{\texttt{pul}}} + 2\pi \Delta f_r\right)(t - kT_{\texttt{rep}})} \cdot \Big[U\big(t - kT_{\texttt{rep}} + \tfrac{T_{\texttt{pul}}}{2}\big) - U\big(t - kT_{\texttt{rep}} - \tfrac{T_{\texttt{pul}}}{2}\big) \Big] \Big\}, \tag{5.2}$$

where $U(\cdot)$ is the unit-step function, and $T_{\texttt{rep}}$ is the radar repetition rate.

Fig. 5.1a illustrates the fundamental issue: Since pulsed radar interference is time-selective, absence of pilot interference results in inaccurate pilot-aided SINR estimates. As shown in Fig. 5.1b and 5.1c, this leads to degradation of throughput and block error rate performance in the case of commonly used limited feedback schemes: minimum, median and maximum CSI feedback (explained in Section 5.2). Note that at the eNB, the modulation and coding scheme (MCS) is chosen such that the rate is maximized while satisfying a maximum BLER constraint, i.e. BLER ≤ 0.1 [118]. The maximum achievable rate (pink curve) in Fig. 5.1b is the maximum rate achieved (using the maximum MCS) under the constraint that the average BLER $= 0.1$.

In such scenarios, blind S-CSI estimation methods can be used, since they do not rely on training sequences using pilot signals. Prior works have investigated maximum likelihood (ML) [130], [131], moment-based [132], and cyclostationary-based [133] SINR estimation methods. However, the accuracy of ML and moment-based methods depend on the availability of accurate fading and interference statistics of the channel, which is often (a) impractical to acquire in real-time, and (b) very challenging to acquire in nonstationary channels with time-varying channel statistics. For cyclostationarity-aided methods, short length of the cyclic prefix, unequal power allocation across subcarriers, and dependence of its accuracy on long-term averaging (for thousands of OFDM symbols) hinder their suitability to practical scenarios. The key drawback of all of these methods is that they do not estimate the *post-equalizer* SINR[1], which is the metric used to aid scheduling decisions and link adaptation procedures in LTE and NR [128].

In addition to inaccurate SINR estimates in Fig. 5.1a, we observe that the channel is *bimodal*, due to periodic transitions between *'interference-free'* and *'interference-impaired'* states. Since limited feedback procedures in LTE and NR support single CSI feedback for a given frequency subband, it is fundamentally impossible to quantize the bimodal nature of the channel using a single value. Therefore, the issues of *S-CSI inaccuracy* and *channel bimodality* needs to be jointly addressed by the CSI estimation and feedback framework, which is the key focus of this chapter.

5.1.3 Contributions

In this chapter, we make the following contributions:

[1]Post-equalizer SINR refers to the SINR of the received signal after channel estimation and equalization stages of the baseband receiver [128], [134].

1. We present a robust max-min heuristic to estimate the post-equalizer SINR with low complexity, and characterize its distribution under a realistic tractable signal model for quadrature amplitude modulated (QAM) symbols. We analyze its accuracy and robustness, to demonstrate its applicability for estimating the post-equalizer interference and noise power on radar-impaired OFDM symbols in practical spectrum sharing scenarios (Section 5.3).

2. We propose a comprehensive framework to estimate the radar parameters, and combine pilot-aided as well as heuristic-aided SINR estimates to calculate the wideband post-equalizer SINR metric (Section 5.4).

3. We propose the *'dual CSI feedback'* scheme as a simple extension to currently used limited CSI feedback mechanisms in cellular systems, to support CSI acquisition for *'fading'* and *'interference-impaired'* channel states (Section 5.5).

4. Using radar-LTE-A Pro spectrum sharing as an example, we demonstrate significant improvements in rate, BLER and retransmission-induced latency using our proposed framework, when compared to conventional *pilot-aided SINR* and *single CSI feedback* schemes (Section 5.5).

The key stages of the SINR estimation framework are shown in Fig. 5.2. The rest of this chapter is organized as follows. Section 5.2 describes the system model, and provides the basics of CSI estimation and limited feedback schemes used in LTE and NR. Section 5.3 proposes the max-min heuristic, derives its distribution under a tractable signal model, and analyzes its accuracy and robustness. Section 5.4 introduces the semi-blind SINR estimation framework, and evaluates the performance of each stage. Section 5.5 develops the dual CSI feedback mechanism, discusses the incurred feedback overhead, and demonstrates its effectiveness through link-level simulation results for radar-LTE-A Pro coexistence scenarios. Finally, Section 5.6 concludes the chapter, and discusses directions for future research.

5.2 System Model and Preliminaries

5.2.1 Cellular Downlink Signal Model

We consider an underlay radar-cellular spectrum sharing scenario, where the cellular downlink coexists with a *wideband pulsed radar system*. For ease of exposition, we consider a single base station (with N antenna ports) serving a single user (with K antenna ports). The cellular downlink is OFDM-based with $N_{\mathtt{sub}}$ subcarriers, where data is transmitted in blocks composed of T OFDM symbols.

On the interference-impaired OFDM symbol, the received signal vector $\mathbf{z}[n,k] \in \mathbb{C}^K$ on the k^{th} subcarrier of the n^{th} OFDM symbol (referred to as a resource element (RE)) indexed by an ordered

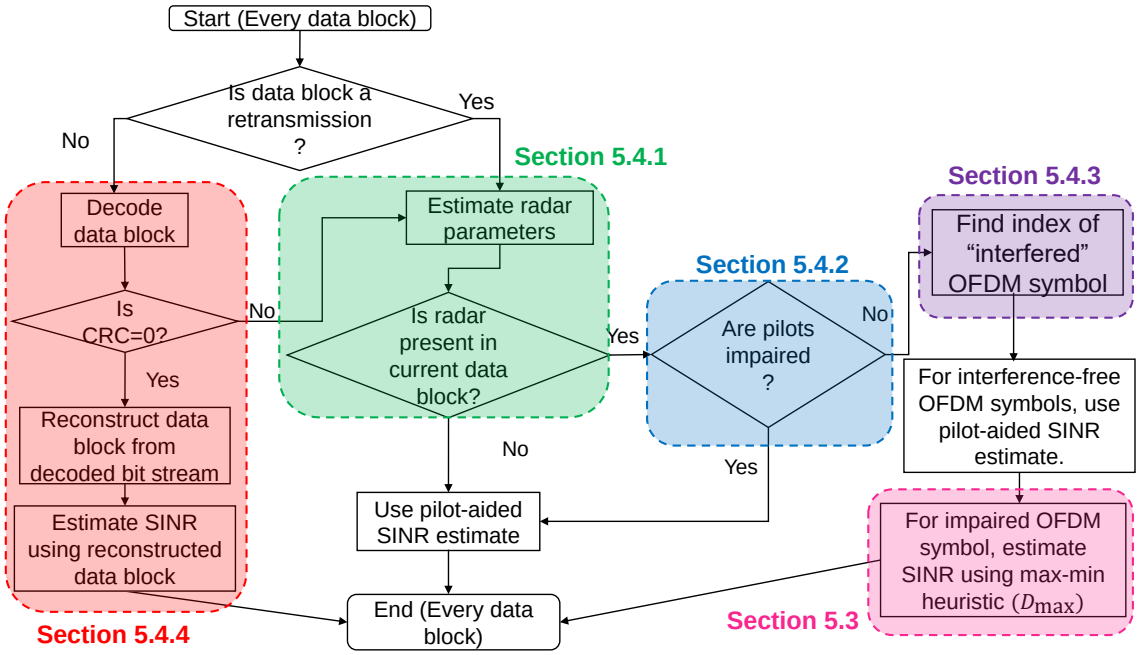

Figure 5.2: Flowchart of the hybrid SINR estimation framework for the cellular downlink in the presence of a pulsed radar. The SINR estimation algorithm is executed for every data block.

pair $[n, k]$, is given by

$$\mathbf{z}[n,k] = \mathbf{H}[n,k]\mathbf{W}[n,k]\mathbf{x}[n,k] + \mathbf{h}_r[n,k]i[n,k] + \mathbf{w}[n,k], \tag{5.3}$$

where $\mathbf{H}[n,k] \in \mathbb{C}^{K\times N}$ is the downlink channel matrix, $\mathbf{W}[n,k] \in \mathbb{C}^{N\times L}$ the precoding matrix, and L the data vector length. The transmitted symbol vector is chosen from $\mathbf{x}[n,k] \in \mathcal{X}^L$, where $\mathcal{X}$ is the set of symbols for the given modulation scheme. The noise vector is i.i.d. such that $\mathbf{w}[n,k] \sim \mathcal{CN}(0, \sigma_w^2\mathbf{I}_K)$. The radar-to-user channel vector on the $[n,k]^{th}$ resource elements (RE) is $\mathbf{h}_r[n,k] \in \mathbb{C}^K$, and the baseband-equivalent interference symbol is $i[n,k]$ such that $\mathbb{E}\big[\mathbf{h}_r[n,k]i[n,k]\big] = \mathbf{0}$ and $\mathbb{E}\big[\mathbf{h}_r[n,k]i[n,k]i^*[n,k]\mathbf{h}_r^H[n,k]\big] = \mathbf{R}_\mathbf{I}[n,k]$.

On the other hand, for an interference-free OFDM symbol with index $n' \neq n$, the received vector is given by

$$\mathbf{z}[n',k] = \mathbf{H}[n',k]\mathbf{W}[n',k]\mathbf{x}[n',k] + \mathbf{w}[n',k]. \tag{5.4}$$

For RE $[n,k]$, if $\hat{\mathbf{H}}[n,k]$ is the estimated channel matrix and $\hat{\sigma}_w^2$ the estimated noise variance, then the decoded data symbol $\hat{\mathbf{x}}[n,k]$ using a minimum mean square error (MMSE) equalizer[2] is given by

$$\hat{\mathbf{x}}[n,k] = (\mathbf{W}^H[n,k]\hat{\mathbf{H}}^H[n,k]\hat{\mathbf{H}}[n,k]\mathbf{W}[n,k] + \hat{\sigma}_w^2\mathbf{I}_K)^{-1}\mathbf{W}^H[n,k]\hat{\mathbf{H}}^H[n,k]\mathbf{z}[n,k]. \tag{5.5}$$

[2]In practical systems, other linear equalizers such as Zero-Forcing (ZF) or Regularized ZF are also commonly used to recover the data symbols.

Table 5.2: Important system parameters in Chapter 5

Parameter	**Description**
$P_{\texttt{rad}}$	Radar transmitted power
$T_{\texttt{rep}}$	Pulsed radar repetition interval
$T_{\texttt{pul}}$	Radar pulse width
$T_{\texttt{pil}}$	Temporal spacing of cellular pilot signals
f_s	Radar sweep frequency
Δf_r	Radar frequency offset
T_{CSI}	CSI estimation window length
CQI	CQI values in the estimation window
P_r	Post-equalizer radar interference power
σ_n^2	Post-equalizer noise variance
$\hat{\gamma}_{p,l}$	Pilot-aided SINR estimate for the l^{th} spatial layer
$\hat{\gamma}_{\texttt{avg}}$	Average post-equalizer SINR estimate
$D_{\texttt{max}}$	Max-min heuristic
K_{RB}	Length of coherence block (in frequency)

For ease of notation we suppress the RE index henceforth, while noting that the symbol on each RE is processed in a similar manner. Defining $\hat{\mathbf{G}}_{\texttt{MMSE}} \triangleq (\mathbf{W}^H\hat{\mathbf{H}}^H\hat{\mathbf{H}}\mathbf{W} + \hat{\sigma}_w^2\mathbf{I}_L)^{-1}\mathbf{W}^H\hat{\mathbf{H}}^H$, the instantaneous SINR $\hat{\gamma}_l$ for the *interference-free OFDM symbol* on the l^{th} antenna port ($1 \leq l \leq L$) is given by

$$\hat{\gamma}_l = \frac{\mathbb{E}[|x_l|^2]}{\mathbb{E}\left[\left|[(\hat{\mathbf{G}}_{\texttt{MMSE}}\mathbf{H}\mathbf{W} - \mathbf{I}_L)\mathbf{x} + \hat{\mathbf{G}}_{\texttt{MMSE}}(\mathbf{w})]_l\right|^2\right]}, \tag{5.6}$$

where $[\mathbf{z}]_l$ denotes the l^{th} element of vector $\mathbf{z}$. Similarly, the instantaneous SINR of the *interference-impaired OFDM symbol* on the l^{th} antenna port is given by

$$\hat{\gamma}_l = \frac{\mathbb{E}[|x_l|^2]}{\mathbb{E}\left[\left|[(\hat{\mathbf{G}}_{\texttt{MMSE}}\mathbf{H}\mathbf{W} - \mathbf{I}_L)\mathbf{x} + \hat{\mathbf{G}}_{\texttt{MMSE}}(\mathbf{h}_r i + \mathbf{w})]_l\right|^2\right]}. \tag{5.7}$$

Since $\hat{\gamma}_l$ is calculated after baseband processing, it is termed as the *post-equalizer/post-processing SINR*. This is used to calculate link quality metric(s) [128], which subsequently aid in scheduling decisions and link adaptation mechanisms.

5.2.2 Pilot-Aided SINR Estimation and Wideband SINR Metrics

Typically, pilot signals are used both for channel estimation as well as for SINR estimation[3]. In this work, we use the pilot-aided linear MMSE estimation method described in [135] assuming unit powered pilot symbols. For interference-free pilots in a MIMO transmission mode, the pilot-aided MMSE post-equalizer SINR estimate on the l^{th} antenna port ($\hat{\gamma}_{p,l}$) is given by [136]

$$\hat{\gamma}_{p,l} = \frac{1}{\left[\frac{\mathbf{W}^H \hat{\mathbf{H}}^H \hat{\mathbf{H}} \mathbf{W}}{\hat{\sigma}_w^2} + \mathbf{I}_L\right]^{-1}_{l,l}} - 1, \tag{5.8}$$

where $[\mathbf{X}]_{i,i}$ denotes the i^{th} element on the main diagonal of matrix $\mathbf{X}$, and p in the subscript of $\hat{\gamma}_{p,l}$ denotes that it is a pilot-aided SINR estimate. Since a data block comprises of contiguous time and frequency resource elements, a *subband/wideband SINR metric* is often calculated to compress the CSI. If the SINR estimate on the $(n,k)^{th}$ RE is $\hat{\gamma}[n,k]$, the wideband SINR is obtained using standard mapping functions such as effective exponential SINR mapping ($\hat{\gamma}_{\mathsf{e}}$) [137] and average SINR mapping ($\hat{\gamma}_{\mathsf{avg}}$) [138], given by

$$\hat{\gamma}_{\mathsf{e}} = \log\left[\frac{1}{|\mathcal{D}|}\sum_{(n,k)\in\mathcal{D}} e^{-\frac{\hat{\gamma}[n,k]}{\beta}}\right]^{-\beta}, \text{ and } \hat{\gamma}_{\mathsf{avg}} = \sum_{(n,k)\in\mathcal{D}} \frac{\hat{\gamma}[n,k]}{|\mathcal{D}|} \tag{5.9}$$

respectively, where $\mathcal{D}$ denotes the RE indices of data symbols in the cellular signal, and β is a function of the modulation scheme [137].

5.2.3 Link Adaptation Using Limited CSI Feedback

LTE and NR adapt the multi-antenna transmission mode (SISO/Diversity/SU-MIMO/MU-MIMO), modulation format, and error control coding scheme, as a function of the channel fading and interference conditions. In order to limit the overhead while balancing performance, they support limited CSI feedback schemes, where CSI estimated in a finite estimation window is quantized and fed back to the transmitter [106]. The finite estimation window is referred to as the *CSI estimation window* henceforth[4]. For the system model in Section 5.2.1, the quantized CSI value consists of the following quantities:

1. Precoding Matrix Indicator (PMI): an index of $\mathbf{W}_k \in \mathcal{W}$ chosen from a codebook $\mathcal{W}$ of predefined matrices.

[3] 3GPP Releases up to LTE-A Pro can use the common reference signal (CRS) and the demodulation reference signal (DMRS) to estimate the channel as well as the SINR. However, pilot signals such as the CSI reference signal (CSI-RS) can only be used to estimate the optimal precoder and SINR.

[4] The estimation window duration is chosen based on the rate at which the channel statistics vary, depending on user mobility. In typical cellular deployments, this interval ranges from tens to hundreds of milliseconds [2].

2. Rank Indicator (RI): the maximum rank supported on the downlink channel, which can be inferred from $\mathbf{W}_k$.

3. Channel Quality Indicator (CQI): a 4-bit value representing the quantized subband/wideband post-equalizer SINR metric ($\hat{\gamma}_{\mathtt{e}}/\hat{\gamma}_{\mathtt{avg}}$ in equation 5.9) of the cellular signal.

The CQI is mapped to a 5-bit modulation and coding scheme (MCS). In the LTE and NR PHY layer, decoding success and PHY layer performance metrics are characterized on units of data known as *transport blocks*. For each transport block, the MCS denotes the most spectrally efficient scheme that simultaneously ensures that a maximum block error rate (BLER) is not exceeded on average. In addition, L is equal to the number of transport blocks allotted to a single user, and $L \leq 2$ in LTE and NR even when the number of antenna ports $K \geq 2$ [2], [37]. Interested readers are referred to Appendix A for more details. For ease of exposition, we refer to the wideband SINR metric of a data block as the *post-equalizer SINR* henceforth.

If $\hat{\gamma}[m]$ is the post-equalizer SINR calculated for the m^{th} data block, then $CQI[m] = f(\hat{\gamma}[m]) \in \mathbb{N}$ is the corresponding CQI, where $f(\cdot)$ is a monotonically non-decreasing function of SINR[5]. Considering a CSI estimation window of length T_{CSI} data blocks, the wideband CQI measurements corresponding to the T_{CSI} subframes are collectively represented by the vector $\mathbf{CQI} = \left[CQI[0], CQI[1], \cdots, CQI[T_{CSI}-1]\right] \in \mathbb{N}^{T_{CSI}}$. In this work, we consider the following conventional CSI quantization and limited feedback schemes:

1. minimum CSI feedback, where $\min(\mathbf{CQI})$ is periodically fed back after every T_{CSI} data blocks, and

2. median CSI feedback, where $\text{med}(\mathbf{CQI})$ is periodically fed back after every T_{CSI} data blocks.

3. maximum CSI feedback, where $\max(\mathbf{CQI})$ is periodically fed back after every T_{CSI} data blocks.

It is evident from Fig. 5.1 that $\min(\cdot)$, $\text{med}(\cdot)$ and $\max(\cdot)$ quantization functions result in overoptimistic CQI values due to inaccurate pilot-aided SINR estimates. However, it is important to note that pilot-aided SINR estimates are accurate (a) in the absence of interference, and (b) when a pilot-bearing OFDM symbol is interference-impaired. Therefore, a key challenge is to accurately estimate the post-equalizer SINR with low computational complexity when pilot-resources are interference-free but data resources are not. In the rest of this chapter, we consider potential interference of pilots that are used to estimate the channel impulse response (CIR) as well as the SINR[6]. In the subsection below, we discuss the post-equalizer signal model of the interference-impaired non-pilot OFDM symbol, when the downlink channel impulse response (CIR) is accurately estimated by interference-free pilot signals.

[5]For an example of the SINR-to-CQI mapping, please refer to equation (3.4) in Chapter 3.

[6]In cellular standards up to LTE-A Pro, the same pilot signal is used for channel estimation as well as SINR estimation, such as the cell-specific reference signal (CRS). Other pilots such as Demodulation Reference Signals (DMRS) can also be used to estimate the SINR, *conditioned on the precoding matrix* ($\mathbf{W}$) used [2].

5.2.4 Baseband Equivalent Post-Processed Signal Model

On the interference-impaired OFDM symbol, using equation (5.5), the resultant post-equalizer baseband signal on subcarrier k will be

$$\hat{\mathbf{x}}[n,k] = \hat{\mathbf{G}}_{\texttt{MMSE}}[n,k]\mathbf{H}[n,k]\mathbf{W}[n,k]\mathbf{x}[n,k] + \hat{\mathbf{G}}_{\texttt{MMSE}}[n,k]\mathbf{h}_r[n,k]i[n,k] + \hat{\mathbf{G}}_{\texttt{MMSE}}[n,k]\mathbf{w}[n,k]. \tag{5.10}$$

To develop a tractable analytical model, we make the following assumptions.

Assumption 5.1. *In a coherence block of K_{RB} subcarriers, the post-equalized signal on each antenna in the presence of accurate channel estimates can be written as*

$$y_k = x_k + \sqrt{P_{r,k}}e^{j\phi_k} + n_k, \text{ for } k = 1, 2, \cdots, K_{RB} \tag{5.11}$$

where $P_{r,k}$ and ϕ_k is the post-equalizer interference power and phase, and $n_k \overset{i.i.d.}{\sim} \mathcal{CN}(0, \sigma_n^2)$ is the Additive white Gaussian noise. The transmitted symbol $x_k \sim \texttt{Uniform}[\mathcal{X}]$, where $\mathcal{X}$ is the set of QAM symbols, and $\texttt{Uniform}[\cdot]$ denotes the uniform distribution.

Assumption 5.2. *Interference power $P_{r,k}$ is constant in the coherence block $k \in \{k_0 + 1, k_0 + 2, \cdots, k_0 + K_{RB}\}$.*

Assumption 5.3. *In the coherence block $k \in \{k_0 + 1, k_0 + 2, \cdots, k_0 + K_{RB}\}$, the interference phase is i.i.d. distributed as $\phi_k \sim \texttt{Uniform}[0, 2\pi]$.*

Assumption 5.1 approximates equation (5.10) in a coherence block by an *interference-impaired AWGN channel* on antenna port l using $\left[\hat{\mathbf{x}}[n,k]\right]_l = y_k$, $\left[(\hat{\mathbf{G}}_{\texttt{MMSE}}[n,k]\mathbf{H}[n,k]\mathbf{W}[n,k] - \mathbf{I}_L)\mathbf{x}[n,k] + \hat{\mathbf{G}}_{\texttt{MMSE}}[n,k]\mathbf{h}_r[n,k]i[n,k]\right]_l = \sqrt{P_{r,k}}e^{j\phi_k}$, and $[\hat{\mathbf{G}}_{\texttt{MMSE}}[n,k]\mathbf{w}[n,k]]_l = n_k$.

Assumption 5.2 is accurate in a coherence block for LFM radar signals[7] with $f_s T_{\texttt{pul}} \gg 1$ where the radar spectrum is approximated by [129]

$$I_{\texttt{LFM}}(f) \approx \sqrt{\frac{P_{\texttt{rad}} T_{\texttt{pul}}}{f_s}} e^{-j\left(\frac{\pi T_{\texttt{pul}}(f - \Delta f_r)^2}{f_s} + \frac{\pi}{4}\right)} \tag{5.12}$$

For an arbitrarily chosen contiguous subcarrier sequence $\{k_0 + i\}$ for $i = 1, 2, \cdots, K_{RB}$ and $\Delta f_r = 0$, Assumption 5.3 approximates the sequence of square-law phase terms using

$$\left\{ \mod\left(\frac{\pi T_{\texttt{pul}}(k_0 + i)^2 \Delta f^2}{f_s}, 2\pi\right) \right\} \overset{\text{i.i.d.}}{\sim} \texttt{Uniform}[0, 2\pi], \text{ for } i = 1, \cdots, K_{RB}, \tag{5.13}$$

after marginalization over a broad range of $0 \leq k_0 \leq (N_{\texttt{sub}} - (K_{RB} + 1))$,$f_s$, and $T_{\texttt{pul}}$, where Δf is the subcarrier spacing. Note that this approximation is used for ease of exposition, and the general form of the distribution is also derived in the next section for scenarios when the phase offset of the radar interference is known *a priori*.

[7] This approximation is accurate in a coherence block of width ~ 100 kHz, in the case of a continuous-wave (CW) radar.

5.2.5 Post-Equalizer SINR Estimation Framework

To accurately estimate the wideband SINR metric in equation (5.9), the receiver must be able to detect the presence of interference and localize its position in the time-frequency grid, so that the appropriate SINR estimate can be used for each RE. In the rest of this chapter, we propose a comprehensive framework to accurately estimate the post-equalizer SINR of a data block. Fig. 5.2 shows the flowchart of the proposed framework, which is composed of the following key stages:

1. Estimation of the radar repetition rate ($f_{\texttt{rep}}$), which is used by the receiver to predict when radar interference will occur in the future.
2. Detection of pulsed radar interference on pilot-bearing OFDM symbols, which is used by the receiver to determine the accuracy of pilot-aided SINR estimate for the interference channel.
3. Detection of the contaminated OFDM symbol index, which helps the receiver localize the interference on the OFDM resource grid. The receiver uses the *max-min heuristic-aided SINR estimation method* only for the interference-impaired data-bearing OFDM symbol.

In the following section, we characterize the properties of the proposed max-min heuristic that blindly estimates the post-equalizer SINR of a coherence block blindly in the presence of accurate downlink channel estimates, and the rest of the framework will be discussed in Section 5.4.

5.3 Low Complexity Max-Min Heuristic to Estimate Post-Equalizer SINR

To estimate the *post-equalizer interference and noise amplitude* in a coherence block of contiguous subcarrier indices $\{1, 2, \cdots, K_{RB}\}$, the heuristic $D_{\texttt{max}}$ is defined as the maximum of the distance between a received symbol and its nearest neighboring constellation point, given by

$$D_{\texttt{max}} = \max_{k=1,2,\cdots,K_{RB}} \min_{x^{(j)} \in \mathcal{X}} \|y_k - x^{(j)}\|_2. \tag{5.14}$$

It is worthwhile to note that the additional complexity incurred is only due to the $\max(\cdot)$ operation, since the nearest neighbor distance calculation is already a part of the *hard/soft decoder* stage in the downlink baseband processing chain in modern cellular systems. Therefore, the maximum of the *minimum distances* calculated over a small coherence block of K_{RB} REs incurs an additional computational complexity of $O(N_{RB}K_{RB})$, where N_{RB} is the number of coherence blocks in the OFDM symbol. The cumulative distribution function (CDF) of $D_{\texttt{max}}$ can be written as

$$F_{D_{\texttt{max}}}(d) = \mathbb{P}[D_{\texttt{max}} \leq d], d \geq 0. \tag{5.15}$$

Let the received symbol $y_l = x + \sqrt{P_r}e^{j\phi} + n$, where $x \triangleq (x_R + jx_I) \in \mathcal{X}$ is the actual transmitted symbol. Defining the nearest-neighbor distance of y_l as $D_l \triangleq \min_{x^{(j)} \in \mathcal{X}} \|y_l - x^{(j)}\|_2$, $y \triangleq y_R + jy_I, n \triangleq n_R + jn_I$, and $x^{(j)} \triangleq x_R^{(j)} + jx_I^{(j)} \in \mathcal{X}$, the nearest neighbor distance can be expressed as

$$D_l = \sqrt{(x_R - x_R^{(j)} + \sqrt{P_r}\cos\phi + n_R)^2 + (x_I - x_I^{(j)} + \sqrt{P_r}\sin\phi + n_I)^2}. \tag{5.16}$$

The following proposition denotes the marginal distribution of D_l as a function of interference power P_r, phase ϕ, and noise variance σ_n^2.

Proposition 5.1. *The CDF of D_l can be written as*

$$F_{D_l}(d) = \sum_{x \in \mathcal{X}} \int_{\mathcal{A}_\Phi} \int_{\mathcal{A}_{n_R}} \int_{\mathcal{A}_{n_I}} \mathbb{1}[D_l \leq d | x, n, \phi] p_X(x) f_\Phi(\phi) f_{N_R}(n_R) f_{N_I}(n_I) \mathrm{d}\phi \, \mathrm{d}n_R \, \mathrm{d}n_I, \tag{5.17}$$

where $\mathbb{1}[\cdot]$ denotes the indicator function, $x \sim \texttt{Uniform}[\mathcal{X}]$, $p_X(x)$ is the probability mass function of $x \in \mathcal{X}$, $f_\Phi(\phi)$ is the density function of the interference phase ϕ, $f_{N_R}(n_R)$ and $f_{N_I}(n_I)$ are the density functions of the real and imaginary components of noise, respectively. The corresponding integration regions are $\mathcal{A}_\Phi, \mathcal{A}_{N_R}$ and $\mathcal{A}_{N_I}$, respectively.

Proof. The conditional event $\{D_l \leq d | x, n, \phi\}$ is represented by the indicator function $\mathbb{1}[\cdot]$. Using the fact that the interference power P_r, phase ϕ and the real and imaginary components of noise are independent of each other, we obtain the desired result when the event of interest is integrated over the appropriate regions of ϕ, n_R and n_I. ■

The marginal distribution of $D_{\texttt{max}}$ is given in the following theorem.

Theorem 5.1. *Under the received signal model $y_l = x_l + \sqrt{P_r}e^{j\phi_l} + n_l$ for $l = 1, 2, \cdots, K_{RB}$, if the interferer's phase relationship is known and given by $\phi_l = h_l(\phi_1)$, where $\phi_1 \sim \texttt{Uniform}[0, 2\pi]$ is the interferer phase on the first symbol in the coherence block, the marginal CDF of $D_{\texttt{max}}$ is given by*

$$F_{D_{\texttt{max}}}(d) = \frac{1}{2\pi |\mathcal{X}|^{K_{RB}}} \int_0^{2\pi} \prod_{l=1}^{K_{RB}} \Big[\sum_{x_l \in \mathcal{X}} F_{D_l}(d | x_l, \phi_1) \Big] \mathrm{d}\phi_1. \tag{5.18}$$

Proof. Using the definition, the marginal CDF of $D_{\texttt{max}}$ can be written as

$$F_{D_{\texttt{max}}}(d) = \int_0^{2\pi} \sum_{\mathbf{x} \in \mathcal{X}^{K_{RB}}} \mathbb{P}[\max(\mathbf{D}) \leq d | \mathbf{x}, \phi] p_{\mathbf{X}}(\mathbf{x}) f_\Phi(\phi) \mathrm{d}\phi, \tag{5.19}$$

where $\mathbf{D} = [D_1, \cdots, D_{K_{RB}}]$ is the vector of minumum distances, and $\mathbf{x} = [x_1, \cdots, x_{K_{RB}}] \sim \texttt{Uniform}[\mathcal{X}^{K_{RB}}]$ are the transmitted symbols. We have equivalent events $\{\max(\mathbf{D}) \leq d\} \Leftrightarrow$

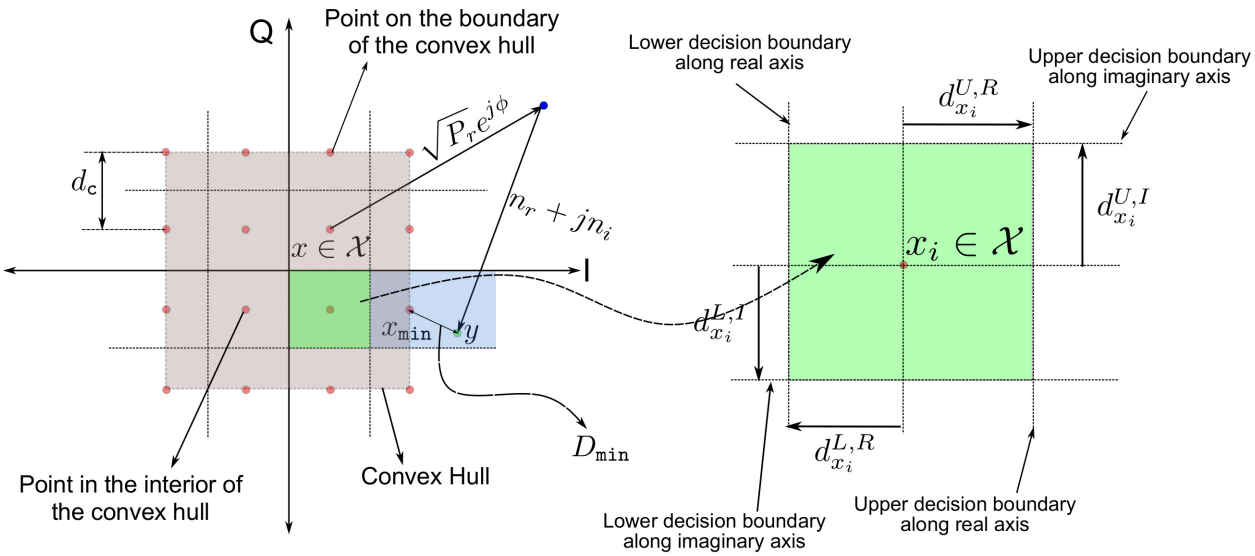

Figure 5.3: Transformation of the input to output symbols via interference and noise addition, and the resulting minimum distance $D_{\min} = \|y - x_{\min}\|_2$. The decision region of $x_{\min}$ is shaded in light blue. The figure on the right shows the decision boundaries for $x_i \in \mathcal{X}$, and their associated parameters $(d^{L,R}, d^{L,I}, d^{U,R}, d^{U,I})$ in the constellation diagram.

$\bigcap_{l=1}^{K_{RB}} \{D_l \leq d\}$. Since the phase relationship is deterministic when conditioned on ϕ_1, the minimum distances (D_l) are conditionally independent. Therefore, marginalizing over the densities of $\mathbf{X}$, Φ, and simplifying equation (5.19), we obtain the desired result. ■

In the case of the i.i.d. interference phase model, all the underlying random variables are independent of each other. Dropping the subcarrier index for notational simplicity, the marginal distribution is obtained using results from order statistics of i.i.d. random variables, and can be written as

$$F_{D_{\max}}(d) = [F_D(d)]^{K_{RB}}, d \geq 0. \tag{5.20}$$

Marginal Distribution of Minimum Distance D

Based on their location w.r.t. the convex hull of the constellation, the transmitted symbols are classified as (a) interior points (denoted by set $\mathcal{X}_{\text{int}}$) and (b) boundary points (denoted by set $\mathcal{X}_{\text{bnd}}$), where $\mathcal{X}_{\text{bnd}} \cap \mathcal{X}_{\text{int}} = \emptyset$.

Fig. 5.3 illustrates the transformation of the baseband transmitted signal due to interference and noise. For a QAM scheme with average unit power per symbol, let $d_{\rfloor}$ be the minimum distance of each point in the constellation. If the nearest neighbor of y is $x^{(j)} \in \mathcal{X}_{\text{int}}$, then $0 \leq D \leq \frac{d_c}{\sqrt{2}}$. On the other hand, if $x^{(j)} \in \mathcal{X}_{\text{bnd}}$, then $0 \leq D \leq \infty$. For each $x \in \mathcal{X}$, we define its decision

Table 5.3: Decision region boundaries for constellation points of 16-QAM

$x_i \in \mathcal{X}_{\texttt{16QAM}}$	$d_{x_i}^{L,R}$	$d_{x_i}^{U,R}$	$d_{x_i}^{L,I}$	$d_{x_i}^{U,I}$
$\frac{1}{\sqrt{10}}(1+j)$	$-\frac{1}{\sqrt{10}}$	$\frac{1}{\sqrt{10}}$	$-\frac{1}{\sqrt{10}}$	$\frac{1}{\sqrt{10}}$
$\frac{1}{\sqrt{10}}(1+3j)$	$-\frac{1}{\sqrt{10}}$	$\frac{1}{\sqrt{10}}$	$-\frac{1}{\sqrt{10}}$	∞
$\frac{1}{\sqrt{10}}(3+j)$	$-\frac{1}{\sqrt{10}}$	∞	$-\frac{1}{\sqrt{10}}$	$\frac{1}{\sqrt{10}}$
$\frac{1}{\sqrt{10}}(3+3j)$	$-\frac{1}{\sqrt{10}}$	∞	$-\frac{1}{\sqrt{10}}$	∞
$\frac{1}{\sqrt{10}}(1-j)$	$-\frac{1}{\sqrt{10}}$	$\frac{1}{\sqrt{10}}$	$-\frac{1}{\sqrt{10}}$	$\frac{1}{\sqrt{10}}$
$\frac{1}{\sqrt{10}}(1-3j)$	$-\frac{1}{\sqrt{10}}$	$\frac{1}{\sqrt{10}}$	$-\infty$	$\frac{1}{\sqrt{10}}$
$\frac{1}{\sqrt{10}}(3-j)$	$-\frac{1}{\sqrt{10}}$	∞	$-\frac{1}{\sqrt{10}}$	$\frac{1}{\sqrt{10}}$
$\frac{1}{\sqrt{10}}(3-3j)$	$-\frac{1}{\sqrt{10}}$	∞	$-\infty$	$\frac{1}{\sqrt{10}}$
$\frac{1}{\sqrt{10}}(-1+j)$	$-\frac{1}{\sqrt{10}}$	$\frac{1}{\sqrt{10}}$	$-\frac{1}{\sqrt{10}}$	$\frac{1}{\sqrt{10}}$
$\frac{1}{\sqrt{10}}(-1+3j)$	$-\frac{1}{\sqrt{10}}$	$\frac{1}{\sqrt{10}}$	$-\frac{1}{\sqrt{10}}$	∞
$\frac{1}{\sqrt{10}}(-3+j)$	$-\infty$	$\frac{1}{\sqrt{10}}$	$-\frac{1}{\sqrt{10}}$	$\frac{1}{\sqrt{10}}$
$\frac{1}{\sqrt{10}}(-3+3j)$	$-\infty$	$\frac{1}{\sqrt{10}}$	$-\frac{1}{\sqrt{10}}$	∞
$\frac{1}{\sqrt{10}}(-1-j)$	$-\frac{1}{\sqrt{10}}$	$\frac{1}{\sqrt{10}}$	$-\frac{1}{\sqrt{10}}$	$\frac{1}{\sqrt{10}}$
$\frac{1}{\sqrt{10}}(-1-3j)$	$-\frac{1}{\sqrt{10}}$	$\frac{1}{\sqrt{10}}$	$-\infty$	$\frac{1}{\sqrt{10}}$
$\frac{1}{\sqrt{10}}(-3-j)$	$-\infty$	$\frac{1}{\sqrt{10}}$	$-\frac{1}{\sqrt{10}}$	$\frac{1}{\sqrt{10}}$
$\frac{1}{\sqrt{10}}(-3-3j)$	$-\infty$	$\frac{1}{\sqrt{10}}$	$-\infty$	$\frac{1}{\sqrt{10}}$

region $\mathcal{A}_x$ given by

$$\mathcal{A}_x = \{(z_x, z_y) | \Re(x) + d_x^{L,R} \leq z_x \leq \Re(x) + d_x^{U,R}, \Im(x) + d_x^{L,I} \leq z_y \leq \Im(x) + d_x^{U,I}\}, \quad (5.21)$$

where $\Re(x)$ denotes the real part and $\Im(x)$ the imaginary part of complex scalar x. The decision region parameters $d^{L,R}, d^{L,I}, d^{U,R}, d^{U,I}$ for constellation points in the first quadrant of 16-QAM are shown in Table 5.3 and illustrated in the right hand side of Fig. 5.3. In the following lemma, we derive the conditional distribution of $\{D|X, \Phi\}$.

Lemma 5.1. *Under the received signal model* $y = x + \sqrt{P_r}e^{j\phi} + n$*, the conditional distribution of*

$\{D|X,\Phi\}$ *is given by*

$$F_D(d|x,\phi)=\begin{cases}\sum\limits_{x^{(j)}\in\mathcal{X}}\left[1-Q_1\left(\frac{\sqrt{2}\nu_j}{\sigma_n},\frac{\sqrt{2}d}{\sigma_n}\right)\right] & \text{if } 0\le d\le\frac{d_c}{2}\\ \sum\limits_{x^{(j)}\in\mathcal{X}}\int\limits_0^d\int\limits_{\mathcal{A}_\theta(x^{(j)},z)}\frac{z}{\pi\sigma_n^2}e^{-\frac{z^2+\nu_j^2+2m_jz}{\sigma_n^2}}\mathrm{d}\theta\mathrm{d}z & \text{if } \frac{d_c}{2}<d\le\frac{d_c}{\sqrt{2}}\\ F_D\left(\frac{d_c}{\sqrt{2}}|x,\phi\right)+\sum\limits_{x^{(j)}\in\mathcal{X}_{\mathtt{bnd}}}\int\limits_0^d\int\limits_{\mathcal{A}_\theta(x^{(j)},z)}\frac{z}{\pi\sigma_n^2}e^{-\frac{z^2+\nu_j^2+2zm_j}{\sigma_n^2}}\mathrm{d}\theta\mathrm{d}z & \text{if } d>\frac{d_c}{\sqrt{2}}.\end{cases}\tag{5.22}$$

where $x=x_R+jx_I$, $m_j=m_{R,j}\cos\theta+m_{I,j}\sin\theta$, $\nu_j=(m_{R,j}^2+m_{I,j}^2)^{1/2}$, $m_{R,j}=x_R-x_R^{(j)}+\sqrt{P_r}\cos\phi$, $m_{I,j}=x_I-x_I^{(j)}+\sqrt{P_r}\sin\phi$, *and* $Q_M(a,b)$ *is the Marcum Q-function with parameters* M,a *and* b *[139]. The region of integration for* Θ *is given by* $\mathcal{A}_\theta(x^{(j)},z)=\left\{\theta\middle|d_{x^{(j)}}^{L,R}\le z\cos\theta\le d_{x^{(j)}}^{U,R},d_{x^{(j)}}^{L,I}\le z\sin\theta\le d_{x^{(j)}}^{U,I},0\le z\le d\right\}$.

Proof. Please refer Appendix B. ■

The distribution of D is obtained in equation (5.23) by marginalizing $\{D|X,\Phi\}$ over $\{X,\Phi\}$ to get

$$F_D(d)=\begin{cases}\frac{1}{2\pi|\mathcal{X}|}\sum\limits_{x\in\mathcal{X}}\sum\limits_{x^{(j)}\in\mathcal{X}}\int\limits_0^{2\pi}\left[1-Q_1\left(\frac{\sqrt{2}\nu_j}{\sigma_n},\frac{\sqrt{2}d}{\sigma_n}\right)\right]\mathrm{d}\phi, & \text{if } 0\le d\le\frac{d_c}{2},\\ F_D\left(\frac{d_c}{2}\right)+\sum\limits_{x\in\mathcal{X}}\sum\limits_{x^{(j)}\in\mathcal{X}}\int\limits_0^{2\pi}\int\limits_{\frac{d_c}{2}}^{d}\int\limits_{\mathcal{A}_\theta(x_j,z)}\frac{z}{2\pi^2|\mathcal{X}|\sigma_n^2}e^{-\frac{z^2+\nu^2+2m_jz}{\sigma_n^2}}\mathrm{d}z\mathrm{d}\theta\mathrm{d}\phi & \text{if } \frac{d_c}{2}\le d\le\frac{d_c}{\sqrt{2}}\\ F_D\left(\frac{d_c}{\sqrt{2}}\right)+\sum\limits_{x\in\mathcal{X}}\sum\limits_{x^{(j)}\in\mathcal{X}_{\mathtt{bnd}}}\int\limits_0^{2\pi}\int\limits_{\frac{d_c}{\sqrt{2}}}^{d}\int\limits_{\mathcal{A}_\theta(x_j,z)}\frac{z}{2\pi^2|\mathcal{X}|\sigma_n^2}e^{-\frac{z^2+\nu^2+2m_jz}{\sigma_n^2}}\mathrm{d}z\mathrm{d}\theta\mathrm{d}\phi & \text{otherwise.}\end{cases}\tag{5.23}$$

Using it in (5.20), we obtain the distribution of $D_{\mathtt{max}}$ under the i.i.d. interferer phase model.

Performance Metrics

To characterize the robustness and accuracy of the interference-plus-noise power estimate, we define the following metrics.

Definition 5.1. Overestimation probability, defined as $P_{\mathtt{overest}}(P_r,\sigma_n^2)=\mathbb{P}[D_{\mathtt{max}}\ge\sqrt{P_r+\sigma_n^2}]$, is the probability that $D_{\mathtt{max}}$ overestimates the interference-plus-noise compared to the average interference-plus-noise power.

Definition 5.2. Accuracy, defined as $\mathbb{P}\left[\left|\log_{10}\left(\frac{D_{\mathtt{max}}^2}{P_r+\sigma_n^2}\right)\right|\le\delta\right]$, is the probability that the estimate of interference-plus-noise-power lies within a range of $\pm\delta$ (dB) of the actual value.

A higher overestimation probability implies a more robust SINR estimate. As we will demonstrate in Section 5.5.2, SINR estimation using the proposed heuristic results in robust link adaptation in the presence of pulsed radar interference.

5.3.1 Numerical Results

Fig. 5.4a shows the theoretical and simulated distributions of $D_{\texttt{max}}$ for different values of P_r and σ_n^2, where 16-QAM modulated data symbols with a coherence block length of $K_{RB} = 12$ are used. We observe that there is an exact match between the theoretical and numerical results, validating the accuracy of equations (5.17)-(5.23). In order to study the estimation accuracy, mismatch in interference-plus-noise of the heuristic compared to that of the average interference-plus-noise power is plotted in Fig. 5.4b for 16-QAM symbols. We observe that the SINR mismatch in the interference-impaired OFDM symbol is within ± 5 dB for more than 90% of the range of typical SINR values (-5 to 30 dB) encountered in cellular communications. As in the case of most pulsed radar interference signals, at most a single radar pulse impacts a data block. In such scenarios, mismatch in the wideband SINR metric ($\hat{\gamma}_{\texttt{avg}}/\hat{\gamma}_{\texttt{e}}$) due to the robust heuristic will be partially mitigated by the availability of accurate pilot-aided SINR estimates for *interference-free OFDM symbols*. This aspect will be revisited in Section 5.4.

Fig. 5.4c shows the probability of overestimation as a function of (P_r, σ_n^2) for different QAM schemes. We observe that the robustness of the heuristic decreases when the modulation order progressively increases from QPSK to 64-QAM. Furthermore, $P_{\texttt{overest}}(P_r, \sigma_n^2) \geq 0.9$ for QPSK for all values of (P_r, σ_n^2). The key underlying factor for this trend relates to robustness of the heuristic when nearest-neighbor association fails to predict the transmitted symbol in presence of interference and noise. For a QAM scheme, robustness of the max-min heuristic under misclassification is determined by the following factors:

- Fraction of constellation points on the convex hull: If the transmitted symbol lies on the boundary, i.e. $x \in \mathcal{X}_{\texttt{bnd}}$, the received symbol y will have a high probability of lying outside the convex hull. If the nearest neighbor $x' \in \mathcal{X}_{\texttt{bnd}}$ also lies on the convex hull, then the misclassification penalty due to nearest-neighbor association will be partially mitigated, i.e. the ratio $\|y - x'\|_2 / \|y - x\|_2$ will be low on average. Hence, higher the value of $|\mathcal{X}_{\texttt{bnd}}|/|\mathcal{X}|$, the lower will be the misclassification penalty on average.
- Minimum distance of constellation: On the other hand, for any $x \in \mathcal{X}$, if the nearest neighbor lies within the convex hull i.e. $x' \in \mathcal{X}_{\texttt{int}}$, then a constellation with a higher minimum distance ($d_{\texttt{c}}$) will be more robust against misclassification. This is because $\|y - x'\| \leq d_{\texttt{c}}/2$, which means that constellations with a higher $d_{\texttt{c}}$ intrinsically have a higher probability of overestimating $\|y - x\|_2$, even in the case of misclassification.

Since QPSK (a) has the highest minimum distance of $d_{c,\texttt{QPSK}} = 1/\sqrt{2}$, and (b) has all points lying on the convex hull, the max-min heuristic is more robust when compared to that for 16-QAM and 64-QAM.

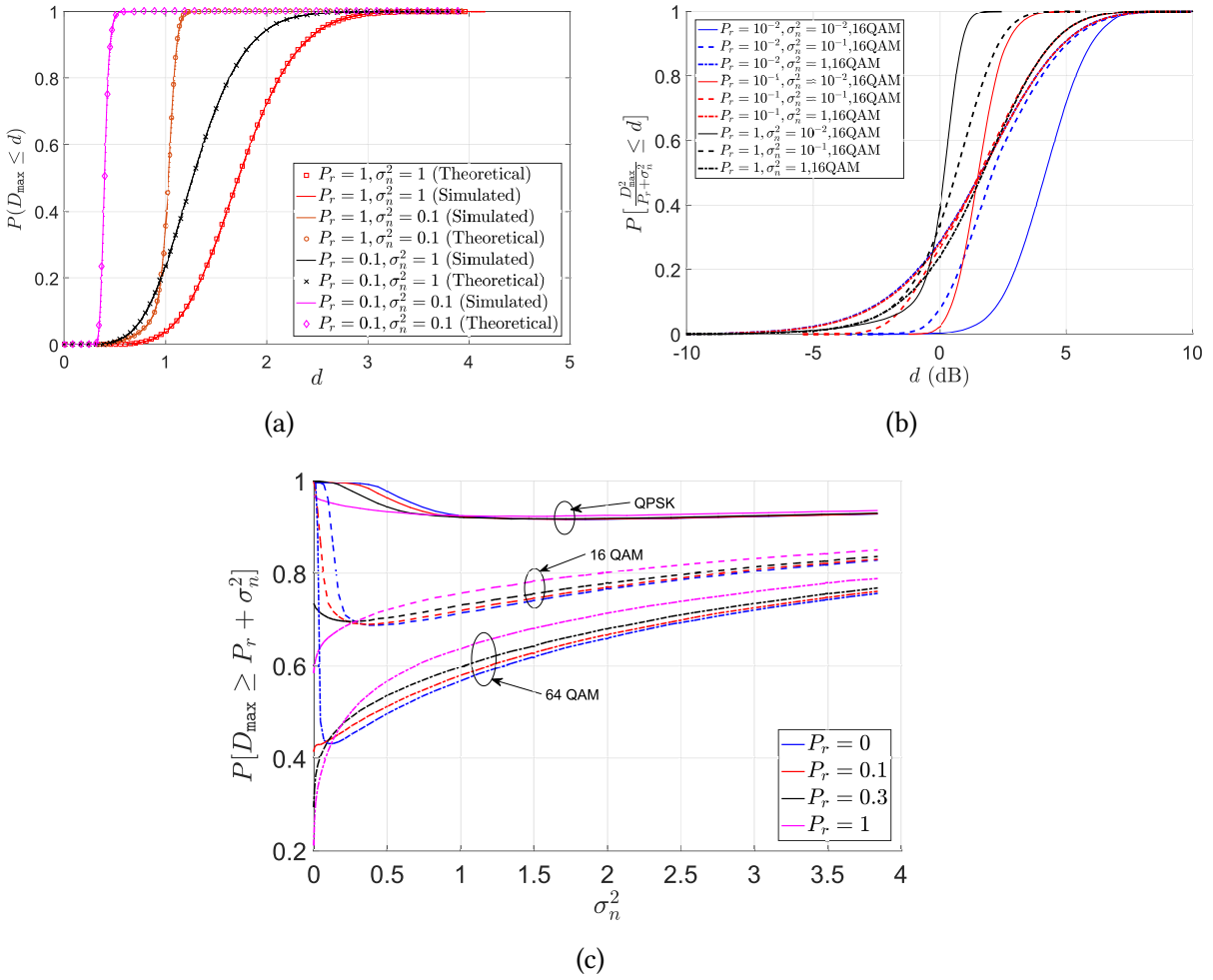

Figure 5.4: (a) Comparison of the simulated and theoretical distribution of $D_{\max}$ (equations (5.17))-(5.23) for 16-QAM, (b) distribution of $D_{\max}^2/(P_r + \sigma_n^2)$ for 16-QAM, and (c) probability of overestimation $P_{\texttt{overest}}(P_r, \sigma_n^2)$ for QPSK, 16-QAM and 64-QAM.

5.3.2 Accuracy and Robustness as a Function of K_{RB}

Robustness as a Function of K_{RB}

Intuitively, decreasing K_{RB} reduces the overestimation probability of the heuristic. This is formally proved in the following lemma.

Lemma 5.2. $\mathbb{P}[D_{\max} \geq \sqrt{P_r + \sigma_n^2}]$ *monotonically increases with* K_{RB}.

Proof. The overestimation probability can be represented using the PDF as $\mathbb{P}[D_{\max} \geq \sqrt{P_r + \sigma_n^2}] = 1 - F_{D_{\max}}(\sqrt{P_r + \sigma_n^2})$. In equation (5.18), if the phase relationship $\phi_l = h_l(\phi_1)$ is known for $l = 1, 2, \cdots, K_{RB}$, we have the following.

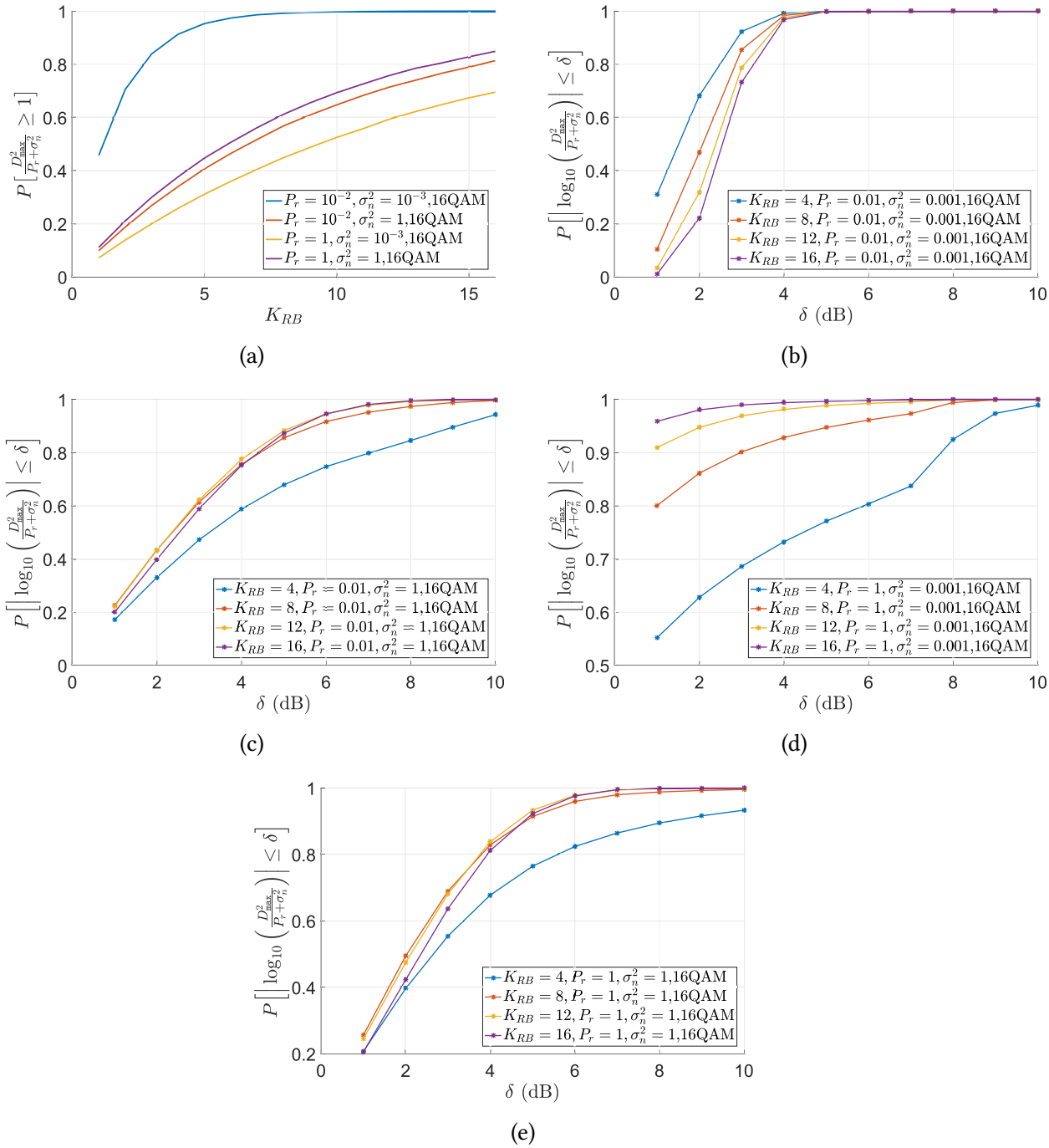

Figure 5.5: (a) $P_{\texttt{overest}}(P_r, \sigma_n^2)$ as a function of K_{RB}, and the accuracy metric for $K_{RB} \in \{4, 8, 12, 16\}$ for (b) $(P_r, \sigma_n^2) = (10^{-2}, 10^{-3})$, (c) $(P_r, \sigma_n^2) = (10^{-2}, 1)$, (d) $(P_r, \sigma_n^2) = (1, 10^{-3})$, and (e) $(P_r, \sigma_n^2) = (1, 1)$.

1. The term $\frac{1}{|\mathcal{X}|^{K_{RB}}}$ monotonically decreases with increasing K_{RB}, and
2. The product of conditional probabilities in the integral, $\prod_{l=1}^{K_{RB}} \left[\sum_{x_l \in \mathcal{X}} F_{D_l}(d|x_l, \phi_1) \right]$ monotonically decrease with increasing K_{RB}, since $0 \leq F_{D_l}(d|x_l, \phi_1) \leq 1 \; \forall \; l$.

Therefore, $(1 - F_{D_{\max}}(d))$ monotonically increases with increasing K_{RB} $\forall d \geq 0$. The desired result is obtained by letting $d = \sqrt{P_r + \sigma_n^2}$. ■

Fig. 5.5a shows the robustness (probability of overestimating interference-plus-noise-power) of the heuristic for 16-QAM as a function of K_{RB}, for different values of (P_r, σ_n^2), which corroborates the above lemma.

Accuracy as a Function of K_{RB}

Unlike the robustness metric, it is not straightforward to infer the dependence of accuracy on K_{RB} using mathematical arguments, due to the double-tailed nature of the metric in Definition 5.2. Hence, we use numerical studies to do investigate the dependence of accuracy on K_{RB}.

Figures 5.5b-5.5e show the accuracy as a function of δ (dB) for $K_{RB} \in \{4, 8, 12, 16\}$, for different values of (P_r, σ_n^2). We observe that (a) accuracy is not a monotonic function of K_{RB}, and (b) the optimal K_{RB} that maximizes the accuracy of the SINR estimate depends on (P_r, σ_n^2), as well as the accuracy threshold δ. In addition, we notice that

1. in high SINR regimes, a low K_{RB} ensures high accuracy (Fig. 5.5b),
2. in interference-limited scenarios (high P_r and low σ_n^2), a high K_{RB} value ensures high accuracy (Fig. 5.5d), and
3. in intermediate noise and interference conditions, a K_{RB} value of $8 - 16$ yields similar accuracy performance (Figs. 5.5c and 5.5e).

Similar trends are observed for QPSK and 64-QAM. Unfortunately, a comprehensive mathematical analysis of the accuracy is beyond the scope of this dissertation. The key takeaway from Figures 5.5b-5.5e is that there is no universal K_{RB} value that maximizes the accuracy of the heuristic-aided SINR estimate. However, memory-based schemes that leverage knowledge of interference and noise conditions in the recent past, can be used to choose K_{RB} to balance the robustness and accuracy of the heuristic-aided SINR estimate.

Remark 5.1. *It is worthwhile to observe that the max-min heuristic is independent on the physical layer waveform used, and yields robust SINR estimates as long as it is evaluated within a coherence block of the interfered signal.*

5.4 Semi-Blind/Hybrid Post-Equalizer SINR Estimation Framework

In this section, we describe the *'semi-blind/hybrid'* post-equalizer SINR estimation framework, which uses pilot-aided (Section 5.2.2) as well as heuristic-aided (Section 5.3) SINR estimates.

Let the data block contain $N_{\texttt{blk}}$ OFDM symbols[8], $\mathcal{A}_{NP} \subset \{1, 2, \cdots, N_{\texttt{blk}}\}$ be the set of non-pilot OFDM symbol indices in the data block, and $k \in \mathcal{K}[m]$ be the subcarrier indices of data resource elements in the m^{th} OFDM symbol, where $m = 1, 2, \cdots, N_{\texttt{blk}}$. As we observed in Fig. 5.1, pilot-aided SINR estimates are accurate (a) if pilot resources are impaired by interference, or (b) in the absence of interference. Therefore, the SINR of the $(n,k)^{th}$ RE can be estimated using

$$\hat{\gamma}[n,k] = \begin{cases} \hat{\gamma}_p[n,k] & \text{for } n = 1, 2, \cdots, N_{\texttt{blk}}, \mathbb{1}[n], \text{ and } n \notin \mathcal{A}_{NP} \\ \hat{\gamma}_p[n,k] & \text{if } n \neq m, \mathbb{1}[m], \text{ and } m \in \mathcal{A}_{\mathcal{NP}} \\ \frac{1}{D_{\texttt{max}}[m,k]} & \text{if } \mathbb{1}[n], \text{ and } n \in \mathcal{A}_{NP}, \end{cases} \tag{5.24}$$

where $\mathbb{1}[m]$ denotes the occurrence of pulsed radar interference on the m^{th} OFDM symbol, $D_{\texttt{max}}[m,k]$ is the heuristic for every RE in the coherence block of the contaminated OFDM symbol. If the coherence block contains K_{RB} subcarriers, then $D_{\texttt{max}}[m, lK_{RB}+1] = \cdots = D_{\texttt{max}}[m,(l+1)K_{RB}]$ for $l \in \mathbb{Z}$. Using equation (5.9), the wideband SINR metric can be calculated to determine the CQI for each data block.

However, to determine the appropriate SINR estimate to be used, the contaminated OFDM symbol needs to be known. As shown in Fig. 5.2, the following intermediate stages are necessary to acquire this information in practice:

1. Pulsed radar parameter estimation,
2. Detection of the pilot symbol interference, and
3. Detection of contaminated OFDM symbol index.

In the following, we describe each of these stages in more detail.

5.4.1 Pulsed Radar Parameter Estimation

Most pulsed radars have a fixed repetition interval ($T_{\texttt{rep}}$) for an extended duration of time (timescale of seconds). Since the interference is periodic, $T_{\texttt{rep}}$ can be estimated by applying Fourier techniques on time-series data of received power per data block, resulting in a low-complexity baseband implementation. Other techniques based on time-of-arrival monitoring of radar pulses [115], [140] can also be used to estimate the radar repetition rate.

[8] In LTE and NR, the data block is termed as the transport block, which is often sent over a subframe consisting of 14 OFDM symbols.

Using the value of the estimate $\hat{T}_{\texttt{rep}}$, the UE can predict future subframes indices which will be impaired by pulsed radar interference.

5.4.2 Threshold-based Detection of Pilot Interference

Interference on pilot symbols result in accurate SINR estimates [73]. Pilot interference can be detected by monitoring pilot-aided SINR estimates in every data block. Hence, for the k^{th} data block, the receiver calculates the wideband SINR metric $\hat{\gamma}_{\texttt{avg},p}[k]$ using pilot-aided methods. Using estimates of $\hat{T}_{\texttt{rep}}$ (Section 5.4.1) and pilot-aided SINR estimates of previous data blocks, the wideband SINR metric for non-pilot radar interference ($\hat{\gamma}_{\texttt{NPI},p}$) is computed. If the current (k^{th}) block is impaired by interference, then

1. if $\hat{\gamma}_{\texttt{NPI},p} - \hat{\gamma}_{\texttt{avg},p}[k] \geq \gamma_{\texttt{th}}$, the k^{th} block is considered to be impaired by pilot interference, and
2. if $\hat{\gamma}_{\texttt{NPI},p} - \hat{\gamma}_{\texttt{avg},p}[k] < \gamma_{\texttt{th}}$, the k^{th} block is considered to be impaired by non-pilot interference.

In practice, a typical value of the threshold is $\gamma_{\texttt{th}} = 1$ dB, since the channel quality indicator (CQI) remains the same with a high probability for a SINR mismatch of ± 1 dB [128].

5.4.3 Log Likelihood-based Detection of the Interference-Impaired OFDM Symbol

OFDM has a long symbol duration (72 μs in sub-6 GHz bands of LTE and NR). Hence, for wideband radars with a short pulse width ($T_{\texttt{pul}} \sim 1$ μs), the probability of two adjacent OFDM symbols being contaminated is *almost zero*[9] for sub-6 GHz cellular systems. Therefore, we ignore the possibility of multiple adjacent OFDM symbols being interfered.

We use a log likelihood-based algorithm to detect the contaminated data-bearing OFDM symbol in every block, which is executed when pilots are detected to be interference-free (Section 5.4.2). Algorithm 4 shows the proposed approach if the estimated $T_{\texttt{rep}}$ indicates a single radar pulse within the data block[10]. The empirical log likelihood function models the absence of interference ($P_r = 0$) and impairment only due to noise, and is calculated for each non-pilot OFDM symbol.

Intuitively, the cost function in equation (5.25) detects the contaminated OFDM symbol due to the following factors:

[9] In sub-6 GHz systems, the typical cyclic prefix duration is $5 - 10$ μs. A radar pulse time-aligned with *two consecutive OFDM symbols* will lie within the cyclic prefix (CP) of the second symbol. Due to CP removal in OFDM, radar interference will not impact the second OFDM symbol in such scenarios.

[10] If $T_{\texttt{rep}}$ estimates indicate that m radar pulses will impair the data block, then Algorithm 4 outputs indices corresponding to the m least values.

Algorithm 4 Detection of Corrupted OFDM Symbol Index

1: **Input:** In each data block,
Set of non-pilot OFDM symbol indices $\mathcal{A}_{NP}$
Data subcarriers of n^{th} *OFDM symbol* $\mathcal{K}[n]$
Post-processed OFDM symbols $y[n,k]\ \forall\ n \in \mathcal{A}_{NP}, k \in \mathcal{K}[n]$
2: Find nearest neighbor of each $y[n,k]$ using $\hat{x}_{\mathtt{nn}}[n,k] = \arg\min_{x\in\mathcal{X}} \|y[n,k]-x\|_2\ \forall\ n \in \mathcal{A}_{NP}, k \in \mathcal{K}[n]$.
3: For each (n,k), obtain the pilot-aided SINR $\hat{\gamma}_p[n,k]$ using (5.8).
4: The contaminated OFDM symbol index ($\hat{n}$) is detected by minimizing the log-likelihood function using

$$\hat{n} = \arg\min_{n\in\mathcal{A}_{NP}} \frac{-1}{|\mathcal{K}[n]|} \sum_{k\in\mathcal{K}[n]} \hat{\gamma}_p[n,k]|y[n,k]-\hat{x}_{\mathtt{nn}}[n,k]|^2. \tag{5.25}$$

5: Go back to step 1 in the next data block.

1. interference-free symbols statistically have a smaller nearest neighbor distance when compared to impaired symbols, and

2. in a coherence block, pilot-aided SINR estimates are almost constant for all REs. As a result, the proposed cost function has a high probability of accurately detecting the impaired OFDM symbol.

5.4.4 SINR Estimation Using Data Block Reconstruction

If the transmitted symbols are known, then the post-equalizer SINR can be estimated at the receiver perfectly. If $x[n,k] \in \mathcal{X}$ is the transmitted symbol on RE $(n,k) \in \mathcal{D}$, and $y[n,k]$ is the corresponding post-processed received symbol. The post-processing SINR of RE (n,k) can be directly estimated using

$$\gamma[n,k] = \frac{|x[n,k]|^2}{|x[n,k]-y[n,k]|^2}, \tag{5.26}$$

and the correspond wideband SINR metrics ($\hat{\gamma}_{\mathtt{avg}}$ or $\hat{\gamma}_{\mathtt{e}}$) can be estimated using (5.9). But $x[n,k]$ can seldom be accurately estimated in the presence of noise and interference. However, it can be perfectly reconstructed if the *post-decoder bit sequence is known to be accurate.*

If $\mathbf{b}$ represents the data bits after turbo-decoding, the receiver can reconstruct the transmitted data symbol on each RE by implementing the transmitter baseband processing chain[11]. However, perfect reconstruction is guaranteed only when $\mathbf{b}$ is accurate. In LTE and NR, the integrity of $\mathbf{b}$ is ensured using a cyclic redundancy check (CRC) at the end of each data block, where CRC $= 0$ (1)

[11]Since 3GPP standardization documents are publicly available [141], it is possible for the receiver to implement the transmitter processing chain if the appropriate control information is decoded correctly.

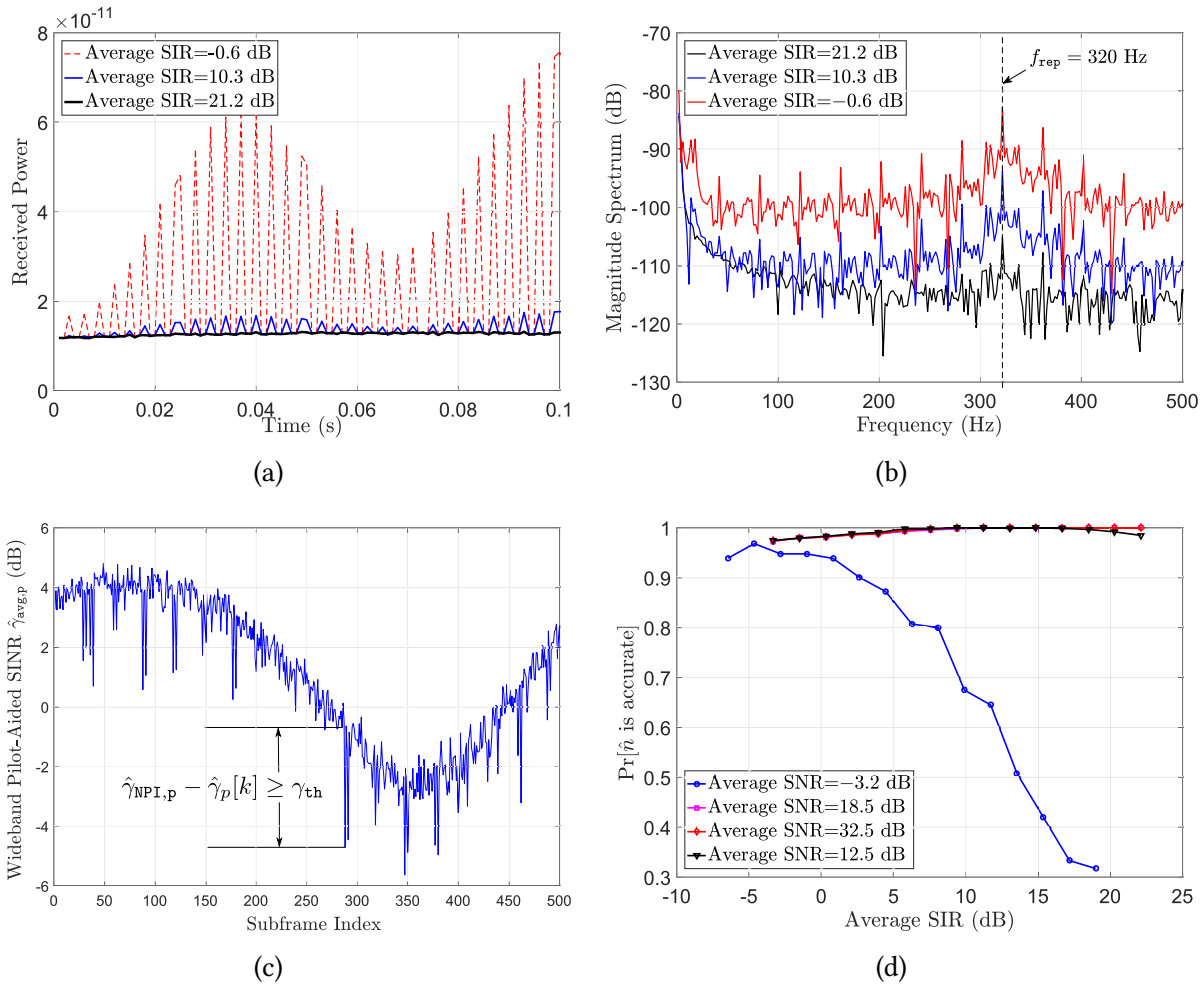

Figure 5.6: Performance of various stages of the hybrid post-equalizer SINR estimation framework: (a) received power per subframe in the LTE downlink with average SNR $= 19.5$ dB, (b) corresponding amplitude spectrum of the received power per subframe for a window length of 500 points, (c) illustration of the threshold-based pilot contamination detection with $\gamma_{\texttt{th}} = 1$ dB when average SNR $= -0.2$ dB, (d) probability of accurate *contaminated symbol* detection.

indicates decoding success (failure). Since an n-bit CRC has a false positive rate of 2^{-n}, (where $n = 24$ in LTE and NR [2]), we use the CRC as an indicator to accurately reconstruct $x[n,k]$ in our proposed framework.

Remark 5.2. *If $x_{\texttt{nn}}[n,k]$ is the nearest neighbor of $y[n,k]$, then $|x[n,k] - y[n,k]|^2 \geq |x_{\texttt{nn}}[n,k] - y[n,k]|^2$. For constant envelope modulation schemes, post-equalizer SINR estimated using the nearest neighbor decision rule forms an upper bound to the actual SINR. In other QAM schemes, nearest neighbor association often overestimates the SINR.*

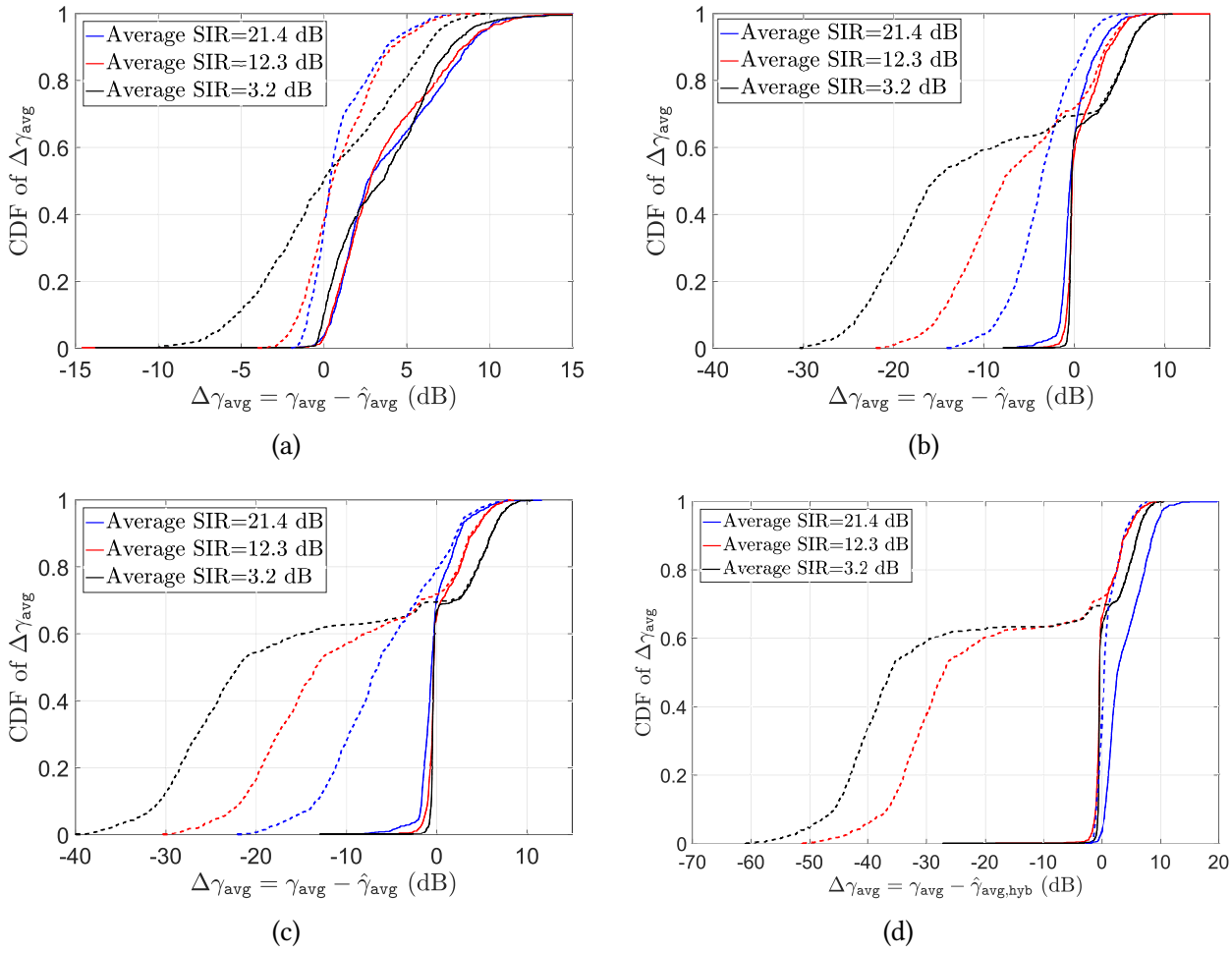

Figure 5.7: Comparison of the average SINR metric mismatch ($\Delta\gamma_{\text{avg}}$ (dB) $= \gamma_{\text{avg}}$ (dB) $- \hat{\gamma}_{\text{avg}}$ (dB)) for interference-impaired subframes using the proposed framework (in solid lines) and the pilot-aided method (in dashed lines) using equation (5.8), when (a) average SNR $= -0.2$ dB, (b) average SNR $= 13.8$ dB, (c) average SNR $= 19.5$ dB, and (d) average SNR=33.8 dB.

5.4.5 Numerical Results

In this subsection, we show the performance results of the proposed SINR estimation framework. We consider the example of the LTE-A Pro downlink sharing spectrum with a linear frequency modulated pulsed radar with the transmitted waveform shown in equation (5.2), and the other system parameters shown in Table 5.1. In addition, the assumptions used to analytically characterize the heuristic performance in Section 5.3 are relaxed in the numerical results presented below.

Fig. 5.6a shows the downlink received power in every subframe. The corresponding windowed FFT computed using a window length of 500 subframes is shown in Fig. 5.6b. We observe that

the amplitude spectrum can accurately estimate $f_{\texttt{rep}} = \frac{1}{T_{\texttt{rep}}}$ for a wide range of SIR values.

Fig. 5.6c illustrates the threshold-based pilot contamination detection method described in Section 5.4.2. Using $f_{\texttt{rep}}$ and memory of received power per subframe in the recent past, the pilot-aided wideband SINR ($\hat{\gamma}_{\texttt{NPI},p}$) is calculated for *interference-free subframes*[12], and compared to pilot-aided SINR estimated in the current subframe. As mentioned earlier, a threshold of $\gamma_{\texttt{th}} = 1$ dB is chosen, since variations greater ± 1 dB will result in use of a different MCS [128].

Fig. 5.6d shows the performance of Algorithm 4, for different values of SINR. At low SNR, we observe that the accuracy of the proposed method improves with increasing INR when the interference power rises above the noise floor. For medium to high SNRs, the probability of accurate detection is greater than 95%, indicating reliable detection performance for a wide range of SIR and INR values.

Fig. 5.7a-5.7d compares SINR estimation performance of the proposed framework ($\hat{\gamma}_{\texttt{avg,hyb}}$) with the pilot-aided method ($\hat{\gamma}_{\texttt{avg,p}}$) *for interference-impaired subframes*. The distribution of the average SINR mismatch $\Delta\gamma_{\texttt{avg}} = (\gamma_{\texttt{avg}} - \hat{\gamma}_{\texttt{avg}})$, for a wide range of SNR and INR conditions are plotted, where negative $\Delta\gamma_{\texttt{avg}}$ values indicate overestimated SINR values. We observe that pilot-aided methods have a high probability of negative $\Delta\gamma_{\texttt{avg}}$ values, that results in degradation of link adaptation performance. In contrast, the proposed framework improves the SINR estimation performance for a large range of SNR and INR values. In the low SNR-high SIR regime, we observe that the proposed framework underestimates the SINR with a probability higher than 95%. This trend can be attributed to the robustness of the heuristic in QPSK, which is typically used in low SINR conditions. In other SNR and SIR regimes, we observe that the semi-blind wideband SINR estimate (a) lies within ± 5 dB of the true value for more than 80% of the subframes, and (b) is skewed towards conservative SINR (positive $\Delta\gamma_{\texttt{avg}}$ value) estimates. As we will demonstrate in the Section 5.5.2, *robust SINR estimates* obtained using the proposed framework significantly improves link-level performance in hostile spectrum sharing environments. However, these improvements are dependent on the availability of accurate SINR estimates for both interference-impaired and interference-free subframes. An explicit scheme to ensure the availability of accurate CSI for both channel states is presented in the next section.

5.5 Dual CSI Feedback

As discussed in Section 5.2.3, current cellular standards support limited CSI feedback of a single set $CSI = \{CQI, \mathbf{W}\}$. While this mechanism is efficient in conventional cellular deployments where interference is homogeneously distributed on all REs, the presence of pulsed radar interference in a spectrum sharing scenario results in two channel states:

1. the fading channel, in interference-free data blocks, and

[12] If $T_{\texttt{rep}}$ is smaller than the subframe duration, then the received power of *each OFDM symbol* needs to be used to estimate $f_{\texttt{rep}}$, and detect pilot contamination.

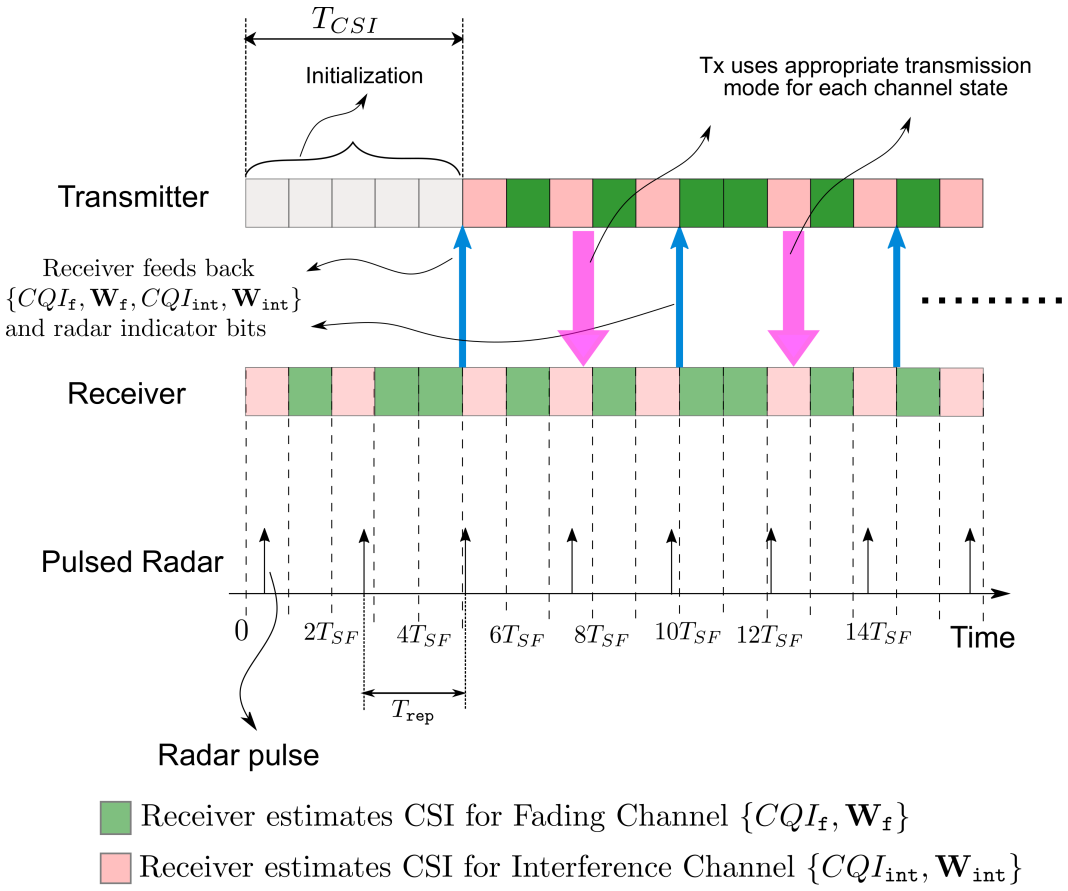

Figure 5.8: Illustration of the dual CSI feedback scheme for $T_{CSI} = 5T_{SF}$, where T_{SF} denotes the duration of each data block. The receiver periodically feeds back the CSI for both channel states $(CQI_{\mathtt{f}}, \mathbf{W}_{\mathtt{f}}, CQI_{\mathtt{int}}, \mathbf{W}_{\mathtt{int}})$, and the radar indicator bits.

2. the interference-impaired channel, when the pulsed radar is present.

Clearly, a single set of quantized CSI cannot accurately approximate a bimodal channel distribution. In order to handle the additional state in radar-cellular spectrum sharing, we propose *'dual CSI feedback'*, where each user periodically feeds back the quantized CSI for both channel states.

5.5.1 Feedback Requirements

In the CSI reporting interval, each user feeds back the set $CSI_{\mathtt{dual}} = \{CQI_{\mathtt{f}}, \mathbf{W}_{\mathtt{f}}, CQI_{\mathtt{int}}, \mathbf{W}_{\mathtt{int}}\}$, where the subscript `f` (`int`) refers to the CSI of the fading (interference-impaired) channel states respectively.

In addition, the transmitter must know the presence of radar interference in advance, to use the optimal transmission mode for future data blocks. This is enabled by *radar indicator* feedback,

which indicates the presence or absence of pulsed radar in each data block, for the *next* T_{CSI} *data blocks*. The receiver can predict the presence of radar interference in a future data block by estimating $\hat{T}_{\texttt{rep}}$ and monitoring the indices of corrupted OFDM symbols, as discussed in Sections 5.4.1 and 5.4.3. However, it is worthwhile to note that *radar indicator feedback from a single designated user* is enough for the transmitter to know the indices of future corrupted data blocks. Fig. 5.8 shows a schematic of the dual CSI feedback scheme, where the *initialization procedure* is used to obtain estimates of $T_{\texttt{rep}}$ and $CSI_{\texttt{dual}}$ for the first time.

Assuming a data block duration of $T_{SF} = 1$ ms, if the CSI reporting interval is T_{CSI}, then radar indicator feedback consumes $b_{\texttt{rad}}$ bits of feedback per CSI reporting interval, where $\lceil \log_2(T_{CSI}) \rceil \leq b_{\texttt{rad}} \leq T_{CSI}$ bits. If the number of active users in the cell is $N_{\texttt{act}}$, the total additional feedback overhead is $b_{\texttt{int}} = (N_{\texttt{act}} N_{\texttt{int}} + b_{\texttt{rad}})$ bits, where $N_{\texttt{int}}$ is the number of additional bits necessary to convey CSI for the interference-impaired channel state. If $\mathbf{W} \in \mathcal{W}$ and $CQI \in \mathcal{C}$, then $N_{\texttt{int}} \geq \left\lceil \log_2 |\mathcal{C}| + \log_2 |\mathcal{W}| \right\rceil$ bits, and the corresponding rate overhead is $R_{\texttt{int}} = \frac{N_{\texttt{act}} b_{\texttt{int}}}{T_{CSI}}$ bps.

5.5.2 Link-Level Performance Improvements

In this subsection, we compare the performance of the *hybrid SINR estimation-dual CSI feedback* framework (henceforth referred to as the 'proposed framework') with the *pilot-aided SINR estimation-single CSI feedback* scheme (henceforth referred to as the 'conventional scheme'). We developed a 3GPP-compliant link-level simulator to analyze radar-LTE coexistence scenarios, using the MATLAB LTE/NR toolboxes™, using the system parameters shown in Table 5.1. For the conventional scheme, we consider (a) mininum CSI feedback, (b) median CSI feedback, and (c) and maximum CSI feedback schemes that were described in section 5.2.3.

Fig. 5.9 compares the link-level performance of the proposed framework with the conventional scheme. Fig. 5.9a shows the throughput as a function of the average INR when the average SNR $=$ 19.5 dB. We observe that our proposed framework achieves a $30\% - 100\%$ rate enhancement when compared to median and maximum CSI feedback, and a $47\% - 225\%$ rate enhancement compared to minimum CSI feedback. In addition, we also observe that our framework achieves $74\% - 96\%$ of the maximum achievable rate over a wide range of INR values, demonstrating a high utilization of the channel capacity.

It is important to observe that the rate improvement due to the proposed framework balances the BLER constraints as shown in Fig. 5.9b, where BLER ≤ 0.1 for INR ≤ 12 dB. Interestingly, the BLER performance at high INR improves significantly when compared to minimum CSI feedback, the most conservative conventional scheme. As expected, median and maximum CSI feedback always result in a higher BLER compared to minimum CSI feedback. This is because it requires a higher number of interference-impaired pilots per estimation window to mimic the performance of minimum CSI feedback.

High BLER due to decoding failures result in degradation of the *HARQ-induced latency*, which

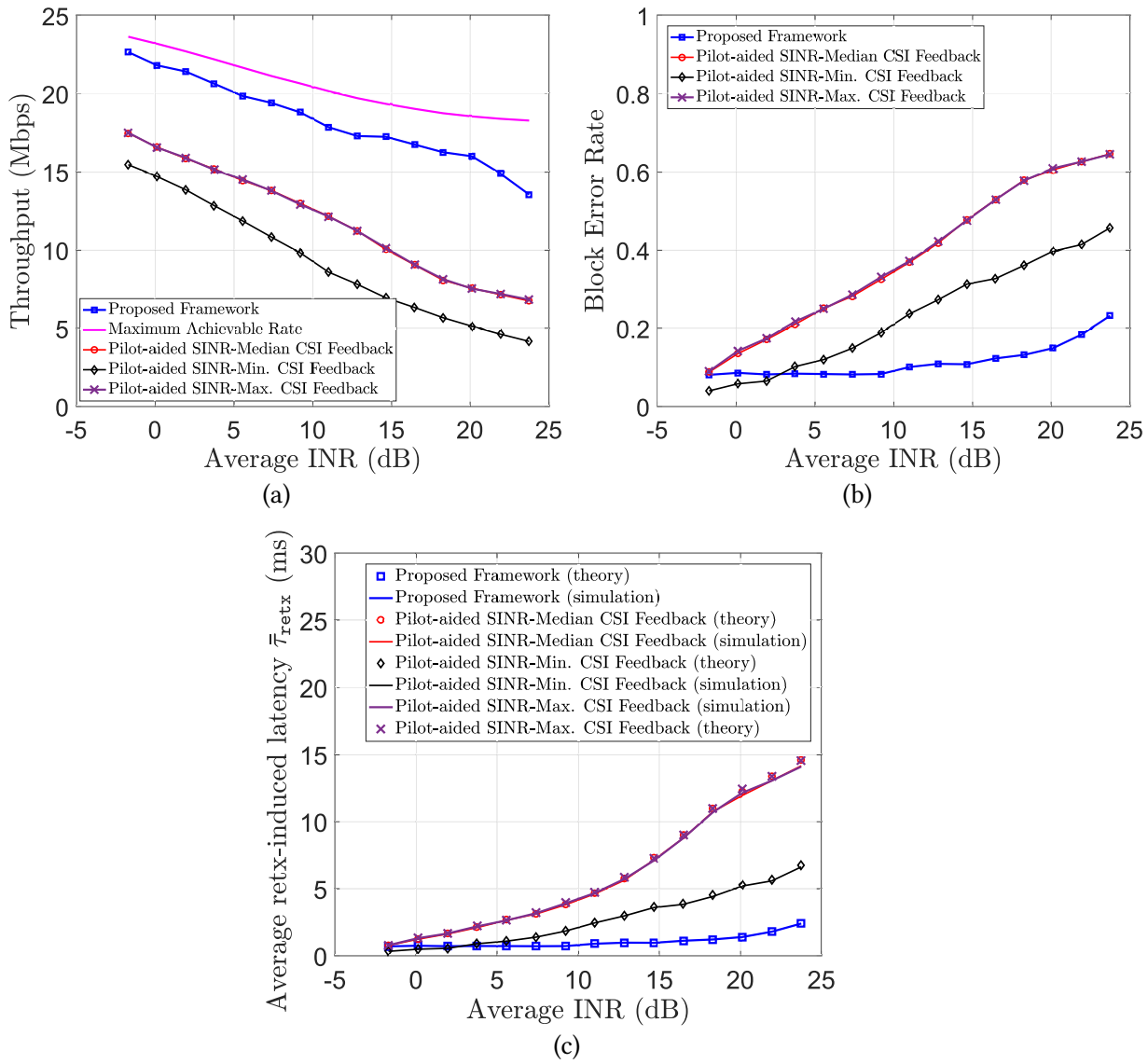

Figure 5.9: Enhancement of (a) throughput, (b) block error rate, and (c) retransmission-induced latency performance, using the proposed hybrid SINR estimation and Dual CSI feedback framework. The average SNR is 19.5 dB.

was defined in Section 3.4 and is approximately given by

$$\bar{\tau}_{\texttt{retx}} = \frac{\texttt{BLER} \times \bar{\tau}_{\texttt{wait}}}{1 - \texttt{BLER}}. \tag{5.27}$$

$\bar{\tau}_{\texttt{wait}}$ is the average wait time between consecutive retransmissions. We assume $\bar{\tau}_{\texttt{wait}} = 8$ ms, which is the typical value in LTE and NR [2], [37]. Fig. 5.9c shows that the proposed framework improves retransmission induced latency by a factor of 3 when compared to minimum CSI feed-

back, and by an order of magnitude when compared to median and maximum CSI feedback. In addition, we observe that the theoretical and simulation values are in good agreement.

In LTE and NR, CSI feedback for single-user transmission modes has a overhead of about $b_{\texttt{fb}} = 10$ bits per CSI estimation interval (T_{CSI}), where $T_{CSI} \geq 2$ ms [2], [37]. Therefore, in a cell with $N_{\texttt{act}} = 100$ active users, the additional rate overhead due to dual CSI feedback will satisfy $r_{\texttt{int}} \leq \frac{100\times(10)}{2\times10^{-3}} + \frac{1}{1\times10^{-3}} = 510$ kbps.

In summary, the proposed framework simultaneously improves throughput, BLER, and latency performance when compared to conventional schemes in the presence of pulsed radar interference. For most operational regimes, the aggregate downlink throughput improvement is significantly high to justify the use of dual CSI feedback. For MU-MIMO transmission modes in NR that typically need 100 bits/user/CSI estimation interval [2], further investigation is needed to evaluate the performance achieved using our framework. In general, dual CSI feedback is beneficial if the *cell-wide throughput gain* is greater than the additional uplink rate overhead.

5.6 Conclusion

In this chapter, we developed a comprehensive semi-blind SINR estimation framework using pilot-aided and heuristic-aided estimates to compute the wideband post-equalizer SINR in radar-cellular coexistence scenarios. We characterized the distribution of a low complexity max-min heuristic under a tractable signal model, and demonstrated its accuracy and robustness for interference-impaired QAM data symbols. To handle channel bimodality due to periodic transitions between the *fading* and the *interference-impaired* channel states, we proposed a *dual CSI feedback* mechanism where the receiver reports quantized CSI for both channel states. Unifying these two schemes and using radar-LTE-A Pro coexistence as an example, we demonstrated significant improvements in key link-level performance metrics such as throughput, BLER and retransmission-induced latency *simultaneously*.

This framework is useful in vehicular communication systems such as C-V2X, link adaptation decisions need to be taken at a faster timescale due to the highly dynamic wireless channel. Co-channel or adjacent channel pulsed radar interference inhibits accurate CSI acquisition, which adversely impacts the rate and latency performance of a vehicular link. The semi-blind SINR estimation and dual CSI feedback framework proposed in this chapter addresses the issue of accurate CSI acquisition in the presence of such wideband intermittent interference signals. Further, the low computational complexity and low overhead of the proposed framework promises a high potential for being effective in dynamic channel conditions, and hence is attractive for implementation in vehicular communication systems sharing spectrum with a high-powered radar.

Investigation of the optimal SU- and MU-MIMO precoder estimation in non-pilot interference is a useful extension to this work, which is especially important in multi-antenna transmission modes of LTE-A Pro and 5G NR. In addition, novel scheduling and resource management schemes based on this framework can also be developed for different applications such as vehicular-to-

everything (V2X) and Internet of Things (IoT) services coexisting with radar. Such scenario-specific frameworks will be of practical importance to enable efficient link adaptation mechanisms in radar-5G/6G coexistence since rate and latency performance often need to be jointly optimized in these scenarios.

Part III

Fundamentals of Underlay Radar-Massive MIMO Spectrum Sharing Scenarios

Chapter 6

Tractable Characterization of Radar Performance in Underlay Spectrum Sharing Scenarios with Massive MIMO Cellular Downlink

6.1 Introduction

Over the last few years, wireless networks have evolved across all layers in order to meet the ever-increasing demand for user data. At the physical layer, technologies such as spectrum sharing [144] and massive MIMO [4] have been investigated by academia and the industry to boost the spectral efficiency by an order of magnitude in comparison to the previous generation.

Massive MIMO boosts the spectral efficiency by multiplexing multiple spatially-distributed users on the same time-frequency resources using large antenna arrays. Pioneering research by industry and academia on the fundamental aspects [4], [5], real-world channel measurements [6], prototyping [8] and standardization [9], has led to the deployment of massive MIMO technologies in the Third Generation Partnership Project (3GPP) Long-Term Evolution-Advanced Pro (LTE-A Pro) [145] and 5G New Radio (NR) wireless networks.

On the other hand, spectrum sharing schemes improve spectral utilization among multiple wireless technologies and services sharing the same frequency band. In the United States, regulatory support through the Federal Communications Commission's (FCC) ratification of spectrum sharing rules for the 3.5 GHz [21] and 5 GHz [22] frequency bands has incentivized network providers to deploy in these bands. Concurrently, the wireless industry's standardization efforts have led to design of cellular networks for operating in unlicensed and shared frequency bands through technologies such as License Assisted Access (LAA) [24] and 5G New Radio-Unlicensed (5G NR-U)

This chapter is based on the works presented in [142], [143].

[102]. Spectrum sharing is particularly attractive in the congested sub-6 GHz frequency bands, where radar systems are the biggest consumer of radio spectrum. Underlay spectrum sharing is a popular method because it allows sharing without explicit coordination, where the establishment of an exclusion zone limits cellular (secondary user) interference to the radar (primary user) below the desired interference threshold, often in the absence of cooperation between the sharing entities. It is fundamentally important to evaluate the impact of the worst-case interference scenario for radar and cellular systems, because of the lack of coordination. Since modern radar and cellular antenna arrays are capable of 3D beamforming, it is necessary to incorporate it into the system model. Unfortunately, systematic modeling of 3D beamforming in the study of large-scale spectrum sharing systems is overlooked in current works. In this chapter, we bridge this knowledge gap by (a) methodically incorporating 3D beamforming capabilities of the radar and massive MIMO BSs in our system model, and (b) comprehensively evaluating the impact of worst-case cellular interference on radar performance metrics, as a function of key deployment parameters.

6.1.1 Related Work

Prior works have considered different approaches to radar-cellular coexistence, which can be broadly classified under:

- Multi-antenna techniques: These leverage the additional spatial degrees of freedom to mitigate mutual interference between the radar and cellular system [121], [146], [122], [120].
- Waveform design: The waveform of the radar [124], [123] and cellular system [125], [126] can be designed to enhance resilience of the receiver to interference.
- Opportunistic spectrum sharing: These schemes improve the secondary system (cellular) performance by exploiting information of the temporal/spectral/spatial variation of primary user interference [14], [17].

Accurate channel state information (CSI) is crucial for multi-antenna techniques to be effective, for which cooperation schemes such as common knowledge of radar and cellular probing waveforms is necessary [105]. However, security concerns make cooperation impossible with military and air traffic control radar systems, which occupy a significant portion of sub-6 GHz bands. Meanwhile, the adoption of interference-resilient waveforms has been very slow, since they require significant modifications to both systems, making their mass deployment infeasible in the near future. While opportunistic spectrum access is feasible in the case of rotating radars in the 'search mode' [14], it is not possible for all base stations to operate when the radar is tracking a target. In the absence of cooperation, a static exclusion zone is defined around the radar to limit cellular interference below a predefined threshold.

To accurately analyze the impact of cellular interference on radar performance metrics, it is important to consider a large-scale cellular network. While system-level simulators are often used

to study such networks, their high complexity result in very lengthy execution times, and it is difficult to benchmark them and extract fundamental insights. Due to its analytical tractability, stochastic geometry has recently become a useful tool to analyze large scale behavior of spectrum sharing scenarios such as LTE-WiFi coexistence [147], [148], [149], radar-WiFi coexistence [12], [150], cellular-D2D coexistence [151], [152] and UAV-D2D coexistence scenarios [153], [154].

In radar-cellular coexistence where both systems are equipped with 3D beamforming capabilities [9], modeling the impact of azimuth as well as elevation beamforming gains are crucial to accurately model the received interference power. However, most of the prior work in stochastic geometry consider uniform linear arrays with *only azimuth beamforming capabilities*, and the beamforming pattern is approximated by a piecewise constant function, often obtained from the main lobe and the two side lobe gains [155], or the exact beamforming pattern [12], [150]. Even though some recent works account for the 3D beamforming capabilities in their analysis, the models does not allow for analytical treatment [156], [157], or focus on fixed downtilt scenarios for optimal coverage in multi-cellular networks [158], [159].

6.1.2 Contributions

In this chapter, we develop a novel and tractable analytical framework to analyze radar performance metrics in a radar-massive MIMO spectrum sharing scenario. We consider a single radar system located at the origin, tracking a target above the horizon using a single beam from a uniform rectangular array (URA). The radar is surrounded by massive MIMO BSs, which are distributed as a homogeneous Poisson point process (PPP). All BSs are equipped with a URA mounted at the same height w.r.t. each other, where each BS is serving multiple users in its cell using hybrid 3D beamforming [5]. Here, beamforming is accomplished in two cascaded stages: analog beamforming that forms user groups, followed by digital beamforming that suppresses multi-user interference. A circular exclusion zone (EZ) is established around the radar, and only the BSs lying outside the EZ are allowed to operate as long as the total interference power lies below a specified threshold.

Worst-Case Average Interference Power

Massive MIMO BS operations result in the worst-case interference for the radar when they serve edge users located in the general direction of the radar. However, incorporating elevation beamforming into the stochastic geometry framework is challenging, since Voronoi cells of the BSs can be arbitrarily large. To overcome this, we devise a novel formulation based on the circumradius distribution of the Voronoi cell [160], termed as the *Circumcircle-based cell (CBC) model*. In addition, the presence of sidelobes result in a beamforming gain pattern that is a non-monotonic function of the elevation angle. We derive an upper bound on the beamforming gain that monotonically decreases with increasing elevation angle, which is crucial to deriving the upper bound on the worst-case average interference. To develop a tractable and easy-to-use approximation,

we also derive the nominal average interference power by modeling each Voronoi cell as a circle of area equal to the average area of a typical cell, termed as the *Average Area-Equivalent Circular Cell (AAECC) model*. Finally, we provide approximations, that lead to the development of intuitive system design insights regarding the worst-case exclusion zone radius, scaling laws, and the gap between the worst-case and nominal average interference values.

Interference Distribution

The CBC model is intractable for characterization of the interference distribution, since it induces correlation in the circumradii of adjacent PV cells. Therefore, under the AAECC model, we use the dominant interferer method [149], [161], [162], [163] to derive an approximate but accurate expression for the interference distribution. However, this approach is non-trivial since receive beamforming at the radar URA distorts the radial symmetry of the equi-interference contour, unlike the case of omnidirectional reception where it is a circle [163]. A novel intermediate result is the derivation of the *equal interference contour*, which resembles a 2D slice of the 3D radar beamforming pattern, when the exclusion zone radius is much larger than the BS antenna height. We use this to characterize the total interference distribution in terms of that of the *farthest distance of the contour from the radar*.

Radar Performance Metrics

Under a Gaussian signaling scheme [164], we characterize the radar detection and false alarm probabilities averaged over the BS point process [151] in a quasi-static target scenario. We derive the exact probabilities, and develop accurate approximations using the dominant interferer method and the central limit theorem. We present extensive numerical results to validate the accuracy of our analytical expressions. Performance trends and tradeoffs are demonstrated using radar receiver operating characteristic (ROC) curves, and system design insights for future radar-massive MIMO spectrum sharing deployments are presented.

6.2 System Model

We consider the radar-massive MIMO spectrum sharing scenario shown in Fig. 6.1a. The radar is the primary user (PU), equipped with a $N_{\mathtt{az}}^{(\mathtt{rad})} \times N_{\mathtt{el}}^{(\mathtt{rad})}$ uniform rectangular array (URA) with $\frac{\lambda}{2}$-spacing, mounted at a height of $h_{\mathtt{rad}}$ m. The massive MIMO downlink is the secondary user (SU), with each BS serving K users with equal power allocation using multi-user MIMO (MU-MIMO). Each BS is equipped with a $N_{\mathtt{az}}^{(\mathtt{BS})} \times N_{\mathtt{el}}^{(\mathtt{BS})}$ URA with $\frac{\lambda}{2}$-spacing, mounted at a height of $h_{\mathtt{BS}}$ m. The subscripts `az` (`el`) are used to denote the azimuth (elevation) elements respectively, and superscripts `rad` (BS) denote the radar (BS) antenna elements respectively. The radar is protected from SU interference by a *circular exclusion zone* of radius $r_{\mathtt{exc}}$. The exclusion zone is chosen to

Table 6.1: Important system parameters in Chapter 6

Parameter	Description
$P_{\mathtt{BS}}$	BS transmit power
K	Number of users per cell co-scheduled on massive MIMO downlink
$\lambda_{\mathtt{BS}}$	BS Intensity
$G_{\mathtt{rad}}$	Radar receive beamforming gain
$G_{\mathtt{BS}}$	BS transmit beamforming gain
$h_{\mathtt{rad}}$	Radar antenna height
$h_{\mathtt{BS}}$	BS antenna height
$r_{\mathtt{exc}}$	Exclusion zone radius
α	Path-loss exponent
$I_{\mathtt{tot}}$	Total (Aggregate) cellular interference power at the radar
$\bar{P}_{\mathtt{fa}}$	Spatial probability of false alarm
$\bar{P}_{\mathtt{d}}$	Spatial probability of detection

be circular since there is no coordination between the cellular network and the radar system, and the radar is assumed to search for a target uniformly at random in the azimuth $[-\frac{\pi}{2}, \frac{\pi}{2})$, as shown in Fig. 6.1.

6.2.1 Channel Model

In quasi-stationary channel conditions, the spatial channel between each BS and the radar can be written as [113]

$$\mathbf{H_R} = \sqrt{\frac{\beta(d)}{1+K_R}}\left(\sqrt{K_R}\mathbf{a}(\theta_{t,L},\phi_{t,L})\mathbf{a}^H(\theta_{r,L},\phi_{r,L}) + \sqrt{\frac{1}{N_c}}\sum_{i=1}^{N_c}\gamma_i\mathbf{a}(\theta_{t,i},\phi_{t,i})\mathbf{a}^H(\theta_{r,i},\phi_{r,i})\right), \tag{6.1}$$

where $\beta(d) = PL(r_0)d^{-\alpha}$ is the path loss at distance d, $PL(r_0)$ is the path-loss at reference distance r_0, α is the path-loss exponent ($\alpha > 2$), d is the 3D distance between the BS and the radar, and N_c is the number of discrete multipath components (MPCs). The Rician factor $K_R \gg 1$, where propagation is dominated by the LoS component[1]. In addition, the random small-scale fading amplitude γ_i satisfies $\mathbb{E}[\gamma_i] = 0$ and $\mathbb{E}[|\gamma_i|^2] = 1$. The azimuth and elevation angles of arrival (departure) of the i^{th} MPC at the radar (from the BS) is denoted by $\theta_{r,i}$ ($\theta_{t,i}$) and $\phi_{r,i}$

[1]Such propagation scenarios are observed in (a) coastal deployments (for e.g., terrestrial BSs sharing spectrum with a naval radar), and (b) terrestrial deployments in flat rural/suburban terrain (for e.g., terrestrial BSs sharing spectrum with a terrestrial radar).

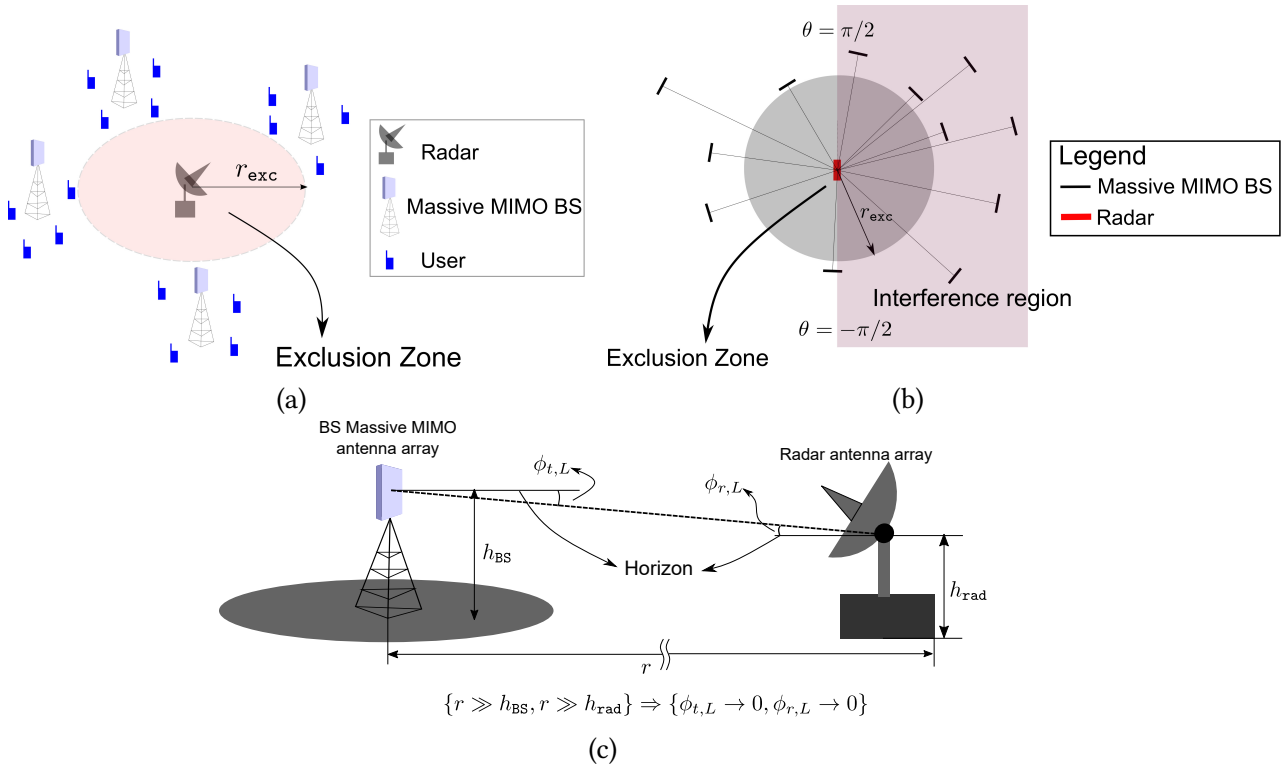

Figure 6.1: (a) Illustration of the radar-massive MIMO spectrum sharing scenario. The radar is protected from massive MIMO downlink interference by an exclusion zone of radius r_{exc}. (b) Top View: the boresight of each BS is aligned along the direction of the radar, and the radar receives interference from the azimuth $[-\pi/2, \pi/2]$ depicted by the shaded region. (c) The LoS component has elevation angle of departure ($\theta_{t,L}$) and arrival ($\theta_{r,L}$) close to 0°, i.e. the horizon. In our convention, $-\pi/2 \leq \phi < 0^\circ$ for elevation angles above the horizon, and $0 < \phi \leq \pi/2$ for elevation angles below the horizon.

($\phi_{t,i}$), respectively. Similarly, the azimuth and elevation angles of departure (arrival) of the LoS component are given by $\theta_{t,L}$ ($\theta_{r,L}$) and $\phi_{t,L}$ ($\phi_{r,L}$), respectively, as shown in Fig. 6.1c. The steering vector $\mathbf{a}(\theta_t, \phi_t) \in \mathbb{C}^{M_{\text{rad}} \times 1}$ (BS), and $\mathbf{a}(\theta_r, \phi_r) \in \mathbb{C}^{M_{\text{rad}} \times 1}$ (radar) is defined in Appendix C.1, where $M_{\text{BS}} = N_{\text{az}}^{(\text{BS})} \times N_{\text{el}}^{(\text{BS})}$ and $M_{\text{rad}} = N_{\text{az}}^{(\text{rad})} \times N_{\text{el}}^{(\text{rad})}$.

6.2.2 Massive MIMO Downlink Beamforming Model

The massive MIMO downlink serves K users located in clusters with mutually disjoint angular support using joint spatial division multiplexing (JSDM) [5]. We consider a highly spatially correlated downlink channel, given by the one-ring model as $\mathbf{h_i} = \sqrt{\beta_i}\mathbf{U_i}\mathbf{\Lambda_i}^{1/2}\mathbf{z_i} \in \mathbb{C}^{M_{\text{BS}} \times 1}$ [5], where β_i is the large-scale pathloss for the i^{th} user, $\mathbf{U_i} \in \mathbb{C}^{M_{\text{BS}} \times r}$ is the orthonormal matrix of

eigenvectors, $\mathbf{\Lambda_i} \in \mathbb{R}^{r\times r}$ is the diagonal matrix of eigenvalues, and $\mathbf{z_i} \sim \mathcal{CN}(\mathbf{0}, \mathbf{I_r}) \in \mathbb{C}^{r\times 1}$ is a complex Gaussian random vector, where $r \ll M_{\text{BS}}$ is the channel rank in the high spatially correlated downlink channel [5]. For simplicity, we consider that all users in the network have the same channel rank. The received signal $\mathbf{y} \in \mathbb{C}^{K\times 1}$ can be written as

$$\mathbf{y} = \mathbf{H}^H \mathbf{W_{RF}} \mathbf{W_{BB}} \mathbf{d} + \mathbf{n}, \tag{6.2}$$

where $\mathbf{W_{RF}} = [\mathbf{w_{RF,1}}\ \mathbf{w_{RF,2}} \cdots \mathbf{w_{RF,K}}] \in \mathbb{C}^{M_{\text{BS}}\times K}$ is the RF beamformer that groups user clusters with disjoint angular support using nearly orthogonal beams, and $\mathbf{W_{BB}} = [\mathbf{w_{BB,1}} \cdots \mathbf{w_{BB,K}}] \in \mathbb{C}^{K\times K}$ is the baseband precoder [5]. If the azimuth and elevation angular support of the k^{th} user cluster is given by $\Theta_k = [\theta_k^{(\text{min})}, \theta_k^{(\text{max})}]$ and $\Phi_k = [\phi_k^{(\text{min})}, \phi_k^{(\text{max})}]$, then without loss of generality we consider that the RF beamformer is given by $\mathbf{w_{RF,k}} = \frac{1}{\sqrt{M_{\text{BS}}}}\mathbf{a}(\theta_k, \phi_k)$, where $\theta_k = (\theta_k^{(\text{min})} + \theta_k^{(\text{max})})/2$ and $\phi_k = (\phi_k^{(\text{min})} + \phi_k^{(\text{max})})/2$. The data $\mathbf{d} = [d_1\ d_2\ \cdots\ d_K]^T \in \mathbb{C}^{K\times 1}$, such that $\mathbb{E}[\mathbf{d}] = \mathbf{0}$ and $\mathbb{E}[\mathbf{d}\mathbf{d}^H] = \frac{P_{BS}}{K}\mathbf{I}$, where d_k is the symbol intended for the k^{th} UE and P_{BS} is the total transmit power per BS. The noise $\mathbf{n} \in \mathbb{C}^{K\times 1}$ is spatially white with $\mathbf{n} \sim \mathcal{CN}(\mathbf{0}, \sigma_n^2\mathbf{I})$.

Proposition 6.1. *For the massive MIMO BS in the asymptotic regime, the baseband precoding matrix $\mathbf{W_{BB}} \approx \mathbf{I}$ for Zero-Forcing (ZF) and Maximum Ratio Transmission (MRT), when K users from different clusters with mutually disjoint angular support are served.*

Proof. (Sketch) The MRT and ZF precoders are $\mathbf{W_{BB}^{(\text{MRT})}} = \mathbf{W_{RF}^H}\mathbf{H}$ and $\mathbf{W_{BB}^{(\text{ZF})}} = (\mathbf{H}^H\mathbf{W_{RF}})^{-1}$ respectively. In the asymptotic regime $\mathbf{W_{RF}^H}\mathbf{W_{RF}} \approx \mathbf{I}$ [5]. For users in clusters with mutually disjoint angular support, $\mathbf{U_i^H}\mathbf{w_{BB,j}} \approx \mathbf{0}, i \neq j$ [5]. Therefore, $\mathbf{H}^H\mathbf{W_{RF}} \approx \mathbf{\Upsilon} = \text{diag}[\upsilon_1\ \upsilon_2 \cdots \upsilon_K]$. Since $\mathbb{E}[\mathbf{d}\mathbf{d}^H] = \frac{P_{BS}}{K}\mathbf{I_K}$, when the sum-power constraint $\mathbb{E}[\|\mathbf{W_{RF}}\mathbf{W_{BB}}\mathbf{d}\|_2] = P_{BS}$ is imposed, we obtain the desired result. ■

Remark 6.1. *The above is true when $N_{\text{az}}^{(\text{BS})}, N_{\text{az}}^{(\text{BS})} \to \infty$. In the case of finite number of antenna elements, we consider a scheduler where the BS co-schedules K users from clusters such that the above approximation is accurate.*

6.2.3 Interference at the Radar due to a Single BS

The radar is assumed to be searching/tracking a target above the horizon ($\phi < 0$) using a receive beamformer $\mathbf{w_{rad}} \in \mathbb{C}^{M_{\text{rad}}\times 1}$. The interference signal prior to beamforming is $\mathbf{y_{rad}} = \mathbf{H_R^H}\mathbf{W_{RF}}\mathbf{W_{BB}}\mathbf{d}$, where $\mathbf{H_R}$ is the high-K_R Rician channel between the BS and the radar from (6.1). Upon receive beamforming, the interference signal is given by $i_{\text{rad}} = \mathbf{w_{rad}^H}\mathbf{H_R^H}\mathbf{W_{RF}}\mathbf{W_{BB}}\mathbf{d}$. Using equation (6.1) and simplifying, we get

$$i_{\text{rad}} = \sqrt{\frac{\beta(d)}{K_R+1}}\Bigg(\sqrt{K_R G_{\text{rad}}(\theta_{r,L}, \phi_{r,L})}e^{-j\alpha_0}\mathbf{a}^H(\theta_{t,L}, \phi_{t,L}) + \sum_{i=1}^{N_c}\sqrt{\frac{G_{\text{rad}}(\theta_{r,i}, \phi_{r,i})}{N_c}}\times$$
$$\gamma_i'\mathbf{a}^H(\theta_{t,i}, \phi_{t,i})\Bigg)\mathbf{W_{RF}}\mathbf{W_{BB}}\mathbf{d}, \tag{6.3}$$

where $\gamma_i' = \gamma_i^* e^{-j\alpha_i}$, the radar beamforming gain $G_{\mathtt{rad}}(\theta_j, \phi_j) = |\mathbf{w}_{\mathbf{rad}}^H \mathbf{a}(\theta_j, \phi_j)|^2$, and α_0 is the residual phase. The specular component can be ignored if $G_{\mathtt{rad}}(\theta_{r,L}, \phi_{r,L}) \gg G_{\mathtt{rad}}(\theta_{r,i}, \phi_{r,i})$. For a tractable worst-case analytical model, we make the following assumptions.

Assumption 6.1. *(LoS beamforming gain dominance) The radar is scanning above the horizon with* $\mathbf{w}_{\mathbf{rad}} = \frac{\mathbf{a}(\theta_{\mathtt{rad}}, \phi_{\mathtt{rad}})}{\sqrt{M_{\mathtt{rad}}}}$ *such that* $G_{\mathtt{rad}}(\theta_{r,L}, \phi_{r,L}) \gg G_{\mathtt{rad}}(\theta_{r,i}, \phi_{r,i}) \; \forall \; 1 \leq i \leq N_c$.

Assumption 6.2. *(Boresight assumption) Boresight of the antenna array of each massive MIMO BS is aligned along the direction of radar* ($\theta_{t,L} = 0$) *as shown in Fig. 6.1b*[2].

Assumption 6.3. *The cellular downlink is exactly co-channel with the radar system, and radar and cellular operating bandwidths are equal. Hence, the frequency-dependent rejection (FDR) factor of the radar is unity*[3].

Assumption 6.4. *In each cell, the scheduler allocates resources to users in different clusters, where all but one cluster have disjoint angular support with the boresight of the BS URA.*

Based on the above assumptions, we have the following lemma.

Lemma 6.1. *The interference to the radar from each BS is only due to data transmissions towards a single cluster whose angular support overlaps with the boresight of the URA.*

Proof. Let the K clusters have azimuth and elevation angles of support given by Θ_k and Φ_k respectively, for $1 \leq k \leq K$. In the asymptotic regime, if there is only one k such that $\Theta_k \cap \{0^\circ\} \neq \emptyset$, then we get $\mathbf{a}^H(\theta_{t,L}, \phi_{t,L}) \mathbf{w}_{\mathbf{RF,j}} \approx 0$ for $j \neq k$ and $\mathbf{a}^H(\theta_{t,L}, \phi_{t,L}) \mathbf{w}_{\mathbf{RF,k}} \neq 0$ [5]. The cluster that has its angular support overlapping with the BS boresight is termed as the "Dominant Interfering User Cluster" (DIUC). ■

Based the above, we have the following key result.

Theorem 6.1. *The worst-case average interference power at the radar due to the DIUC is*

$$\bar{I}_{\mathtt{rad}} < I_{\mathtt{rad}}^{(\mathtt{w})} = \frac{\beta(d) G_{\mathtt{rad}}(\theta_{\mathtt{rad}}, \phi_{\mathtt{rad}}, \theta_{r,L}, \phi_{r,L}) |\mathbf{a}^H(0, \phi_{t,L}) \mathbf{a}(\theta_k, \phi_k)|^2 P_{BS}}{M_{\mathtt{BS}} K}, \tag{6.4}$$

where $G_{\mathtt{rad}}(\theta_{\mathtt{rad}}, \phi_{\mathtt{rad}}, \theta_{r,L}, \phi_{r,L}) = \frac{|\mathbf{a}^H(\theta_{\mathtt{rad}}, \phi_{\mathtt{rad}}) \mathbf{a}(\theta_{r,L}, \phi_{r,L})|^2}{M_{\mathtt{rad}}}$.

[2] As we will discuss in Appendix C.1, Assumption 6.2 facilitates worst-case analysis of average interference.

[3] The FDR is dependent on the radar receiver architecture, spectrum of the interfering signal, and is independent of other parameters. The interference power at the radar is inversely proportional to the FDR. Interested readers are referred to [12] for more details.

Proof. Under the realistic assumption that each MPC is uncorrelated with the others, the average interference power $\bar{I}_{rad} = \mathbb{E}[|i_{rad}|^2]$ is given by

$$\bar{I}_{\mathtt{rad}} = \frac{\beta(d)}{K_R+1}\Big(K_R G_{\mathtt{rad}}(\theta_{\mathtt{rad}},\phi_{\mathtt{rad}},\theta_{r,L},\phi_{r,L})\mathbb{E}[\|\mathbf{a}^H(0,\phi_{t,L})\mathbf{W_{RF}}\mathbf{W_{BB}}\mathbf{d}\|_2^2] + \sum_{i=1}^{N_c}\frac{G_{\mathtt{rad}}(\theta_{\mathtt{rad}},\phi_{\mathtt{rad}},\theta_{r,i},\phi_{r,i})\mathbb{E}[\gamma_i'^2\|\mathbf{a}^H(\theta_{t,i},\phi_{t,i})\mathbf{W_{RF}}\mathbf{W_{BB}}\mathbf{d}\|_2^2]}{N_c}\Big). \tag{6.5}$$

Using Assumption 6.1, we get $\bar{I}_{\mathtt{rad}} < \beta(d)G_{\mathtt{rad}}(\theta_{\mathtt{rad}},\phi_{\mathtt{rad}},\theta_{r,L},\phi_{r,L})\cdot\mathbb{E}[\|\mathbf{a}^H(\theta_{t,L},\phi_{t,L})\mathbf{W_{RF}}\mathbf{W_{BB}}\mathbf{d}\|_2^2]$ since $\mathbb{E}[|\gamma_i'|^2] = 1$. In addition, by Proposition 6.1, Assumption 6.2, and Lemma 6.1, we get $\bar{I}_{\mathtt{rad}} < \mathbb{E}[|\mathbf{a}^H(0,\phi_{t,L})\mathbf{w_{RF,k}}d_k|^2]\beta(d)G_{\mathtt{rad}}(\theta_{\mathtt{rad}},\phi_{\mathtt{rad}},\theta_{r,L},\phi_{r,L})$. Finally, using $\mathbb{E}[|d_k|^2] = P_{BS}/K$ and substituting the RF beamformer for the DIUC, we obtain the desired result. ■

In summary, the worst-case average interference in high-K_R Rician channels in the asymptotic regime resembles the Friis transmission equation, with the power scaled by the beamforming gains, and the fraction of power allocated to the scheduled user in the DIUC. With this general result, we analyze the average interference due to the cellular network in the next section.

6.3 Analysis of Average Interference Power

We consider a single radar located at the origin, and model the spatial distribution of the massive MIMO BSs as a homogeneous PPP $\mathbf{\Phi_{BS}}$, of intensity $\lambda_{\mathtt{BS}}$[4]. The set of locations in the exclusion zone of radius $r_{\mathtt{exc}}$ is denoted by the set $\mathcal{A}_{\mathtt{exc}} = \{(x,y)|(x^2+y^2) \leq r_{\mathtt{exc}}^2\} \subset \mathbb{R}^2$, in which the BSs are prohibited from operating. The BS locations in the interference region is denoted by the set $\mathbf{\Phi_{int}} = \mathbf{\Phi_{BS}} \setminus \mathcal{A}_{\mathtt{exc}}$. While the range of azimuth of a randomly selected point in the cell is independent of the cell size, the elevation angle depends on the cell size and hence, on $\lambda_{\mathtt{BS}}$. Compared to prior works [12], [150], which focus on beamforming in the azimuth, mathematical modeling of elevation beamforming presents technical challenges due to (a) lack of radial symmetry in the PV cell, (b) possibility of arbitrarily large PV cells, and (c) correlation between the shapes and sizes of adjacent cells, which can affect the *joint elevation distribution*. It is worthwhile to note that even though the presence of correlation hinders the analytical characterization of the *worst-case interference distribution*, it does not impact the *average worst-case interference*. However, the lack of radial symmetry and possibility of arbitrarily large cells need a more thoughtful treatment as far as average interference is concerned. To complicate matters further, the presence of side-lobes in the beamforming pattern makes it non-trivial to represent the worst-case beamforming gain as a function of the cell-size. Below, we develop the techniques to address these technical challenges, and present the worst-case and nominal average interference analysis.

[4]The density of a homogeneous PPP is equal to the average number of points per unit area. In this case, $\lambda_{\mathtt{BS}}$ is the average number of cellular base stations per m^{-2}.

Lemma 6.2. *For a $N_{\mathtt{az}} \times N_{\mathtt{el}}$ URA with $\lambda/2$-spacing, if $\phi \in [-\pi/2, \pi/2), 0 \leq \phi_{\mathtt{m}} \leq \frac{\pi}{2}$, and $\theta \in [-\pi/2, \pi/2)$, then the upper bound of the beamforming gain is given by*

$$G_{\mathtt{BS}}^{(\mathtt{max})}(\phi, \phi_{\mathtt{m}}) = \max_{\substack{\phi_k \in [\phi_{\mathtt{m}}, \pi/2) \\ \theta_k \in [-\pi/2, \pi/2)}} G_{\mathtt{BS}}(\theta, \phi, \theta_k, \phi_k) = \begin{cases} N_{\mathtt{az}} N_{\mathtt{el}}, & \text{if } \phi_{\mathtt{m}} \leq \phi, \\ G_{\mathtt{BS}}(0, \phi, 0, \phi_{\mathtt{m}}), & \text{if } \sin\phi_{\mathtt{m}} \leq \frac{1+N_{\mathtt{el}} \sin\phi}{N_{\mathtt{el}}} \\ \frac{N_{\mathtt{az}}}{N_{\mathtt{el}} \sin^2\left(\frac{\pi(\sin\phi_{\mathtt{m}} - \sin\phi)}{2}\right)}, & \text{otherwise} \end{cases} \tag{6.6}$$

where $G_{\mathtt{BS}}(\theta, \phi, \theta_k, \phi_k) = \frac{1}{N_{\mathtt{az}} N_{\mathtt{el}}} |\mathbf{a}^H(\theta, \phi) \mathbf{a}(\theta_k, \phi_k)|^2$.

Proof. See Appendix C.1. ■

6.3.1 Circumcircle-Based Cell (CBC) Model

To induce radial symmetry in the setup, the Voronoi cell needs to be modeled as a circle. When beamforming in the azimuthal direction of the radar, the worst-case interference occurs when the BS serving a user beamforms as close to horizon as possible[5], along which the radar is located. This corresponds to the scenario where the BS beamforms to the *farthest point in the cell*, according to Lemma 6.2. Since the circumradius determines the distance to the farthest point in a cell, we propose a circumcircle-based construction as shown in Fig. 6.2, with the following probability density function.

Proposition 6.2. *The probability density function of the circumradius r_c ($r_c > 0$) of a Poisson-Voronoi cell is*

$$\begin{aligned} f_{R_C}(r_c) =& 8\pi\lambda_{\mathtt{BS}} r_c e^{-4\pi\lambda_{\mathtt{BS}} r_c^2} \Bigg[1 + \sum_{k \geq 1} \Bigg\{ \frac{(-4\pi\lambda_{\mathtt{BS}} r_c^2)^k}{k!} \cdot \left(\frac{\psi_k(r_c)}{8\pi\lambda_{\mathtt{BS}} r_c} - \zeta_k(r_c) \right) \\ & - \frac{(-4\pi\lambda_{\mathtt{BS}} r_c^2)^{k-1} \zeta_k(r_c)}{(k-1)!} \Bigg\} \Bigg], \\ \zeta_k(r_c) =& \int_{\|\mathbf{u}\|_1 = 1, u_i \in [0,1]} \left[\prod_{i=1}^{k} F(u_i) \right] \exp\left(4\pi\lambda_{\mathtt{BS}} r_c^2 \sum_{i=1}^{k} \int_0^{u_i} F(t) \mathrm{d}t \right) \mathrm{d}\mathbf{u}, \\ \psi_k(r) =& \frac{\mathrm{d}\zeta_k(r)}{\mathrm{d}r}, \text{ and } F(t) = \sin^2(\pi t) \mathbb{1}(0 \leq t \leq \tfrac{1}{2}) + \mathbb{1}(t > \tfrac{1}{2}), \end{aligned} \tag{6.7}$$

where $\mathbb{1}(\cdot)$ denotes the indicator function.

Proof. The result is obtained by differentiating the CDF of the circumradius ($F_{R_C}(r_c)$) [160] w.r.t. r_c using Leibniz's rule. ■

[5]We focus on the regime where antenna heights are chosen such that the curvature of the earth is negligible for exclusion radii of hundreds of kilometers.

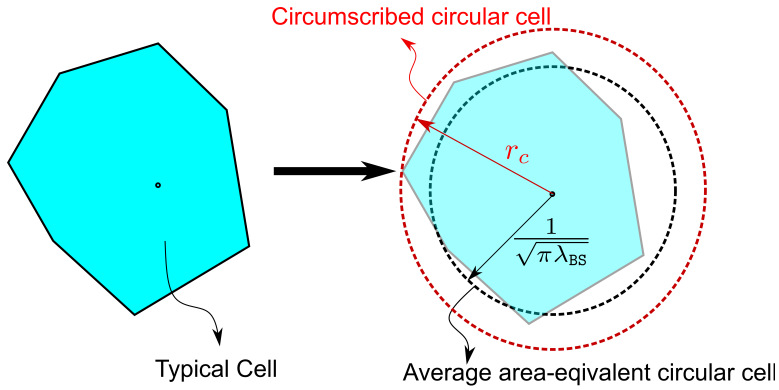

Figure 6.2: Radial symmetry can be induced by modeling the Voronoi cell (i.e. coverage area of a cell) as a (a) circumcircle, or (b) circle of area equal to that of the average typical cell.

Using $f_{R_C}(r_c)$ and Lemma 6.2, we obtain the upper bound on the average interference in the following key result.

Theorem 6.2. *The worst-case average interference at the radar is given by*

$$\bar{I}_{\mathtt{rad,c}} = \frac{\lambda_{\mathtt{BS}} P_{BS} PL(r_0)}{K} \int_{-\frac{\pi}{2}}^{\frac{\pi}{2}} \int_{r_{\mathtt{exc}}}^{\infty} \int_{0}^{\infty} \frac{r G_{\mathtt{rad}}(\theta_{\mathtt{rad}}, \phi_{\mathtt{rad}}, \theta_{r,L}, -\phi_{t,L}(r)) G_{\mathtt{BS}}^{(\mathtt{max})}(\phi_{t,L}(r), \phi_{\mathtt{m}}(r_c))}{(r^2 + (h_{\mathtt{rad}} - h_{\mathtt{BS}})^2)^{\alpha/2}} \cdot f_{R_C}(r_c) \mathrm{d}r_c \mathrm{d}r \mathrm{d}\theta_{r,L},$$

$$\phi_{t,L}(r) = \tan^{-1}\left(\frac{h_{\mathtt{BS}} - h_{\mathtt{rad}}}{r}\right), \phi_{\mathtt{m}}(r_c) = \tan^{-1}\left(\frac{h_{\mathtt{BS}}}{r_c}\right). \tag{6.8}$$

Proof. See Appendix C.2. ■

Corollary 6.1. *The approximate worst-case average interference at the radar is given by*

$$\bar{I}_{\mathtt{rad,c}}^{(\mathtt{app})} = \frac{\lambda_{\mathtt{BS}} P_{BS} PL(r_0)}{K(\alpha - 2) r_{\mathtt{exc}}^{\alpha-2}} \left[\int_{-\frac{\pi}{2}}^{\frac{\pi}{2}} G_{\mathtt{rad}}(\theta_{\mathtt{rad}}, \phi_{\mathtt{rad}}, \theta_{r,L}, 0) \mathrm{d}\theta_{r,L} \right] \cdot \left[\int_{0}^{\infty} G_{\mathtt{BS}}^{(\mathtt{max})}(0, \phi_{\mathtt{m}}(r)) f_{R_C}(r) \mathrm{d}r \right]. \tag{6.9}$$

Proof. Since $r \gg h_{\mathtt{BS}}$ and $r \gg h_{\mathtt{rad}}$, we have $\phi_{t,L}(r) = -\phi_{r,L}(r) \approx 0$, and $(r^2 + (h_{\mathtt{BS}} - h_{\mathtt{rad}})^2)^{\frac{\alpha}{2}} \approx r^{\alpha}$. Using these approximations in $\bar{I}_{\mathtt{rad,c}}$, grouping the integrands, and integrating over r yields the desired result. ■

6.3.2 Average Area-Equivalent Circular Cell (AAECC) Model

The circumcircle-based cell model results in a conservative value for average interference. A simpler, more optimistic model is to replace the Voronoi cell by a circle with an area equal to the average area of a typical cell given by $\frac{1}{\lambda_{\mathtt{BS}}}$. In this case, the cell radius $r_c = r_a = \frac{1}{\sqrt{\pi\lambda_{\mathtt{BS}}}}$, and the nominal average interference is given by the following theorem.

Theorem 6.3. *The nominal mean and standard deviation of the interference power is*

$$\bar{I}_{\mathtt{rad,a}} = \frac{\lambda_{\mathtt{BS}} P_{BS} PL(r_0)}{K} \int_{-\frac{\pi}{2}}^{\frac{\pi}{2}} \int_{r_{\mathtt{exc}}}^{\infty} \frac{r G_{\mathtt{rad}}(\theta_{\mathtt{rad}}, \phi_{\mathtt{rad}}, \theta_{r,L}, \phi_{r,L}(r)) G_{\mathtt{BS}}^{(\mathtt{max})}\big(\phi_{t,L}(r), \phi_{\mathtt{m}}(r_a)\big)}{(r^2 + (h_{\mathtt{rad}} - h_{\mathtt{BS}})^2)^{\alpha/2}} \mathrm{d}r \mathrm{d}\theta_{r,L}, \tag{6.10}$$

$$\sigma_{\mathtt{rad,a}} = \frac{\sqrt{\lambda_{\mathtt{BS}}} P_{BS} PL(r_0)}{K} \sqrt{\int_{-\frac{\pi}{2}}^{\frac{\pi}{2}} \int_{r_{\mathtt{exc}}}^{\infty} \frac{r G_{\mathtt{rad}}^2(\theta_{\mathtt{rad}}, \phi_{\mathtt{rad}}, \theta_{r,L}, \phi_{r,L}(r)) [G_{\mathtt{BS}}^{(\mathtt{max})}(\phi_{t,L}(r), \phi_{\mathtt{m}}(r_a))]^2}{(r^2 + (h_{\mathtt{rad}} - h_{\mathtt{BS}})^2)^{\alpha}} \mathrm{d}r \mathrm{d}\theta_{r,L}}. \tag{6.11}$$

Proof. This model is a special case of Theorem 6.2, where $f_{R_c}(r_c) = \delta\big(r_c - \frac{1}{\sqrt{\pi\lambda_{\mathtt{BS}}}}\big)$. Using the sifting property of the Dirac delta function $\delta(\cdot)$ in equation (6.8), we obtain equation (6.10). The variance is obtained using Campbell's theorem, in a similar manner as Appendix C.2. ■

Corollary 6.2. *The approximate nominal average and variance of the interference power is*

$$\bar{I}_{\mathtt{rad,a}}^{(\mathtt{app})} = \frac{\lambda_{\mathtt{BS}} P_{BS} PL(r_0) G_{\mathtt{BS}}^{(\mathtt{max})}\big(0, \phi_{\mathtt{m}}(r_a)\big)}{K(\alpha - 2) r_{\mathtt{exc}}^{\alpha-2}} \int_{-\frac{\pi}{2}}^{\frac{\pi}{2}} G_{\mathtt{rad}}(\theta_{\mathtt{rad}}, \phi_{\mathtt{rad}}, \theta, 0) \mathrm{d}\theta,$$

$$\sigma_{\mathtt{rad,a}}^{(\mathtt{app})} = \frac{\sqrt{\lambda_{\mathtt{BS}}} P_{BS} PL(r_0) G_{\mathtt{BS}}^{(\mathtt{max})}\big(0, \phi_{\mathtt{m}}(r_a)\big)}{\sqrt{(2\alpha - 2)} K r_{\mathtt{exc}}^{\alpha-1}} \sqrt{\int_{-\frac{\pi}{2}}^{\frac{\pi}{2}} G_{\mathtt{rad}}^2(\theta_{\mathtt{rad}}, \phi_{\mathtt{rad}}, \theta, 0) \mathrm{d}\theta}.$$

Proof. The proof follows the same steps as Corollary 6.1. ■

6.3.3 System Design Insights

6.3.3.1 Scaling of average interference power with BS density

From (6.8) and (6.10), we see that $\lambda_{\mathtt{BS}}$ impacts the average interference through the linear term and the BS beamforming gain ($G_{\mathtt{BS}}$) term. It is related to the cell size via the circumradius distribution

and the average area of the typical cell, which impacts the *minimum elevation angle* ($\phi_{\mathtt{m}}$). Note that this dependence is not observed in azimuth-only beamforming models. However, when $h_{\mathtt{BS}} \ll r_c$, the elevation angle $\phi_{\mathtt{m}}(r_c) \to 0$ and hence, $G_{\mathtt{BS}} \to M_{\mathtt{BS}}$. In this regime, the worst-case average interference power scales linearly with $\lambda_{\mathtt{BS}}$.

6.3.3.2 Exclusion Zone Radius

In practice, exclusion zones are defined based on the average aggregate interference power (for e.g. see [21]). Using Corollaries 6.1 and 6.2, for an average interference threshold $\bar{I}_{\mathtt{th}}$ and $\alpha > 2$, the worst-case exclusion zone radius ($r_{\mathtt{exc}}^{(\mathtt{w})}$) can be obtained using

$$r_{\mathtt{exc}}^{(\mathtt{w})} \approx \left(\frac{\lambda_{\mathtt{BS}} P_{BS} PL(r_0)}{K(\alpha-2)\bar{I}_{\mathtt{th}}} \left[\int_{-\frac{\pi}{2}}^{\frac{\pi}{2}} G_{\mathtt{rad}}(\theta_{\mathtt{rad}}, \phi_{\mathtt{rad}}, \theta, 0) \mathrm{d}\theta \right] \cdot \left[\int_0^{\infty} G_{\mathtt{BS}}^{(\mathtt{max})}(0, \phi_{\mathtt{m}}(r_c)) f_{R_C}(r) \mathrm{d}r \right] \right)^{\frac{1}{\alpha-2}}.$$

6.3.3.3 Constant Gap in Average Interference Predicted by CBC and AAECC Models

By Corollaries (6.1) and (6.2), we observe that the ratio of average interference powers is nearly independent of $r_{\mathtt{exc}}$, given by

$$\eta_{\mathtt{ca}} = \frac{\bar{I}_{\mathtt{rad,c}}^{(\mathtt{app})}}{\bar{I}_{\mathtt{rad,a}}^{(\mathtt{app})}} = \frac{\int_0^{\infty} G_{\mathtt{BS}}^{(\mathtt{max})}(0, \phi_{\mathtt{m}}(r_c)) f_{R_C}(r_c) \mathrm{d}r_c}{G_{\mathtt{BS}}^{(\mathtt{max})}\left(0, \phi_{\mathtt{m}}\left(\frac{1}{\sqrt{\pi\lambda_{\mathtt{BS}}}}\right)\right)}. \tag{6.12}$$

Note that $\eta_{\mathtt{ca}} \to 1$ when $h_{\mathtt{BS}}\sqrt{\pi\lambda_{\mathtt{BS}}} \to 0$ due to BS gain saturation.

In the next section, we analyze the distribution of interference at the radar caused by the massive MIMO cellular downlink.

6.4 Distribution of Massive-MIMO Downlink Interference at the Radar

To study the impact of large-scale network interference on aggregate radar performance metrics such as *spatial probability of detection and false alarm* [151], deriving the distribution of interference while considering spatial randomness in the BS locations is a key intermediate step. To accomplish this, a common approach in stochastic geometry literature is to characterize the Laplace transform of the interference distribution, which leverages the presence of an exponential term in Rayleigh fading channels [165]. However in our case, the Laplace transform method is not applicable, since we ignore the small scale fading term in the high-K_R Rician channel to model the worst-case interference scenario. Instead, we use the dominant interferer approximation [149], [161], [162], [163] described below.

Assumption 6.5. *In the cellular network, if the interference power of the dominant interfering BS is $I_{\mathtt{dom}}$ and the interference power of the rest of the network is $I_{\mathtt{rest}}$, then the total interference power ($I_{\mathtt{tot}}$) is approximated by the sum of the dominant BS interference power and the average interference power caused by the rest of the network, conditioned on the dominant interference power. Mathematically, it can be written as*

$$I_{\mathtt{tot}} \approx I_{\mathtt{dom}} + \mathbb{E}_{I_{\mathtt{dom}}}[I_{\mathtt{rest}}|I_{\mathtt{dom}}]. \tag{6.13}$$

In the case of omnidirectional reception at the receiver, the distribution of $I_{\mathtt{dom}}$ is directly related to the distance distribution of the nearest transmitter in the point process [166], since the contour of equal interference power is a circle [163]. However in our case, receive beamforming at the radar distorts radial symmetry, since received power depends on the azimuth and elevation angle, in addition to the distance from the interfering BS. Therefore, the first step is to characterize the contour curves of equal interference power. This is fundamental to calculating the void probability[6] [165] and hence, the distribution of $I_{\mathtt{dom}}$. In the rest of this chapter, we assume cell-edge beamforming in the AAECC model to derive useful expressions for the interference distribution. In the following subsection, we characterize the equal interference contours in our radar-cellular coexistence scenario.

6.4.1 Equal Interference Contours in Radar-Massive MIMO Spectrum Sharing

The equal interference power contour $\mathcal{C}(I)$ contains points (r,θ) such that the received power due to a transmitter at location $(r,\theta) \in \mathcal{C}(I)$ is I. The following proposition denotes the contour lying outside the exclusion zone in the radar-cellular spectrum sharing scenario.

Proposition 6.3. *Under the AAECC model, the contour $\mathcal{C}(I_{\mathtt{dom}})$ is given by*

$$\mathcal{C}(I_{\mathtt{dom}}) = \Big\{ (r,\theta) \Big| G_{\mathtt{rad}}\big(\theta_{\mathtt{rad}},\phi_{\mathtt{rad}},\theta,\phi(r)\big) G_{\mathtt{BS}}^{(\mathtt{max})}\big(-\phi(r),\phi_{\mathtt{m}}(1/\sqrt{\pi\lambda_{\mathtt{BS}}})\big) r^{-\alpha} = \frac{K I_{\mathtt{dom}}}{PL(r_0)P_{BS}},$$
$$r \geq r_{\mathtt{exc}}, \theta \in \big[-\tfrac{\pi}{2},\tfrac{\pi}{2}\big] \Big\}$$
$$\textit{where } \phi(r) = \tan^{-1}\left(\frac{h_{\mathtt{rad}} - h_{\mathtt{BS}}}{r}\right), \phi_{\mathtt{m}}(r') = \tan^{-1}(h_{\mathtt{BS}}/r'). \tag{6.14}$$

Proof. The worst-case interference power due to a massive MIMO BS at (r,θ) is given by (6.4).

[6] In stochastic geometry, the void probability of a point process is the probability that there is no point in a region of interest.

Since the BSs inside the exclusion zone are inactive, the contour can be written as

$$\mathcal{C}(I_{\mathtt{dom}}) = \Bigg\{ (r,\theta) \Bigg| \frac{PL(r_0)P_{BS}G_{\mathtt{rad}}(\theta_{\mathtt{rad}},\phi_{\mathtt{rad}},\theta,\phi(r))G_{\mathtt{BS}}^{(\mathtt{max})}(-\phi(r),\phi_{\mathtt{m}}(1/\sqrt{\pi\lambda_{\mathtt{BS}}}))}{Kr^{\alpha}} = I_{\mathtt{dom}}, \\ r \geq r_{\mathtt{exc}}, \theta \in \Big[-\frac{\pi}{2},\frac{\pi}{2}\Big] \Bigg\}. \tag{6.15}$$

Rearranging the terms independent of (r,θ), we obtain the desired result. ■

In the case of large exclusion zone radii, we show in the following lemma that the equi-interference contour can be represented by the *farthest distance between the contour and the radar*, when conditioned on the radar beamforming vector.

Lemma 6.3. *Under the AAECC model, when $h_{\mathtt{BS}} \ll r_{\mathtt{exc}}$ and $h_{\mathtt{rad}} \ll r_{\mathtt{exc}}$, the equal interference contour is given by*

$$\mathcal{C}(I_{\mathtt{dom}}) = \Bigg\{ (r,\theta) \Bigg| r = r_{\mathtt{dom}} \Bigg[\frac{\sin\left(\frac{\pi}{2}N_{\mathtt{az}}^{(\mathtt{rad})}(\sin\theta_{\mathtt{rad}}\phi_{\mathtt{rad}} - \sin\theta)\right)}{N_{\mathtt{az}}^{(\mathtt{rad})}\sin\left(\frac{\pi}{2}(\sin\theta_{\mathtt{rad}}\phi_{\mathtt{rad}} - \sin\theta)\right)} \Bigg]^{2/\alpha}, r_{\mathtt{dom}} \geq r_{\mathtt{exc}}, \theta \in \Big[-\frac{\pi}{2},\frac{\pi}{2}\Big] \Bigg\}, \\ \textit{where } I_{\mathtt{dom}} \triangleq \frac{P_{BS}PL(r_0)G_{\mathtt{BS}}^{(\mathtt{max})}(0,\phi_{\mathtt{m}}(1/\sqrt{\pi\lambda_{\mathtt{BS}}}))}{Kr_{\mathtt{dom}}^{\alpha}} \cdot \frac{N_{\mathtt{az}}^{(\mathtt{rad})}\sin^2\left(\frac{\pi}{2}N_{\mathtt{el}}^{(\mathtt{rad})}\sin\phi_{\mathtt{rad}}\right)}{N_{\mathtt{el}}^{(\mathtt{rad})}\sin^2\left(\frac{\pi}{2}\sin\phi_{\mathtt{rad}}\right)}. \tag{6.16}$$

Proof. Please refer to Appendix C.3. ■

From equation (6.16), we observe that there is a bijection between $r_{\mathtt{dom}}$, the farthest distance of the contour from the radar, and interference power $I_{\mathtt{dom}}$ under the AAECC model. Therefore, we can equivalently denote the equal interference contour by $\mathcal{C}(r_{\mathtt{dom}})$. Fig. 6.3a shows an example of the *equal interference contour*, which resembles a horizontal cross section of the radar's 3D beamforming pattern at elevation $\phi = 0°$. In the following subsection, we derive the distribution of the dominant interference power $I_{\mathtt{dom}}$.

6.4.2 Distribution of $I_{\mathtt{dom}}$

The distribution of $I_{\mathtt{dom}}$ is related to the void probability of a PPP in the region outside the exclusion zone enclosed by the equal interference contour [165], as shown in Fig. 6.3b. In the following key result, we derive an analytical expression for the area of this region $A(r_{\mathtt{dom}})$, which is needed to characterize the distribution of $I_{\mathtt{dom}}$.

Lemma 6.4. *Under the AAECC model, when $r_{\mathtt{exc}} \gg h_{\mathtt{BS}}$ and $r_{\mathtt{exc}} \gg h_{\mathtt{rad}}$, $A(r_{\mathtt{dom}})$ is given by*

$$A(r_{\mathtt{dom}}) = \frac{1}{2}\int_{-\frac{\pi}{2}}^{\frac{\pi}{2}} \max\left(r_{\mathtt{exc}}^2, r_{\mathtt{dom}}^2 \Bigg[\frac{\sin\left(\frac{\pi}{2}N_{\mathtt{az}}^{(\mathtt{rad})}(\sin\theta_{\mathtt{rad}}\cos\phi_{\mathtt{rad}} - \sin\theta)\right)}{N_{\mathtt{az}}^{(\mathtt{rad})}\sin\left(\frac{\pi}{2}(\sin\theta_{\mathtt{rad}}\cos\phi_{\mathtt{rad}} - \sin\theta)\right)} \Bigg]^{\frac{4}{\alpha}}\right) \mathrm{d}\theta - \frac{\pi r_{\mathtt{exc}}^2}{2}, \tag{6.17}$$

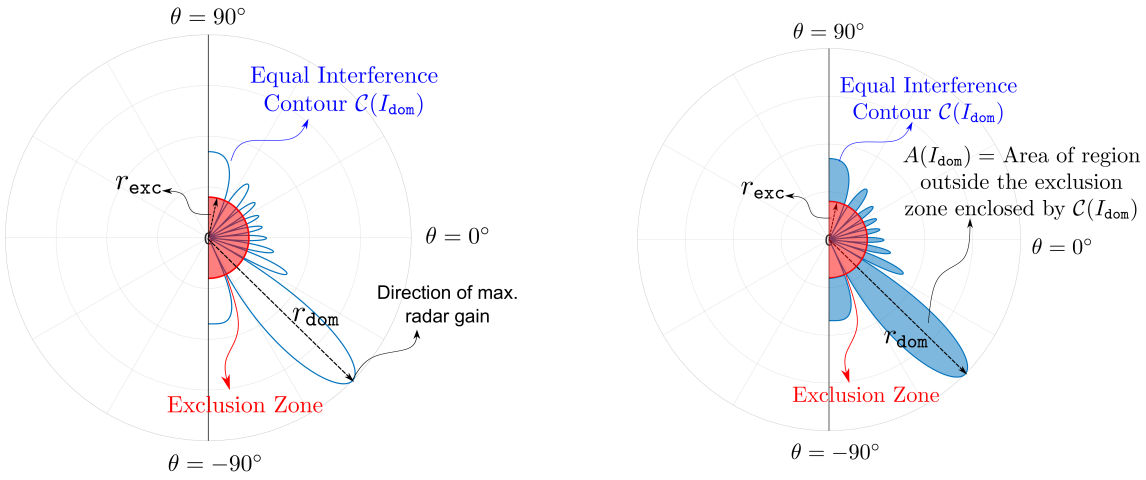

Figure 6.3: (a) Schematic of the equal interference power contour $\mathcal{C}(I_{\texttt{dom}})$ in polar coordinates, for a radar with $N_{\texttt{az}}^{(\texttt{rad})} = N_{\texttt{az}}^{(\texttt{rad})} = 8$, scanning a target at $(\theta_{\texttt{rad}}, \phi_{\texttt{rad}}) = (-60°, -5°)$, with $\alpha = 3.5$, $r_{\texttt{exc}} = 4$ km, and $r_1 = 20$ km. Distance of the farthest point on the contour is denoted by $r_{\texttt{dom}}$. (b) Area of the region outside the exclusion zone but enclosed by $\mathcal{C}(I_{\texttt{dom}})$ is denoted by $A(I_{\texttt{dom}})$.

Proof. Please refer Appendix C.4. ■

Using the above result, the density and distribution of $r_{\texttt{dom}}$ is characterized in the following lemma.

Lemma 6.5. *The distribution and density function of $r_{\texttt{dom}}$ are given by*

$$F_{R_{\texttt{dom}}}(r_{\texttt{dom}}) = 1 - \exp\Big(- \frac{\lambda_{\texttt{BS}}}{2} \int_{-\frac{\pi}{2}}^{\frac{\pi}{2}} \max\left(r_{\texttt{exc}}^2, \tilde{r}_{\texttt{dom}}^2(\theta)\right) \mathrm{d}\theta + \frac{\pi \lambda_{\texttt{BS}} r_{\texttt{exc}}^2}{2} \Big), \tag{6.18}$$

$$f_{R_{\texttt{dom}}}(r_{\texttt{dom}}) = \lambda_{\texttt{BS}} \left[\int_{-\frac{\pi}{2}}^{\frac{\pi}{2}} r_{\texttt{dom}} \left[\frac{\sin\left(\frac{\pi}{2} N_{\texttt{az}}^{(\texttt{rad})} (\sin\theta_{\texttt{rad}} \cos\phi_{\texttt{rad}} - \sin\theta)\right)}{N_{\texttt{az}}^{(\texttt{rad})} \sin\left(\frac{\pi}{2} (\sin\theta_{\texttt{rad}} \cos\phi_{\texttt{rad}} - \sin\theta)\right)} \right]^{\frac{4}{\alpha}} \cdot \mathbb{1}[\tilde{r}_{\texttt{dom}}(\theta) \geq r_{\texttt{exc}}] \mathrm{d}\theta \right] \cdot$$
$$\exp\Big(- \frac{\lambda_{\texttt{BS}}}{2} \int_{-\frac{\pi}{2}}^{\frac{\pi}{2}} \max\left(r_{\texttt{exc}}^2, \tilde{r}_{\texttt{dom}}^2(\theta)\right) \mathrm{d}\theta + \frac{\pi \lambda_{\texttt{BS}} r_{\texttt{exc}}^2}{2} \Big), \tag{6.19}$$

where $\tilde{r}_{\texttt{dom}}(\theta) \triangleq r_{\texttt{dom}} \left[\frac{\sin\left(\frac{\pi}{2} N_{\texttt{az}}^{(\texttt{rad})} (\sin\theta_{\texttt{rad}} \cos\phi_{\texttt{rad}} - \sin\theta)\right)}{N_{\texttt{az}}^{(\texttt{rad})} \sin\left(\frac{\pi}{2} (\sin\theta_{\texttt{rad}} \cos\phi_{\texttt{rad}} - \sin\theta)\right)} \right]^{\frac{2}{\alpha}}$, *and* $\mathbb{1}[\cdot]$ *is the indicator function.*

Proof. Please refer Appendix C.5. ■

Since a bijection exists between $r_{\texttt{dom}}$ and $I_{\texttt{dom}}$, the density and distribution of $I_{\texttt{dom}}$ can be derived in a similar manner as Lemma 6.5, and are given in the following result.

Lemma 6.6. *The distribution and density of $I_{\mathtt{dom}}$ under the AAECC model are given by*

$$F_{I_{\mathtt{dom}}}(i_{\mathtt{dom}}) = \exp\Big(- \frac{\lambda_{\mathtt{BS}}\kappa^{\frac{2}{\alpha}}}{2}\Big[\int_{-\frac{\pi}{2}}^{\frac{\pi}{2}} \max\big(I_{\mathtt{exc}}^{-2/\alpha}, \tilde{i}_{\mathtt{dom}}^{-2/\alpha}(\theta)\big)\mathrm{d}\theta - \pi I_{\mathtt{exc}}^{-2/\alpha}\Big]\Big), \tag{6.20}$$

$$f_{I_{\mathtt{dom}}}(i_{\mathtt{dom}}) = \frac{\lambda_{\mathtt{BS}}\kappa^{2/\alpha}}{\alpha}\Bigg[\int_{-\frac{\pi}{2}}^{\frac{\pi}{2}} i_{\mathtt{dom}}^{-(\alpha+2)/\alpha}\Bigg[\frac{\sin\left(\frac{\pi}{2}N_{\mathtt{az}}^{(\mathtt{rad})}(\sin\theta_{\mathtt{rad}}\cos\phi_{\mathtt{rad}}-\sin\theta)\right)}{N_{\mathtt{az}}^{(\mathtt{rad})}\sin\left(\frac{\pi}{2}(\sin\theta_{\mathtt{rad}}\cos\phi_{\mathtt{rad}}-\sin\theta)\right)}\Bigg]^{\frac{2}{\alpha}}\mathbb{1}[\tilde{i}_{\mathtt{dom}}(\theta)\le I_{\mathtt{exc}}]\mathrm{d}\theta\Bigg]\cdot$$
$$\exp\Big(- \frac{\lambda_{\mathtt{BS}}\kappa^{\frac{2}{\alpha}}}{2}\Big[\int_{-\frac{\pi}{2}}^{\frac{\pi}{2}} \max\big(I_{\mathtt{exc}}^{-2/\alpha}, \tilde{i}_{\mathtt{dom}}^{-2/\alpha}(\theta)\big)\mathrm{d}\theta - \pi I_{\mathtt{exc}}^{-2/\alpha}\Big]\Big), \tag{6.21}$$

where $\kappa = \dfrac{P_{BS}PL(r_0)G_{\mathtt{BS}}^{(\mathtt{max})}(0,\phi_{\mathtt{m}}(1/\sqrt{\pi\lambda_{\mathtt{BS}}}))}{K}\cdot\dfrac{N_{\mathtt{az}}^{(\mathtt{rad})}\sin^2\left(\frac{\pi}{2}N_{\mathtt{el}}^{(\mathtt{rad})}\sin\phi_{\mathtt{rad}}\right)}{N_{\mathtt{el}}^{(\mathtt{rad})}\sin^2\left(\frac{\pi}{2}\sin\phi_{\mathtt{rad}}\right)}$, *and* $\tilde{i}_{\mathtt{dom}}(\theta) = i_{\mathtt{dom}}\dfrac{N_{\mathtt{az}}^{(\mathtt{rad})}\sin\left(\frac{\pi}{2}(\sin\theta_{\mathtt{rad}}\cos\phi_{\mathtt{rad}}-\sin\theta)\right)}{\sin\left(\frac{\pi}{2}N_{\mathtt{az}}^{(\mathtt{rad})}(\sin\theta_{\mathtt{rad}}\cos\phi_{\mathtt{rad}}-\sin\theta)\right)}$.

Proof. From equation (6.16), we observe that the bijection between the dominant interference power $I_{\mathtt{dom}}$ and the corresponding farthest contour distance $r_{\mathtt{dom}}$ can be represented by $I_{\mathtt{dom}} = \kappa r_{\mathtt{dom}}^{-\alpha}$. Since I monotonically decreases with increasing r, the CDF of $I_{\mathtt{dom}}$ is given by $\mathbb{P}[I_{\mathtt{dom}} \le i_{\mathtt{dom}}] = \mathbb{P}[R_{\mathtt{dom}} \ge r_{\mathtt{dom}}]$. Using equation (6.18), we get $F_{I_{\mathtt{dom}}}(i_{\mathtt{dom}}) = \exp\big(-\lambda_{\mathtt{BS}}A(r_{\mathtt{dom}})\big)$ for $r_{\mathtt{dom}} \ge r_{\mathtt{exc}}$. Using the bijection and simplifying, we get the desired CDF. The density is obtained in a similar manner as Lemma 6.5, by differentiating equation (6.20) w.r.t. $i_{\mathtt{dom}}$. ■

6.4.3 Total Interference Power at the Radar

Since $r_{\mathtt{dom}}$ can equivalently represent the equal interference contour $\mathcal{C}(I_{\mathtt{dom}})$, we use Lemma 6.5 in the following result to approximate the total interference power at the radar, using the dominant interferer method.

Theorem 6.4. *The total interference power at the radar under the AAECC model and Assumption 6.5 is given by*

$$I_{\mathtt{tot,DI}}(r_{\mathtt{dom}}) = \kappa\Bigg[r_{\mathtt{dom}}^{-\alpha} + \frac{\lambda_{\mathtt{BS}}}{\alpha-2}\int_{-\frac{\pi}{2}}^{\frac{\pi}{2}}\Bigg[\frac{\sin\left(\frac{\pi}{2}N_{\mathtt{az}}^{(\mathtt{rad})}(\sin\theta_{\mathtt{rad}}\cos\phi_{\mathtt{rad}}-\sin\theta)\right)}{N_{\mathtt{az}}^{(\mathtt{rad})}\sin\left(\frac{\pi}{2}(\sin\theta_{\mathtt{rad}}\cos\phi_{\mathtt{rad}}-\sin\theta)\right)}\Bigg]^2\big(\max\big(r_{\mathtt{exc}},\tilde{r}_{\mathtt{dom}}(\theta)\big)\big)^{-\alpha+2}\mathrm{d}\theta\Bigg]. \tag{6.22}$$

Proof. Please refer Appendix C.6. ■

Remark 6.2. *It is worthwhile to note that $I_{\mathtt{tot,DI}}(r_{\mathtt{dom}})$ has finite support, i.e. $I_{\mathtt{tot,DI}} \in (0, I_{\mathtt{exc}} + \bar{I}_{\mathtt{rad,a}})$. This is because the maximum dominant interference power is upper bounded by $I_{\mathtt{exc}}$, and the corresponding conditional average interference power is $\bar{I}_{\mathtt{rad,a}}$ (equation 6.10).*

In the following corollary, we prove that a bijection exists between $I_{\texttt{tot,DI}}$ and $r_{\texttt{dom}}$.

Corollary 6.3. *Under the dominant interferer approximation, $I_{\texttt{tot,DI}}$ monotonically decreases with $r_{\texttt{dom}}$.*

Proof. The proof follows by showing that both terms in equation (6.22) monotonically decrease with $r_{\texttt{dom}}$. It is clear that $I_{\texttt{dom}}$ monotonically decreases with increasing $r_{\texttt{dom}}$. In addition, we note that $\mathcal{A}(r_{\texttt{dom}}) \subset \mathcal{A}(kr_{\texttt{dom}})\ \forall\ k \in \mathbb{R}, k > 1$. As a result, the integration region and, hence, the average interference power in equation (C.9) shrinks as $r_{\texttt{dom}}$ increases. Therefore, the sum of these terms decreases monotonically with $r_{\texttt{dom}}$. ■

Even though a bijection exists between $r_{\texttt{dom}}$ and $I_{\texttt{tot,DI}}$ under the dominant interferer approximation, the mapping from $I_{\texttt{tot,DI}}$ to $r_{\texttt{dom}}$ cannot be expressed in closed-form. For tractability, we compute the expectation of the radar performance metrics w.r.t. $r_{\texttt{dom}}$ in the following section.

6.5 Characterization of Radar Performance Metrics

In this section, we use the distribution of $r_{\texttt{dom}}$ to characterize the impact of cellular interference on the radar's detection and false alarm performance.

6.5.1 Radar Received Signal Model

In the presence of cellular interference and noise, the aggregate received signal depends on the presence or absence of a target at $(\theta_{\texttt{rad}}, \phi_{\texttt{rad}})$, when the radar performs receive beamforming using the weights $\mathbf{w_{rad}} = \frac{1}{\sqrt{M_{\texttt{rad}}}}\mathbf{a}(\theta_{\texttt{rad}}, \phi_{\texttt{rad}})$. Denoting the received signal post-beamforming at time index n is $y_{\texttt{rad}}[n]$, we assume that the radar calculates the test statistic $P_{\texttt{rad}} = \sum_{n=1}^{N} \frac{|y_{\texttt{rad}}[n]|^2}{N}$ in an estimation window of N samples. Let $\mathcal{H}_0$ denote the hypothesis that there is no target, and $\mathcal{H}_1$ denote the hypothesis that there is a target. We assume that each BS transmits i.i.d. complex Gaussian signals[7], and noise is i.i.d. circularly symmetric complex Gaussian. In near-LoS channel conditions, when BSs transmit i.i.d. Gaussian signals, the aggregate interference signal is Gaussian distributed *when conditioned on the BS locations* $\mathbf{\Phi_{int}}$. Thus, the received signal under each hypothesis can be written as

$$\mathcal{H}_0 : y_{\texttt{rad},0}[n] = \sqrt{(I_{\texttt{tot}}(\mathbf{\Phi_{int}}) + \sigma_n^2)}w[n], \tag{6.23}$$

$$\mathcal{H}_1 : y_{\texttt{rad},1}[n] = \sqrt{(I_{\texttt{tot}}(\mathbf{\Phi_{int}}) + \sigma_n^2)}w[n] + \sqrt{P_{\texttt{tar}}}e^{j\alpha[n]}, \tag{6.24}$$

[7]The time-domain samples of a wideband multicarrer waveform such as OFDM can be accurately modeled using a zero-mean stationary Gaussian random process with a non-zero temporal correlation [167]. In practice, when the OFDM symbol duration is much smaller than the radar repetition interval, the resultant interfering cellular signal can be modeled as an i.i.d. Gaussian random process.

where $I_{\mathtt{tot}}(\mathbf{\Phi_{int}})$ is the aggregate interference power, σ_n^2 denotes the noise variance, $w[n] \sim \mathcal{CN}(0,1)$, $P_{\mathtt{tar}}$ is the received power due to target scatter, and $\alpha[n]$ is the phase of the target return at time n. Using this system model, we have the following results regarding the distribution of $P_{\mathtt{rad}}$ under the two hypotheses.

Lemma 6.7. *The conditional distributions of the test statistic under the two hypotheses can be expressed as*

$$\begin{aligned}\mathcal{H}_0 : F_{P_{\mathtt{rad},0}}(p|I_{\mathtt{tot}}(\mathbf{\Phi_{int}})) &= \frac{1}{(N-1)!}\gamma_l\Big(N, \frac{Np}{I_{\mathtt{tot}}(\mathbf{\Phi_{int}})+\sigma_n^2}\Big),\\ \mathcal{H}_1 : F_{P_{\mathtt{rad},1}}(p|I_{\mathtt{tot}}(\mathbf{\Phi_{int}})) &= 1 - Q_N\left(\sqrt{\frac{2NP_{\mathtt{tar}}}{I_{\mathtt{tot}}(\mathbf{\Phi_{int}})+\sigma_n^2}}, \sqrt{\frac{2Np}{I_{\mathtt{tot}}(\mathbf{\Phi_{int}})+\sigma_n^2}}\right),\end{aligned} \tag{6.25}$$

where $\gamma_l(a,x) = \int_0^x z^{a-1}e^{-z}\mathrm{d}z$ *is the lower incomplete gamma function,* $Q_N(a,b) = \int_b^\infty z^N/a^{N-1}\cdot \exp(-(z^2+a^2)/2)I_{N-1}(az)\mathrm{d}z$ *is the Marcum Q-function, and* $I_{N-1}(z)$ *is the modified Bessel function of order* $(N-1)$.

Proof. We observe from equation (6.23) that under hypothesis $\mathcal{H}_0$, each sample in the estimation window is i.i.d. complex Gaussian distributed such that $\Re\Big(\frac{y_{\mathtt{rad},0}[n]\sqrt{2N}}{\sqrt{I_{\mathtt{tot}}(\mathbf{\Phi_{int}})+\sigma_n^2}}\Big) \sim \mathcal{N}(0,1)$ and $\Im\Big(\frac{y_{\mathtt{rad},0}[n]\sqrt{2N}}{\sqrt{I_{\mathtt{tot}}(\mathbf{\Phi_{int}})+\sigma_n^2}}\Big) \sim \mathcal{N}(0,1)$ for $n = 1, 2, \cdots, N$, where $\Re(\cdot)$ and $\Im(\cdot)$ denote the real and imaginary parts. Taking the squared sum of these terms, we observe that $\frac{2NP_{\mathtt{rad},0}}{I_{\mathtt{tot}}(\mathbf{\Phi_{int}})+\sigma_n^2}$ is chi-squared distributed with $2N$ degrees of freedom, and the CDF follows accordingly.

Similarly, the received signal samples under $\mathcal{H}_1$ are independent such that $\Re\Big(\frac{y_{\mathtt{rad},1}[n]\sqrt{2N}}{\sqrt{I_{\mathtt{tot}}(\mathbf{\Phi_{int}})+\sigma_n^2}}\Big) \sim \mathcal{N}\Big(\frac{\sqrt{2NP_{\mathtt{tar}}}\cos(\alpha[n])}{\sqrt{I_{\mathtt{tot}}(\mathbf{\Phi_{int}})+\sigma_n^2}}, 1\Big)$ and $\Im\Big(\frac{y_{\mathtt{rad},1}[n]\sqrt{2N}}{\sqrt{I_{\mathtt{tot}}(\mathbf{\Phi_{int}})+\sigma_n^2}}\Big) \sim \mathcal{N}\Big(\frac{\sqrt{2NP_{\mathtt{tar}}}\sin(\alpha[n])}{\sqrt{I_{\mathtt{tot}}(\mathbf{\Phi_{int}})+\sigma_n^2}}, 1\Big)$, for $n = 1, 2, \cdots, N$. Taking the squared sum of these terms, we see that $\frac{2NP_{\mathtt{rad},1}}{I_{\mathtt{tot}}(\mathbf{\Phi_{int}})+\sigma_n^2}$ has a non-central chi-squared distribution with $2N$ degrees of freedom and non-central parameter $\lambda = \frac{2NP_{\mathtt{tar}}}{I_{\mathtt{tot}}(\mathbf{\Phi_{int}})+\sigma_n^2}$. The CDF follows accordingly. ■

Corollary 6.4. *When* $N \to \infty$*, the conditional distributions of the test statistic under the two hypotheses become*

$$\begin{aligned}\mathcal{H}_0 : F_{P_{\mathtt{rad},0}}(p|I_{\mathtt{tot}}(\mathbf{\Phi_{int}})) &= 1 - Q\left(\frac{\sqrt{N}(p - I_{\mathtt{tot}}(\mathbf{\Phi_{int}}) - \sigma_n^2)}{I_{\mathtt{tot}}(\mathbf{\Phi_{int}})+\sigma_n^2}\right),\\ \mathcal{H}_1 : F_{P_{\mathtt{rad},1}}(p|I_{\mathtt{tot}}(\mathbf{\Phi_{int}})) &= 1 - Q\left(\frac{\sqrt{N}(p - P_{\mathtt{tar}} - I_{\mathtt{tot}}(\mathbf{\Phi_{int}}) - \sigma_n^2)}{\sqrt{(P_{\mathtt{tar}} + I_{\mathtt{tot}}(\mathbf{\Phi_{int}})+\sigma_n^2)^2 - P_{\mathtt{tar}}^2}}\right),\end{aligned} \tag{6.26}$$

where $Q(x) = 1/\sqrt{2\pi}\int_x^\infty \exp(-u^2/2)\mathrm{d}u$ *is the Q-function.*

Proof. Observe that when $y_i \overset{\text{i.i.d.}}{\sim} \mathcal{CN}(0,\sigma^2), i = 1, 2, \cdots, N$ and $N \to \infty$, we have $\frac{1}{N}\sum_{i=1}^{N} |y_i|^2 \sim \mathcal{N}(\sigma^2, N^{-1}\sigma^4)$ [164]. Hence, the CDF of $P_{\mathtt{rad},0}$ follows by replacing σ^2 by $\mathrm{Var}(y_{\mathtt{rad},0}[n]) = I_{\mathtt{tot}}(\mathbf{\Phi_{int}}) + \sigma_n^2$.

On the other hand, the mean and variance of $|y_{\mathtt{rad},1}[n]|^2$ is finite and is given by $\mathbb{E}[|y_{\mathtt{rad},1}[n]|^2] = P_{\mathtt{tar}} + I_{\mathtt{tot}} + \sigma_n^2$ and $\mathrm{Var}(|y_{\mathtt{rad},1}[n]|^2) = (I_{\mathtt{tot}} + \sigma_n^2)^2 + 2P_{\mathtt{tar}}(I_{\mathtt{tot}} + \sigma_n^2)$ respectively, for $n = 1, 2, \cdots, N$. Using the central limit theorem, the distribution of $P_{\mathtt{rad},1}$ approaches a Gaussian distribution with mean $\mathbb{E}[P_{\mathtt{rad},1}] = P_{\mathtt{tar}} + I_{\mathtt{tot}} + \sigma_n^2$ and variance $\mathrm{Var}(P_{\mathtt{rad},1}) = N^{-1}[(I_{\mathtt{tot}} + \sigma_n^2)^2 + 2P_{\mathtt{tar}}(I_{\mathtt{tot}} + \sigma_n^2)]$, when $N \to \infty$. The CDF follows accordingly. ■

6.5.2 Radar Performance Metrics

When conditioned on the interference $I_{\mathtt{tot}}(\mathbf{\Phi_{int}})$, noise power σ_n^2, and the detection threshold $P_{\mathtt{th}}$, the probability of detection ($P_{\mathtt{d}}$) and false alarm ($P_{\mathtt{fa}}$) are calculated using

$$P_{\mathtt{d}} = \mathbb{P}[P_{\mathtt{rad}} > P_{\mathtt{th}} | \mathcal{H}_1, I_{\mathtt{tot}}(\mathbf{\Phi_{int}}), \sigma_n^2], \quad P_{\mathtt{fa}} = \mathbb{P}[P_{\mathtt{rad}} > P_{\mathtt{th}} | \mathcal{H}_0, I_{\mathtt{tot}}(\mathbf{\Phi_{int}}), \sigma_n^2]. \tag{6.27}$$

We assume that the noise variance is constant. However, since the cellular downlink network is a PPP, we are interested in a spatially averaged variant of these probabilities. These are termed as the spatial detection probability ($\bar{P}_{\mathtt{d}}$), and the probability of spatial false alarm ($\bar{P}_{\mathtt{fa}}$), which are defined as [151]

$$\begin{aligned} \bar{P}_{\mathtt{d}} &= \int_0^\infty \mathbb{P}[P_{\mathtt{rad}} > P_{\mathtt{th}} | \mathcal{H}_1, I_{\mathtt{tot}}] f_{I_{\mathtt{tot}}}(x) \mathrm{d}x, \\ \bar{P}_{\mathtt{fa}} &= \int_0^\infty \mathbb{P}[P_{\mathtt{rad}} > P_{\mathtt{th}} | \mathcal{H}_0, I_{\mathtt{tot}}] f_{I_{\mathtt{tot}}}(x) \mathrm{d}x. \end{aligned} \tag{6.28}$$

where $P_{\mathtt{rad}}$ is the test statistic, and $f_{I_{\mathtt{tot}}}(\cdot)$ is the density functions of the cellular interference power. For notational simplicity, the dependence of $I_{\mathtt{tot}}$ on the random BS locations ($\mathbf{\Phi_{int}}$) is omitted. In the following result, we provide a tractable approximation to the spatial detection and false alarm probabilities.

Theorem 6.5. *The probability of spatial detection and spatial false alarm are given by*

$$\begin{aligned} \bar{P}_{\mathtt{fa},\chi^2} &= 1 - \frac{1}{(N-1)!} \int_{r_{\mathtt{exc}}}^\infty \gamma_l \left(N, \frac{N P_{\mathtt{th}}}{I_{\mathtt{tot,DI}}(r_{\mathtt{dom}}) + \sigma_n^2} \right) f_{R_{\mathtt{dom}}}(r_{\mathtt{dom}}) \mathrm{d}r_{\mathtt{dom}}, \\ \bar{P}_{\mathtt{d},\chi^2} &= \int_{r_{\mathtt{exc}}}^\infty Q_N \left(\sqrt{\frac{2N P_{\mathtt{tar}}}{I_{\mathtt{tot,DI}}(r_{\mathtt{dom}}) + \sigma_n^2}}, \sqrt{\frac{2N P_{\mathtt{th}}}{I_{\mathtt{tot,DI}}(r_{\mathtt{dom}}) + \sigma_n^2}} \right) f_{R_{\mathtt{dom}}}(r_{\mathtt{dom}}) \mathrm{d}r_{\mathtt{dom}}, \end{aligned} \tag{6.29}$$

where $f_{R_{\mathtt{dom}}}(\cdot)$ is the PDF of $r_{\mathtt{dom}}$ (6.19), and $I_{\mathtt{tot,DI}}$ is the total interference power under the dominant interferer approximation (6.22).

Proof. Please refer Appendix C.7. ■

Table 6.2: Approximate values of $\eta_{\mathtt{ca}}$ (6.12)

$h_{\mathtt{BS}}\sqrt{\pi\lambda_{\mathtt{BS}}}$	0.0089	0.0198	0.028	0.044	0.0886	0.1253
$\eta_{\mathtt{ca}}$	1.004	1.022	1.045	1.254	1.608	2.905

Corollary 6.5. *When $N \to \infty$, the probability of spatial detection and spatial false alarm can be simplified as*

$$\bar{P}_{\mathtt{fa,CLT}} = \int_{r_{\mathtt{exc}}}^{\infty} Q\left(\frac{\sqrt{N}(P_{\mathtt{th}} - I_{\mathtt{tot,DI}}(r_{\mathtt{dom}}) - \sigma_n^2)}{I_{\mathtt{tot,DI}}(r_{\mathtt{dom}}) + \sigma_n^2}\right) f_{R_{\mathtt{dom}}}(r_{\mathtt{dom}})\mathrm{d}r_{\mathtt{dom}},$$
$$\bar{P}_{\mathtt{d,CLT}} = \int_{r_{\mathtt{exc}}}^{\infty} Q\left(\frac{\sqrt{N}(P_{\mathtt{th}} - P_{\mathtt{tar}} - I_{\mathtt{tot,DI}}(r_{\mathtt{dom}}) - \sigma_n^2)}{\sqrt{(P_{\mathtt{tar}} + I_{\mathtt{tot,DI}}(r_{\mathtt{dom}}) + \sigma_n^2)^2 - P_{\mathtt{tar}}^2}}\right) f_{R_{\mathtt{dom}}}(r_{\mathtt{dom}})\mathrm{d}r_{\mathtt{dom}}. \tag{6.30}$$

Proof. The proof is similar to Theorem 6.5, and follows from the complementary CDF of the Gaussian distribution in Corollary 6.4. ■

6.6 Numerical Results and Discussion

In this section, we validate our theoretical results using Monte-Carlo simulations. We consider a typical radar operating at $f_c = 5$ GHz, located at the origin equipped with a $N_{\mathtt{az}}^{(\mathtt{rad})} \times N_{\mathtt{el}}^{(\mathtt{rad})}$ URA, mounted at a height of $h_{\mathtt{rad}} = 20$ m. The radar is scanning a region above the horizon at $(\theta_{\mathtt{rad}}, \phi_{\mathtt{rad}}) = (60°, -10°)$. The BSs are distributed as a PPP, with varying intensities. Each massive MIMO BS is co-channel with the radar, and is equipped with a $N_{\mathtt{az}}^{(\mathtt{BS})} \times N_{\mathtt{el}}^{(\mathtt{BS})}$ URA deployed at a height of $h_{\mathtt{BS}} = 50$ m. The circular exclusion zone around the radar has a *minimum radius* of $r_{\mathtt{exc}}^{(\mathtt{min})} = 5$ km [16]. The boresight of each massive MIMO BS URA is aligned along the direction of the radar ($\theta_k = 0$ in the LCS). In each cell, the massive MIMO BS transmits a total power of $P_{BS} = 1$ W, equally allocated among co-scheduled UEs from $K = 4$ clusters with mutually disjoint angular support. To model the pathloss in the downlink and the BS to radar channels, we assume the 3GPP 3D Urban Macro (3D UMa) LoS pathloss model [113],

$$PL(d) = P(h_{\mathtt{BS}}, h_{\mathtt{rad}}) + 20\log_{10}(f_c) + 40\log_{10}(d) \quad \text{(dB)},$$
$$P(h_{\mathtt{BS}}, h_{\mathtt{rad}}) = 28 - 9\log_{10}((h_{\mathtt{BS}} - h_{\mathtt{rad}})^2) \quad \text{(dB)},$$

where f_c is the center frequency in GHz, and d the distance in meters.

6.6.1 Comparison of Worst-Case Average Interference under CBC and AAECC Models

Fig. 6.4 shows the average interference power derived in Section 6.3 under different cell models, as a function of exclusion zone radius for different BS intensities. We observe that the upper

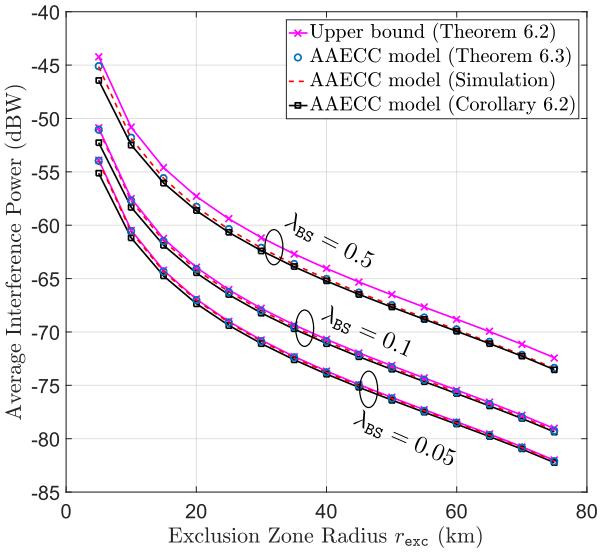

Figure 6.4: Worst-case average interference power at the radar, as a function of exclusion zone radius for different base station densities $\lambda_{\mathtt{BS}}$ (km^{-2}). $h_{\mathtt{rad}} = 20$ m, $h_{\mathtt{BS}} = 50$ m, $N_{\mathtt{az}}^{(\mathtt{BS})} = N_{\mathtt{el}}^{(\mathtt{BS})} = 10$, $N_{\mathtt{az}}^{(\mathtt{rad})} = N_{\mathtt{el}}^{(\mathtt{rad})} = 40$, $\theta_{\mathtt{rad}} = 60°$, $\phi_{\mathtt{rad}} = -10°$.

bound is remarkably tight, especially for low values of $\lambda_{\mathtt{BS}} \leq 0.1$. For reference, we also plot the approximate average interference power from Corollary 6.1. It can be seen that its accuracy improves as $r_{\mathtt{exc}}$ increases, due to the accuracy of the underlying approximations regarding the elevation angle $\phi_{r,L}$. The approximately linear scaling of average interference power with $\lambda_{\mathtt{BS}}$ can also be observed, since the average interference power drops by ≈ 10 dB when $\lambda_{\mathtt{BS}}$ is decreased by an order of magnitude.

We also observe that the ratio of average interference powers $\eta_{\mathtt{ca}}$ is approximately constant, and is tabulated for the *elevation parameter* $h_{\mathtt{BS}}\sqrt{\pi\lambda_{\mathtt{BS}}}$ in Table 6.2. For 3GPP UMa deployments with inter-site distance $r_{\mathtt{ISD}}$, the typical $h_{\mathtt{BS}}/r_{\mathtt{ISD}} = 0.05$ [113]. The corresponding $h_{\mathtt{BS}}\sqrt{\pi\lambda_{\mathtt{BS}}} = 0.095$, for which 2 dB $< \eta_{\mathtt{ca}} <$ 4.6 dB (Table 6.2). Thus the bound is remarkably tight, which make them valuable for worst-case analysis of practical radar-5G NR spectrum sharing deployments.

6.6.2 Distribution of the Total Interference Power

Fig. 6.5 shows the distribution of the total interference power as a function of the exclusion zone radius, $r_{\mathtt{exc}}$. Interestingly, we observe that the distribution concentrates in narrower intervals around the average interference power, with increasing $r_{\mathtt{exc}}$. This is due to the fact that under the AAECC model, the average interference power scales as $r_{\mathtt{exc}}^{-\alpha+2}$, while the corresponding standard deviation scales as $r_{\mathtt{exc}}^{-\alpha+1}$, as shown in Corollary 6.2 (also refer to [12]). Since the standard deviation decays faster with $r_{\mathtt{exc}}$ when compared to the average, the distribution of $I_{\mathtt{tot}}$ concen-

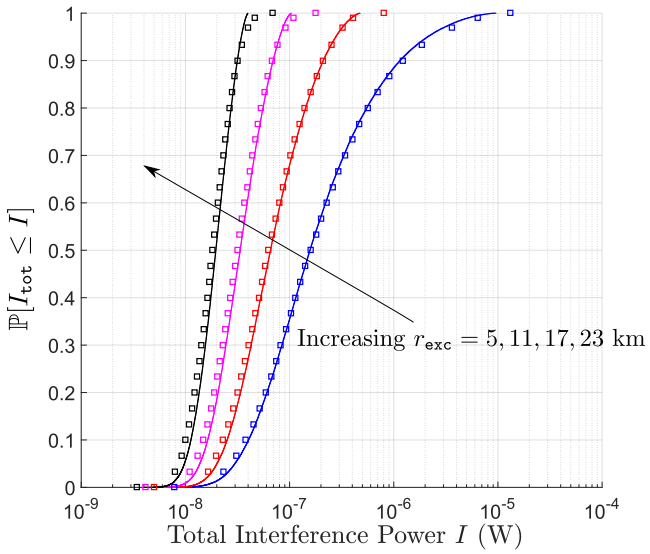

Figure 6.5: Distribution of total interference power ($I_{\mathtt{tot}}$) for $\lambda_{\mathtt{BS}} = 0.01$ (km^{-2}), and different exclusion zone radii. Markers and solid lines represent the simulation and theoretical (Theorem 6.4) results respectively. $h_{\mathtt{rad}} = 20$ m, $h_{\mathtt{BS}} = 50$ m, $N_{\mathtt{az}}^{(\mathtt{BS})} = N_{\mathtt{el}}^{(\mathtt{BS})} = 10, N_{\mathtt{az}}^{(\mathtt{rad})} = N_{\mathtt{el}}^{(\mathtt{rad})} = 10, \theta_{\mathtt{rad}} = 60°, \phi_{\mathtt{rad}} = -10°$.

trates around the average power $\bar{I}_{\mathtt{rad,a}}$, when $r_{\mathtt{exc}}$ increases.

Overall, the analytical expression in Theorem 6.4 obtained using the dominant interferer approximation matches well with the numerical results. However, we observe that the deviation between the theoretical and numerical result is more prominent at the upper tail of the CDF. This can be attributed to the finite support of the interference power under the dominant interferer method, as discussed in Remark 6.2.

6.6.3 Radar Performance Metrics

Fig. 6.6 shows the radar performance metrics for different exclusion zone radii, in the case of a quasi-static target in the interference-limited regime. Fig. 6.6a and Fig. 6.6b show the spatial probability of detection and false alarm, as a function of the detection threshold ($P_{\mathtt{th}}$). As expected, $\bar{P}_{\mathtt{d}}$ ($\bar{P}_{\mathtt{fa}}$) monotonically increases (decreases) with $r_{\mathtt{exc}}$ respectively, for a fixed detection threshold. This is so because expanding the exclusion zone improves the SINR of the received signal. We observe that there is a good match between the simulation results and the analytical results from Theorem 6.5. Furthermore, we also observe that the CLT approximation in Corollary 6.4 is remarkably accurate, even for a relatively small estimation window size of $N = 10$.

Fig. 6.6c shows the radar receiver operating characteristic (ROC) curve for different $r_{\mathtt{exc}}$ values. We observe that the trends follow Figs. 6.6a-6.6b, and that the analytical and simulation results

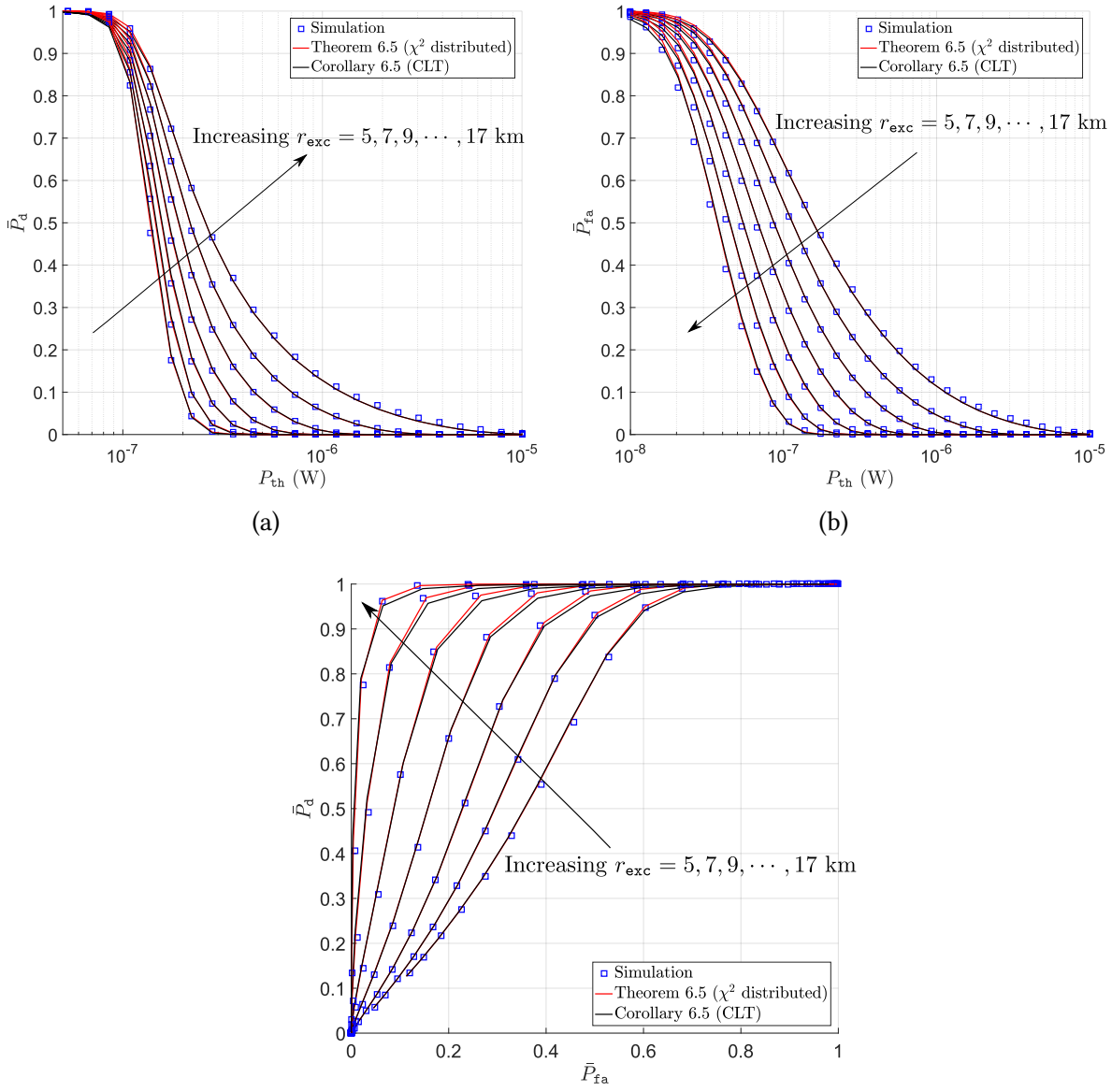

Figure 6.6: Variation of (a) spatial probability of detection ($\bar{P}_{\mathtt{d}}$), and (b) spatial probability of false alarm ($\bar{P}_{\mathtt{fa}}$) as a function of the detection threshold ($P_{\mathtt{th}}$) for different $r_{\mathtt{exc}}$ values. (c) Radar receiver operating characteristic (ROC) curve for different $r_{\mathtt{exc}}$ values. $\lambda_{\mathtt{BS}} = 0.01$ km^{-2}, $P_{\mathtt{tar}} = 10^{-6}$ W, $\sigma_n^2 = 10^{-9}$ W, $h_{\mathtt{rad}} = 20$ m, $h_{\mathtt{BS}} = 50$ m, $N_{\mathtt{az}}^{(\mathtt{BS})} = N_{\mathtt{el}}^{(\mathtt{BS})} = 10, N_{\mathtt{az}}^{(\mathtt{rad})} = N_{\mathtt{el}}^{(\mathtt{rad})} = 10, \theta_{\mathtt{rad}} = 60°$, and $\phi_{\mathtt{rad}} = -10°, N = 10$.

match. However, the inaccuracy due to the CLT approximation (Corollary 6.4) can be observed in the high $\bar{P}_{\mathtt{d}}$ and low $\bar{P}_{\mathtt{fa}}$ regime. This mismatch is likely due to the difference in tail behavior of the Gaussian and χ^2-distributions. Obtaining the ROC curves as a function of the operational parameters such as the $r_{\mathtt{exc}}$ and operating SNR can be very helpful to determine the feasible set of deployment parameters in radar-cellular coexistence. For example, assuming target values of $\bar{P}_{\mathtt{d}} \geq 0.95$ and $\bar{P}_{\mathtt{fa}} \leq 10^{-2}$, Figs. 6.6a-6.6c indicate that radar operation is *not feasible* for $r_{\mathtt{exc}} = 17$ km, and a larger exclusion zone is necessary to meet these performance requirements.

Therefore, a key outcome of this work is a powerful mathematical tool to rapidly evaluate the radar system performance metrics in spectrum sharing scenarios with large massive MIMO cellular networks.

6.7 Conclusion and Proposed Work

In this chapter, we presented an analytical framework to evaluate radar performance metrics in underlay radar-massive MIMO cellular spectrum sharing scenarios, where both systems are equipped with 3D beamforming capabilities. We devised a novel construction based on modeling a PV cell by its circumcircle, to upper bound the worst-case average interference at the radar due to a co-channel massive MIMO downlink in near LoS channel conditions. We also proposed and analyzed the nominal average and variance of the interference power using a more tractable model, where each cell is replaced by a circle of area equal to the average area of a typical cell. We provided system design insights regarding the worst-case exclusion zone radius, scaling of interference power with BS density, and the approximate gap between the worst-case and nominal average interference power. We then derived the *equi-interference contour* under the nominal interference model, and used it to characterize the interference distribution, using the *dominant interference approximation*. Under a quasi-static target detection scenario based on coherent integration across multiple radar pulses and threshold detection, we leveraged the interference distribution to characterize the spatial probability of detection and false alarm.

Our analytical results were validated using Monte-Carlo simulations. We showed that the upper bound under the circumcircle-based model is remarkably tight for 3GPP-recommended system parameters [113]. More importantly, we demonstrated the usefulness of our proposed approach by applying it for evaluation of radar performance metrics, especially ROC curves. With the deployment of 5G NR base stations intensifying over the next few years, and the Federal Communications Commission (FCC) opening up new frequency bands currently occupied by radar bands, operators will need to study the feasibility of 5G deployments that share spectrum with radars. The analytical framework presented in this chapter can be used for network planning and evaluation in these scenarios. Specifically,

1. It enables network designers to systematically isolate and evaluate the impact of important system parameters (BS density, antenna height, transmit power, exclusion zone radius, etc.)

on the worst-case radar performance. This can then be leveraged to design detailed site-specific studies.

2. It complements industry-standard simulation methodologies, by establishing a baseline performance for each set of system parameters in practical spectrum sharing scenarios.

There are several extensions to this work. Firstly, this analysis can be extended to incorporate the impact of downlink scheduling by modeling the azimuth and elevation distributions of the scheduled user in the dominant interfering user cluster of each cell. From a systems standpoint, investigation of the impact of cellular uplink interference on radar performance and developing optimization frameworks to jointly maximize the radar as well as cellular network performance are of interest for spectrum sharing deployments in 1.3 GHz [20], 3.5 GHz [21], and 5 GHz [22] bands.

Chapter 7

Conclusions and Future Work

In this dissertation, we made fundamental and practical contributions to three distinct problems in the areas of spectrum sharing and vehicular communication systems, by analyzing and improving the performance of next-generation wireless networks. In the first two parts, we analyzed and designed advanced channel state information (CSI) estimation and link adaptation techniques for vehicular communications and pulsed radar-cellular spectrum sharing scenarios. In the third part, we developed a tractable analytical model to characterize the impact of worst-case interference on radar performance metrics caused by the co-channel downlink of massive MIMO base stations in underlay spectrum sharing scenarios. Below, we summarize the main conclusions of this work, followed by a brief discussion on future research directions.

7.1 Novel CSI Estimation, Feedback, and Link Adaptation Scheme for Next-Generation Vehicular Communication Systems

In Chapter 2, we proposed an efficient low-complexity channel statistics estimation and feedback scheme, to implement rate-maximizing pilot configurations in SISO and MIMO-OFDM systems in doubly selective nonstationary vehicular channels. Inspired by codebook-based feedback that is used for link adaptation in contemporary wireless standards, we proposed and designed *'channel statistics codebook'*. The codebook was designed by quantizing the channel frequency /temporal correlation functions by representing it in terms of the power delay profile/Doppler spread respectively. We also extended this scheme to carrier aggregation-OFDM (CA-OFDM) systems, and presented implicit and explicit feedback mechanisms. We also highlighted the conditions where implicit feedback has the potential to reduce channel statistics feedback. In vehicular channels, We demonstrated throughput gains of (a) up to 80% in the case of no power control, and (b) 40% in the case of perfect power control, without significant increases in computational complexity and feedback overhead.

Impact

Evolution of Cellular-assisted Vehicular-to-Everything (CV2X) and Unmanned Aerial Vehicle (UAV)-to-UAV/UAV-to-ground communications represent the next frontier in next-generation cellular deployments. This contribution presented a CSI estimation and limited feedback framework which is compatible with LTE and 5G NR's link adaptation mechanisms. The types of pilots/reference signals have been progressively increasing in the cellular evolution from 4G LTE to 5G NR. With the deployments of cellular vehicular-to-everything (CV2X) systems anticipated on an unprecedented scale globally over the next decade, this framework represents, to the best of the authors' knowledge, the first work that addresses challenging practical issues of *low-complexity estimation* and *low-overhead feedback* of fading channel statistics in vehicular channel conditions. The general ideas of this framework can be leveraged by standardization bodies for designing CSI feedback and link adaptation schemes for UAV and vehicular use-cases in 5G and beyond-5G systems.

Future Work

Waveform flexibility has been embraced by 5G NR, and adapting the waveform as a function of the radio conditions is crucial to exploit this feature to the maximum. While the proposed framework is waveform-independent, further research is needed to implement and evaluate it for multi-user massive MIMO transmissions, which will be the most important transmission mode in 5G NR and beyond-5G systems. Since the pilot overhead scales linearly with the number of antennas, this framework holds great potential for optimizing throughput and reliability in scenarios where massive MIMO meets CV2X. Grouping of users with similar channel statistics will be a key intermediate step in this problem. In addition, integration of this waveform adaptation framework with multi-user scheduling that satisfies the various QoS requirements of 5G (rate, latency, reliability etc.) will continue to be an important direction of research as wireless networks evolve beyond 5G.

7.2 Robust CSI Estimation and Feedback for 4G and 5G Cellular Systems in Shared Spectrum with Pulsed Radars

In Chapter 3, we demonstrated the detrimental impact of frequency-domain non-pilot interference (NPI) on statistical-CSI (S-CSI) estimation and cellular link adaptation mechanisms using empirical and link-level simulation results. This *S-CSI contamination* led to significant degradation in throughput and retransmission-induced latency performance of the cellular system (Fig. 3.7). This chapter established that pilot interference is necessary for link adaptation purposes of modern wireless systems, in that *pilot interference (PI) yields accurate S-CSI estimates of the interference channel.*

In Chapter 4, we considered an underlay pulsed radar-cellular spectrum sharing scenario, and rigorously proved that the S-CSI contamination problem will plague cellular systems in shared spectrum. This was shown to be because of *zero probability that pulsed radar behaves as a time-domain NPI*, which contaminated the S-CSI acquired using limited feedback schemes.

Building on the insights developed in Chapters 3 and 4, we presented a novel framework to address this issue in Chapter 5. We proposed and analyzed the performance of a low-complexity semi-blind SINR estimation method in the presence of pulsed radar interference. Recognizing that the channel is bimodal due to periodic impairments by interference and small-scale fading respectively, we proposed *dual CSI feedback*, an effective and low-overhead extension to CSI feedback mechanisms used in LTE and NR. Link-level simulation results demonstrated that for practical use cases, our framework simultaneously achieves (a) throughput improvements of up to $2.2\times$, (b) block error rate reduction of up to $5\times$, and (c) retransmission-induced latency reduction by an order of magnitude, when compared to conventional CSI estimation and feedback schemes.

Impact

To the best of our knowledge, this is the first work that demonstrated and reported the detrimental effects of structured non-pilot interference on cellular systems. Prior to this research, it was a widely held notion that pilot signals must be protected from interference, which intuitively makes sense. However going against conventional widsom, this research exposed scenarios where it is actually necessary to have PI. This is motivated by the inherent sophisticated adaptation mechanisms of advanced cellular protocols, and the manner in which they deal with interference. Our research also showed that that ultra-low latency applications are especially vulnerable to non-pilot interference/jamming, due to delay outage as a consequence of retransmissions. To make matters worse in 5G NR, pilots meant for S-CSI estimation are highly sparse by design, making emerging systems vulnerable to link adaptation failure. Hence, protocol mechanisms in current wireless standards need to be strengthened to detect and mitigate these evasive jammers.

Radar-cellular spectrum sharing in sub-7 GHz frequency bands promises tremendous benefits to meet the growing demands in spectral efficiency, since radar systems occupy the biggest fraction of spectrum in these bands. Our results led to important insights on the choice of practical CSI acquisition and link adaptation mechanisms in the presence of pulsed radar signals, which is a natural source of NPI in shared spectrum environments. These discussions will have a tangible impact on standardization (especially 3GPP RAN1 standards bodies), as network providers move forward with cellular deployments in shared spectrum containing intermittent sources of interference.

Future Work

Since massive MIMO transmission modes are extensively used in 5G NR systems, a natural extension to this work is to investigate and design semi-blind methods to estimate the optimal precoder from a dictionary, in the presence of pulsed radar interference. Furthermore, the diverse set of use cases in NR necessitate investigation of novel scheduling schemes that incorporate this framework. An especially challenging edge-case is to design schedulers that maximize throughput under a latency constraint in the presence of NPI sources, which will be important for latency-sensitive and high throughput applications such as augmented/virtual reality (AR/VR) and tactile internet.

Since modern radar systems incorporate advanced signal processing techniques such as *pulse staggering* to improve its interference resilience, the time intervals of future interference will no longer be deterministic. In such cases, we need to study the conditions when the S-CSI contamination issues persist in the presence of such radar waveforms. Finally, to address the issue of seemingly *random interference*, techniques such as reinforcement learning can be explored, that *learn the short- and long-term behavior of the radar signal through experience.* In this paradigm, the scheduler decisions will be guided by predictions of the channel state of current and near-future future time slots.

7.3 Fundamental Analysis of Underlay Radar-Massive MIMO Spectrum Sharing Scenarios

In Chapter 6, we developed a tractable analytical framework to characterize the impact of worst-case cellular downlink interference on radar detection and false alarm performance, in underlay spectrum sharing scenarios. We considered a single radar located at the origin, and modeled the locations of BSs using a homogeneous Poisson point process (PPP). A circular exclusion zone centered around the radar was assumed, so that only the BSs located outside the circle were allowed to operate. We considered a 5G-like massive MIMO cellular network and modern phased array radars, where both systems were capable of 3D beamforming, operating in LoS/near-LoS channel conditions. By formulating a novel construction based on modeling a Poisson-Voronoi (PV) cell by its circumcircle, we upper bounded the *worst-case* average interference at the radar. We also proposed and analyzed the nominal average and variance of the interference power using a more tractable model, where each cell was replaced by a circle of area equal to the average area of a typical cell. We provided useful insights regarding the worst-case exclusion zone radius, scaling of interference power with BS density, and the approximate gap between the worst-case and nominal average interference power. We then derived the *equi-interference contour* under the nominal interference model, and used it to characterize the interference distribution, using the *dominant interference approximation*. Under a quasi-static target detection scenario where the radar uses coherent integration across multiple radar pulses and threshold detection, we used the

interference distribution to characterize the spatial probability of detection and false alarm.

Using extensive Monte-Carlo simulations, we showed that the upper bound using the circumcircle-based model was remarkably tight for 3GPP-recommended system parameters [113]. We also verified the accuracy of the dominant interferer approximation, and demonstrated its usefulness by applying it to obtain the radar ROC curves for each exclusion zone radius, for the given system parameters.

Impact

With the deployment of 5G NR base stations intensifying over the next few years, and the Federal Communications Commission (FCC) opening up new frequency bands currently occupied by radar bands, operators will need to study the feasibility of 5G deployments that share spectrum with radars. The analytical framework presented in this contribution (a) enables network designers to systematically isolate and evaluate the impact of each system parameter (BS density, antenna height, transmit power, exclusion zone radius, etc.) on the worst-case radar performance, and (b) complements industry-standard simulation methodologies, by establishing a baseline performance for each set of system parameters in practical spectrum sharing scenarios.

Future Work

A natural extension of this work is to incorporate the impact of downlink scheduling, by modeling the azimuth and elevation distributions of the scheduled user in the dominant interfering user cluster (DIUC) of each cell. Then, by considering the system parameters of actual radar and cellular systems, this analysis can also be applied to evaluate the feasibility of transition in the $3200 - 3550$ MHz and 1.3 GHz bands. Furthermore, analyzing spectrum sharing scenarios between airborne/terrestrial cellular users and airborne/terrestrial radars are relevant extensions to this contribution. Under the dominant interferer method, characterizing the equal interference contour (similar to Section 6.4.1) is the starting point to undertake these analyses. Other techniques such as density approximation of the aggregate interference [168] can also be explored.

Finally, developing optimization frameworks that maximize the radar performance under cellular network performance constraints, and vice-versa, will be important for obtaining system-design insights for harmonious spectrum sharing deployments in the next decade.

Appendix A

Data Channel Processing Chain in LTE and NR

The baseband processing stages to generate the physical downlink shared channel (the downlink data channel in LTE) are shown in Fig. A.1. A *transport block (TB)* in LTE and NR is a block of data bits, for which performance metrics are defined, and it can be diagnosed whether the data block was decoded correctly or not. Most transmissions occur in time durations called as the transmission time interval (TTI). The TTI has a fixed value of 1 ms in LTE, and it can be as short as hundreds of microseconds in NR.

To each transport block, a 24-bit cyclic redundancy check (CRC) sequence is attached that allows for receiver-size error detection. The same is also used to send acknowledgments (ACKs) or negative ACKs (NACKs) to initiate a hybrid ARQ-based (HARQ) retransmission. The TB together with the CRC is then segmented into several *codeblocks*, on which the LTE turbo coder's interleaver operates. In order to ensure that a TB of arbitrary size can be segmented into code blocks that match the set of available code-block sizes, the LTE specification includes the possibility to insert "dummy" filler bits at the head of the first code block. These code blocks are then channel-coded using turbo coding with the generator polynomials and interleaver functions that are standardized in 3GPP [169]. Upon turbo coding, the hybrid ARQ and rate matching blocks extract the exact set of code bits to be transmitted within a TTI. Rate matching involves puncturing or repetition of interleaved bits of the turbo encoder placed in a circular buffer, in such a manner that the resulting length of the bit sequence fits the number of physical resources available for transmission on the downlink.

In the FDD LTE downlink, HARQ is supported for 8 independent processes using a stop-and-wait (SAW) mechanisms, with a typical *round-trip time (RTT) of 8 ms*. Each HARQ process requires a separate soft buffer allocation for the purpose of recombining the retransmissions. In the LTE downlink, HARQ can be configured to be asynchronous and adaptive, meaning that each HARQ retransmission can (a) have a different MCS, frequency allocation than the original transmission, and (b) take place at any arbitrary time after the *NACK is received by the eNB*, based on the scheduler policy. Since HARQ can be adaptive, each downlink transmission is accompanied by explicit control signaling. However, since the HARQ retransmission occurs after receiving a NACK from

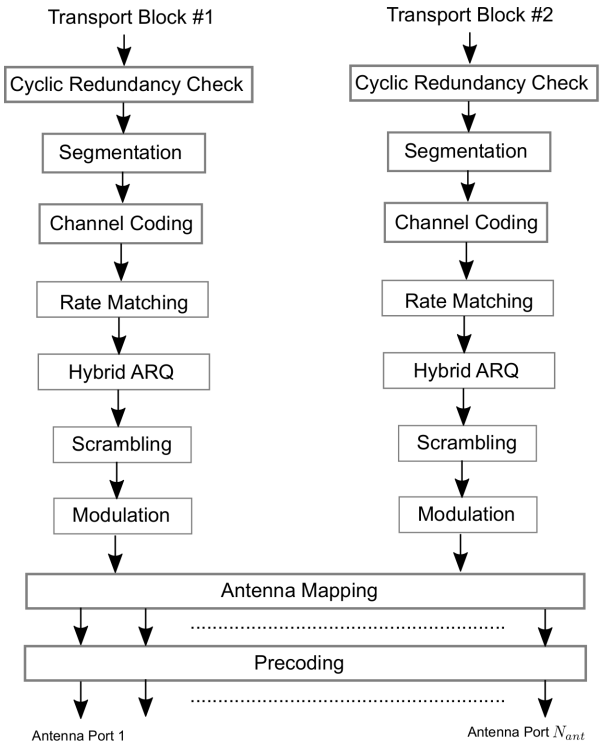

Figure A.1: Schematic diagram of the physical downlink shared channel (PDSCH) processing in LTE, LTE-Advanced and LTE-Advanced Pro [2].

the user [37], the minimum retransmission-induced latency will be $\tau_{\texttt{retx}} = 4$ ms in LTE-A Pro in the event of block decoding failure.

The output of the HARQ processing block is *bit-XORed* with a bit-level scrambling sequence, which aims to suppress narrow-band/bursty interference by spreading the errors across the sequence. The scrambled sequence is then digitally modulated using QPSK/16-QAM/64-QAM (LTE) and 256-QAM (LTE-A onwards) modulation schemes, which is determined by the MCS value used for the codeword by the scheduler. The sequence of data symbols, is then precoded using a codebook-based or non-codebook based method, if a multi-antenna transmission mode is used. Finally, the precoded transmit symbols are mapped to resource blocks to be transmitted on each antenna port, which is determined by the scheduler in LTE and beyond.

As observed in Fig. A.1, a maximum of up to *two transport blocks* (with potentially different sizes) can be allocated in one transmission time interval (TTI) for each user in LTE and NR. If spatial multiplexing is not used, the number of transport blocks allocated per TTI will be 1, and 2 otherwise. However, if a MIMO transmission mode with more than two spatial layers are used, then the appropriate precoding matrix $\mathbf{W}[n,k]$ (equations (5.3)-(5.4) of Chapter 5) is applied on the data symbols $\mathbf{x}[n,k]$, to send the precoded data vector $\mathbf{W}[n,k]\mathbf{x}[n,k]$ across all antenna ports. In other words, even if the transmission mode is supported for more than two spatial layers, the length L of the data vector $\mathbf{x}[n,k]$ for a single user cannot be more than 2.

Appendix B

Proof of Lemma 5.1

The conditional CDF of $\{D|X,\Phi\}$ can be written as

$$F_D(d|x,\phi) = \int_{\mathcal{A}_{n_R}} \int_{\mathcal{A}_{n_I}} \mathbb{P}[D \leq d|x,\phi,n] f_N(n) \mathrm{d}n,$$

where $f_N(n) = f_{N_R}(n_R) f_{N_I}(n_I)$. By equation (5.16) we can observe that D is a Rician random variable, since it is the amplitude of a complex Gaussian where the real/imaginary parts have a different mean. Thus, the integral can be transformed into polar coordinates (z,θ) to get an integral of the form

$$F_D(d|x,\phi) = \int_0^d \int_{\mathcal{A}_\theta(z)} f_{Z,\Theta}(z,\theta|x,\phi) \mathrm{d}\theta \mathrm{d}z, d \geq 0, \tag{B.1}$$

where $f_{Z,\Theta}(z,\theta|x,\phi)$ is the conditional density function of $\{Z,\Theta\}$. Depending on the value of D, there are 3 distinct regions of integration for QAM constellations: (a) $0 \leq d \leq \frac{d_c}{2}\ \forall\ x \in \mathcal{X}$, (b) $\frac{d_c}{2} \leq d \leq \frac{d_c}{\sqrt{2}}\ \forall\ x \in \mathcal{X}$, and (c) $\frac{d_c}{\sqrt{2}} \leq d \leq +\infty$ for $x \in \mathcal{X}_{\mathtt{bnd}}$. Fig. B.1 shows these regions for 16-QAM. We denote the distance of each point $x_i \in \mathcal{X}$ along the x- and y-axes to the edges of its decision region is given by $d_{x_i}^{L,R}, d_{x_i}^{U,R}$ and $d_{x_i}^{L,I}, d_{x_i}^{U,I}$ respectively. Table 5.3 shows these boundaries for points in the first quadrant of a 16-QAM constellation. Below, we derive the conditional distribution of $\{D|X,\Phi\}$ for each region, by leveraging the properties of Rician random variables.

B.1 Case 1: $0 \leq d \leq \frac{d_c}{2}\ \forall\ x^{(j)} \in \mathcal{X}$

In this case, the region of integration is *circular* with radius d as shown in Fig. B.1 (red shaded region). Defining $m_{R,j} \triangleq [x_R - x_R^{(j)} + \sqrt{P_r}\cos(\phi) + n_R], m_{I,j} \triangleq [x_I - x_I^{(j)} + \sqrt{P_r}\sin(\phi) + n_I]$, and

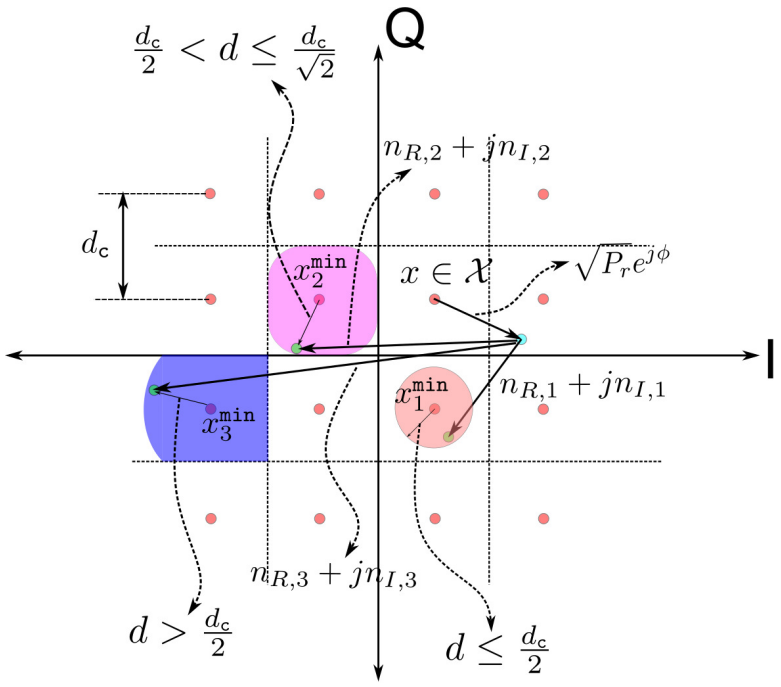

Figure B.1: Illustration of the different range of values for d, and the corresponding region of integration to derive $F_D(d)$. Cases 1 and 2 are possible for all $x \in \mathcal{X}$, but case 3 is possible only for $x \in \mathcal{X}_{\texttt{bdry}}$.

$\theta \triangleq \tan^{-1}\left(\frac{m_{I,j}}{m_{R,j}}\right)$ in equation (5.16), and conditioning on $x, x^{(j)} \in \mathcal{X}$ and $\phi \in [0, 2\pi]$, we observe that when the nearest neighbor is $x^{(j)} \in \mathcal{X}$, $\{D_{\texttt{min}}|X, \phi\} \sim \texttt{Rician}(\nu_j, \sigma^2)$ with parameters $\nu_j^2 = m_{R,j}^2 + m_{I,j}^2$ and $\sigma^2 = \frac{\sigma_n^2}{2}$. Therefore, we have

$$
\begin{aligned}
f_Z(z|x,\phi) &= \sum_{x^{(j)} \in \mathcal{X}} \frac{2z}{\sigma_n^2} e^{-\frac{z^2+\nu_j^2}{\sigma_n^2}} I_0\Big(\frac{2\nu_j d}{\sigma_n^2}\Big), \text{ for } z \geq 0, \text{ and} \\
F_D(d|x,\phi) &= \sum_{x^{(j)} \in \mathcal{X}} \int_0^d \frac{2z}{\sigma_n^2} e^{-\frac{z^2+\nu_j^2}{\sigma_n^2}} I_0\Big(\frac{2\nu_j d}{\sigma_n^2}\Big) \mathrm{d}z, \\
&\overset{(a)}{=} \sum_{x^{(j)} \in \mathcal{X}} \Big[1 - Q_1\Big(\frac{\sqrt{2}\nu_j}{\sigma_n}, \frac{\sqrt{2}d}{\sigma_n}\Big)\Big],
\end{aligned}
\tag{B.2}
$$

where $I_0(\cdot)$ is the Bessel function of the first kind with order zero, and (a) is obtained by simplifying the CDF of a Rician random variable in the form of a Marcum Q-function $Q_M(a,b)$ with parameters (M,a,b) [139].

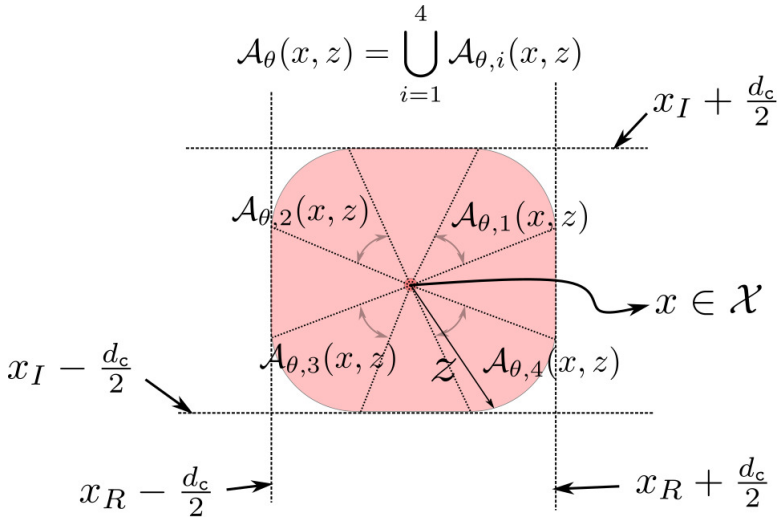

Figure B.2: Illustration of the limits of θ in equation (B.4) when $x \in \mathcal{X}_{\texttt{int}}$.

B.2 Case 2: $\frac{d_c}{2} \leq d \leq \frac{d_c}{\sqrt{2}} \; \forall \; x^{(j)} \in \mathcal{X}$

In this case, the integration region for each point x_j is a *'truncated' circle*, as shown in Fig. B.1 (pink colored region). The minimum distance D is a Rician random variable with a *radially asymmetric integration region.* Therefore, the conditional density in polar coordinates is given by

$$f_{Z,\Theta}(z,\theta|x,\phi) = \sum_{x^{(j)} \in \mathcal{X}} \frac{z}{\pi\sigma_n^2} e^{-\frac{z^2+\nu_j^2+2zm_j}{\sigma_n^2}}, \tag{B.3}$$

for $z \geq 0, 0 \leq \theta \leq 2\pi$. The region of integration of Θ for $x \in \mathcal{X}$ is a function of z, given by

$$\mathcal{A}_\theta(x,z) = \left\{\theta \middle| d_x^{L,R} \leq z\cos\theta \leq d_x^{U,R}, d_x^{L,I} \leq z\sin\theta \leq d_x^{U,I}\right\}.$$

For $x \in \mathcal{X}_{\texttt{int}}$, the above can be simplified as

$$\begin{aligned}\mathcal{A}_\theta(x,z) =& \bigcup_{i=1}^{4} \mathcal{A}_{\theta,i}(x,z), \text{ where} \\ \mathcal{A}_{\theta,i}(x,z) =& \left\{\theta \middle| (i-1)\frac{\pi}{2} + \cos^{-1}\left(\frac{d_c}{2z}\right) \leq \theta \leq (i-1)\frac{\pi}{2} + \sin^{-1}\left(\frac{d_c}{2z}\right)\right\}.\end{aligned} \tag{B.4}$$

Fig. B.2 shows an example of the integration region for $x^{(j)} \in \mathcal{X}_{\texttt{int}}$. Using (B.3)-(B.4) and marginalizing Θ and X, we obtain the desired result.

$$F_D(d|x,\phi) = \sum_{x^{(j)} \in \mathcal{X}} \int_0^d \int_{\mathcal{A}_\theta(x^{(j)},z)} \frac{z}{\pi\sigma_n^2} e^{-\frac{z^2+\nu_j^2+2zm_j}{\sigma_n^2}} \mathrm{d}\theta\mathrm{d}z. \tag{B.5}$$

B.3 Cases 3 and 4: $d \geq \frac{d_{\mathtt{c}}}{\sqrt{2}}$ for all $x^{(j)} \in \mathcal{X}$

Derivation of the conditional CDF is similar to that in Case 2. The additional constraint here is that $F_{D|X,\Phi}(d|x,\phi)$ is non-zero iff $x^{(j)} \in \mathcal{X}_{\mathtt{bnd}}$. This is because for interior points, $0 \leq D_{\mathtt{min}} \leq \frac{d_{\mathtt{c}}}{\sqrt{2}}$ is always true for QAM modulation schemes, as illustrated in Fig. B.1. Therefore, the conditional distribution is given by

$$F_D(d|x,\phi) = F_D\Big(\frac{d_{\mathtt{c}}}{\sqrt{2}}\Big|x,\phi\Big) + \sum_{x^{(j)}\in\mathcal{X}_{\mathtt{bnd}}} \int_0^d \int_{\mathcal{A}_\theta(x^{(j)},z)} \frac{z}{\pi\sigma_n^2} e^{-\frac{z^2+\nu_j^2+2zm_j}{\sigma_n^2}} \mathrm{d}\theta \mathrm{d}z, \text{ for } d \geq \frac{d_{\mathtt{c}}}{\sqrt{2}}. \quad \text{(B.6)}$$

Appendix C

Proofs from Chapter 6

C.1 Proof of Lemma 6.2

The steering vector of a $N_{\mathtt{az}} \times N_{\mathtt{el}}$ URA is $\mathbf{a}(\theta,\phi) = \mathbf{a}_{\mathtt{az}}(\theta,\phi) \otimes \mathbf{a}_{\mathtt{el}}(\phi)$, where $\otimes$ is the Kronecker product. For $\frac{\lambda}{2}$-spacing,

$$\begin{aligned}\mathbf{a}_{\mathtt{az}}(\theta,\phi) &= [1\ e^{-j\pi \sin\theta\cos\phi} \cdots e^{-j\pi(N_{\mathtt{az}}-1)\sin\theta\cos\phi}] \in \mathbb{C}^{N_{\mathtt{az}}\times 1},\\ \mathbf{a}_{el}(\phi) &= [1\ e^{-j\pi \sin\phi} \cdots e^{-j\pi(N_{\mathtt{el}}-1)\sin\phi}] \in \mathbb{C}^{N_{\mathtt{el}}\times 1}.\end{aligned}$$

Using the properties of the Kronecker product, expanding and simplifying, we get

$$G_{\mathtt{BS}}(\theta,\phi,\theta_k,\phi_k) = \frac{\sin^2\left(\frac{\pi}{2}N_{\mathtt{az}}(\sin\theta\cos\phi - \sin\theta_k\cos\phi_k)\right)}{N_{\mathtt{az}}\sin^2\left(\frac{\pi}{2}(\sin\theta\cos\phi - \sin\theta_k\cos\phi_k)\right)} \cdot \frac{\sin^2\left(\frac{\pi}{2}N_{\mathtt{el}}(\sin\phi - \sin\phi_k)\right)}{N_{\mathtt{el}}\sin^2\left(\frac{\pi}{2}(\sin\phi - \sin\phi_k)\right)} \leq N_{\mathtt{az}}N_{\mathtt{al}}. \tag{C.1}$$

Since $\frac{\sin^2(Na)}{\sin^2 a} \leq N^2$ for $a \in \mathbb{R}$, the universal upper bound is obtained above, and is achieved when $a = 0$. To obtain a tighter bound $G_{\mathtt{BS}}^{(\mathtt{max})}$ defined in (6.6), we consider the following.

C.1.1 Case 1

If $\phi_{\mathtt{m}} \leq \phi \leq \frac{\pi}{2}$, $G_{\mathtt{BS}}(\theta,\phi,\theta_k,\phi_k)$ is maximized by $\phi_k = \phi, \theta_k = \theta$, yielding $G_{\mathtt{BS}}^{(\mathtt{max})}(\phi,\phi_{\mathtt{m}}) = N_{\mathtt{az}}N_{\mathtt{el}}$.

C.1.2 Case 2

By upper bounding the *azimuth beamforming gain* in (C.1), we get

$$G_{\mathtt{BS}}(\theta,\phi,\theta_k,\phi_k) \leq N_{\mathtt{az}}\frac{\sin^2\left(\frac{\pi}{2}N_{\mathtt{el}}(\sin\phi - \sin\phi_k)\right)}{N_{\mathtt{el}}\sin^2\left(\frac{\pi}{2}(\sin\phi - \sin\phi_k)\right)}. \tag{C.2}$$

The RHS monotonically decreases w.r.t. ϕ_k when $0 \leq \sin\phi_{\mathtt{m}} \leq \frac{1+N_{\mathtt{el}}\sin\phi}{N_{\mathtt{el}}} \leq \frac{\pi}{2}$ and hence, the upper bound is $G_{\mathtt{BS}}^{(\mathtt{max})}(\phi,\phi_{\mathtt{m}}) = \frac{N_{\mathtt{az}}\sin^2\left(\frac{\pi}{2}N_{\mathtt{el}}(\sin\phi-\sin\phi_{\mathtt{m}})\right)}{N_{\mathtt{el}}\sin^2\left(\frac{\pi}{2}(\sin\phi-\sin\phi_{\mathtt{m}})\right)}$.

C.1.3 Case 3

If $\frac{1+N_{\mathtt{el}}\sin\phi}{N_{\mathtt{el}}} \leq \sin\phi_{\mathtt{m}}$, the numerator of $G_{\mathtt{BS}}^{(\mathtt{max})}(\cdot)$ in case 2 can be upper bounded as $\sin^2(b) \leq 1\ \forall\ b \in \mathbb{R}$, resulting in a monotonically decreasing function of $\phi_{\mathtt{m}}$. Hence, $G_{\mathtt{BS}}^{(\mathtt{max})}(\phi,\phi_{\mathtt{m}}) = \frac{N_{\mathtt{az}}}{N_{\mathtt{el}}\sin^2\left(\frac{\pi}{2}(\sin\phi-\sin\phi_{\mathtt{m}})\right)}$.

Remark C.1. *The upper bound on the beamforming gain is independent of the azimuth angle, since the maximum azimuth beamforming gain can be upper bounded by $N_{\mathtt{az}}$. Therefore for the sake of simplicity, we consider that the boresight of each BS is aligned along the direction of the radar, which corresponds to $\theta = 0^\circ$ as discussed in Assumption 6.2.*

C.2 Proof of Theorem 6.2

Since the massive MIMO BS locations are modeled as an independent PPPs $\mathbf{\Phi_{BS}}$ with intensity $\lambda_{\mathtt{BS}}$, the worst-case average interference at the radar is given by Campbell's theorem using

$$\begin{aligned}\bar{I}_{\mathtt{rad,c}} &= \mathbb{E}\Big[\mathbb{E}\Big[\sum_{\mathbf{X}\in\mathbf{\Phi_{int}}}\{I_{\mathtt{rad}}^{(\mathtt{w})}(\mathbf{X},h_{\mathtt{BS}},h_{\mathtt{rad}})|r_c\}\Big]\Big|r_c\Big]\\ &= \mathbb{E}\Big[\int_{\mathbf{x}\in\mathbf{\Phi_{int}}}\lambda_{\mathtt{BS}}\{I_{\mathtt{rad}}^{(\mathtt{w})}(\mathbf{x},h_{\mathtt{BS}},h_{\mathtt{rad}})|r_c\}\mathrm{d}\mathbf{x}\Big|r_c\Big],\end{aligned}$$

where $\mathbf{x} = [r\cos\theta_{r,L}\ r\sin\theta_{r,L}]$, $\mathbf{\Phi_{int}} = \mathbf{\Phi_{BS}} \setminus \{(x,y)|(x^2+y^2) \leq r_{\mathtt{exc}}^2\}$, and r_c is the cell radius that determines $G_{\mathtt{BS}}^{(\mathtt{max})}(\phi,\phi_{\mathtt{m}})$ in equation (6.6). Substituting (6.4) above, noting that $\phi_{r,L}(r) = -\phi_{t,L}(r) = \tan^{-1}\left(\frac{h_{\mathtt{rad}}-h_{\mathtt{BS}}}{r}\right)$, and converting to polar coordinates we get

$$\bar{I}_{\mathtt{rad,c}} = \mathbb{E}\Big[\int_{r_{\mathtt{exc}}}^{\infty}\int_{-\frac{\pi}{2}}^{\frac{\pi}{2}}\lambda_{\mathtt{BS}}\beta(d)G_{\mathtt{rad}}(\theta_{\mathtt{rad}},\phi_{\mathtt{rad}},\theta_{r,L},\phi_{r,L}(r))G_{\mathtt{BS}}^{(\mathtt{max})}(\phi_{t,L}(r),\phi_{\mathtt{m}}(r_c))\tfrac{P_{BS}}{K}r\mathrm{d}r\mathrm{d}\theta_{r,L}\Big|r_c\Big],$$

where $d = \sqrt{r^2+(h_{\mathtt{BS}}-h_{\mathtt{rad}})^2}$, and $\beta(d) = PL(r_0)d^{-\alpha}$ is the pathloss model. Using these and integrating over $r_c \sim f_{R_c}(r_c)$, we get the desired result.

C.3 Proof of Lemma 6.3

Since $r_{\texttt{exc}}$ is much larger than the antenna heights, we have $\phi(r) \to 0$ for $r \geq r_{\texttt{exc}}$ in equation (6.14) and (6.15). Using this, the radar beamforming gain can be upper bounded similar to (C.1) using

$$\begin{aligned} G_{\texttt{rad}}(\theta_{\texttt{rad}}, \phi_{\texttt{rad}}, \theta, 0) &= \frac{\sin^2\left(\frac{\pi}{2} N_{\texttt{az}}^{(\texttt{rad})}(\sin\theta_{\texttt{rad}}\cos\phi_{\texttt{rad}} - \sin\theta)\right)\sin^2\left(\frac{\pi}{2} N_{\texttt{el}}^{(\texttt{rad})}\sin\phi_{\texttt{rad}}\right)}{N_{\texttt{az}}^{(\texttt{rad})} N_{\texttt{el}}^{(\texttt{rad})}\sin^2\left(\frac{\pi}{2}(\sin\theta_{\texttt{rad}}\cos\phi_{\texttt{rad}} - \sin\theta)\right)\sin^2\left(\frac{\pi}{2}\sin\phi_{\texttt{rad}}\right)} \\ &\leq \frac{N_{\texttt{az}}^{(\texttt{rad})}\sin^2\left(\frac{\pi}{2} N_{\texttt{el}}^{(\texttt{rad})}\sin\phi_{\texttt{rad}}\right)}{N_{\texttt{el}}^{(\texttt{rad})}\sin^2\left(\frac{\pi}{2}\sin\phi_{\texttt{rad}}\right)}. \end{aligned}$$

We note that the maximum azimuth beamforming gain of $N_{\texttt{az}}$ is always achieved at $\theta_{\texttt{max}} = \sin^{-1}(\sin\theta_{\texttt{rad}}\cos\phi_{\texttt{rad}})$. Therefore, the maximum radar beamforming gain is only a function of $\phi_{\texttt{rad}}$. For similar reasons, when $\phi(r) \to 0$, $G_{BS}^{(\texttt{max})}(\cdot)$ is only a function of the minimum elevation angle, which in turn is a function of $h_{\texttt{BS}}\sqrt{\lambda_{\texttt{BS}}}$.

Defining $I_{\texttt{dom}}$ to be the interference power due to the BS at $(r_{\texttt{dom}}, \theta_{\texttt{max}})$, given by

$$I_{\texttt{dom}} = \frac{P_{BS} PL(r_0) G_{\texttt{BS}}^{(\texttt{max})}(0, \phi_{\texttt{m}}(1/\sqrt{\pi\lambda_{\texttt{BS}}}))}{K r_{\texttt{dom}}^{\alpha}} \cdot \frac{N_{\texttt{az}}^{(\texttt{rad})}\sin^2\left(\frac{\pi}{2} N_{\texttt{el}}^{(\texttt{rad})}\sin\phi_{\texttt{rad}}\right)}{N_{\texttt{el}}^{(\texttt{rad})}\sin^2\left(\frac{\pi}{2}\sin\phi_{\texttt{rad}}\right)}, r_{\texttt{dom}} \geq r_{\texttt{exc}}. \quad \text{(C.3)}$$

Substituting this into equation (6.15) and simplifying, we get the analytical expression of $\mathcal{C}(I_{\texttt{dom}})$.

C.4 Proof of Lemma 6.4

Let $\mathcal{A}(r_{\texttt{dom}})$ denote the region outside the exclusion zone enclosed by $\mathcal{C}(r_{\texttt{dom}})$, and $A(r_{\texttt{dom}})$ denote the corresponding area. Using equation (6.14), this region can be written as

$$\begin{aligned} \mathcal{A}(r_{\texttt{dom}}) = \Bigg\{(r,\theta)\Bigg| & r_{\texttt{exc}} \leq r \leq \max\left(r_{\texttt{exc}}, r_{\texttt{dom}}\left[\frac{\sin\left(\frac{\pi}{2} N_{\texttt{az}}^{(\texttt{rad})}(\sin\theta_{\texttt{rad}}\cos\phi_{\texttt{rad}} - \sin\theta)\right)}{N_{\texttt{az}}^{(\texttt{rad})}\sin^2\left(\frac{\pi}{2}(\sin\theta_{\texttt{rad}}\cos\phi_{\texttt{rad}} - \sin\theta)\right)}\right]^{\frac{2}{\alpha}}\right), \\ & -\frac{\pi}{2} \leq \theta \leq \frac{\pi}{2}\Bigg\}. \end{aligned} \quad \text{(C.4)}$$

Defining $\tilde{r}_{\texttt{dom}}(\theta) \triangleq r_{\texttt{dom}}\left[\frac{\sin\left(\frac{\pi}{2}N_{\texttt{az}}^{(\texttt{rad})}(\sin\theta_{\texttt{rad}}\cos\phi_{\texttt{rad}}-\sin\theta)\right)}{N_{\texttt{az}}^{(\texttt{rad})}\sin\left(\frac{\pi}{2}(\sin\theta_{\texttt{rad}}\cos\phi_{\texttt{rad}}-\sin\theta)\right)}\right]^{\frac{2}{\alpha}}$ and using equation (C.4), the area $A(r_{\texttt{dom}})$ is given by

$$\begin{aligned} A(r_{\texttt{dom}}) &= \int_{-\frac{\pi}{2}}^{\frac{\pi}{2}} \int_{r_{\texttt{exc}}}^{\max(r_{\texttt{exc}},\tilde{r}_{\texttt{dom}}(\theta))} r\mathrm{d}r\mathrm{d}\theta \\ &= \frac{1}{2}\int_{-\frac{\pi}{2}}^{\frac{\pi}{2}} \max\left(r_{\texttt{exc}}^2, \tilde{r}_{\texttt{dom}}^2(\theta)\right)\mathrm{d}\theta - \frac{\pi r_{\texttt{exc}}^2}{2}. \end{aligned} \tag{C.5}$$

Expanding and simplifying, we get the desired result.

C.5 Proof of Lemma 6.5

The distribution of $r_{\texttt{dom}}$ is given by $F_{R_{\texttt{dom}}}(r_{\texttt{dom}}) = \mathbb{P}[R_{\texttt{dom}} \leq r_{\texttt{dom}}]$. Since the area outside the exclusion zone enclosed by the contour is $A(r_{\texttt{dom}})$, the CDF is the void probability given by

$$F_{R_{\texttt{dom}}}(r_{\texttt{dom}}) = 1 - \exp\left(-\lambda_{\texttt{BS}}A(r_{\texttt{dom}})\right), \text{ for } r_{\texttt{dom}} \geq r_{\texttt{exc}}. \tag{C.6}$$

Substitution equation (6.17) in the above, we get the desired CDF. Further, differentiating equation (C.6), the density of $r_{\texttt{dom}}$ can be written as

$$f_{R_{\texttt{dom}}}(r_{\texttt{dom}}) = \frac{\mathrm{d}A(r_{\texttt{dom}})}{\mathrm{d}r_{\texttt{dom}}} \cdot \lambda_{\texttt{BS}} e^{-\lambda_{\texttt{BS}}A(r_{\texttt{dom}})}, \text{ for } r_{\texttt{dom}} \geq r_{\texttt{exc}}. \tag{C.7}$$

Due to the presence of the $\max(\cdot)$ term in equation (6.17), it can be shown that $A(r_{\texttt{dom}})$ depends on $r_{\texttt{dom}}$ only in certain ranges of θ, which can also be observed in Fig. 6.3b. Hence, we get

$$\frac{\mathrm{d}[\max(r_{\texttt{exc}}^2, \tilde{r}_{\texttt{dom}}^2(\theta))]}{\mathrm{d}r_{\texttt{dom}}} = \begin{cases} 2r_{\texttt{dom}}\left[\frac{\sin^2\left(\frac{\pi}{2}N_{\texttt{az}}(\sin\theta_{\texttt{rad}}\cos\phi_{\texttt{rad}}-\sin\theta)\right)}{N_{\texttt{az}}^2\sin^2\left(\frac{\pi}{2}(\sin\theta_{\texttt{rad}}\cos\phi_{\texttt{rad}}-\sin\theta)\right)}\right]^{2/\alpha} & \text{if } \tilde{r}_{\texttt{dom}}(\theta) \geq r_{\texttt{exc}} \\ 0 & \text{otherwise} \end{cases}, \tag{C.8}$$

Substituting this into (C.7) and representing it in terms of the indicator function, we obtain the desired result.

C.6 Proof of Theorem 6.4

The dominant interference power is given by $I_{\texttt{dom}} = \kappa r_{\texttt{dom}}^{-\alpha}$. Next, we compute the average interference power due to the rest of the network, conditioned on $I_{\texttt{dom}}$, i.e. $\mathbb{E}[I_{\texttt{rest}}|I_{\texttt{dom}}]$. Due to

the bijection between $r_{\mathtt{dom}}$ and $I_{\mathtt{dom}}$ in the AAECC model, we have $\mathbb{E}[I_{\mathtt{rest}}|I_{\mathtt{dom}}] = \mathbb{E}[I_{\mathtt{rest}}|r_{\mathtt{dom}}]$. Hence, we can compute the conditional average interference power using

$$\mathbb{E}[I_{\mathtt{rest}}|I_{\mathtt{dom}}] = \frac{P_{BS}\lambda_{\mathtt{BS}}G_{\mathtt{BS}}(0,\phi_{\mathtt{m}}(1/\sqrt{\pi\lambda_{\mathtt{BS}}}))PL(r_0)}{K}\int_{-\frac{\pi}{2}}^{\frac{\pi}{2}}\int_{\max(r_{\mathtt{exc}},\tilde{r}_{\mathtt{dom}}(\theta))}^{\infty} G_{\mathtt{rad}}(0,\phi_{\mathtt{rad}},\theta,0)r^{-\alpha+1}\mathrm{d}r\mathrm{d}\theta$$

$$\overset{(a)}{=} \frac{\kappa}{\alpha-2}\int_{-\frac{\pi}{2}}^{\frac{\pi}{2}}\left[\max\left(r_{\mathtt{exc}},\tilde{r}_{\mathtt{dom}}(\theta)\right)\right]^{-\alpha+2}\frac{G_{\mathtt{rad}}(\theta_{\mathtt{rad}},\phi_{\mathtt{rad}},\theta,0)}{G_{\mathtt{rad}}(0,\phi_{\mathtt{rad}},0,0)}\mathrm{d}\theta. \tag{C.9}$$

The equality in (a) is obtained by defining $\kappa \triangleq \frac{P_{BS}\lambda_{\mathtt{BS}}G_{\mathtt{rad}}(0,\phi_{\mathtt{rad}},0,0)G_{\mathtt{BS}}(0,\phi_{\mathtt{m}}(1/\sqrt{\pi\lambda_{\mathtt{BS}}}))PL(r_0)}{K}$, and evaluating the inner integral. Using Lemma 6.3 and equation (C.9) in equation (6.13) and simplifying, we get the desired result.

C.7 Proof of Theorem 6.5

We note that under hypothesis $\mathcal{H}_i$, the received power is $P_{\mathtt{rad},i}$ for $i = \{0,1\}$. In addition, by definition we have $\mathbb{P}[P_{\mathtt{rad},i} > P_{\mathtt{th}}|I_{\mathtt{tot}}] = 1 - F_{P_{\mathtt{rad},i}}(P_{\mathtt{th}}|I_{\mathtt{tot}})$. Therefore, using Lemma 6.7, we can write equation (6.28) as

$$\bar{P}_{\mathtt{d}} = 1 - \int_0^{\infty} Q_N\left(\sqrt{\frac{2NP_{\mathtt{tar}}}{I_{\mathtt{tot}}+\sigma_n^2}}, \sqrt{\frac{2NP_{\mathtt{th}}}{I_{\mathtt{tot}}+\sigma_n^2}}\right) f_{I_{\mathtt{tot}}}(x)\mathrm{d}x,$$

$$\bar{P}_{\mathtt{fa}} = 1 - \int_0^{\infty} \frac{1}{(N-1)!}\gamma_l\left(N, \frac{NP_{\mathtt{th}}}{I_{\mathtt{tot}}+\sigma_n^2}\right) f_{I_{\mathtt{tot}}}(x)\mathrm{d}x. \tag{C.10}$$

Using Assumption 6.5 and Theorem 6.4, and changing the upper limit to $I_{\mathtt{exc}} + \bar{I}_{\mathtt{rad,a}}$ (Remark 6.2), we get an approximation $I_{\mathtt{tot,DI}}$ of total interference power $I_{\mathtt{tot}}$. Using the bijection between $r_{\mathtt{dom}}$ and $I_{\mathtt{tot,DI}}$ (Corollary 6.3), the final result is obtained by substituting $I_{\mathtt{tot,DI}}$ by $r_{\mathtt{dom}}$, and applying the chain rule.

Bibliography

[1] V. Marojevic, D. Chheda, R. M. Rao, R. Nealy, J. M. Park, and J. H. Reed, "Software-Defined LTE Evolution Testbed Enabling Rapid Prototyping and Controlled Experimentation," in *2017 IEEE Wireless Communications and Networking Conference (WCNC)*, March 2017, pp. 1–6.

[2] E. Dahlman, S. Parkvall, and J. Skold, *5G NR: The Next Generation Wireless Access Technology*. Academic Press, 2018.

[3] "Cisco Visual Networking Index: Global Mobile Data Traffic Forecast Update, 2017–2022 White Paper," *Cisco*, 2019. [Online]. Available: https://www.cisco.com/c/en/us/solutions/collateral/service-provider/visual-networking-index-vni/white-paper-c11-738429.html

[4] T. L. Marzetta, "Noncooperative Cellular Wireless with Unlimited Numbers of Base Station Antennas," *IEEE Transactions on Wireless Communications*, vol. 9, no. 11, pp. 3590–3600, November 2010.

[5] A. Adhikary, J. Nam, J. Ahn, and G. Caire, "Joint Spatial Division and Multiplexing—The Large-Scale Array Regime," *IEEE Transactions on Information Theory*, vol. 59, no. 10, pp. 6441–6463, Oct 2013.

[6] X. Gao, O. Edfors, F. Rusek, and F. Tufvesson, "Massive MIMO Performance Evaluation Based on Measured Propagation Data," *IEEE Transactions on Wireless Communications*, vol. 14, no. 7, pp. 3899–3911, July 2015.

[7] J. Flordelis, F. Rusek, F. Tufvesson, E. G. Larsson, and O. Edfors, "Massive MIMO Performance—TDD Versus FDD: What Do Measurements Say?" *IEEE Transactions on Wireless Communications*, vol. 17, no. 4, pp. 2247–2261, April 2018.

[8] G. Xu, Y. Li, J. Yuan, R. Monroe, S. Rajagopal, S. Ramakrishna, Y. H. Nam, J. Seol, J. Kim, M. M. U. Gul, A. Aziz, and J. Zhang, "Full Dimension MIMO (FD-MIMO): Demonstrating Commercial Feasibility," *IEEE Journal on Selected Areas in Communications*, vol. 35, no. 8, pp. 1876–1886, Aug 2017.

[9] H. Ji, Y. Kim, J. Lee, E. Onggosanusi, Y. Nam, J. Zhang, B. Lee, and B. Shim, "Overview of Full-Dimension MIMO in LTE-Advanced Pro," *IEEE Communications Magazine*, vol. 55, no. 2, pp. 176–184, February 2017.

[10] 3GPP, "5G; NR; Physical Channels and Modulation," *3GPP TS 38.211 v15.4.0*, Jan 2019.

[11] G. I. Tsiropoulos, O. A. Dobre, M. H. Ahmed, and K. E. Baddour, "Radio Resource Allocation Techniques for Efficient Spectrum Access in Cognitive Radio Networks," *IEEE Communications Surveys Tutorials*, vol. 18, no. 1, pp. 824–847, Firstquarter 2016.

[12] F. Hessar and S. Roy, "Spectrum Sharing Between a Surveillance Radar and Secondary Wi-Fi Networks," *IEEE Transactions on Aerospace and Electronic Systems*, vol. 52, no. 3, pp. 1434–1448, June 2016.

[13] M. Mehrnoush and S. Roy, "Coexistence of WLAN Network With Radar: Detection and Interference Mitigation," *IEEE Transactions on Cognitive Communications and Networking*, vol. 3, no. 4, pp. 655–667, 2017.

[14] R. Saruthirathanaworakun, J. M. Peha, and L. M. Correia, "Opportunistic Sharing Between Rotating Radar and Cellular," *IEEE Journal on Selected Areas in Communications*, vol. 30, no. 10, pp. 1900–1910, November 2012.

[15] A. Khawar, A. Abdel-Hadi, and T. C. Clancy, "Spectrum Sharing between S-Band Radar and LTE Cellular System: A Spatial Approach," in *2014 IEEE International Symposium on Dynamic Spectrum Access Networks (DYSPAN)*, April 2014, pp. 7–14.

[16] J. H. Reed, A. W. Clegg, A. V. Padaki, T. Yang, R. Nealy, C. Dietrich, C. R. Anderson, and D. M. Mearns, "On the Co-Existence of TD-LTE and Radar Over 3.5 GHz Band: An Experimental Study," *IEEE Wireless Communications Letters*, vol. 5, no. 4, pp. 368–371, Aug 2016.

[17] Z. Khan, J. J. Lehtomaki, R. Vuohtoniemi, E. Hossain, and L. A. Dasilva, "On Opportunistic Spectrum Access in Radar Bands: Lessons Learned from Measurement of Weather Radar Signals," *IEEE Wireless Communications*, vol. 23, no. 3, pp. 40–48, June 2016.

[18] X. Yuan, X. Qin, F. Tian, Y. T. Hou, W. Lou, S. F. Midkiff, and J. H. Reed, "Coexistence Between Wi-Fi and LTE on Unlicensed Spectrum: A Human-Centric Approach," *IEEE Journal on Selected Areas in Communications*, vol. 35, no. 4, pp. 964–977, April 2017.

[19] S. Han, Y. Liang, Q. Chen, and B. Soong, "Licensed-Assisted Access for LTE in Unlicensed Spectrum: A MAC Protocol Design," *IEEE Journal on Selected Areas in Communications*, vol. 34, no. 10, pp. 2550–2561, Oct 2016.

[20] Michael Kratsios, "Emerging Technologies and their Expected Impact on Non-Federal Spectrum Demand," *Executive Office of the President of the United States*, May 2019.

[21] FCC, "Amendment of the Commission's Rules with Regard to Commercial Operations in the 3550-3650 MHz Band," *Federal Communications Commission, Report and Order and Second Further Notice of Proposed Rulemaking*, April 2015.

[22] ——, "Revision of Part 15 of the Commission's Rules to Permit Unlicensed National Information Infrastructure (U-NII) Devices in the 5 GHz Band," *Federal Communications Commission, First Report and Order*, April 2014.

[23] ——, "Use of Spectrum Bands Above 24 GHz for Mobile Radio Services, document GN Docket 14–177," *Federal Communications Commission, Report and Order and Second Further Notice of Proposed Rulemaking*, July 2016.

[24] H. Kwon, J. Jeon, A. Bhorkar, Q. Ye, H. Harada, Y. Jiang, L. Liu, S. Nagata, B. L. Ng, T. Novlan, J. Oh, and W. Yi, "Licensed-Assisted Access to Unlicensed Spectrum in LTE Release 13," *IEEE Communications Magazine*, vol. 55, no. 2, pp. 201–207, February 2017.

[25] "3GPP Commits to 5G NR in Unlicensed Spectrum in its Next Release," *Qualcomm Technologies Inc.*, 2018. [Online]. Available: https://www.qualcomm.com/news/onq/2018/12/13/3gpp-commits-5g-nr-unlicensed-spectrum-its-next-release

[26] ETSI, "LTE, Evolved Universal Terrestrial Radio Access (E-UTRA), Requirements for support of radio resource management (3GPP TS 36.133 v 10.1.0), Release 10," *3GPP*, 2011.

[27] E. Uhlemann, "Initial Steps Toward a Cellular Vehicle-to-Everything Standard [Connected Vehicles]," *IEEE Vehicular Technology Magazine*, vol. 12, no. 1, pp. 14–19, March 2017.

[28] 3GPP, "3rd Generation Partnership Project; Technical Specification Group Radio Access Network; Study on New Radio (NR) to support non terrestrial networks (Release 15)," *3rd Generation Partnership Project; Technical Specification Group Radio Access Network; Evolved Universal Terrestrial Radio Access*, 2014.

[29] R. M. Rao, V. Marojevic, and J. H. Reed, "Adaptive Pilot Patterns for CA-OFDM Systems in Nonstationary Wireless Channels," *IEEE Transactions on Vehicular Technology*, vol. 67, no. 2, pp. 1231–1244, Feb 2018.

[30] R. M. Rao, V. Marojevic, and J. Reed, "Rate-Maximizing OFDM Pilot Patterns for UAV Communications in Nonstationary A2G Channels," in *2018 IEEE Vehicular Technology Conference (VTC-Fall2018)*, Aug 2018, pp. 1–5.

[31] 3GPP, "5G New Radio: 3GPP Release 15," 2017. [Online]. Available: http://www.3gpp.org/release-15

[32] M. Agiwal, A. Roy, and N. Saxena, "Next Generation 5G Wireless Networks: A Comprehensive Survey," *IEEE Communications Surveys Tutorials*, vol. 18, no. 3, pp. 1617–1655, 3rd Quarter 2016.

[33] A. A. Zaidi, R. Baldemair, V. Moles-Cases, N. He, K. Werner, and A. Cedergren, "OFDM Numerology Design for 5G New Radio to Support IoT, eMBB, and MBSFN," *IEEE Communications Standards Magazine*, vol. 2, no. 2, pp. 78–83, 2018.

[34] S. Schwarz and M. Rupp, "Society in Motion: Challenges for LTE and Beyond Mobile Communications," *IEEE Communications Magazine*, vol. 54, no. 5, pp. 76–83, May 2016.

[35] F. Zhu, A. Liu, and V. Lau, "Compressive CSIT Estimation for Multi-User Massive MIMO with Autonomous Adaptation of Pilot and Feedback," in *2016 IEEE International Conference on Communications (ICC)*, May 2016, pp. 1–6.

[36] J. Kakar and V. Marojevic, "Waveform and Spectrum Management for Unmanned Aerial Systems beyond 2025," in *Proc. IEEE International Symposium on Personal, Indoor and Mobile Radio Communications (PIMRC)*, October 2017.

[37] S. Sesia, M. Baker, and I. Toufik, *LTE-The UMTS Long Term Evolution: From Theory to Practice*. John Wiley & Sons, 2011.

[38] I. Barhumi, G. Leus, and M. Moonen, "Optimal Training Design for MIMO-OFDM Systems in Mobile Wireless Channels," *IEEE Transactions on Signal Processing*, vol. 51, no. 6, pp. 1615–1624, June 2003.

[39] W. Zhang, X.-G. Xia, and P.-C. Ching, "Optimal Training and Pilot Pattern Design for OFDM Systems in Rayleigh Fading," *Broadcasting, IEEE Transactions on*, vol. 52, no. 4, pp. 505–514, 2006.

[40] O. Simeone and U. Spagnolini, "Adaptive Pilot Pattern for OFDM Systems," in *Communications, 2004 IEEE International Conference on*, vol. 2. IEEE, 2004, pp. 978–982.

[41] J. Byun and N. P. Natarajan, "Adaptive Pilot Utilization for OFDM Channel Estimation in a Time Varying Channel," in *IEEE 10th Annual Wireless and Microwave Technology Conference (WAMICON'09)*. IEEE, 2009, pp. 1–5.

[42] A. R. Ali, A. Balalem, T. Khanzada, J. Machac, and A. Omar, "Adaptive Pilot Distribution for OFDM Systems in Time-Variant Channels," in *IEEE Asia-Pacific Microwave Conference*, 2008, pp. 1–4.

[43] Z. Sheng, H. D. Tuan, Y. Fang, H. H. M. Tam, and Y. Sun, "Data Rate Maximization based Power Allocation for OFDM System in a High-Speed Train Environment," in *Signal and Information Processing (GlobalSIP), IEEE Global Conference on*. IEEE, 2015, pp. 265–269.

[44] M. Karami and N. C. Beaulieu, "Channel Adaptive Power Allocation and Pilot Optimization for OFDM Systems," in *Global Communications Conference (GLOBECOM), 2012 IEEE*. IEEE, 2012, pp. 4893–4898.

[45] M. Šimko, Q. Wang, and M. Rupp, "Optimal Pilot Symbol Power Allocation under Time-variant Channels," *EURASIP Journal on Wireless Communications and Networking*, vol. 2012, no. 1, p. 225, 2012.

[46] M. Simko, P. S. Diniz, Q. Wang, and M. Rupp, "Adaptive Pilot-Symbol Patterns for MIMO OFDM Systems," *Wireless Communications, IEEE Transactions on*, vol. 12, no. 9, pp. 4705–4715, 2013.

[47] Y. Kim, G. Miao, and T. Hwang, "Energy Efficient Pilot and Link Adaptation for Mobile Users in TDD Multi-User MIMO Systems," *IEEE Transactions on Wireless Communications*, vol. 13, no. 1, pp. 382–393, January 2014.

[48] N. Ksairi, B. Tomasi, and S. Tomasin, "Pilot Pattern Adaptation for 5G MU-MIMO Wireless Communications," in *2016 IEEE 17th International Workshop on Signal Processing Advances in Wireless Communications (SPAWC)*, July 2016, pp. 1–6.

[49] X. Xu, G. He, S. Zhang, Y. Chen, and S. Xu, "On Functionality Separation for Green Mobile Networks: Concept Study over LTE," *IEEE Communications Magazine*, vol. 51, no. 5, pp. 82–90, May 2013.

[50] ETSI, "3rd Generation Partnership Project; Technical Specification Group Radio Access Network; NR; Physical layer procedures for control (3GPP TS 38.213), Release 15," *3GPP*, November 2017.

[51] "WiMAX System Evaluation Methodology," *WiMAX Forum*, July 7, 2008. [Online]. Available: http://www.cse.wustl.edu/~jain/wimax/ftp/wimax_system_evaluation_methodology_v2_1.pdf

[52] G. Matz, "On Non-WSSUS Wireless Fading Channels," *IEEE Transactions on Wireless Communications*, vol. 4, no. 5, pp. 2465–2478, Sept 2005.

[53] L. Bernado, T. Zemen, F. Tufvesson, A. F. Molisch, and C. F. Mecklenbrauker, "Delay and Doppler Spreads of Nonstationary Vehicular Channels for Safety-Relevant Scenarios," *IEEE Transactions on Vehicular Technology*, vol. 63, no. 1, pp. 82–93, Jan 2014.

[54] R. Sun and D. W. Matolak, "Air-Ground Channel Characterization for Unmanned Aircraft Systems Part II: Hilly and Mountainous Settings," *IEEE Transactions on Vehicular Technology*, vol. 66, no. 3, pp. 1913–1925, March 2017.

[55] D. Matolak and R. Sun, "Air-Ground Channel Characterization for Unmanned Aircraft Systems–Part I: Methods, Measurements, and Models for Over-water Settings," *IEEE Transactions on Vehicular Technology*, vol. PP, no. 99, pp. 1–1, 2016.

[56] D. W. Matolak and R. Sun, "Air-Ground Channel Characterization for Unmanned Aircraft Systems–Part III: The Suburban and Near-Urban Environments," *IEEE Transactions on Vehicular Technology*, vol. 66, no. 8, pp. 6607–6618, Aug 2017.

[57] B. Yang, K. B. Letaief, R. S. Cheng, and Z. Cao, "Channel Estimation for OFDM Transmission in Multipath Fading Channels Based on Parametric Channel Modeling," *IEEE Transactions on Communications*, vol. 49, no. 3, pp. 467–479, Mar 2001.

[58] J.-W. Choi and Y.-H. Lee, "Optimum Pilot Pattern for Channel Estimation in OFDM Systems," *IEEE Transactions on Wireless Communications*, vol. 4, no. 5, pp. 2083–2088, 2005.

[59] D. Gore, R. W. Heath, and A. Paulraj, "On Performance of the Zero Forcing Receiver in Presence of Transmit Correlation," in *Proceedings of the IEEE International Symposium on Information Theory*, 2002, p. 159.

[60] Y. Li and L. J. Cimini, "Bounds on the Interchannel Interference of OFDM in Time-varying Impairments," *IEEE Transactions on Communications*, vol. 49, no. 3, pp. 401–404, 2001.

[61] Y. Li, "Pilot-Symbol-aided Channel Estimation for OFDM in Wireless Systems," *IEEE Transactions on Vehicular Technology*, vol. 49, no. 4, pp. 1207–1215, Jul 2000.

[62] J. Kim, J. Park, and D. Hong, "Performance Analysis of Channel Estimation in OFDM Systems," *Signal Processing Letters, IEEE*, vol. 12, no. 1, pp. 60–62, Jan 2005.

[63] W. C. Jakes and D. C. Cox, *Microwave mobile communications*. Wiley-IEEE Press, 1994.

[64] T. Cui and C. Tellambura, "Power Delay Profile and Noise Variance Estimation for OFDM," *IEEE Communications Letters*, vol. 10, no. 1, pp. 25–27, Jan 2006.

[65] H. Xu, G. Wei, and J. Zhu, "A Novel SNR Estimation Algorithm for OFDM," in *2005 IEEE 61st Vehicular Technology Conference*, vol. 5, May 2005, pp. 3068–3071 Vol. 5.

[66] F. A. Dietrich and W. Utschick, "Pilot-Assisted Channel Estimation based on Second-Order Statistics," *IEEE Transactions on Signal Processing*, vol. 53, no. 3, pp. 1178–1193, 2005.

[67] ITU, "ITURM Recommendation M.1225: Guidelines for Evaluation of Radio Transmission Technologies for IMT-2000," *International Telecommunication Union*, 1997.

[68] 3GPP, "User Equipment (UE) Radio Transmission and Reception," *3rd Generation Partnership Project; Technical Specification Group Radio Access Network; Evolved Universal Terrestrial Radio Access*, 2014.

[69] Y. Zeng, R. Zhang, and T. J. Lim, "Wireless Communications with Unmanned Aerial Vehicles: Opportunities and Challenges," *IEEE Communications Magazine*, vol. 54, no. 5, pp. 36–42, May 2016.

[70] J. C. Ikuno, M. Wrulich, and M. Rupp, "System Level Simulation of LTE Networks," in *2010 IEEE 71st Vehicular Technology Conference*, May 2010, pp. 1–5.

[71] M. K. Ozdemir and H. Arslan, "Channel Estimation for Wireless OFDM Systems," *IEEE Communications Surveys Tutorials*, vol. 9, no. 2, pp. 18–48, second quarter 2007.

[72] Z. Shen, A. Papasakellariou, J. Montojo, D. Gerstenberger, and F. Xu, "Overview of 3GPP LTE-Advanced Carrier Aggregation for 4G Wireless Communications," *IEEE Communications Magazine*, vol. 50, no. 2, pp. 122–130, February 2012.

[73] R. M. Rao, V. Marojevic, and J. H. Reed, "Analysis of Non-Pilot Interference on Link Adaptation and Latency in Cellular Networks," in *IEEE 89th Vehicular Technology Conference (VTC2019-Spring)*, April 2019, pp. 1–5.

[74] P. Andres-Maldonado, P. Ameigeiras, J. Prados-Garzon, J. Navarro-Ortiz, and J. M. Lopez-Soler, "Narrowband IoT Data Transmission Procedures for Massive Machine-Type Communications," *IEEE Network*, vol. 31, no. 6, pp. 8–15, November 2017.

[75] A. Kumbhar, F. Koohifar, İ. Guvenc, and B. Mueller, "A Survey on Legacy and Emerging Technologies for Public Safety Communications," *IEEE Communications Surveys Tutorials*, vol. 19, no. 1, pp. 97–124, Firstquarter 2017.

[76] G. C. Madueño, J. J. Nielsen, D. M. Kim, N. K. Pratas, Č. Stefanović, and P. Popovski, "Assessment of LTE Wireless Access for Monitoring of Energy Distribution in the Smart Grid," *IEEE Journal on Selected Areas in Communications*, vol. 34, no. 3, pp. 675–688, 2016.

[77] M. Lichtman, R. P. Jover, M. Labib, R. M. Rao, V. Marojevic, and J. H. Reed, "LTE/LTE-A Jamming, Spoofing, and Sniffing: Threat Assessment and Mitigation," *IEEE Communications Magazine*, vol. 54, no. 4, pp. 54–61, April 2016.

[78] R. M. Rao, S. Ha, V. Marojevic, and J. H. Reed, "LTE PHY Layer Vulnerability Analysis and Testing Using Open-Source SDR Tools," in *MILCOM 2017 - 2017 IEEE Military Communications Conference (MILCOM)*, 2017, pp. 744–749.

[79] V. Marojevic, R. M. Rao, S. Ha, and J. H. Reed, "Performance Analysis of a Mission-Critical Portable LTE System in Targeted RF Interference," in *2017 IEEE 86th Vehicular Technology Conference (VTC-Fall)*, 2017, pp. 1–6.

[80] C. Shahriar, M. L. Pan, M. Lichtman, T. C. Clancy, R. McGwier, R. Tandon, S. Sodagari, and J. H. Reed, "PHY-Layer Resiliency in OFDM Communications: A Tutorial," *IEEE Communications Surveys Tutorials*, vol. 17, no. 1, pp. 292–314, Firstquarter 2015.

[81] A. El-Keyi, O. Ureten, H. Yanikomeroglu, and T. Yensen, "LTE for Public Safety Networks: Synchronization in the Presence of Jamming," *IEEE Access*, vol. 5, pp. 20 800–20 813, 2017.

[82] T. C. Clancy, "Efficient OFDM Denial: Pilot Jamming and Pilot Nulling," in *2011 IEEE International Conference on Communications (ICC)*, June 2011, pp. 1–5.

[83] J. A. Mahal and T. C. Clancy, "The Closed-form BER Expressions of PSK Modulation for OFDM and SC-FDMA under Jamming and Imperfect Channel Estimation," in *2014 IEEE International Conference on Communications (ICC)*, June 2014, pp. 2221–2226.

[84] C. Shahriar, R. McGwier, and T. C. Clancy, "Performance Impact of Pilot Tone Randomization to Mitigate OFDM Jamming Attacks," in *2013 IEEE 10th Consumer Communications and Networking Conference (CCNC)*, Jan 2013, pp. 813–816.

[85] M. Karlsson, E. Björnson, and E. G. Larsson, "Jamming a TDD Point-to-Point Link Using Reciprocity-Based MIMO," *IEEE Transactions on Information Forensics and Security*, vol. 12, no. 12, pp. 2957–2970, Dec 2017.

[86] D. Xu, P. Ren, and J. A. Ritcey, "Independence-Checking Coding for OFDM Channel Training Authentication: Protocol Design, Security, Stability, and Tradeoff Analysis," *IEEE Transactions on Information Forensics and Security*, vol. 14, no. 2, pp. 387–402, Feb 2019.

[87] J. Kakar, K. McDermott, V. Garg, M. Lichtman, V. Marojevic, and J. H. Reed, "Analysis and Mitigation of Interference to the LTE Physical Control Format Indicator Channel," in *IEEE Military Communications Conference*, Oct 2014, pp. 228–234.

[88] M. Lichtman, T. Czauski, S. Ha, P. David, and J. H. Reed, "Detection and Mitigation of Uplink Control Channel Jamming in LTE," in *IEEE Military Communications Conference*, Oct 2014, pp. 1187–1194.

[89] M. Labib, V. Marojevic, and J. H. Reed, "Analyzing and Enhancing the Resilience of LTE/LTE-A Systems to RF Spoofing," in *IEEE Conference on Standards for Communications and Networking (CSCN)*, Oct 2015, pp. 315–320.

[90] M. Labib, V. Marojevic, J. H. Reed, and A. I. Zaghloul, "Enhancing the Robustness of LTE Systems: Analysis and Evolution of the Cell Selection Process," *IEEE Communications Magazine*, vol. 55, no. 2, pp. 208–215, February 2017.

[91] R. P. Jover, J. Lackey, and A. Raghavan, "Enhancing the security of LTE networks against jamming attacks," *EURASIP Journal on Information Security*, vol. 2014, no. 1, pp. 1–14, 2014.

[92] M. Lichtman, R. M. Rao, V. Marojevic, J. Reed, and R. P. Jover, "5G NR Jamming, Spoofing, and Sniffing: Threat Assessment and Mitigation," in *2018 IEEE International Conference on Communications Workshops (ICC Workshops)*, May 2018, pp. 1–6.

[93] R. P. Jover and V. Marojevic, "Security and Protocol Exploit Analysis of the 5G Specifications," *IEEE Access*, vol. 7, pp. 24 956–24 963, 2019.

[94] J. Nam, A. Adhikary, J. Ahn, and G. Caire, "Joint Spatial Division and Multiplexing: Opportunistic Beamforming, User Grouping and Simplified Downlink Scheduling," *IEEE Journal of Selected Topics in Signal Processing*, vol. 8, no. 5, pp. 876–890, Oct 2014.

[95] W. Shen, L. Dai, B. Shim, Z. Wang, and R. W. Heath, "Channel Feedback Based on AoD-Adaptive Subspace Codebook in FDD Massive MIMO Systems," *IEEE Transactions on Communications*, vol. 66, no. 11, pp. 5235–5248, Nov 2018.

[96] M. Lichtman, J. H. Reed, T. C. Clancy, and M. Norton, "Vulnerability of LTE to Hostile Interference," in *2013 IEEE Global Conference on Signal and Information Processing*, 2013, pp. 285–288.

[97] G. Ku and J. M. Walsh, "Resource Allocation and Link Adaptation in LTE and LTE Advanced: A Tutorial," *IEEE Communications Surveys Tutorials*, vol. 17, no. 3, pp. 1605–1633, 3rd Quarter 2015.

[98] S. Schwarz, J. Ikuno, M. Simko, M. Taranetz, Q. Wang, and M. Rupp, "Pushing the Limits of LTE: A Survey on Research Enhancing the Standard," *IEEE Access*, vol. 1, pp. 51–62, 2013.

[99] H. Zhuang, "Rate Adaptive Hybrid ARQ With Optimal Spectral Efficiency and Delay Tradeoff," *IEEE Transactions on Wireless Communications*, vol. 16, no. 6, pp. 4052–4064, June 2017.

[100] B. Toghi, M. Saifuddin, H. N. Mahjoub, M. O. Mughal, Y. P. Fallah, J. Rao, and S. Das, "Multiple Access in Cellular V2X: Performance Analysis in Highly Congested Vehicular Networks," in *2018 IEEE Vehicular Networking Conference (VNC)*, 2018, pp. 1–8.

[101] R. M. Rao, V. Marojevic, and J. H. Reed, "Probability of Pilot Interference in Pulsed Radar-Cellular Coexistence: Fundamental Insights on Demodulation and Limited CSI Feedback," *IEEE Communications Letters*, vol. 24, no. 8, pp. 1678–1682, Aug 2020.

[102] A. Ghosh, A. Maeder, M. Baker, and D. Chandramouli, "5G Evolution: A View on 5G Cellular Technology Beyond 3GPP Release 15," *IEEE Access*, vol. 7, pp. 127 639–127 651, 2019.

[103] ITU, "Characteristics of and Protection Criteria for Radars Operating in the Radiodetermination Service in the Frequency Band 3100-3700 MHz," *Rec. ITU-R M.1465-3*, Jan 2018.

[104] S. Qiu, Da Chen, D. Qu, K. Luo, and T. Jiang, "Downlink Precoding With Mixed Statistical and Imperfect Instantaneous CSI for Massive MIMO Systems," *IEEE Transactions on Vehicular Technology*, vol. 67, no. 4, pp. 3028–3041, April 2018.

[105] F. Liu, A. Garcia-Rodriguez, C. Masouros, and G. Geraci, "Interfering Channel Estimation in Radar-Cellular Coexistence: How Much Information Do We Need?" *IEEE Transactions on Wireless Communications*, vol. 18, no. 9, pp. 4238–4253, Sep. 2019.

[106] D. J. Love, R. W. Heath, V. K. N. Lau, D. Gesbert, B. D. Rao, and M. Andrews, "An Overview of Limited Feedback in Wireless Communication Systems," *IEEE Journal of Selected Areas in Communications*, vol. 26, no. 8, pp. 1341–1365, October 2008.

[107] 3GPP, "5G NR;Physical Layer Procedures for Data," *3GPP TS 138.214 v15.2.0*, July 2018.

[108] H. Safavi-Naeini, C. Ghosh, E. Visotsky, R. Ratasuk, and S. Roy, "Impact and Mitigation of Narrow-Band Radar Interference in Downlink LTE," in *2015 IEEE International Conference on Communications (ICC)*, June 2015, pp. 2644–2649.

[109] I. V. L. Clarkson, J. E. Perkins, and I. M. Y. Mareels, "Number/Theoretic Solutions to Intercept Time Problems," *IEEE Transactions on Information Theory*, vol. 42, no. 3, pp. 959–971, May 1996.

[110] R. M. Rao, "Perspectives of Jamming, Mitigation and Pattern Adaptation of OFDM Pilot Signals for the Evolution of Wireless Networks," Master's thesis, Virginia Polytechnic Institute and State University, Blacksburg, VA, 24061, USA, 2016.

[111] C. D'Andrea, S. Buzzi, and M. Lops, "Communications and Radar Coexistence in the Massive MIMO Regime: Uplink Analysis," *IEEE Transactions on Wireless Communications*, vol. 19, no. 1, pp. 19–33, Jan 2020.

[112] A. Khawar, A. Abdelhadi, and T. C. Clancy, "Coexistence Analysis Between Radar and Cellular System in LoS Channel," *IEEE Antennas and Wireless Propagation Letters*, vol. 15, pp. 972–975, 2016.

[113] ETSI, "5G;Study on Channel Model for Frequencies from 0.5 to 100 GHz (3GPP TR 38.901 version 14.0.0 Release 14)," *3GPP*, May 2017.

[114] B. Hassibi and B. M. Hochwald, "How Much Training is Needed in Multiple-Antenna Wireless Links?" *IEEE Transactions on Information Theory*, vol. 49, no. 4, pp. 951–963, April 2003.

[115] Y. Liu and Q. Zhang, "Improved Method for Deinterleaving Radar Signals and Estimating PRI Values," *IET Radar, Sonar Navigation*, vol. 12, no. 5, pp. 506–514, 2018.

[116] R. M. Rao, V. Marojevic, and J. H. Reed, "Semi-Blind Post-Equalizer SINR Estimation and Dual CSI Feedback for Radar-Cellular Coexistence," *IEEE Transactions on Vehicular Technology*, vol. 69, no. 9, pp. 1–1, Sept 2020.

[117] W. L. Ross, "Annual Report on the Status of Spectrum Repurposing," August 2019. [Online]. Available: https://www.ntia.doc.gov/files/ntia/publications/spectrum_repurposing_report_august_2019.pdf

[118] 3GPP, "LTE; Evolved Universal Terrestrial Radio Access (E-UTRA);Physical layer procedures (release 14)," *ETSI TS 136 213 v14.3.0*, June 2017.

[119] G. Naik, B. Choudhury, and J. Park, "IEEE 802.11bd 5G NR V2X: Evolution of Radio Access Technologies for V2X Communications," *IEEE Access*, vol. 7, pp. 70 169–70 184, 2019.

[120] J. A. Mahal, A. Khawar, A. Abdelhadi, and T. C. Clancy, "Spectral Coexistence of MIMO Radar and MIMO Cellular System," *IEEE Transactions on Aerospace and Electronic Systems*, vol. 53, no. 2, pp. 655–668, April 2017.

[121] F. Liu, C. Masouros, A. Li, and T. Ratnarajah, "Robust MIMO Beamforming for Cellular and Radar Coexistence," *IEEE Wireless Communications Letters*, vol. 6, no. 3, pp. 374–377, June 2017.

[122] B. Li, A. P. Petropulu, and W. Trappe, "Optimum Co-Design for Spectrum Sharing between Matrix Completion Based MIMO Radars and a MIMO Communication System," *IEEE Transactions on Signal Processing*, vol. 64, no. 17, pp. 4562–4575, Sep. 2016.

[123] B. Tang and J. Li, "Spectrally Constrained MIMO Radar Waveform Design Based on Mutual Information," *IEEE Transactions on Signal Processing*, vol. 67, no. 3, pp. 821–834, Feb 2019.

[124] M. Bica, K. Huang, V. Koivunen, and U. Mitra, "Mutual Information Based Radar Waveform Design for Joint Radar and Cellular Communication Systems," in *2016 IEEE International Conference on Acoustics, Speech and Signal Processing (ICASSP)*, March 2016, pp. 3671–3675.

[125] S. Kim, J. Choi, and C. Dietrich, "PSUN: An OFDM-Pulsed Radar Coexistence Technique with Application to 3.5 GHz LTE," *Mobile Information Systems*, vol. 2016, 2016.

[126] M. Carrick, J. H. Reed, and C. M. Spooner, "Mitigating Linear-Frequency-Modulated Pulsed Radar Interference to OFDM," *IEEE Transactions on Aerospace and Electronic Systems*, vol. 55, no. 3, pp. 1146–1159, June 2019.

[127] M. Ghorbanzadeh, E. Visotsky, P. Moorut, and C. Clancy, "Radar Interference into LTE Base Stations in the 3.5 GHz Band," *Physical Communication*, vol. 20, pp. 33–47, 2016.

[128] M. Rupp, S. Black, and M. Taranetz, *The Vienna LTE-Advanced Simulator*. Springer, 2016, vol. 31.

[129] E. Charles and B. Marvin, *Radar Signals: An Introduction to Theory and Application*, 1993.

[130] S. Baumgartner and G. Hirtz, "A Blind ML-SNR Estimation Method for OFDM Systems in Dispersive Fading Channels," in *2014 IEEE Fourth International Conference on Consumer Electronics Berlin (ICCE-Berlin)*, Sept 2014, pp. 475–479.

[131] F. X. Socheleau, A. Aissa-El-Bey, and S. Houcke, "Non Data-aided SNR Estimation of OFDM Signals," *IEEE Communications Letters*, vol. 12, no. 11, pp. 813–815, November 2008.

[132] Y. Chen and N. C. Beaulieu, "NDA Estimation of SINR for QAM Signals," *IEEE Communications Letters*, vol. 9, no. 8, pp. 688–690, Aug 2005.

[133] S. Hong, Y. Li, Y. C. He, G. Wang, and M. Jin, "A Cyclic Correlation-Based Blind SINR Estimation for OFDM Systems," *IEEE Communications Letters*, vol. 16, no. 11, pp. 1832–1835, November 2012.

[134] S. K. Pulliyakode, S. Kalyani, and K. Narendran, "Rate Prediction and Selection in LTE Systems Using Modified Source Encoding Techniques," *IEEE Transactions on Wireless Communications*, vol. 15, no. 1, pp. 416–429, Jan 2016.

[135] A. M. Mansour, A. E. R. Nada, and A. H. Mehana, "Effect of Noise Variance Estimation on Channel Quality Indicator in LTE Systems," in *2015 IEEE Global Conference on Signal and Information Processing (GlobalSIP)*, Dec 2015, pp. 156–160.

[136] Ping Li, D. Paul, R. Narasimhan, and J. Cioffi, "On the Distribution of SINR for the MMSE MIMO Receiver and Performance Analysis," *IEEE Transactions on Information Theory*, vol. 52, no. 1, pp. 271–286, Jan 2006.

[137] S. N. Donthi and N. B. Mehta, "An Accurate Model for EESM and its Application to Analysis of CQI Feedback Schemes and Scheduling in LTE," *IEEE Transactions on Wireless Communications*, vol. 10, no. 10, pp. 3436–3448, October 2011.

[138] R. C. Daniels, C. M. Caramanis, and R. W. Heath, "Adaptation in Convolutionally Coded MIMO-OFDM Wireless Systems Through Supervised Learning and SNR Ordering," *IEEE Transactions on Vehicular Technology*, vol. 59, no. 1, pp. 114–126, Jan 2010.

[139] M. Abramowitz and I. A. Stegun, *Handbook of Mathematical Functions: with Formulas, Graphs, and Mathematical Tables*. Courier Corporation, 2012.

[140] K. Nishiguchi and M. Kobayashi, "Improved Algorithm for Estimating Pulse Repetition Intervals," *IEEE Transactions on Aerospace and Electronic Systems*, vol. 36, no. 2, pp. 407–421, 2000.

[141] 3GPP, "LTE; Evolved Universal Terrestrial Radio Access (E-UTRA);Physical layer procedures," *ETSI TS 136 213 v12.4.0*, Feb 2015.

[142] R. M. Rao, H. S. Dhillon, V. Marojevic, and J. H. Reed, "Underlay Radar-Massive MIMO Spectrum Sharing: Modeling Fundamentals and Performance Analysis," *arXiv preprint arXiv:2008.02100*, 2020.

[143] R. M. Rao, H. Dhillon, V. Marojevic, and J. Reed, "Analysis of Worst-Case Interference in Underlay Radar-Massive MIMO Spectrum Sharing Scenarios," in *2019 IEEE Global Communications Conference (GLOBECOM)*, Dec 2019, pp. 1–6.

[144] S. M. Dudley, W. C. Headley, M. Lichtman, E. Y. Imana, X. Ma, M. Abdelbar, A. Padaki, A. Ullah, M. M. Sohul, T. Yang, and J. H. Reed, "Practical Issues for Spectrum Management With Cognitive Radios," *Proceedings of the IEEE*, vol. 102, no. 3, pp. 242–264, 2014.

[145] R. M. Rao, D. Bethanabhotla, and R. C. Palat, "Enhancing Throughput Using Agile Beam Switching and User Scheduling in Cellular Systems," in *2019 IEEE 90th Vehicular Technology Conference (VTC2019-Fall)*, 2019, pp. 1–7.

[146] S. Biswas, K. Singh, O. Taghizadeh, and T. Ratnarajah, "Coexistence of MIMO Radar and FD MIMO Cellular Systems With QoS Considerations," *IEEE Transactions on Wireless Communications*, vol. 17, no. 11, pp. 7281–7294, Nov 2018.

[147] Y. Li, F. Baccelli, J. G. Andrews, T. D. Novlan, and J. C. Zhang, "Modeling and Analyzing the Coexistence of Wi-Fi and LTE in Unlicensed Spectrum," *IEEE Transactions on Wireless Communications*, vol. 15, no. 9, pp. 6310–6326, Sep. 2016.

[148] H. Hu, Y. Gao, J. Zhang, X. Chu, Q. Chen, and J. Zhang, "Density Analysis of LTE-LAA Networks Coexisting With WiFi Sharing Multiple Unlicensed Channels," *IEEE Access*, vol. 7, pp. 148 004–148 018, 2019.

[149] P. Parida, H. S. Dhillon, and P. Nuggehalli, "Stochastic Geometry-Based Modeling and Analysis of Citizens Broadband Radio Service System," *IEEE Access*, vol. 5, pp. 7326–7349, 2017.

[150] S. Kim and C. Dietrich, "Coexistence of Outdoor Wi-Fi and Radar at 3.5 GHz," *IEEE Wireless Communications Letters*, vol. 6, no. 4, pp. 522–525, Aug 2017.

[151] H. Chen, L. Liu, H. S. Dhillon, and Y. Yi, "QoS-Aware D2D Cellular Networks With Spatial Spectrum Sensing: A Stochastic Geometry View," *IEEE Transactions on Communications*, vol. 67, no. 5, pp. 3651–3664, 2019.

[152] H. Chen, L. Liu, T. Novlan, J. D. Matyjas, B. L. Ng, and J. Zhang, "Spatial Spectrum Sensing-Based Device-to-Device Cellular Networks," *IEEE Transactions on Wireless Communications*, vol. 15, no. 11, pp. 7299–7313, 2016.

[153] M. Mozaffari, W. Saad, M. Bennis, and M. Debbah, "Unmanned Aerial Vehicle With Underlaid Device-to-Device Communications: Performance and Tradeoffs," *IEEE Transactions on Wireless Communications*, vol. 15, no. 6, pp. 3949–3963, 2016.

[154] B. Shang, L. Liu, R. M. Rao, V. Marojevic, and J. H. Reed, "3D Spectrum Sharing for Hybrid D2D and UAV Networks," *IEEE Transactions on Communications*, vol. 68, no. 9, pp. 1–1, 2020.

[155] T. Bai and R. W. Heath, "Coverage and Rate Analysis for Millimeter-Wave Cellular Networks," *IEEE Transactions on Wireless Communications*, vol. 14, no. 2, pp. 1100–1114, 2015.

[156] M. Rebato, J. Park, P. Popovski, E. De Carvalho, and M. Zorzi, "Stochastic Geometric Coverage Analysis in mmWave Cellular Networks With Realistic Channel and Antenna Radiation Models," *IEEE Transactions on Communications*, vol. 67, no. 5, pp. 3736–3752, 2019.

[157] S. Kim, E. Visotsky, P. Moorut, K. Bechta, A. Ghosh, and C. Dietrich, "Coexistence of 5G With the Incumbents in the 28 and 70 GHz Bands," *IEEE Journal on Selected Areas in Communications*, vol. 35, no. 6, pp. 1254–1268, June 2017.

[158] M. Baianifar, S. Khavari, S. M. Razavizadeh, and T. Svensson, "Impact of User Height on the Coverage of 3D Beamforming-enabled Massive MIMO Systems," in *2017 IEEE 28th Annual International Symposium on Personal, Indoor, and Mobile Radio Communications (PIMRC)*, Oct 2017, pp. 1–5.

[159] J. Yang, M. Ding, G. Mao, Z. Lin, D. Zhang, and T. H. Luan, "Optimal Base Station Antenna Downtilt in Downlink Cellular Networks," *IEEE Transactions on Wireless Communications*, pp. 1–1, 2019.

[160] P. Calka, "The Distributions of the Smallest Disks Containing the Poisson-Voronoi Typical Cell and the Crofton Cell in the Plane," *Advances in Applied Probability*, vol. 34, no. 4, pp. 702–717, 2002.

[161] V. V. Chetlur and H. S. Dhillon, "Downlink Coverage Analysis for a Finite 3-D Wireless Network of Unmanned Aerial Vehicles," *IEEE Transactions on Communications*, vol. 65, no. 10, pp. 4543–4558, 2017.

[162] J. Schloemann, H. S. Dhillon, and R. M. Buehrer, "Toward a Tractable Analysis of Localization Fundamentals in Cellular Networks," *IEEE Transactions on Wireless Communications*, vol. 15, no. 3, pp. 1768–1782, 2016.

[163] R. W. Heath, M. Kountouris, and T. Bai, "Modeling Heterogeneous Network Interference Using Poisson Point Processes," *IEEE Transactions on Signal Processing*, vol. 61, no. 16, pp. 4114–4126, 2013.

[164] X. Kang, Y. Liang, H. K. Garg, and L. Zhang, "Sensing-Based Spectrum Sharing in Cognitive Radio Networks," *IEEE Transactions on Vehicular Technology*, vol. 58, no. 8, pp. 4649–4654, 2009.

[165] J. G. Andrews, A. K. Gupta, and H. S. Dhillon, "A Primer on Cellular Network Analysis using Stochastic Geometry," *arXiv preprint arXiv:1604.03183*, 2016.

[166] M. Haenggi, "On Distances in Uniformly Random Networks," *IEEE Transactions on Information Theory*, vol. 51, no. 10, pp. 3584–3586, 2005.

[167] Y. Hung and S. L. Tsai, "PAPR Analysis and Mitigation Algorithms for Beamforming MIMO OFDM Systems," *IEEE Transactions on Wireless Communications*, vol. 13, no. 5, pp. 2588–2600, 2014.

[168] H. ElSawy, E. Hossain, and M. Haenggi, "Stochastic Geometry for Modeling, Analysis, and Design of Multi-Tier and Cognitive Cellular Wireless Networks: A Survey," *IEEE Communications Surveys Tutorials*, vol. 15, no. 3, pp. 996–1019, 2013.

[169] ETSI, "Evolved Universal Terrestrial Radio Access (E-UTRA); Multiplexing and channel coding (3GPP TS 36.212 version 14.2.0), Release 14," *3GPP*, April 2017.